

DIGITAL ACCESS TO SCHOLARSHIP AT HARVARD
DASH.HARVARD.EDU

HARVARD LIBRARY


An Improved Measurement of the Electron Magnetic Moment

Citation

Fan, Xing. 2022. An Improved Measurement of the Electron Magnetic Moment. Doctoral dissertation, Harvard University Graduate School of Arts and Sciences.

Link

https://nrs.harvard.edu/URN-3:HUL.INSTREPOS:37373668

Terms of use

This article was downloaded from Harvard University's DASH repository, and is made available under the terms and conditions applicable to Other Posted Material (LAA), as set forth at

https://harvardwiki.atlassian.net/wiki/external/NGY5NDE4ZjgzNTc5NDQzMGIzZWZhMGFlOWI2M2EwYTg

Accessibility

https://accessibility.huit.harvard.edu/digital-accessibility-policy

Share Your Story

The Harvard community has made this article openly available.
Please share how this access benefits you. Submit a story

HARVARD UNIVERSITY
Graduate School of Arts and Sciences



DISSERTATION ACCEPTANCE CERTIFICATE

The undersigned, appointed by the

Department of Physics

have examined a dissertation entitled

An Improved Measurement of the Electron Magnetic Moment

presented by Xing Fan

candidate for the degree of Doctor of Philosophy and hereby certify that it is worthy of acceptance.

Signature _____

Typed name: Professor Gerald Gabrielse, Chair

Signature _____

Typed name: Professor Masahiro Morii

Signature _____

Typed name: Professor Ronald Walsworth (Univ. of Maryland)

Date: August 25, 2022

An Improved Measurement of the Electron Magnetic Moment

A dissertation presented

by

Xing Fan

to

The Department of Physics

in partial fulfilment of the requirements

for the degree of

Doctor of Philosophy

in the subject of

Physics

Faculty Advisor: Gerald Gabrielse

Harvard University

Cambridge Massachusetts

August 2022

©2022 - Xing Fan

All rights reserved.

Dissertation advisor | Author

Gerald Gabrielse | **Xing Fan**

An Improved Measurement of the Electron Magnetic Moment

Abstract

A single isolated electron in a Penning trap yields a new measurement of the electron magnetic moment $g/2 = 1.001\ 159\ 652\ 180\ 59\ (13)$. Combined with the Standard Model calculation, this yields an independent determination of the fine structure constant $\alpha^{-1} = 137.035\ 999\ 166\ (16)$. Comparison of the measured g-factor and the predicted g-factor using an independent measurement of the fine structure constant yields the most stringent test of the Standard Model.

A new dilution refrigerator–superconducting solenoid system with significantly improved stability has been constructed. The new system has a more robust mechanical joint, which improves the long-term stability of the magnetic field. A Helium-3-based cryogenic NMR probe has been invented and used to optimize the homogeneity and the drift rate of the cryogenic bore magnet. The achieved low drift rate and robustness enables measurement of the g-factor at many widely different fields for the first time.

The statistical uncertainty has been improved by a factor of 4 because of the newly developed system. The large systematic shift—microwave cavity correction—is studied in an eight times wider parameter range. A new correction model and characterization methods have been proposed. The g-factor is measured at 11 fields to confirm the new systematic correction method.

Three developments to improve the systematic error and precision for future measurements have been proposed and demonstrated. A new trap with an order of magnitude better anharmonicity is proposed and designed. The new trap is smaller than the current trap to suppress the microwave cavity correction. A new scheme to measure g-factor with direct measurement of the spin frequency is proposed and demonstrated. A superconducting quan-

tum limited detector has been also developed to achieve 20 times narrower linewidth. All developments promise an improved measurement of the electron's g-factor.

The constructed system has been also used to search dark photon dark matter. The single trapped electron is used as a background-free detector at 0.6 meV. A new limit on dark photon is set with a week of data. The search demonstrates the sensitivity of the single electron and guarantees a future search in the 0.1–1 meV range.

The newly constructed system and a better understanding of the systematic error allow tests of the Standard Model and theories beyond it in many aspects. The same technique can be applied for the positron's g-factor measurement, which will be the most precise test of CPT in the lepton sector.

Publications

Parts of this dissertation have been previously reported in the following papers.

1. "Towards an Improved Test of the Standard Models Most Precise Prediction"

   G. Gabrielse, S. E. Fayer, T. G. Myers, and X. Fan, *Atoms*, **7**, 45 (2019)

2. "Gaseous ^{3}He Nuclear Magnetic Resonance Probe for Cryogenic Environments"

   X. Fan, S. E. Fayer, and G. Gabrielse, *Rev. Sci. Instrum.* **90**, 083107 (2019)

3. "Two-Symmetry Penning-Ioffe Trap for Antihydrogen Cooling and Spectroscopy"

   E. Tardiff, X. Fan, G. Gabrielse, D. Grzonka, C. Hamley, E. A. Hessels, N. Jones, G. Khatri, S. Kolthammer, D. M. Zambrano, C. Meisenhelder, T. Morrison, E. Nottet, E. Novitski, C. H. Storry, *Nucl. Instrum. Meth. A* **977**, 164279 (2020)

4. "Switchable Damping for a One-Particle Oscillator"

   X. Fan, S. E. Fayer, T. G. Myers, B. A. D.Sukra, G. Nahal, and G. Gabrielse, *Rev. Sci. Instrum.* **92**, 023201 (2021)

5. "Circumventing Detector Backaction on a Quantum Cyclotron"

   X. Fan and G. Gabrielse, *Phys. Rev. Lett.* **126**, 070402 (2021)

6. "Driven One-Particle Quantum Cyclotron"

   X. Fan and G. Gabrielse, *Phys. Rev. A* **103**, 022824 (2021)

7. "One-Electron Quantum Cyclotron as a Milli-eV Dark-Photon Detector"

   X. Fan, G. Gabrielse, P. W. Graham, R. Harnik, T. G. Myers, H. Ramani, B. A. D. Sukra, S. S. Y. Wong, Y. Xiao, *arxiv e-print* 2208.06519 (2022), submitted to *Phys. Rev. Lett.*

8. "An Improved Measurement of the Electron Magnetic Moment"

   X. Fan, G. Gabrielse, T. G. Myers, B. A. D. Sukra, manuscript in preparation.

Contents

Title Page **i**

Copyright **ii**

Abstract **iii**

Publications **v**

List of Figures **ix**

List of Tables **xvi**

Acknowledgements **xviii**

1 The Electron Magnetic Moment **1**

1.1 The Standard Model Calculation 2

1.2 The Fine Structure Constant α 4

1.3 Physics Beyond the Standard Model 8

1.4 New Measurement of the Electron g-Factor 11

2 The Penning Trap **13**

2.1 Motion of an Electron in a Penning Trap 15

2.2 Apparatus 22

2.3 Detecting the Motion of the Electron 33

2.4 Summary 53

3 Gaseous Helium-3 Cryogenic NMR Probe 54

3.1 Principle of Pulsed Fourier Transform NMR 55

3.2 Design and Construction of the Probe 64

3.3 Spin Precession Signal 68

3.4 Longitudinal and Transverse Time Constants 73

3.5 Stability of a Cold Bore Solenoid Magnet 79

3.6 Future Improvements 81

4 Measurement of the Electron Magnetic Moment 83

4.1 Principle of Measurement 83

4.2 Spectroscopy 96

4.3 Microwave Cavity Correction 107

4.4 Other Systematic Effects 137

4.5 Determination of g-factor 149

5 Towards Relativistic Bottle Detection with a Quantum Limited Detector 155

5.1 Relativistic Bottle 157

5.2 Orthogonalized and Compensated $C_6 = 0$ Trap 157

5.3 Directly Driven Spin Flip 163

5.4 Quantum Limited Detector With a New Magnet 168

5.5 Summary of Improvements and Remaining Developments 180

6 Search for Dark Photon using a Single Electron 185

6.1 Dark Matter and Dark Photon 185

6.2 Principle of the Search 190

6.3 Search for Dark Photon Dark Matter 195

6.4 Future Improvements 199

7 Conclusion **206**

A Microwave Resonances Probed by a Cloud of Electrons **208**

A.1 Mapping Penning Trap Microwave Resonances 209

A.2 Characterizing the Internal Motion 214

A.3 Summary 221

Bibliography **224**

List of Figures

1.1 Examples of Feynman diagrams to calculate g-factor. 3

1.2 Comparison of the inverse of the fine structure constant α^{-1}. 7

1.3 Comparison of measured g-factors with prediction. 8

1.4 Contribution of the dark photon to the electron magnetic moment. 9

1.5 Limit on dark photon coupling coefficient χ and mass $m_{A'}$. 10

2.1 Schematic picture of trapping an electron with a Penning trap. 14

2.2 Classical picture of an electron's motion in a Penning trap. 16

2.3 Quantum levels of a trapped electron. 20

2.4 The entire setup of the experiment. 22

2.5 The cylindrical penning trap. 24

2.6 Schematic of titanium trap chamber and silver tripod. 27

2.7 Cross section of the dilution refrigerator and magnet system. 29

2.8 The ringing-in method to suppress drift after changing the magnetic field. . . 30

2.9 Wiring diagram of the Penning trap. 31

2.10 FEP current as a function of bias voltage. 34

2.11 Induced current from trapped particle and resonant circuit. 36

2.12 Location of the helical resonator. 38

2.13 Four drives to detect the axial motion, dip detection, axial excitation, parametric excitation, and self excitation (from left to right). 38

2.14 noise spectrum of the Johnson noise from the LCR resonance circuit without electrons trapped (black) and with about $N = 2000$ electrons trapped (red). 39
2.15 Probing the anharmonicity of the trap using one electron. 41
2.16 Counting the discrete loading of electrons using the parametric drive. 42
2.17 Measurement of the number of trapped electrons and its damping rate γ_z using the decay of parametrically excited motion. 43
2.18 Frequency spectrum of the self-excited one electron. 44
2.19 Split of electron's noise dip at axial frequency due to magnetron-axial sideband coupling. 45
2.20 Shift of magnetic field (top) and axial frequency (bottom) when antisymmetric bias V_A is applied to shift electron's position. 48
2.21 The system to generate and control cyclotron drive at microwave frequency ν_c. 49
2.22 Measured microwave drive width (left) and attenuation on output power (right). 50
2.23 Quantum cyclotron transitions detected by monitoring axial frequency shift with self excitation. 51
2.24 Manipulation of spin state using cyclotron and anomaly drive at $\nu_z = 90$ MHz and $B_2 = 1500$ T/m^2. 53

3.1 Two energy levels of a spin in a magnetic field B. 56
3.2 Change of spin vector $\tilde{S}_y$ and $\tilde{S}_z$ versus the product of drive power and time $\Omega_R t$. 60
3.3 (left) Overview of an NMR probe and support. (right) Expanded view of the NMR sample bulb and its pickup coil. 66
3.4 Circuit used to drive and detect the $\omega_{\rm NMR}/2\pi = 172.3$ MHz NMR signal. . . 67
3.5 The drive pulse sequences for free induction decay (Sec. 3.3) and for both simple and CPMG spin echos (Sec. 3.4). 68
3.6 Dependence of the magnitude of the NMR precession signal upon the drive pulse's duration. 69

3.7 The NMR spin precession signal from the ^{3}He nuclei at 5.3 T, mixed down from 172.3 MHz to 1.5 kHz 70
3.8 Fourier transform of the NMR spin precession signal shown in Fig. 3.7. . . . 70
3.9 The superconducting solenoid system with the ^{3}He NMR probe inserted into the 4.2 K cold bore. 71
3.10 Dependence of the NMR center frequency and linewidth on the azimuthal angle of the probe. 72
3.11 Measurement of the longitudinal relaxation time T_1 with saturation recovery method. 74
3.12 Spin echo signal observed with the ^{3}He NMR probe. 76
3.13 Spin echo signals observed with the ^{3}He NMR probe. 77
3.14 CPMG spin echo decay of ^{3}He measured by the probe with the echo time $\tau = 5$ ms. 78
3.15 Measurement of the ^{3}He center frequency drift. 80
3.16 Design of the cryogenic XY stage. 81

4.1 Quantum spin and cyclotron states of the trapped electron and the cyclotron (blue) and anomaly (red) transitions that are measured for g-factor measurement. . 85
4.2 Line shapes in the classical limit for four different $\gamma_z/\Delta\omega$'s. 88
4.3 Line shape of axially driven electron for different drive broadening parameters $\Delta_p\omega/\Delta\omega$ in loose coupling limit (left) and tight coupling limit (right). 90
4.4 Cycle of g-factor measurement. 95
4.5 Change of axial frequency due to cyclotron and anomaly transitions. 97
4.6 Correction of magnetic field drift. 100
4.7 p-value of the fitting models. 105
4.8 Different fitting of cyclotron line depending on the line shape model. 106
4.9 Typical line shape of cyclotron transition (left) and anomaly transition (right) for one day of data. 107

4.10 Statistical distribution of data around 150 GHz. 108
4.11 Mode mapping using parametrically driven electrons. 110
4.12 Circuit model of superconducting magnet and charging unit. 111
4.13 Change of current on the power supply when (a) swept up and (b) swept down. 112
4.14 Calibration dip in the parametrically excited cloud of electrons' response on TE_{243} mode. 113
4.15 Fitting of measured dip frequency and current (a) in the sweeping up scan and (b) in the sweeping down scan. 113
4.16 Discrepancies of obtained resonant frequencies between sweep up and down in the 135–160GHz range. 114
4.17 Discrepancy of measured resonant frequency from the calculated resonant frequency. 117
4.18 Determination of ρ_0 and z_0 using the TE_{0np} modes. 118
4.19 Three methods to measure γ_c using single electron. 119
4.20 Oscillation power of a parametrically driven single electron with $C_4 = 0$ and $C_6 = -0.1$, with a square-root fitting function shown in red. 121
4.21 Confirmation of mode mapping by a cloud of electrons by the single electron measurements. 122
4.22 Dependence of the correction $\Delta g/2$ at 115 GHz as a function of the number of included modes. 128
4.23 Examples of measurement of microwave offset using p-even modes. 129
4.24 Measured microwave resonant mode's offset using an electron near TE_{116} (left) and TE_{136} (right). 131
4.25 (a) Observed splitting of the degeneracy of TM_{143} mode. (b) Effect of splitting on the measured g-factor. 133
4.26 (top) Applied cavity correction from the measured resonances. (bottom) Uncertainty of the cavity correction. 136

4.27 Measurement of cyclotron drive induced anomaly frequency shift. 138
4.28 Dependence of measured g-factor on the peak cyclotron transition probability. 138
4.29 Observed shift of axial frequency from much stronger anomaly drive power. . 140
4.30 Power shift from the anomaly drive. 142
4.31 Dependence of measured g-factor on the peak anomaly transition probability. 142
4.32 Fluctuation of axial frequency during a run. 143
4.33 S_{21} measurement of the axial detection resonator. 144
4.34 The axial damping rate γ_z measured in three different methods, (a) dip detection, (b) axial driven scan, and (c) free decay method. 145
4.35 Dependence of cyclotron frequency on the temperature of trap can. 147
4.36 Dependence of g-factor on line shape model. 148
4.37 Correlation matrix C_{ij} of the microwave cavity correction uncertainty. Strong correlations among the measurements at nearby fields are visible. 152
4.38 Measured g-factor as a function of the magnetic field. 154

5.1 Dependence of self-excitation frequency on oscillation amplitude. 158
5.2 z_c/z_0 to make $D_2/D_4 = 0$ for given ρ_0/z_0. 160
5.3 C_6 for given ρ_0/z_0. 161
5.4 Microwave resonant modes of the newly designed $C_6 = 0$ trap. 162
5.5 Observation of directly driven spin-flip transition. 165
5.6 Measured lineshape of the spin-flip transition. 165
5.7 Temperature increase of pinbase by spin-flip drives. 166
5.8 Measure axial frequency stability for averaging time. 167
5.9 Measured axial frequency fluctuation $\sigma(\Delta\nu_z)$ for different averaging times. . 168
5.10 The schematics of a DC SQUID. 169
5.11 Schematic diagram of a microstrip SQUID amplifier. 170
5.12 The gain of our fabricated microstrip SQUID amplifier. 172
5.13 Measured noise temperature of the MSA at 3.6 K. 173

5.14 Measurement of saturation of the MSA gain. 175
5.15 RF electronics to detect and impedance match the particle to the MSA amplifier. 175
5.16 Noise resonance observed with the MSA compared to HEMT amplifier. . . . 176
5.17 The schematic of the newly designed magnet (a) and magnetic field of the newly designed magnet (b) 178
5.18 Superconducting double layer magnetic shield by niobium and Bi-2223. . . . 179
5.19 Current model for generating transverse magnetic field drive B_1 by split compensation electrode. 182

6.1 Feynman diagram showing the kinetic mixing of DP field and the ordinary electromagnetic field. 188
6.2 Calculation of κ for wide range (left) and for the range around this search (right). 194
6.3 Enhancement of DP induced electric field (red arrow) by a cylindrical trap (a) and a spherical trap (b). 194
6.4 Measurement cycle for the DPDM search. 195
6.5 Measured line shape with the axial self-excitation on. 196
6.6 Measured n_c every 3 hours. 197
6.7 Monitored quantum state $\tilde{n}_c$ for the first 24 hours. 198
6.8 Distribution of measured $\tilde{n}_c$. 199
6.9 Obtained limit on dark photon dark matter. 200
6.10 Observed axial frequency shift by cyclotron transition for $n_e = 2$ trapped electrons. 201
6.11 Calculation of the enhancement factor κ^2 for a spherical trap. 203
6.12 Expected DPDM limit with $n_e = 10$ electrons using a cavity of radius $\rho_0 =$ 25 mm, with 1 year scan between 20 GHz and 170 GHz. 205

A.1 Mapping the microwave cavity resonances with (a) parametric drive (b) axial drive and (c) magnetron sideband drive. 211

A.2 Fourier spectrum around the axial frequency ν_z when cyclotron frequency is on cavity resonance (black) and off cavity resonance (gray) for (a) parametric drive (b) axial drive and (c) magnetron sideband drive. 212
A.3 Excitation of internal motion of $N = 100$ electrons for different anharmonicity C_4 by (a) parametric drive (b) axial drive, and (c) sideband drive. 214
A.4 Excitation of internal motion of $N = 100$ electrons for different drive power by (a) parametric drive (b) axial drive, and (c) sideband drive with $C_4 = -0.036$. 215
A.5 Exciting the internal motion of $N = 100$ electrons by a microwave drive with anharmonicity parameter $C_4 = -0.036$. 216
A.6 Relaxation of the dip frequency after microwave drive is turned off. 217
A.7 Center of mass oscillation of a cloud for large and small γ_c's with $C_4 = -0.01$ and $P_{\text{axial}} = -30$ dBm axial drive. 218
A.8 Scanning the cyclotron frequency around the TM_{127} mode with different temperatures. 219
A.9 Dependence of threshold power to excite the internal motion on temperature. 220
A.10 (a) Mode mapping with different drive power. (b) Mode mapping with different detuning. 221
A.11 Observed hysteresis of trapped cloud excited by (a) axial drive and (b) magnetron sideband drive for three different excitation powers. 222

List of Tables

1.1 Contribution to the $g/2$ calculation and uncertainties, compared with experimentally measured $g/2$. 5

2.1 Typical frequencies, damping rate, and quantum number for the electron in the Penning trap used for the measurement at 5.3 T. 21

2.2 Typical parameters of the Penning trap. 23

2.3 Anharmonicity parameters that defines the trap potential with $\rho_0 = 4.539$ mm, $z_0 = 3.906$ mm, and $z_c = 0.766$ mm. 26

3.1 Comparison of NMR samples at $B = 5.3$ T. 65

4.1 Data sets used for the g-factor determination. 98

4.2 Summary of calculated and measured modes, with its calculated coupling strength λ_M^2 at the trap center (Sec.4.3.2). 116

4.3 Observed z_{offset} and its uncertainty. 130

4.4 Measurement of radial offset, upper limit of $\gamma_c/(2\pi)$ and calculated ρ_{offset}. . . 131

4.5 Estimated uncertainty from the unmeasured higher frequency resonances at 150.411 GHz. 134

4.6 Estimated uncertainty from the unmeasured lower frequency resonances on measured g-factor at 87.010 GHz. 135

4.7 Summary of measured $g/2-1.001\,159\,652\,180\,59$, microwave cavity correction and its dominant errors. 150

4.8 Summary of statistical and systematic uncertainties. 153

5.1 Designed parameters for the $C_6 = 0$ trap. 163

5.2 List of possible improvements for g-factor measurement. 180

6.1 Data sets for DPDM search in March 2022. 197

Acknowledgments

I would like to thank Professor Gerald Gabrielse for giving me the chance to work on this research. His intuition and experience on experiments, as well as his patience, have always been helpful and have led me to the right approach. I am especially grateful to the people whom I have worked with. Benedict Sukra, Thomas Myers, and Samuel Fayer have been helpful in many aspects: construction and operation of the system, general maintenance of lab issues, analysis, and discussions about the future direction of the experiment. I would like to thank Benedict Sukra and Thomas Myers particularly for running the experiment together most of the time. I have also enjoyed helpful conversations with my committee members, Ron Walsworth and Masahiro Morii. They have been very encouraging about both science and my general Ph.D. life.

I also thank the people whom I overlapped with. The students and postdocs in the Gabrielse group have helped me a lot. I am also proud of having worked with the excellent undergrads—Abhishek Anand, Samuel Detmer, Chi Li, Shungo Fukaya, Alyssa Matthews, and Saif Salim. They have provided wonderful time both in the lab and out the lab.

I am honored to work with our collaborators, Peter Graham, Harikrishnan Ramani, Samuel S. Y. Wong, and Yawen Xiao from Stanford University, and Roni Harnik from Fermi National Accelerator Laboratory. They stimulated the work in Chap. 6 and brought new insight to our system.

The technicians in the machine shop, Salomon Rodriguez, Thang Bui, John Bussan, Bob Golenia, and Dinka Spirovska constructed many substantial parts of our experiment.

Without their efforts, we would never be able to operate the system reliably.

The cryogen technicians at Northwestern University, Steve Jacobson and Robert Pratt, provided generous support. The stable operation of our system is made possible by their continuous assistance.

I would like to thank my parents and family. I am most thankful to my wife Ayami Hiramoto, who makes it all worthwhile. My graduate education and research was generously supported by the Masason Foundation. I am thankful for the continuous support of this experiment by the National Science Foundation, U.S. Department of Energy, Superconducting Quantum Materials and Systems Center, the John Templeton Foundation, and the Masason Foundation.

Chapter 1

The Electron Magnetic Moment

The electron magnetic moment μ_s is measured in the unit of Bohr magneton μ_B as

$$\mu_s = -\frac{g}{2}\left(\frac{e\hbar}{2m}\right) = -\frac{g}{2}\mu_B, \tag{1.1}$$

where e is the elementary charge, $\hbar$ is the reduced Plank constant, m is the mass of an electron, and g is the g-factor. The prediction of g-factor and its measurement are deeply related to the history of the Standard Model (SM) of particle physics. For a classical non-relativistic rotating charge, the g-factor is exactly equal to 1. In 1928, the theory of relativistic quantum mechanics, Dirac's theory [1], predicts $g = 2$. The actual g-factor was found to be about 0.1% larger than 2 in 1947 by the measurement of Kusch and Foley [2]. This discrepancy was called the "anomaly", and at the end of the same year, Schwinger first succeeded in calculating this discrepancy through quantum-electrodynamics (QED) [3]. In the same year, Feynman, Tomonaga, and Schwinger established the renormalization method to calculate higher order corrections of QED [4–6]. Both higher order calculation and experimental precision have evolved up to 10^{-13} or better precision. Together, this allows for the most precise test of the SM [7, 8]. The most precise determination is reported in this thesis as

$$\frac{g}{2} = 1.001\ 159\ 652\ 180\ 59\ (13). \tag{1.2}$$

The g-factor of the electron is the most precisely measured quantity of any elementary particle. Comparison with the theoretical prediction gives the most stringent test of the SM's calculation.

In this chapter, the physics of the electron's g-factor and its implication is summarized. The SM calculation is summarized in Sec. 1.1, the role of the fine structure constant α—an important input parameter in the g-factor calculation—is discussed in Sec. 1.2, the impact on the physics beyond the SM is summarized in Sec. 1.3, and Sec. 1.4 briefly outlines the new measurement of the g-factor.

1.1 The Standard Model Calculation

The Standard Model predicts the g-factor by a series expansion in the fine structure constant α. The calculation requires not only higher order correction from QED but also contributions from virtual hadron creations and weak interaction.

$$\frac{g}{2} = 1 + C_2 \left(\frac{\alpha}{\pi}\right) + C_4 \left(\frac{\alpha}{\pi}\right)^2 + C_6 \left(\frac{\alpha}{\pi}\right)^3 + C_8 \left(\frac{\alpha}{\pi}\right)^4 + C_{10} \left(\frac{\alpha}{\pi}\right)^5 + ... + a_{\mu,\tau} + a_{\text{hadron}} + a_{\text{weak}}. \quad (1.3)$$

Here, the coefficients C_i's are the contribution from virtual electron loops and are predicted by perturbation calculations from QED theory, $a_{\mu,\tau}$ represents the contribution from virtual muon and tauon creation, a_{hadron} represents hadronic interaction, and a_{weak} represents weak interaction. Some examples of Feynman diagrams for the C_i terms are shown in Fig. 1.1. The numbers in the brackets show how many diagrams exist in each order [8].

The coefficients C_2, C_4, C_6, C_8, and C_{10} have been calculated or evaluated with intensive

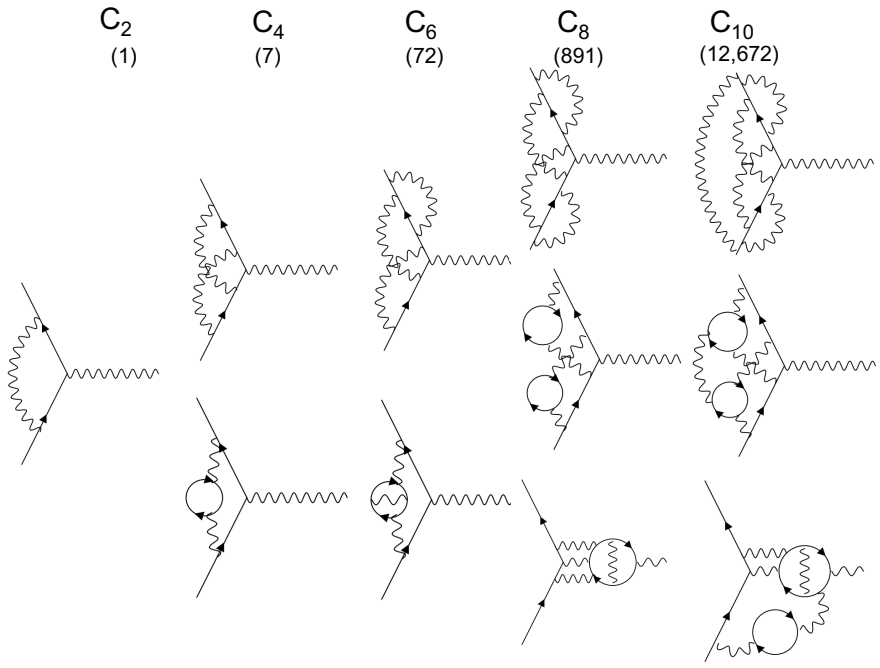


Figure 1.1: Examples of Feynman diagrams to calculate g-factor. The numbers in the bracket show the number of Feynman diagrams in each order.

effort using higher order QED theory,

$$C_2 = \frac{1}{2} = 0.5 \quad [3] \tag{1.4}$$

$$\begin{aligned} C_4 &= \frac{197}{144} + \frac{\pi^2}{12} + \frac{3}{4}\zeta(3) - \frac{1}{2}\pi^2 \ln 2 \\ &= -0.328\ 478\ 965\ 579\ 193... \quad [9,10] \end{aligned} \tag{1.5}$$

$$\begin{aligned} C_6 &= \frac{83}{72}\pi^2\zeta(3) - \frac{215}{24}\zeta(5) \\ &+ \frac{100}{3}\left[\left(\sum_{n=1}^{\infty}\frac{1}{2^n n^4} + \frac{1}{24}\ln^4 2\right) - \frac{1}{24}\pi^2 \ln^2 2\right] - \frac{239}{2160}\pi^4 + \frac{139}{18}\zeta(3) \\ &- \frac{298}{9}\pi^2 \ln 2 + \frac{17101}{810}\pi^2 + \frac{28259}{5184} = 1.181\ 241\ 456\ 587... \quad [11] \end{aligned} \tag{1.6}$$

$$C_8 = -1.912\ 245\ 764\ 926... \text{ (evaluated up to 1100 digits)} \quad [12,13] \tag{1.7}$$

$$C_{10} = 6.737\ (159) \quad [8,14], \tag{1.8}$$

where $\zeta(s)$ is the Riemann zeta function. The contribution from the muon and tauon loop

is evaluated as

$$a_{\mu,\tau} = 2.747\ 572(1) \times 10^{-12} \quad [8, 13, 15\text{–}21]. \tag{1.9}$$

using experimentally measured muon mass [22] and tauon mass [23]. The hadronic and weak contributions are respectively given by

$$a_{\text{hadron}} = 1.693\ (12) \times 10^{-12} \quad [24] \tag{1.10a}$$

$$a_{\text{weak}} = 0.030\ 53\ (23) \times 10^{-12} \quad [24] \tag{1.10b}$$

In Eq. 1.3, α is the fine structure constant. The value of α, determined independently from the electron's g-factor, is

$$\alpha^{-1} = \left(\frac{1}{4\pi\epsilon_0}\frac{e^2}{\hbar c}\right)^{-1} = 137.035\ 999\ 206\ (11), \tag{1.11}$$

where ϵ_0 is the vacuum permittivity, and c is the speed of light. The value of α is experimentally determined independently from measurement of the Rydberg constant [25–27], mass ratio of electron and ^{87}Rb or ^{133}Cs [28, 29] and absolute mass of ^{87}Rb [30] and ^{133}Cs [31] correspondingly. The value above is using the result from ^{87}Rb, and the value using ^{133}Cs is shown in the following section. The determination of α will be reviewed in detail in the next section. Table 1.1 summarizes the contribution of each terms above to the prediction of $g/2$.

1.2 The Fine Structure Constant α

Among the parameters above, the fine structure constant α has the largest uncertainty. The fine structure constant is determined from several measured quantities. With an atom

term	contribution
tree level	1.000 000 000 000 000
$C_2\left(\frac{\alpha}{\pi}\right)$	0.001 161 409 731 851 (000)(093)
$C_4\left(\frac{\alpha}{\pi}\right)^2$	−0.000 001 772 305 060 (000)(000)
$C_6\left(\frac{\alpha}{\pi}\right)^3$	0.000 000 014 804 204 (000)(000)
$C_8\left(\frac{\alpha}{\pi}\right)^4$	−0.000 000 000 055 668 (000)(000)
$C_{10}\left(\frac{\alpha}{\pi}\right)^5$	0.000 000 000 000 456 (011)(000)
$a_{\mu,\tau}$	0.000 000 000 002 748 (000)
a_{hadron}	0.000 000 000 001 693 (012)
a_{weak}	0.000 000 000 000 031 (000)
total SM prediction	1.001 159 652 180 252 (011)(012)(093)
measured $g/2$ (2022)	1.001 159 652 180 593 (134)

Table 1.1: Contribution to the $g/2$ calculation and uncertainties, compared with experimentally measured $g/2$ using $\alpha(^{87}\text{Rb})$ [8, 30]. In C_i's, the first bracket represents calculation error, and the second bracket represents error from α. In the total SM prediction, the uncertainties are the uncertainty of C_{10}, the hadronic term's uncertainty, and the uncertainty of the fine structure constant α, respectively.

X, either cesium (^{133}Cs) or rubidium (^{87}Rb), α is determined by

$$\alpha(X) = \left[\frac{2R_\infty}{c}\frac{A(X)}{A(e)}\frac{h}{m(X)}\right]^{1/2}, \tag{1.12}$$

where $R_\infty = me^4/(8\epsilon_0^2 h^3 c)$ is the Rydberg constant, $A(X)$ is the atomic mass of X, $A(e)$ is the atomic mass of an electron, and $m(X)$ is the absolute mass of the atom X. The Rydberg constant is determined by the Hydrogen spectroscopy. We use the CODATA 2018 value, which reflects all hydrogen spectroscopies [32–34] and the determination using a muonic-hydrogen [35].

$$R_\infty(\text{CODATA 2018}) = 10\ 973\ 731.568\ 160\ (21)\ \text{m}^{-1} \quad 1.9\ \text{ppt}\ [36]. \tag{1.13}$$

The atomic masses are measured using trapped ions in a Penning trap [36, 37],

$$A(e) = \quad 0.000\ 548\ 579\ 909\ 065\ (16) \quad 29 \text{ ppt} \quad [29, 38] \tag{1.14a}$$

$$A(^{87}\text{Rb}) = \quad 86.909\ 180\ 531\ (6) \quad 69 \text{ ppt} \quad [36, 37, 39, 40] \tag{1.14b}$$

$$A(^{133}\text{Cs}) = 132.905\ 451\ 961\ (8) \quad 60 \text{ ppt} \quad [36, 37, 39\text{–}41]. \tag{1.14c}$$

The largest uncertainty comes from the determination of the absolute mass $m(X)$. The absolute mass is determined by measuring the recoil momentum of an atom when absorbing a photon using atom interferometer experiments. The results are

$$\frac{h}{m(^{87}\text{Rb})} = 4.591\ 359\ 258\ 90\ (65) \times 10^{-9}\ \text{m}^2/\text{s} \quad 140 \text{ ppt } [30] \tag{1.15a}$$

$$\frac{h}{m(^{133}\text{Cs})} = 3.002\ 369\ 472\ 1\ (12) \quad \times 10^{-9}\ \text{m}^2/\text{s} \quad 400 \text{ ppt } [31] \tag{1.15b}$$

From the values above, the inverse of fine structure constant α^{-1} is determined using Eq. 1.12

$$\alpha^{-1}(^{87}\text{Rb}) = 137.035\ 999\ 206\ (11) \quad (81 \text{ ppt}) \tag{1.16a}$$

$$\alpha^{-1}(^{133}\text{Cs}) = 137.035\ 999\ 046\ (27) \quad (200 \text{ ppt}). \tag{1.16b}$$

The fine structure constant can also be determined inversely from the measured g-factor and the Standard Model calculations (Sec. 1.1). In calculating the g-factor, the uncertainties of C_i's, hadronic term, and weak interaction term are relatively small. Therefore, by taking the inverse of Eq. 1.3, the fine structure constant determined using the measurement of

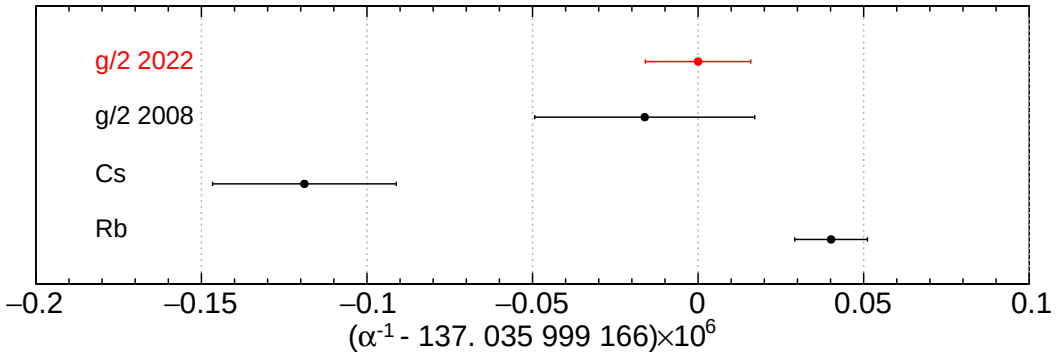


Figure 1.2: Comparison of the inverse of the fine structure constant α^{-1}.

g-factor in 2008 and this thesis are [7]

$$\alpha^{-1}(g/2,\ 2008) = 137.035\ 999\ 149\ 8\ (13)\ (14)\ (330), \tag{1.17a}$$

$$\alpha^{-1}(g/2,\ 2022) = 137.035\ 999\ 165\ 9\ (13)\ (14)\ (161), \tag{1.17b}$$

$$\tag{1.17c}$$

where uncertainties are uncertainty of C_{10}, hadronic term's uncertainty, and the uncertainty of $g/2$ measurement. Figure 1.2 shows the comparison of α^{-1} among various recent experiments by this method.

Instead, we can also convert measured α's to the prediction on $g/2$ and compare them,

$$\frac{g}{2}(^{133}\mathrm{Cs}) = 1.001\ 159\ 652\ 181\ 606\ (12)\ (11)\ (229) \tag{1.18a}$$

$$\frac{g}{2}(^{87}\mathrm{Rb}) = 1.001\ 159\ 652\ 180\ 252\ (12)\ (11)\ (93) \tag{1.18b}$$

$$\frac{g}{2}(2008) = 1.001\ 159\ 652\ 180\ 730\ (280) \tag{1.18c}$$

$$\frac{g}{2}(2022) = 1.001\ 159\ 652\ 180\ 593\ (134), \tag{1.18d}$$

where the uncertainties are the hadronic term's uncertainty, the uncertainty of C_{10}, and the uncertainty of the fine structure constant α, respectively. Figure 1.3 shows the comparison of $g/2$ among recent experiments and the SM predictions. It is important to notice that

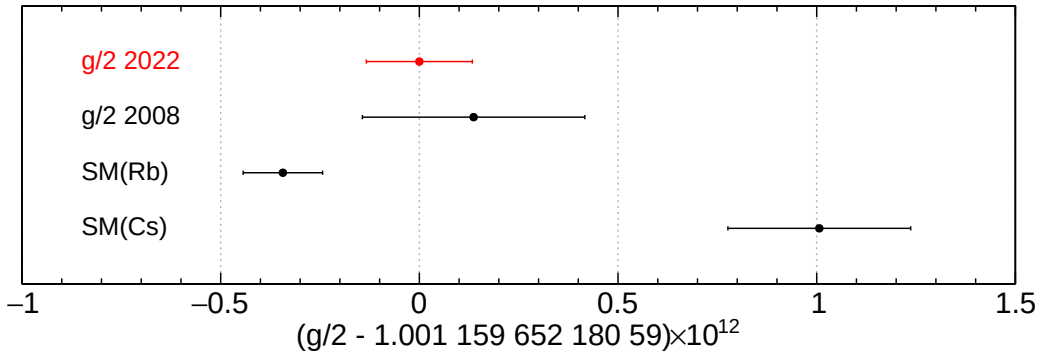


Figure 1.3: Comparison of measured g-factors with prediction.

the measured g-factor is discrepant with the calculated g-factor using the fine structure constant using ^{87}Rb or ^{133}Cs atom by 2.1 σ or 3.8 σ, respectively. This could trigger many new theoretical proposals beyond the SM.

1.3 Physics Beyond the Standard Model

The comparison of the measured electron's magnetic moment and the theory provides a precise test of the Standard Model of physics and search for the beyond standard model physics (Eq. 1.18). The relative uncertainty (with the α measured using ^{87}Rb)

$$\frac{g}{2}(\text{measured}) - \frac{g}{2}(\text{theory}) = (3.41 \pm 1.64) \times 10^{-13} \tag{1.19}$$

is the most stringent test of the Standard Model. It also shows a discrepancy with 2.1 standard deviation.

1.3.1 Dark Photon

Dark photon is a proposed vector Boson that carries an additional $U(1)$ charge—analog to the ordinary electromagnetic photon. It can interact with ordinary photons via kinetic mixing. The dark photon can turn into an ordinary photon and can couple to an electron.

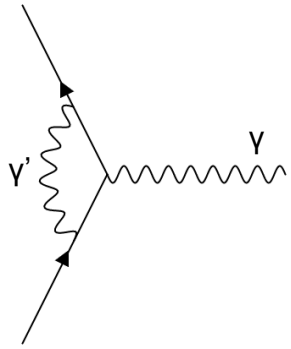


Figure 1.4: Contribution of the dark photon to the electron magnetic moment.

It adds a new term to the Standard Model's Lagrangian (in natural units)

$$\mathcal{L}_{\mathrm{DP}} = -\frac{1}{4}F'_{\mu\nu}F'^{\mu\nu} - \frac{\chi}{2}F_{\mu\nu}F'^{\mu\nu} + \frac{m^2_{A'}}{2}A'_{\mu}A'^{\mu}, \tag{1.20}$$

where A'_μ and $F'^{\mu\nu}$ are the vector field and the tensor field of the dark photon, respectively, $F^{\mu\nu}$ is the tensor field of the ordinary photon, and χ represents the mixing coefficient between the dark photon and ordinary photon.

The dark photon can contribute to the magnitude of the electron magnetic moment, as shown in Fig. 1.4. The contribution is similar to the first order loop correction from the ordinary photon, but with coupling coefficient χ and finite mass m_B.

$$\delta\left(\frac{g_e}{2}\right)_{\text{dark photon}} = \chi^2\frac{\alpha}{2\pi}F\left(\frac{m_{A'}}{m_e}\right), \tag{1.21}$$

where

$$F(x) = \int_0^1 2z(1-z)^2/\left[(1-z)^2 + x^2z\right]dz. \tag{1.22}$$

Another type of dark photon search in the same mass range is the invisible decay method. In this method, the additional assumption that the dark photon will mainly decay to another dark sector's particle is required. NA64 [42], NA62 [43], Babar [44], E787 and E949 [45] set limits by this method. One advantage of using the magnetic moment to search for the

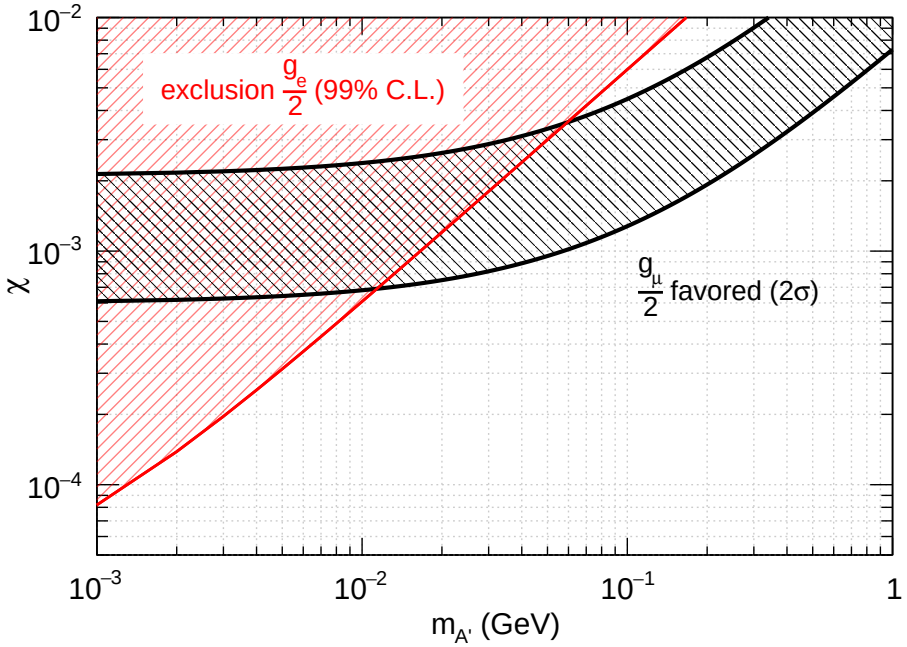


Figure 1.5: Limit on dark photon coupling coefficient χ and mass $m_{A'}$.

dark photon is that it does not require the assumption of the invisible decay method, and thus can set limits to different models. The limit on the dark photon can be obtained from our result (Eq. 1.2) using Bayesian's statistics [46]. For the theory that predicts positive correction $\delta(g_e/2) > 0$, our result gives $\delta(g_e/2) < 7.2 \times 10^{-13}$ with 99 % confidence level. Figure 1.5 shows the limit on dark photon with 99 % confidence level from the measured $g/2$. The favored result from the muon's anomalous magnetic moment is also shown.

We have also developed a new method to search for the dark photon (Chap. 6). We use the cyclotron motion of the single electron as a probe of dark matter dark photon. The cyclotron motion is at meV energy scale and is very different from the traditional search here. The newly developed method probes meV mass dark photon at $\chi \approx 10^{-10}$ level.

1.3.2 Relation to Muon $g/2$

It has been known that the same anomalous magnetic moment of another lepton—muon—also shows a discrepancy between the SM calculation and measured value [47–49]

$$\delta\left(\frac{g_\mu}{2}\right) = \frac{g_\mu}{2}(\text{Measured}) - \frac{g_\mu}{2}(\text{Theory}) = (25.1 \pm 5.9) \times 10^{-10}. \tag{1.23}$$

Although the absolute uncertainty is about three orders of magnitude larger than the uncertainty of the electron's uncertainty (Eq. 1.19), the muon is more sensitive to high energy new physics because its mass is about $(m_\mu/m_e) \approx 200$ times higher. This long-standing discrepancy has triggered several hypotheses of new physics.

The muon's result can be scaled to the electron's magnetic moment. If some new physics shifts the muon's magnetic moment and it is flavor blind, it also shifts the electron's magnetic moment by $(m_e/m_\mu)^2 = 2.3 \times 10^{-5}$ smaller amount. Based on this estimation, if one scales the discrepancy of the muon's anomalous moment to the electron's magnetic moment, it corresponds to

$$\delta\left(\frac{g_e}{2}\right)_{\text{scaled from muon}} = \delta\left(\frac{g_\mu}{2}\right)\left(\frac{m_e}{m_\mu}\right)^2 = 5.9 \times 10^{-14} \tag{1.24}$$

Although the precision in this thesis is not sufficient to test this discrepancy, another factor of 3 improved measurement of the electron's magnetic moment, combined with a factor of 2 improved determination of the fine structure constant, will test whether the observed muon's discrepancy is real or not.

1.4 New Measurement of the Electron g-Factor

The most recently established methods to measure the g-factor use a single electron in a Penning trap [7, 50, 51]. The electron is cooled to its quantum cyclotron ground state by a dilution refrigerator, and its cyclotron frequency and anomaly frequency—the difference between spin frequency and cyclotron frequency—is measured. A cylindrical Penning trap

is used to control microwave cavity correction [52, 53].

Two systematic effects were known in the previous measurement [7]. First, the observed linewidths of the cyclotron and anomaly transition were broader than the theoretical line shape. Displacement of the refrigerator and the magnet of the apparatus caused by vibration was suspected to be the cause. Despite huge efforts to improve its mechanical stability, the ideal line shape was never achieved. The second is the correction of g-factor from Penning trap's microwave cavity effect. The effect was studied by measuring the electron's g-factor at four fields between 5.27 T and 5.40 T. The measured g-factors were consistent among them.

In this thesis, we constructed a new refrigerator-magnet system that achieves better mechanical stability (Chap. 2). A newly dedicated cryogenic helium-3 NMR probe has been invented to optimize the homogeneity and stability of the magnet (Chap. 3). The statistical sensitivity has been improved by a factor of 4. The systematic error has been studied by measuring at 11 different fields, from 3.10 T to 5.38 T. A new systematic correction method has been developed and applied. A factor of two improved determination of g-factor, together with the details of the methods and analysis, is reported (Chap. 4).

Chapter 2

The Penning Trap

The magnetic moment of an electron is measured using an electron in a magnetic field. From Eq. 1.1, in a magnetic field B, the energy of a spin flip for a spin 1/2 particle is

$$\hbar\omega_s = |2\mu_s B| = \frac{g}{2}\frac{\hbar e B}{m}. \tag{2.1}$$

The last term on the right hand is equal to the energy of electron cyclotron motion in the same field,

$$\hbar\omega_c = \frac{\hbar e B}{m}. \tag{2.2}$$

Ideally, the g-factor can be measured using an electron in a magnetic field by measuring the relation

$$\frac{g}{2} = \frac{\omega_s}{\omega_c} = \frac{\nu_s}{\nu_c}. \tag{2.3}$$

of its spin frequency $\nu_s = \omega_s/(2\pi)$ and cyclotron frequency $\nu_c = \omega_c/(2\pi)$.

Experimentally, a Penning trap is used to keep the electron in a small region of a homogeneous magnetic field. The Penning trap is a static trap for charged particles [54] using an electric field and a magnetic field (Fig. 2.1). An electron in a Penning trap has three orthogonal motional modes, a cyclotron motion in the Penning trap ν_c' slightly modified by the electrostatic trap potential, axial motion ν_z, and magnetron motion ν_m. Here, the

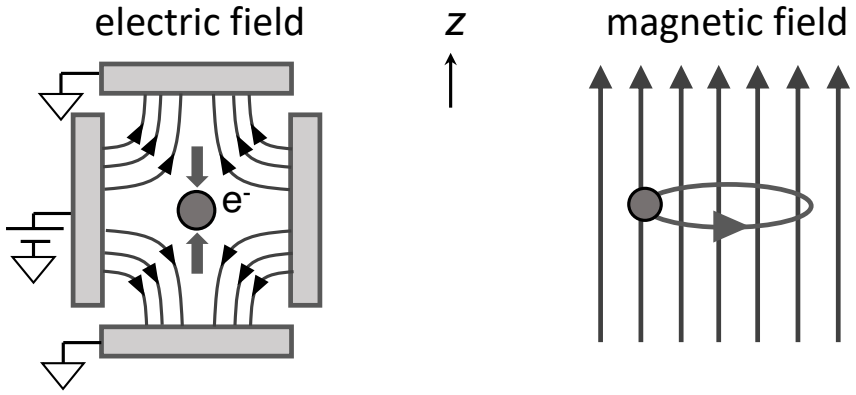


Figure 2.1: Schematic picture of trapping an electron with a Penning trap. The electric field confines the electron along the z direction, and the magnet field confines it in the transverse direction.

quantities with prime represent frequencies in a Penning trap.

From the Brown-Gabrielse invariance theorem [55], the free space cyclotron frequency can be extracted from the square sum of the three frequencies,

$$\nu_c = \sqrt{\nu_c'^2 + \nu_z^2 + \nu_m^2}. \tag{2.4}$$

The spin frequency in the Penning trap is unchanged from its free space value

$$\nu_s' = \nu_s = \frac{g}{2}\nu_c, \tag{2.5}$$

therefore the g-factor can be measured by measuring these frequencies in a Penning trap.

Instead of measuring the spin frequency, we measure the anomaly frequency—the difference between the spin frequency and the cyclotron frequency—to determine the g-factor

$$\nu_a \equiv \nu_s - \nu_c. \tag{2.6}$$

The equation for the g-factor is now

$$\frac{g}{2} = \frac{\nu_s}{\nu_c} = 1 + \frac{\nu_a}{\nu_c}. \tag{2.7}$$

All quantities, ν_c, ν_s, and ν_a can be measured at about the 10^{-10} level. By measuring the difference between the two large quantities, ν_s and ν_c, the uncertainty of g-factor can be reduced by about $g/2 - 1 \approx 0.00115$. This follows from simple error propagation formula.

$$\frac{\Delta\left(g/2\right)}{g/2} = \frac{1}{g/2}\sqrt{\left(\frac{\Delta\nu_a}{\nu_c}\right)^2 + \left(\frac{\nu_a \Delta\nu_c}{\nu_c^2}\right)^2} = \frac{1}{g/2}\frac{\nu_a}{\nu_c}\sqrt{\left(\frac{\Delta\nu_a}{\nu_a}\right)^2 + \left(\frac{\Delta\nu_c}{\nu_c}\right)^2}. \tag{2.8}$$

The ratio $\frac{1}{g/2}\frac{\nu_a}{\nu_c}$ is about 0.00115..., so the relative uncertainty for $g/2$ is about 1000 times better than the fractional uncertainty of determination of ν_c and ν_a.

In this chapter, we introduce the Penning trap and discuss the motion of an electron in the trap in Sec. 2.1. The details of the apparatus are described in Sec. 2.2. The methods to detect the electron's motion are described in Sec. 2.3. In this and the following chapters, we use the familiar relation between frequency and angular frequency $\omega = 2\pi\nu$.

2.1 Motion of an Electron in a Penning Trap

In an ideal Penning trap, a uniform magnetic field

$$\mathbf{B}(\rho, z) = B\hat{\boldsymbol{z}} \tag{2.9}$$

and a quadratic electric potential

$$\phi(\rho, z) = -\phi_0\left(\frac{z^2 - \rho^2/2}{2}\right) \tag{2.10}$$

is applied. The electric field from Eq. 2.10 is explicitly given as

$$\mathbf{E}(\rho, z) = -\boldsymbol{\nabla}\phi(\rho, z) = \phi_0\left(-\frac{x\hat{\boldsymbol{x}} + y\hat{\boldsymbol{y}}}{2} + z\hat{\boldsymbol{z}}\right). \tag{2.11}$$

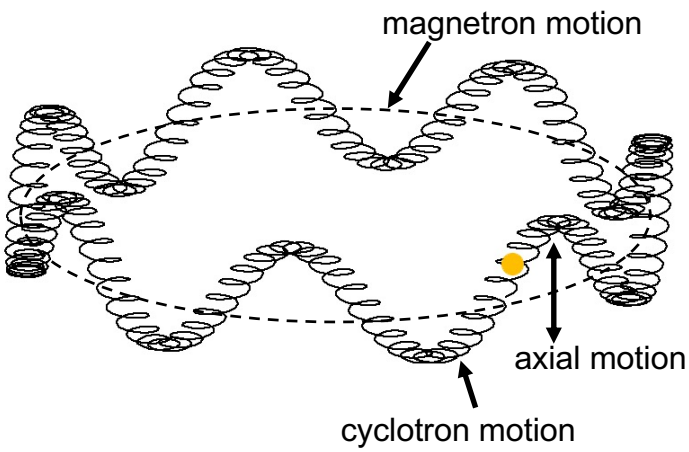


Figure 2.2: Classical picture of an electron's motion in a Penning trap.

The explicit equation of motion of an electron with charge $-e$ includes the force the electric field and the Lorentz force

$$m\frac{d^2}{dt^2}\begin{pmatrix} x \\ y \\ z \end{pmatrix} = \frac{e\phi_0}{2}\begin{pmatrix} x \\ y \\ -2z \end{pmatrix} + eB\begin{pmatrix} -\frac{dy}{dt} \\ \frac{dx}{dt} \\ 0 \end{pmatrix}, \tag{2.12}$$

The applied magnetic field and quadruple electric field generate the three orthogonal motional modes, as illustrated in Fig. 2.2.

Along the z axis, the electron oscillates in the electric potential with the axial frequency

$$\omega_z = \sqrt{\frac{e\phi_0}{m}}. \tag{2.13}$$

This motion is the result of the electric trapping potential, and its motion is described by a simple harmonic oscillation along the $\hat{z}$ direction [54].

The transverse motion is a superposition of two circular motions [54]—modified cyclotron motion and magnetron motion. To see this, Eq. 2.12 is transformed using $u \equiv x + iy$ as

$$\frac{d^2u}{dt^2} - i\omega_c\frac{du}{dt} - \frac{\omega_z^2}{2}u = 0, \tag{2.14}$$

where $\omega_c = eB/m$ is the free space cyclotron frequency. Two solutions for Eq. 2.14 are given in the form $u_\pm = \rho_\pm e^{i\omega_\pm t}$, with the eigenfrequencies given by

$$\omega_\pm = \frac{1}{2}\left(\omega_c \pm \sqrt{\omega_c^2 - 2\omega_z^2}\right) \tag{2.15}$$

The motion with faster frequency (ω_+) is called the modified cyclotron motion, and that with slower frequency (ω_-) is called the magnetron motion. The modified cyclotron motion is analogous to that in the free space, with small corrections from the electric field $\phi(\rho, z)$. The magnetron motion is a result of $\vec{E} \times \vec{B}$ drift, which arises from the magnetic field and the off-center electric field [54].

For typical experimental parameters, because the free space cyclotron frequency is about three orders of magnitude larger than the axial frequency, $\omega_z/\omega_c \approx 10^{-3}$, we can approximate the magnetron frequency and the modified cyclotron frequency as

$$\omega_- = \frac{1}{2}\left(\omega_c - \sqrt{\omega_c^2 - 2\omega_z^2}\right) \approx \frac{\omega_z^2}{2\omega_c} \equiv \omega_m, \tag{2.16}$$

$$\omega_+ = \frac{1}{2}\left(\omega_c + \sqrt{\omega_c^2 - 2\omega_z^2}\right) \approx \omega_c - \frac{\omega_z^2}{2\omega_c} = \omega_c - \omega_m \equiv \omega_c'. \tag{2.17}$$

The approximation holds to better than $(\omega_z/\omega_c)^4 \approx 10^{-12}$ for all experimental parameters in this thesis. There is thus a hierarchy among the three frequencies

$$\omega_c' \gg \omega_z \gg \omega_m. \tag{2.18}$$

The intervals are typically $\omega_c'/\omega_z = \mathcal{O}(10^3)$ and $\omega_z/\omega_m = \mathcal{O}(10^3)$ respectively.

The energies associated with the three motional modes can be easily derived. The most simple expression is the axial motion. For an axial motion with amplitude z_A, the associated energy is simply the energy of simple harmonic motion,

$$E_z = \frac{1}{2} m \omega_z^2 z_A^2. \tag{2.19}$$

The energies for the modified cyclotron motion with radius ρ_c and the magnetron motion ρ_m is given by the sum of the kinetic energy $\frac{1}{2}m\left(\frac{d\rho}{dt}\right)^2$ and the electrostatic potential energy in the radial direction $-\frac{1}{4}\omega_z^2\rho^2$,

$$E_c = \frac{1}{2}m\left(\omega_c'^2 - \frac{1}{2}\omega_z^2\right)\rho_c^2 \approx \frac{1}{2}m\omega_c'^2\rho_c^2 \tag{2.20}$$

and

$$E_m = \frac{1}{2}m\left(\omega_m^2 - \frac{1}{2}\omega_z^2\right)\rho_m^2 \approx -\frac{1}{4}m\omega_z^2\rho_m^2. \tag{2.21}$$

We used the hierarchy (Eq. 2.18) in the approximations. Notice that the energy for the magnetron motion is negative. If the particle is left in the trap for a very long time, the magnetron radius will grow until the particle collides with the wall and is lost from the trap. However, we will see in the next section that the spontaneous growth rate of magnetron radius is much slower than the experimental time scale, and we can reduce the magnetron radius by applying a radio frequency (RF) cooling drive. Therefore, the radius of the magnetron orbit can be kept small and stable.

The three motions thermalize to the equilibrium temperature with very different time scales. The cyclotron motion radiates its energy by the synchrotron radiation with a time constant

$$\tau_c = \frac{1}{\gamma_c} = 4\pi\epsilon_0\frac{3mc^3}{4e^2\omega_c^2}. \tag{2.22}$$

The time constant is about $\tau_c = 0.09$ s in free space at 5.3 Tesla. The radiation is suppressed by trapping the electron in a high quality factor cylindrical Penning trap [56]. We use this inhibition of spontaneous emission to achieve a longer cyclotron lifetime τ_c of about 5–10 s, which produces long enough averaging time to detect one-quantum cyclotron transitions.

The axial motion is strongly damped by a detection resonator. Its equilibrium temperature is determined by resonator's temperature and the following amplifier. The typical time constant for damping is about $\tau_z = \gamma_z^{-1} = 0.03$ s. The detection and damping of axial motion are described in Sec. 2.3.

The time constant for the spontaneous increase of the magnetron radius [54]

$$\tau_m = \frac{1}{\gamma_m} = 4\pi\epsilon_0 \frac{3mc^3}{4e^2\omega_m^2} \frac{\omega_c' - \omega_m}{\omega_m} \approx 4\pi\epsilon_0 \frac{3mc^3\omega_c'}{4e^2\omega_m^3} \tag{2.23}$$

is typically at the order of 10^{10} years and is much longer than any experimental time scale. This ensures that in the time scale of experiment, the particle will not be lost from the trap if the magnetron radius is properly "cooled" to a small radius (Sec. 2.3).

In addition to the three kinetic motions, the spin motion has two quantum states, up and down (denoted as $m_s = +1/2$ and $m_s = -1/2$). The spin precession frequency $\omega_s = 2\pi\nu_s$ is given by

$$\omega_s = \frac{g}{2}\frac{eB}{m} = \frac{g}{2}\omega_c. \tag{2.24}$$

The spin frequency is determined by the magnetic field and is not modified by the electric field potential. Among the two spin states, the spin-up state ($m_s = +1/2$) has higher energy and is effectively meta-stable. The radiative decay rate from spin up to spin down state ($m_s = +1/2 \rightarrow m_s = -1/2$), given by

$$\tau_s = \frac{1}{\gamma_s} = 4\pi\epsilon_0 \frac{6m^2c^5}{g^2\hbar e^2\omega_s^3} \tag{2.25}$$

is about 5 years at 5.3 T. Therefore, the spin transition rate is also negligibly small compared to the experimental timescale.

An accurate description of the motion requires quantum mechanics (Fig. 2.3). Spin motion can take one of two states, up or down. Cyclotron, axial, and magnetron motions are described by quantum harmonic oscillators that are orthogonal to each other. The Hamiltonian is explicitly given as

$$\mathcal{H} = \hbar\omega_c' \left(\hat{a}_c^\dagger \hat{a}_c + \frac{1}{2}\right) + \hbar\omega_z \left(\hat{a}_z^\dagger \hat{a}_z + \frac{1}{2}\right) - \hbar\omega_m \left(\hat{a}_m^\dagger \hat{a}_m + \frac{1}{2}\right) + \hbar\omega_s \frac{1}{2}\hat{\sigma}_z, \tag{2.26}$$

where $\hat{a}_i$ and $\hat{a}_i^\dagger$ $(i = c, z, m)$ are the annihilation and creation operator respectively, and $\hat{\sigma}_z$

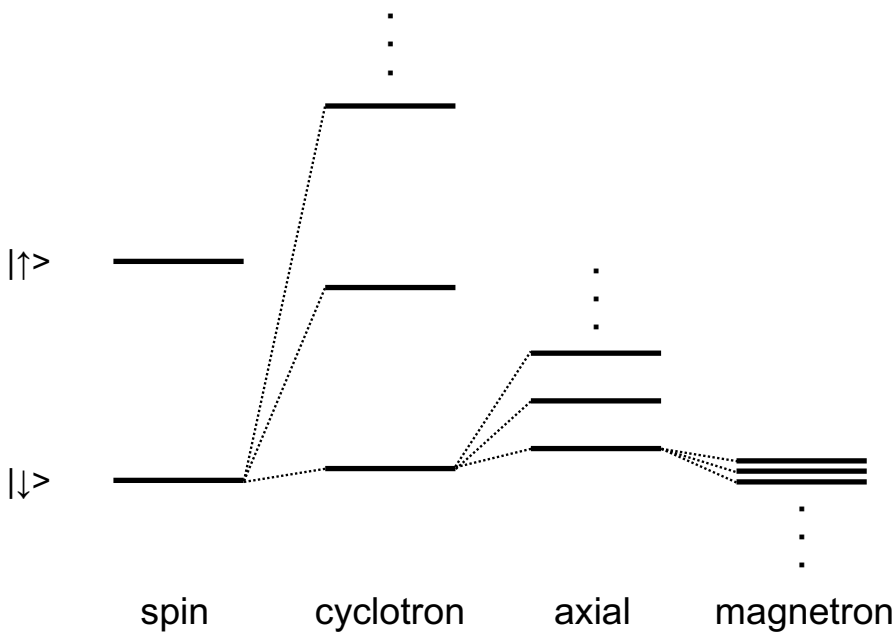


Figure 2.3: Quantum levels of a trapped electron. Each spin has cyclotron, axial, and magnetron sub levels. The energy intervals among the levels are not to the scale.

is the z component operator of the Pauli's matrix. The quantum numbers are conventionally denoted as n_i $(i = c, z, m)$ for the three kinetic motions respectively and $m_s = \pm 1/2$ for spin up and down state.

In thermal equilibrium, the electron's population density is distributed over the quantum states with a Boltzmann distribution. The average quantum number is given by

$$\bar{n}_i = \left[\exp\left(\frac{\hbar\omega_i}{k_{\mathrm{B}}T}\right) - 1\right]^{-1}. \tag{2.27}$$

The Penning trap and its surrounding system are mounted onto a dilution refrigerator (Sec. 2.2). The temperature of the Penning trap is cooled below 100 mK. The temperature of cyclotron motion is equal to the physical temperature of the trap, 100 mK. By cooling to this low temperature, the cyclotron quantum state is always in the ground state unless excited

$$\bar{n}_c = 5.6 \times 10^{-32} \approx 0. \tag{2.28}$$

	frequency	damping time	quantum number
spin	$\omega_s/2\pi \approx 149.7$ GHz	$\gamma_s^{-1} \approx 5$ year	$m_s = \frac{1}{2}$ or $m_s = -\frac{1}{2}$
cyclotron	$\omega_c'/2\pi \approx 149.5$ GHz	$\gamma_c^{-1} \approx 10$ s	$\bar{n}_c = 5.6 \times 10^{-32}$
axial	$\omega_z/2\pi \approx 115$ MHz	$\gamma_z^{-1} \approx 0.03$ s	$\bar{n}_z = 100$
magnetron	$\omega_m/2\pi \approx 48$ kHz	$\gamma_m^{-1} \approx 10^{12}$ s	$\bar{n}_m = 100$

Table 2.1: Typical frequencies, damping rate, and quantum number for the electron in the Penning trap used for the measurement at 5.3 T.

Therefore, after loading an electron in the trap, the electron radiates its cyclotron energy by synchrotron radiation until it reaches the quantum ground state $n_c = 0$.

The axial motion's temperature T_z is thermalized to the detection resonator and amplifier. The physical temperature of the resonator is below 100 mK, but T_z is mainly heated by the effective input temperature of the amplifier (currently high electron mobility transistor amplifier, HEMT), and is about $T_z = 0.5$ K in this thesis. The magnetron motion is "cooled" by magnetron-axial coupling drive to $T_m = -(\omega_m/\omega_z)T_z \approx -10^{-3} \times T_z$ (Sec.2.3 [57]). The minus sign is because of the meta-stable energy (Eq. 2.21). With $T_z = 0.5$ K, the magnetron will be cooled to $T_m = -0.5$ mK, and the quantum numbers for the axial and magnetron motion are $\bar{n}_z = 100$ and $\bar{n}_m = 100$ respectively. Therefore, they are close to the quantum regime but not quite there yet. A new quantum limited detector is also being prepared to achieve $T_z = 20$ mK or below (Chap. 5).

Table 2.1 summarizes the typical frequencies, damping rates, and average quantum numbers of the electron in the trap. The cyclotron damping rate γ_c is a value achieved in a closed cylindrical cavity [56, 58] at 5.3 T, the axial damping rate γ_z is a value when coupled to a resonant circuit, and the average quantum number of the magnetron motion $\bar{n}_m$ is the value after magnetron cooling.

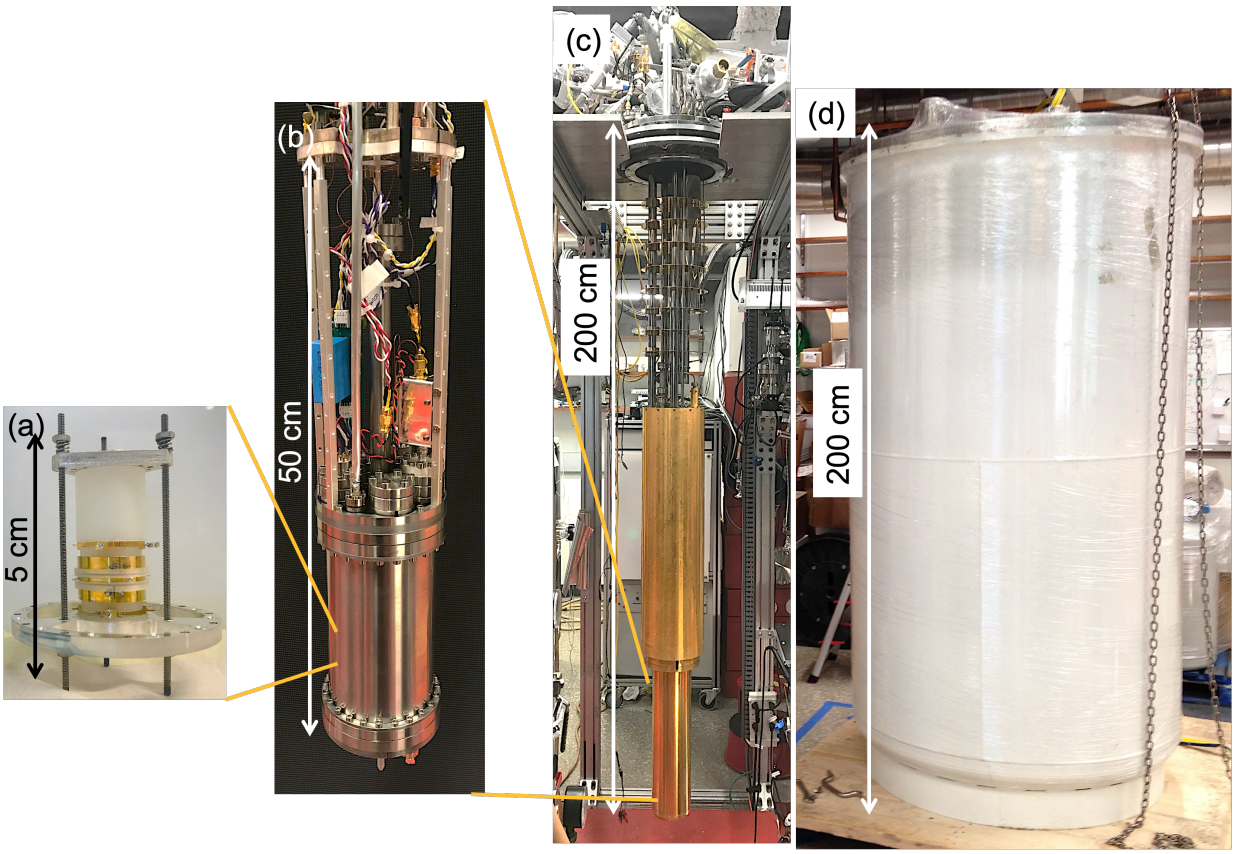


Figure 2.4: The entire setup of the experiment. A Penning trap (a) is housed in a titanium vacuum chamber (b), and the vacuum chamber is suspended at the bottom of a dilution refrigerator (c). The dilution refrigerator is inserted into the dewar (d), which has the superconducting magnet at its bottom. See also Fig. 2.7.

2.2 Apparatus

To realize the ideal environment for the g-factor measurement, a Penning trap, a vacuum chamber, filters, and amplifiers are fabricated and mounted onto a dilution refrigerator. The dilution refrigerator is inserted into a cold bore superconducting magnet (Fig, 2.7). A drastic improvement of the magnet and the dilution refrigerator has been made since the last measurement of g-factor in 2008. We review the apparatus for the g-factor measurement in this section.

parameter	value
magnetic field: B	5.3 T
temperature: T	100 mK
radius of the trap: ρ_0	4.539 mm
half height of the trap: z_0	3.906 mm
height of compensation electrode: z_c	0.716 mm
magnetic bottle gradient: B_2	300 T/m^2
image charge parameter on endcap: c_1	0.784
antisymmetric bias parameter: c_3	0.320

Table 2.2: Typical parameters of the Penning trap.

2.2.1 Penning Trap System

At the heart of the experimental apparatus is the Penning trap. The trap is a five-electrode orthogonal cylindrical trap [59]. The trap electrodes are made of 99.999% pure silver, and the spacers are made of quartz to eliminate nuclear para-magnetism [60]. A nickel magnetic bottle is used to generate quadratic magnetic field for detection (Sec. 2.3). The entire trap assembly is enclosed in a high-vacuum can and cooled down by a dilution refrigerator to 100 mK or below. The vacuum inside the trap chamber is estimated to be better than 5×10^{-17} Torr [61,62], which allows stable trapping of an electron. In this thesis, we operate the single electron trap for more than a year and have never observed difficulty in trapping. Table 2.2 summarizes the parameters of the trap.

The Penning trap electrodes are the same as those used in the 2008 measurement. A closed endcap cylindrical trap [59] is used (Fig. 2.5) to suppress the spontaneous cyclotron decay [58]. The trap is designed such that the compensation electrode is used to tune the fourth order anharmonicity at the trap center without changing the quadratic trap potential [59]. The trap has been disassembled and reassembled several times.

Three parameters characterize the the trap geometry: the trap radius $\rho_0 = 4.539\ (31)$ mm, half of the trap height $z_0 = 3.906\ (35)$ mm, and the length of the compensation electrode $z_c = 0.766\ (3)$ mm. The electric potential of a Penning trap around its center is characterized

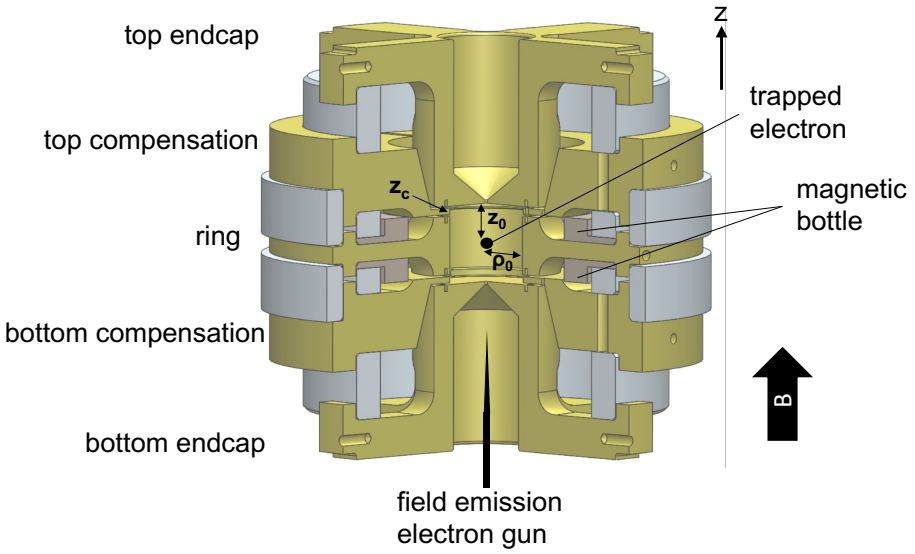


Figure 2.5: The cylindrical penning trap.

by the parameters C_k, defined as

$$\phi(\rho, z) = -V_R \left(\frac{z^2 - \rho^2/2}{2d^2} \right) - \frac{V_R}{2} \sum_{\substack{k=0 \\ \text{even}}} C_k \left(\frac{r}{d} \right)^k P_k \left(\cos\theta \right), \tag{2.29}$$

where V_R is the voltage on the ring electrode, $d = \sqrt{\frac{1}{2}(z_0^2 + \rho_0^2/2)} = 3.575$ mm is the trap dimension parameter, and the cylindrical coordinate $\rho = \sqrt{x^2 + y^2}$, spherical coordinate $r = \sqrt{x^2 + y^2 + z^2}$, polar angle $\theta = \cos^{-1}(z/r)$, and the Legendre polynomial function $P_k(x)$ are used [58, 59, 63]. The trapping potential along the z axis can be simplified as

$$\phi(z) \equiv \phi(0, z) = -\frac{V_R}{2} \left(\frac{z}{d} \right)^2 - \frac{V_R}{2} \sum_{\substack{k=0 \\ \text{even}}} C_k \left(\frac{z}{d} \right)^k, \tag{2.30}$$

Near the center of the trap, the potential is symmetric under the reversal $z \to -z$, so that all odd k components are negligible. The axial oscillation frequency in this notation is

$$\nu_z = \frac{1}{2\pi} \sqrt{\frac{eV_R}{md^2}(1 + C_2)}. \tag{2.31}$$

The harmonic potential of the trap is mainly determined by the main ring voltage V_R. In addition, the compensation electrode is used to control the anharmonicity. In Eq. 2.30, the coefficients C_k are function of the voltage on the compensation electrode V_c as

$$C_k = C_k^0 + D_k \left(\frac{1}{2} - \frac{V_c}{V_R} \right), \tag{2.32}$$

where C_k^0 represents the potential from the ring electrode, and D_k represents the tuning coefficient from the compensation electrode. These coefficients are analytically calculated from the trap geometry [59]

$$C_k^0 = -\delta_{k2} + \frac{(-1)^{k/2}}{k!} \frac{\pi^{k-1}}{2^{k-3}} \left(\frac{d}{z_0} \right)^k \sum_{n=0}^{\infty} \frac{(-1)^{n+1}(2n+1)^{k-1} \cos^2 \left[\frac{1}{2} \left(n + \frac{1}{2} \right) \pi z_c / z_0 \right]}{J_0 \left[i(n+\frac{1}{2}) \pi \rho_0 / z_0 \right]} \tag{2.33}$$

and

$$D_k = \frac{(-1)^{k/2}}{k!} \frac{\pi^{k-1}}{2^{k-3}} \left(\frac{d}{z_0} \right)^k \sum_{n=0}^{\infty} \frac{(-1)^{n}(2n+1)^{k-1}\ 2\sin^2 \left[\frac{1}{2} \left(n + \frac{1}{2} \right) \pi z_c / z_0 \right]}{J_0 \left[i(n+\frac{1}{2}) \pi \rho_0 / z_0 \right]}. \tag{2.34}$$

The values of coefficients for our trap are summarized in Table 2.3. The trap is designed so that D_2 is much smaller than D_4. Under this condition, the fourth order anharmonicity C_4 can be tuned without changing the axial frequency ν_z (Eq. 2.32). The amplitude dependence of axial frequency is minimal at the tuned condition $C_4 = 0$, which corresponds to $V_c/V_R = 0.704$. When the self-excitation is used, we excite the electron to high axial amplitude, and C_4 is set to be slightly positive $C_4 = 2.8 \times 10^{-4}$ to cancel the shift from $C_6 = -0.1$. We will also intentionally tune C_4 to a large value to create anharmonic potential to diagnose the trapped electrons' internal motion (App. A). A new trap that can achieve a smaller anharmonicity $C_4 = C_6 = 0$ is designed in Chap. 5.

Occasionally, we apply antisymmetric bias to the top and bottom endcap electrodes to move the electron up or down. The electric field potential when $+V_A/2$ and $-V_A/2$ are

parameter	value	parameter	value when $C_4 = 0$
C_2^0	0.125	C_2	0.125
D_2	0.002		
C_4^0	-0.013	C_4	0
D_4	-0.067		
C_6^0	-0.091	C_6	-0.094
D_6	0.014		
C_8^0	0.016	C_8	0.013
D_8	0.016		

Table 2.3: Anharmonicity parameters that defines the trap potential with $\rho_0 = 4.539$ mm, $z_0 = 3.906$ mm, and $z_c = 0.766$ mm. The right two rows show the coefficients when V_c is tuned to get a harmonic potential ($V_c/V_R = 0.704$ and $C_4 = 0$).

applied to the top endcap electrode and bottom endcap electrode respectively is

$$\phi_A(\rho, z) = \frac{1}{2} \sum_{k=\text{odd}} c_k \left(\frac{r}{z_0}\right)^k P_k(\cos\theta). \tag{2.35}$$

The expansion coefficient c_k is easily obtained in Eq. (31) in [59] (note that the reference is missing $(-1)^n$ in the numerator)

$$c_k = \delta_{k1} + \frac{2(i\pi)^{k-1}}{k!} \sum_{n=1}^{\infty} \frac{(-1)^n n^{k-1}}{J_0\left[in\pi\rho_0/z_0\right]}. \tag{2.36}$$

For large ρ_0/z_0, c_1 approaches 1 and others approach 0. Qualitatively, c_1 represents how close the endcap electrodes are to ideal infinite planes. The next leading order c_3 is important when calculating the shift of axial frequency when moving electrons to $z \neq 0$. The calculated values for c_1 and c_3 in the trap are also included in Table 2.2.

The trap chamber has been redesigned (Fig. 2.6). Grade 2 titanium is used for the chamber to minimize nuclear paramagnetism [60]. The new chamber has more space and modularity to allow flexibility and quick troubleshooting. Standard 1.33 inch diameter conflat flanges are used at the pinbase with non-magnetic feedthroughs with titanium flange (MPF products, 8x pin non-magnetic feedthrough). The trap chamber is sealed with indium and copper pinch-off tubes. The chamber is mounted to the silver tripod with filters and HEMT

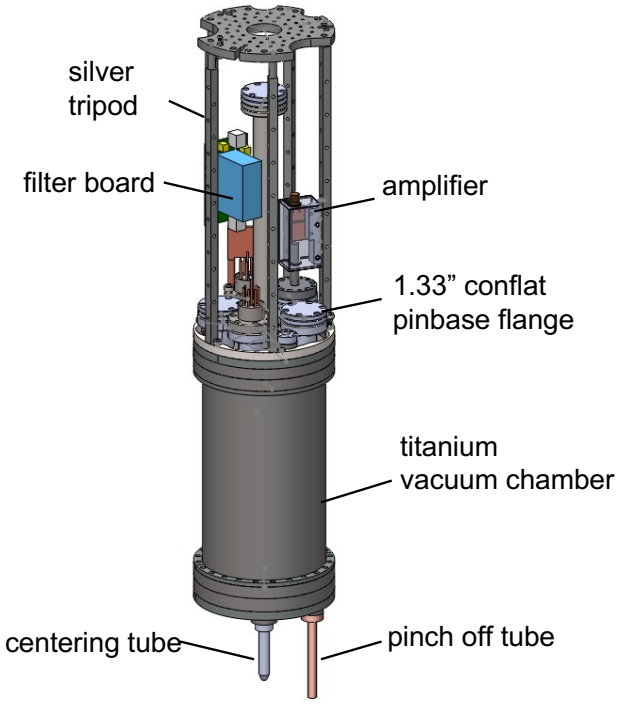


Figure 2.6: Schematic of titanium trap chamber and silver tripod.

amplifiers attached. The silver tripod is rigidly attached to the mixing chamber stage of the dilution refrigerator. Ruthenium oxide temperature sensors are attached at the mixing chamber stage and at the bottom of the tripod. The temperature gradient between the bottom of the tripod and the mixing chamber stage is less than 1 mK when the HEMT amplifier is off, and is about 20 mK when the amplifier is on. This confirms that the thermal link between the mixing chamber and the trap chamber is good, but the HEMT amplifier is by far the largest heat load.

2.2.2 Dilution Refrigerator and Superconducting Magnet

The Penning trap and its surrounding amplifiers and filters are mounted to a dilution refrigerator. The dilution refrigerator is constructed by the Janis ULT. The dilution refrigerator is inserted into the dewar, which has a niobium-titanium 6 Tesla solenoid magnet at its bottom (Fig. 2.7). The magnet and the dilution refrigerator share the same liquid

helium space, which allows the dilution refrigerator to be directly mechanically engaged to the magnet.

The design of the dilution refrigerator directly engaging the magnet minimizes the relative fluctuation of the magnet center and the trap. In the 2008 measurement [7], the largest systematic uncertainty was due to the relative motion of the magnet and the dilution refrigerator. Data collection was not possible during the daytime because of the high sensitivity of the magnetic field to ambient conditions. Careful time-consuming shimming of the magnet is required every time the magnetic field is changed. Temperature fluctuation of the room changes the relative position of the refrigerator and the magnet. The current new system requires neither frequent shimming nor careful room temperature regulation. The improved stability allows continuous data-acquisition. This allows about 20 times more statistics and measurements of g-factor at widely different fields.

The dewar's helium boil-off rate is about 0.7 L/hour when the dilution refrigerator is inserted. The boiled gas helium is collected and reliquified by a commercial reliquifier, modified based on PT420RL-RM (Cryomech). The reliquifier is on during commissioning and optimization, but is turned off during the g-factor measurement. Outside the liquid helium bath, there are thermal shielding layers cooled by 190 L liquid nitrogen dewar. This combined wet system allows minimal vibration and quiet operation of the system.

The dilution refrigerator has a specified cooling power of 150 μW at 100 mK and 10 μW at 30 mK. With our Penning trap system attached, the base temperature reaches 25 mK when the HEMT amplifier is off and 70 mK when the amplifier is turned on with typically 100 μW of power dissipation. The dilution refrigerator can maintain its base temperature continuously for about a year.

The superconducting magnet has 11 shim coils in addition to the main coil that applies a 6 Tesla field at maximum. The shim coils are adjusted to optimize the homogeneity of the magnetic field at its center. The shim coils are labeled as X, Y, Z, ZX, ZY, Z^2, C^2, S^2, Z^2X, Z^2Y, and Z^3. Each shim coil is designed to generate a field along the z direction to

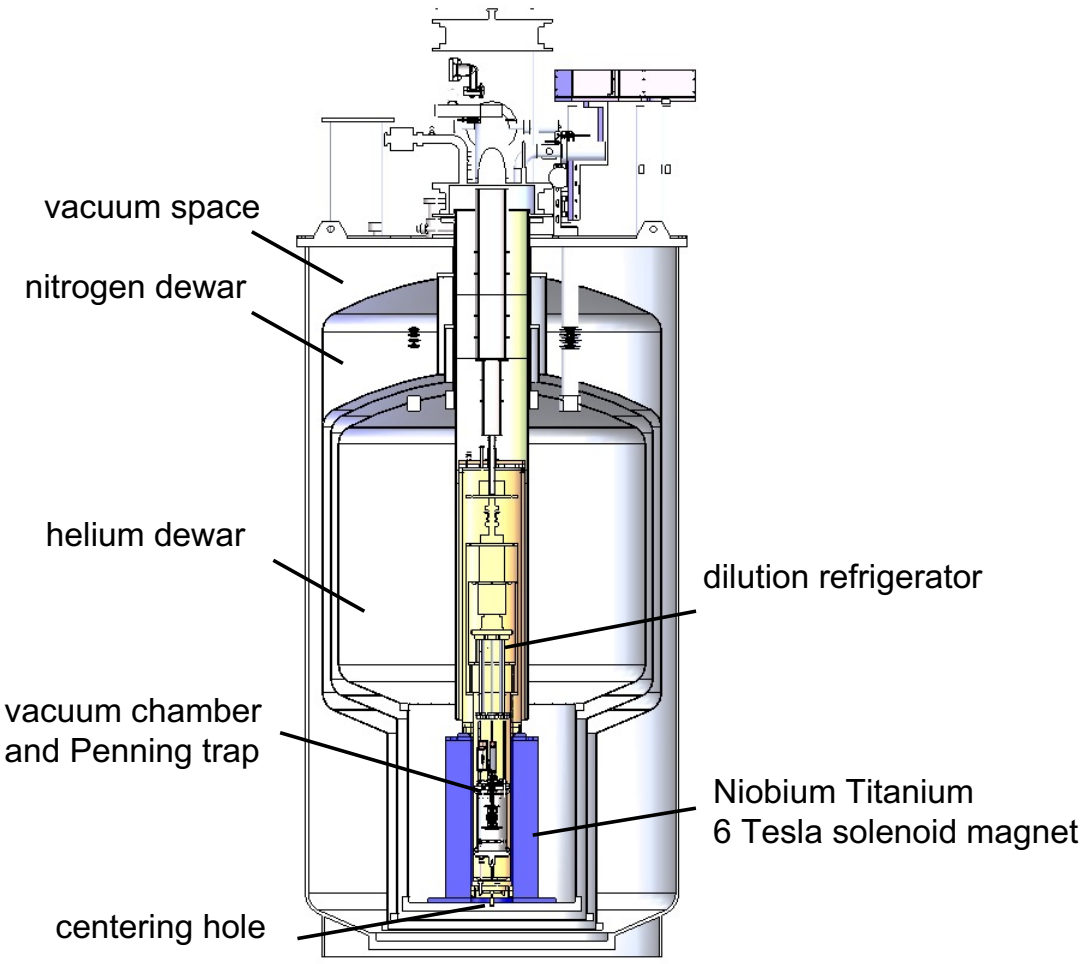


Figure 2.7: Cross section of the dilution refrigerator and magnet system. The Penning trap is mounted at the bottom of the dilution refrigerator and inserted into the bore of the magnet.

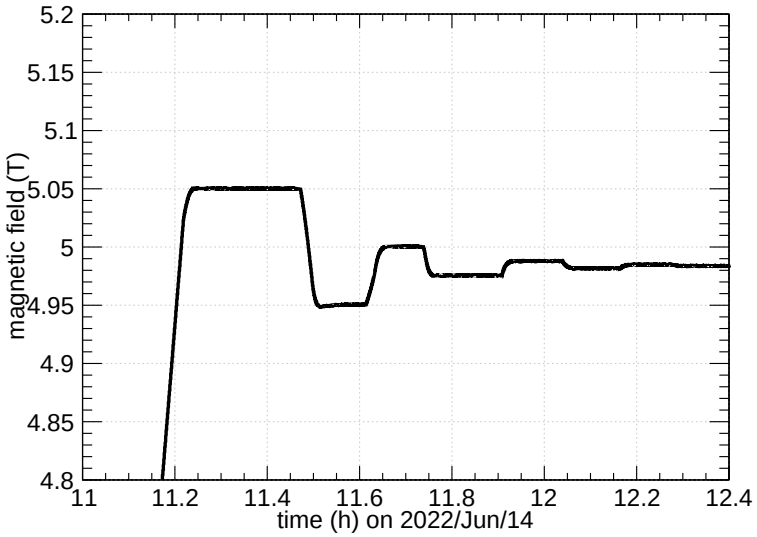


Figure 2.8: The ringing-in method to suppress drift after changing the magnetic field.

compensate spacial gradient associated with its name. For example, the X coil generates field as $b_{\mathrm{X}} x\hat{\boldsymbol{z}}$, the ZX coil generates $b_{\mathrm{ZX}} zx\hat{\boldsymbol{z}}$, and the C^2 coil generates $b_{\mathrm{C}^2} \cos^2\phi\hat{\boldsymbol{z}}$, where ϕ is the azimuth angle in the x–y plane. They are designed to essentially not interfere with each other, which allows efficient shimming of the homogeneity. We first optimize the homogeneity of the magnetic field using a purpose-built ^{3}He NMR probe (Chap. 3).

In the past, a large drift of $\mathcal{O}(10\ \mathrm{ppb})$/hour was observed after changing the magnet. The drift stayed high for a few months, and it was impossible to perform g-factor measurement during that period. A new method, called the "ringing-in" method, is used to suppress this drift. For example, when changing the magnet field from 5.140 T to 5.300 T, we first charge to 5.367 T, then 5.267 T, 5.317 T, 5.292 T, 5.304 T, 5.298 T, 5.301 T, and then to 5.300 T (Fig.2.8). At each value, we settle for about 5 minutes. This method suppresses drift to less than 0.3 ppb/h level even only after a day, making measurement at many different fields possible.

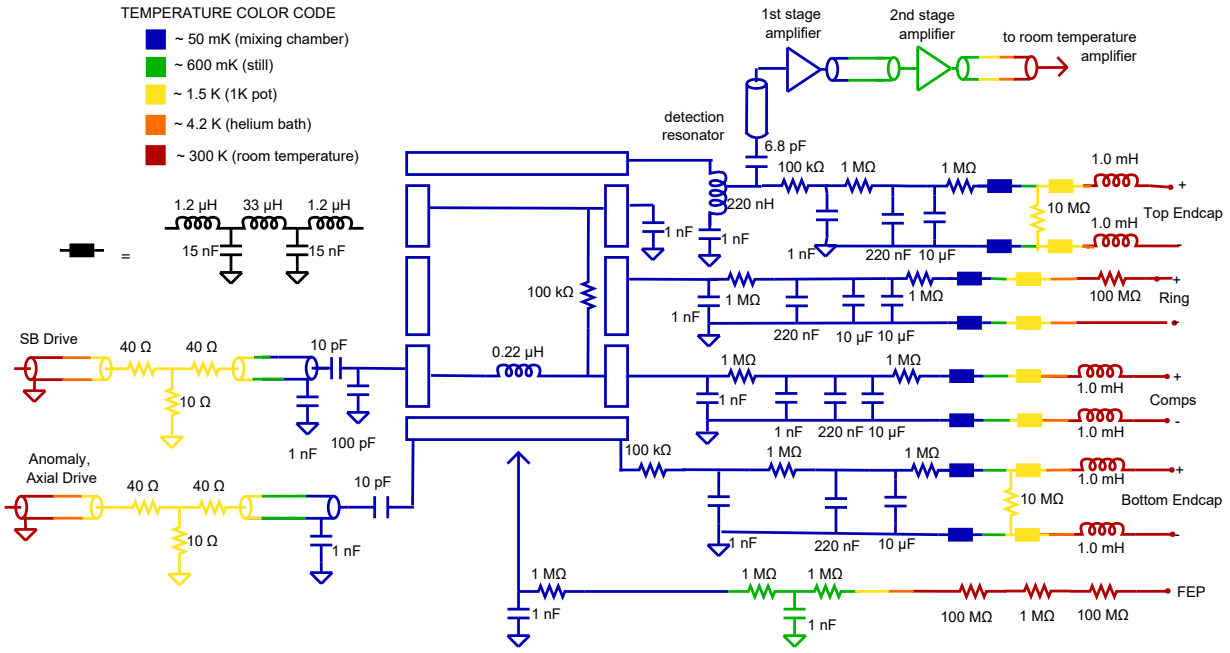


Figure 2.9: Wiring diagram of the Penning trap.

2.2.3 DC and RF Circuitry

The bias voltages on the electrodes determine the axial oscillation frequency as in Eq. 2.31. The relative width of a single electron is about $\gamma_z/\omega_z = 5$ Hz/115 MHz $= 5\times10^{-9}$, and the shift of axial frequency per quantum cyclotron jump is $\delta_c/\omega_z = 1.3$ Hz/115 MHz $= 1.1\times10^{-9}$. Therefore, the short-term voltage fluctuation on the electrodes needs to be better than a few ppb for reliable detection of the electron and identification of its quantum state.

Figure 2.9 shows the wiring of our Penning trap. All DC lines are filtered at room temperature and at each stage by a 200 kHz LC low pass filter. The primary low pass filters are located at the trap chamber. The time constant for the ring electrode filter is 2000 seconds, and those for the other electrodes are 10 seconds. The top endcap electrode and bottom endcap electrode are grounded through a 10 MΩ resistor at the 1K pot stage, but can also be biased to shift electron's position in the trap[1].

For the ring electrode, we stack three of the Stahl ultra high precision DC power supply

[1]These 10 MΩ resistors are limiting the filter time constant for the endcap electrodes and should be removed in the future.

UM1-14-LN-SW. Fluke 5720A and 5440B voltage supplies are used for the compensation electrode and endcap electrode, respectively. They are all floating power supplies and are grounded at the pinbase. To achieve sufficient voltage stability, the main ring power supply needs to be temperature stabilized. The Stahl UM1-14-LN-SW power supply has a temperature coefficient of about $\pm 500 \times 10^{-9}/°\mathrm{C}$. Even a 0.1 °C change of temperature causes much larger drift than the requirement for quantum jump detection $\delta_c/\omega_z = 1.1 \times 10^{-9}$. The slow drift of the axial frequency can be compensated with feedback, but a fast jump at second-scale is indistinguishable from a true cyclotron or spin transition. Therefore, the power supplies are enclosed in a thermally shielded box. The drift of temperature is suppressed below 0.1 °C. This drift has a time scale of one day, which is easily suppressed by feedback using the measured shift of axial frequency.

Two RF drive lines are wired to the Penning trap using micro-coaxial cables (UT-034C) with 50 Ω impedance. 20 dB attenuators are attached at the 1 K pot stage to reduce the room temperature Johnson noise. These lines are capacitively coupled to the trap. The axial drive line used to drive anomaly transition requires higher drive power due to the low transition probability of the anomaly transition. The value of the coupling capacitor is optimized by measuring the transmission from the hat to the trap. Attenuation of the compensation electrode drive line and the endcap electrode drive line are about 45 dB and 25 dB, respectively.

The electron's axial motion is detected using the resonant circuit (Sec. 2.3). Physically, an inductor is attached to the top endcap electrode. The electron is coupled and thermalized to the resonant detection circuit. Its equivalent temperature is determined by the temperature of the resonator and the equivalent input temperature of the detection amplifier. We have observed a noise temperature of the resonant circuit of about 0.1–1 K, depending on the bias power of the amplifier. The input stage of the room temperature amplifier has a noise temperature of about 100 K. Therefore more than 30 dB of cryogenic amplification is required. The first stage amplifier is currently a HEMT-based amplifier (but will be replaced

by the SQUID amplifier in the future), and the second stage amplifier is a HEMT-based amplifier. The details of the design of the amplifiers are discussed in [64].

2.2.4 Loading Electron with Field Emission

The electrons can be loaded using a field emission point (FEP) [64], a very sharp tungsten needle. To load electrons, a high negative voltage (typically ranging from -100 to -1000 V) is applied to the FEP. The electric field near the tip of the tungsten needle is so strong that electrons inside the tungsten tunnel through the work function's potential.

In general, the emission current follows the simple Fowler-Nordheim's law [65]

$$J = \alpha |V|^2 \exp\left(-\frac{\beta}{|V|}\right), \tag{2.37}$$

where V is the applied voltage on the field emission gun, and α and β are two parameters that contain other physical information such as work function, geometrical correction, and others. Figure 2.10 shows the measured emission current by a shunt resistor versus the applied FEP voltage. The measured current agrees with the fitting curve Eq. 2.37.

2.3 Detecting the Motion of the Electron

Among the four motional modes, only the axial motion is directly detected. The spin and cyclotron states are detected by monitoring the axial frequency. Their frequencies are too high to be directly detected. The magnetron motion cannot be monitored because of its meta-stable potential energy. Any dissipative interaction with magnetron motion will increase its radius until the electron escapes from the trap. Therefore, the axial motion is the only probe of the trapped electron.

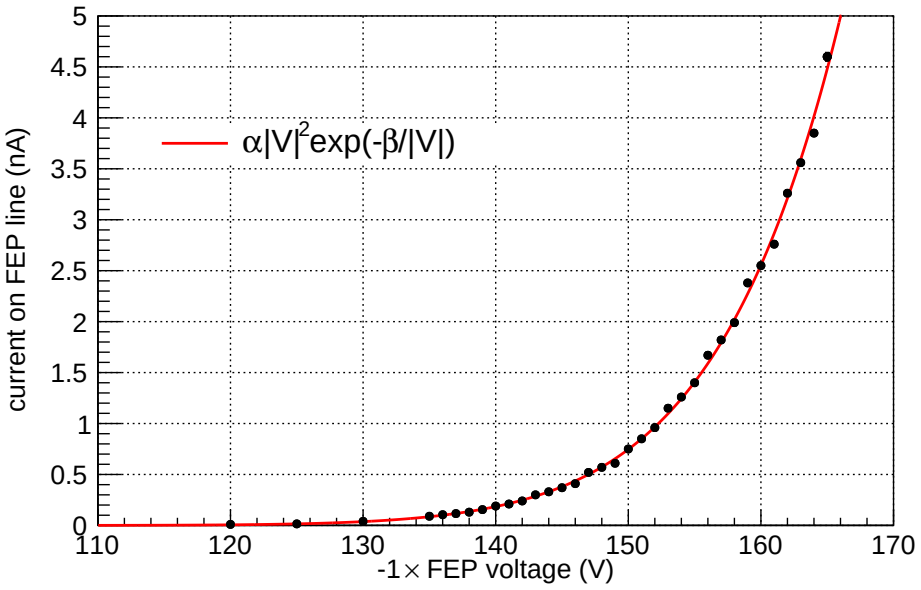


Figure 2.10: FEP current as a function of bias voltage.

2.3.1 Resonant Circuit Detection of the Axial Motion

The equation of motion for a trapped electron without damping force is given by

$$m\left(\frac{d^2z}{dt^2}+\omega_z^2 z\right)=F, \tag{2.38}$$

where $F(t)$ is externally applied force. Axially oscillating particle induces a current on the electrodes due to its image charge [66]. The induced current I on an electrode is

$$I=\frac{ec_1}{2z_0}\frac{dz}{dt}, \tag{2.39}$$

where dz/dt is the instantaneous axial velocity, $c_1=0.784$ is the constant that characterizes the fractional amount of induced current on the electrode.

By moving to the general frequency domain representation, $z(t)=\tilde{z}(\omega)e^{i\omega t}$, $F(t)=\tilde{F}(\omega)e^{i\omega t}$, and $I(t)=\tilde{I}(\omega)e^{i\omega t}$, the equation of motion and the induced current becomes

$$m\left(-\omega^2+\omega_z^2\right)\tilde{z}(\omega)=\tilde{F}(\omega) \tag{2.40}$$

and

$$\tilde{I}(\omega) = i\omega \frac{ec_1}{2z_0} \tilde{z}(\omega). \tag{2.41}$$

We detect the induced current on the top endcap electrode and ground other electrodes at the axial frequency. We denote the impedance between the detection electrode and the ground as $Z(\omega)$. Then the induced current $\tilde{I}(\omega)$ generates voltage difference $\tilde{V}(\omega)$ between the detection electrode and ground,

$$\tilde{V}(\omega) = \tilde{I}(\omega) Z(\omega) = i\omega \frac{ec_1}{2z_0} Z(\omega) \tilde{z}(\omega). \tag{2.42}$$

The induced voltage $\tilde{V}(\omega)$, in turn, acts on the trapped electron as

$$\tilde{F}(\omega) = -\frac{ec_1}{2z_0} \tilde{V}(\omega). \tag{2.43}$$

Therefore, the force from the induced voltage is

$$\tilde{F}(\omega) = -i\omega \left(\frac{ec_1}{2z_0} \right)^2 Z(\omega) \tilde{z}(\omega). \tag{2.44}$$

By putting this expression back to Eq. 2.40, we get

$$m \left[-\omega^2 + i\omega \left(\frac{ec_1}{2z_0} \right)^2 \frac{Z(\omega)}{m} + \omega_z^2 \right] \tilde{z}(\omega) = 0. \tag{2.45}$$

By solving this equation with the conditions $\tilde{z}(\omega) \neq 0$ and $\left(\frac{ec_1}{2z_0} \right)^2 \frac{Z(\omega)}{m} \ll \omega_z$, we get damping term γ_z and the shift of axial frequency $\delta\omega_z|_{\text{resonator}}$ by the coupling to the detection impedance,

$$\gamma_z = \frac{1}{m} \left(\frac{ec_1}{2z_0} \right)^2 \text{Re}\left[Z(\omega) \right] \tag{2.46}$$

and

$$\delta\omega_z|_{\text{resonator}} = -\frac{1}{2m} \left(\frac{ec_1}{2z_0} \right)^2 \text{Im}\left[Z(\omega) \right] = -\frac{\gamma_z}{2} \tan\left[\arg\left[Z(\omega) \right] \right]. \tag{2.47}$$

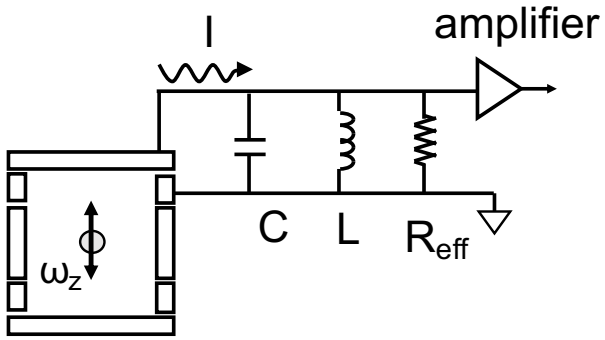


Figure 2.11: Induced current from trapped particle and resonant circuit. The only component physically attached is the inductor L. C mainly comes from the parasitic capacitance between the top endcap electrode and the top compensation electrode. R_{eff} represents the effective loss in the LCR resonance circuit is made as high as possible.

The axial damping rate γ_z needs to be maximized to achieve the best detection sensitivity. The impedance $Z(\omega)$ would be dominated by the capacitance C between the detection electrode and ground except that an inductor L attached in parallel forms an LCR circuit and cancels its imaginary component near ω_z (Fig. 2.11). The resonator is designed in a way that its resonant frequency

$$\omega_0 = \frac{1}{\sqrt{LC}} \tag{2.48}$$

is matched to the axial frequency ω_z. By doing this, the real part of its impedance at axial frequency $Z(\omega_z)$ is maximized, and the resonator shift $\delta\omega_z|_{\text{resonator}}$ is minimized. The real component of the impedance at its resonance ω_0 is given by effective parallel resistance $Z(\omega_0) = R_{\text{eff}}$. In this three-component model, the impedance is given by

$$Z(\omega) = \left(i\omega C + \frac{1}{R_{\text{eff}}} + \frac{1}{i\omega L} \right)^{-1} \tag{2.49}$$

The effective parallel resistance R_{eff} is related to the quality factor of the resonator Q by

$$R_{\text{eff}} = Q\omega_0 L. \tag{2.50}$$

For better detection sensitivity, a higher quality factor Q is desired. Any dissipative factor

decreases the Q-factor. A silver inductor is used for the resonator to minimize conductive loss. The resonator is shielded within a well-grounded can to suppress the radiative loss. The tap ratio is optimized so that the loss from input coupling to the amplifier is minimized but still large enough to get measurable signal.

The inductor is tapped and impedance matched to the input of the amplifier. Notice that the total capacitance C is not only from the trap capacitance but also from other components, such as the capacitance of the resonator, and the input capacitance of the amplifier. The quality factor Q is determined by all components of the circuit, such as conductivity of the inductor's material, radiation loss, and the input impedance of the amplifier.

Our resonator is a silver helical resonator, placed next to the trap inside the trap chamber (Fig. 2.12). The helical resonator is connected to the top endcap electrode. The resonator is tapped with a tap ratio of about 1/3 from the grounded end and capacitively coupled to the feedthrough. Then the signal is sent to the amplifier is placed outside the trap cap. With the resonator placed in the trap chamber, we achieve a parallel resistance of $R_{\text{eff}} = 380$ kΩ at 90 MHz ($Q = 1500$), $R_{\text{eff}} = 240$ kΩ at 114 MHz ($Q = 1200$), and $R_{\text{eff}} = 60$ kΩ at 207 MHz ($Q = 550$). The design is more modular and tunable than the previous design using the transmission line, and still yields better parallel resistance R_{eff}.

So far, we have only discussed the detection of the axial motion. The other motions are monitored via the change of axial motion. Figure 2.13 shows the four main methods to detect and diagnose the axial motion. We first discuss our four main methods to detect the axial motion, and then discuss how to measure other motions using the axial motion.

Dip Detection

The simplest method to detect the axial motion is to Fourier transform the output from the amplifier. By connecting the output from the amplifier to the spectrum analyzer, we can observe the Johnson noise resonance from the detection resonator and a dip from the trapped electron.

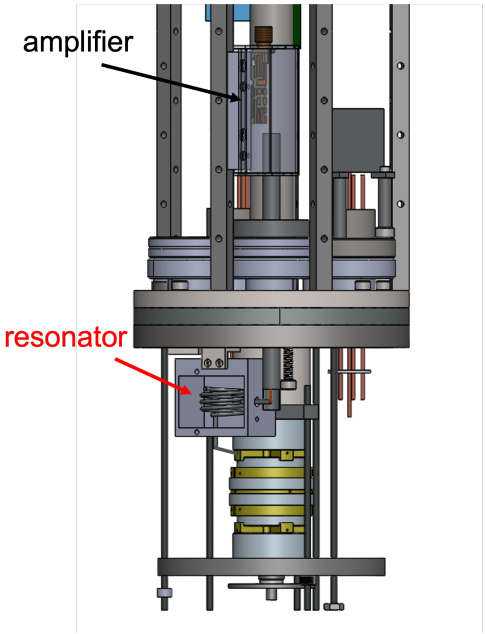


Figure 2.12: Location of the helical resonator. The cylindrical trap chamber is opened. The resonator is placed next to the trap inside the trap chamber to minimize the loss on the wire from the detection electrode (top endcap).

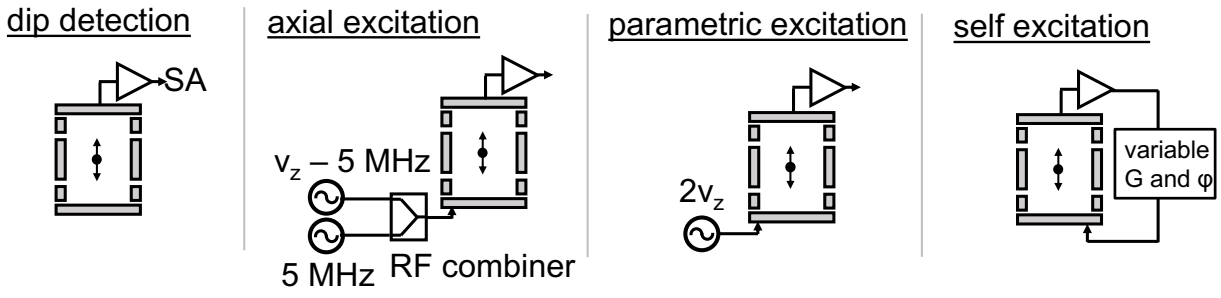


Figure 2.13: Four drives to detect the axial motion, dip detection, axial excitation, parametric excitation, and self excitation (from left to right).

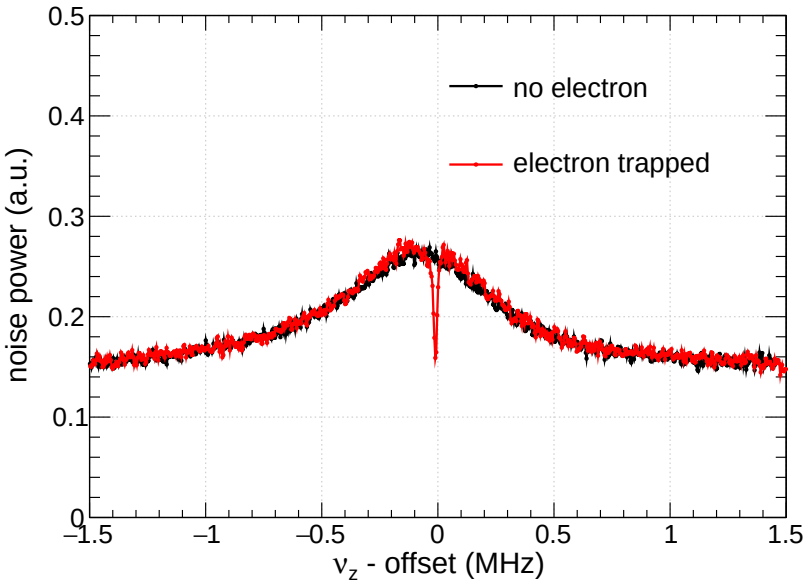


Figure 2.14: noise spectrum of the Johnson noise from the LCR resonance circuit without electrons trapped (black) and with about $N = 2000$ electrons trapped (red).

The ideal output voltage from the first stage amplifier is the Johnson noise of the LCR circuit. For a bandwidth Δf, the Johnson noise voltage is

$$V_N(\omega) = \sqrt{4k_{\mathrm{B}}T\mathrm{Re}[Z(\omega)]\Delta f}, \tag{2.51}$$

where k_B is the Boltzmann constant.

The electric behavior of the electron in the trap chamber be represented by an equivalent series LC circuit [66]. The electron shorts out the parallel LCR circuit at the axial frequency. As a result, the Johnson noise resonance has a dip when particles are trapped, as shown in Fig. 2.14. For one electron, the full width of the dip is given by $\gamma_z/(2\pi)$. For N trapped electrons, its width is given by $N\gamma_z/(2\pi)$ [66]. We can measure this width to deduce how many electrons are trapped. This scheme does not require any external drive. The measured axial frequency in this method is the frequency when the electron is at its thermal equilibrium state.

Axial Excitation with Two Drives

The axial motion can be excited by an external drive. The drive excite the electron to a higher amplitude, which makes detection easier. A single drive near the electron's axial frequency ν_z will suffer from strong direct feedthrough from the drive electrode to the first stage amplifier. To avoid this, a modulation drive at 5 MHz and an excitation drive at $\nu_d - 5$ MHz is used to drive at frequency ν_d. Typically, a modulation drive of about 150 mV_{pp} and excitation drive of about -60 dBm is applied to the endcap electrode for one electron. By exciting the trapped electron to a higher amplitude, we can also probe the anharmonicity of the trap. The anharmonicity, mainly C_4, can be tuned by changing the bias voltage on the compensation electrode V_c. Figure 2.15 shows the response from an axially excited electron for three different anharmonicities.

Parametric Excitation

The axial motion can also be excited by modulating the trap potential at twice its frequency $2\nu_z$. The parametric excitation generates a large and broadband response, which is useful for detecting the initially loaded electrons. When the electron is initially loaded, its axial frequency has a large uncertainty due to the initial large magnetron orbit. Since the parametric drive's frequency response is much broader than this uncertainty, we can count the number of loaded electrons by monitoring the excited power. Figure 2.16 (a) shows the newly developed electron counting method using the parametric excitation.

We can also reduce the number of trapped particles by applying a strong parametric drive. Figure 2.16 (b) shows the excited power from a strong parametric drive. Clear steps that correspond to the escape of electrons from the trap are observed. This method is critical when loading positrons in the future. If, by any chance, more than one positron are loaded, we can use this excitation to reduce the number of trapped positrons.

Another newly invented application is to use the parametric drive to measure the axial damping rate γ_z (Fig. 2.17). Due to its large response and absence of direct feedthrough,

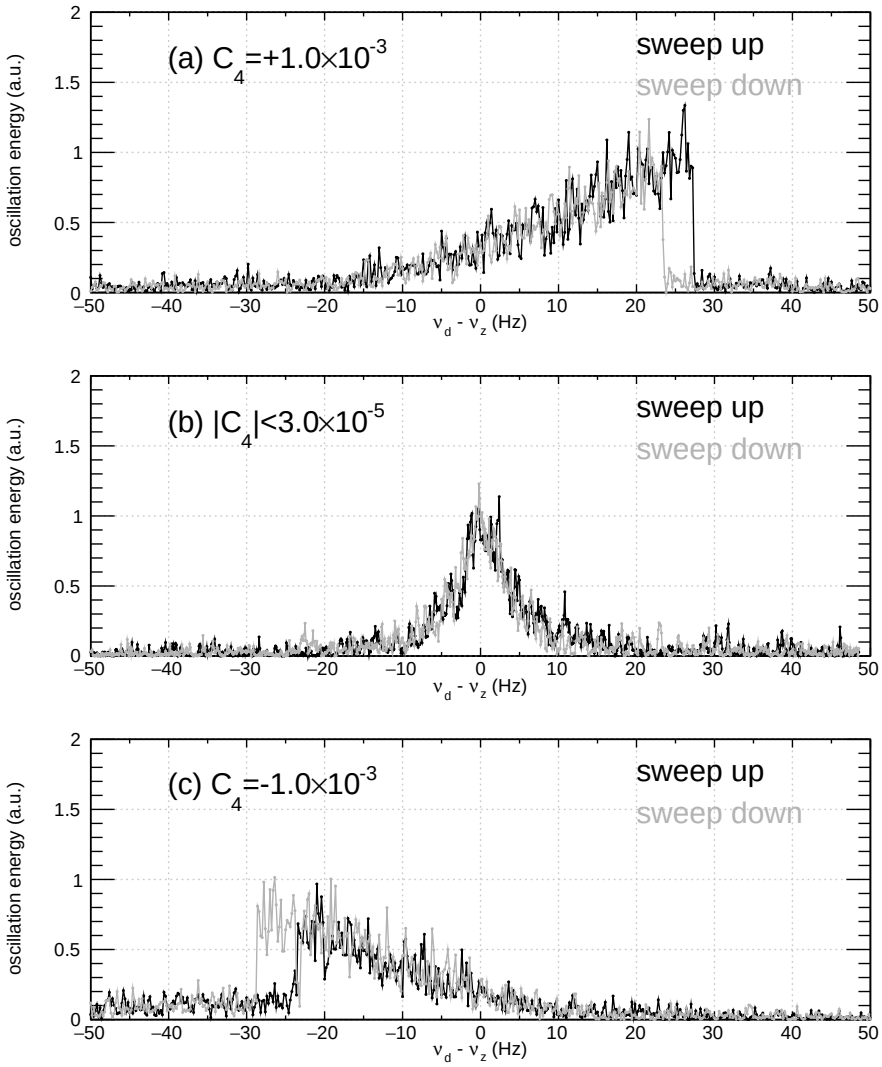


Figure 2.15: Probing the anharmonicity of the trap using one electron. The voltage on the compensation electrode is adjusted to set C_4.

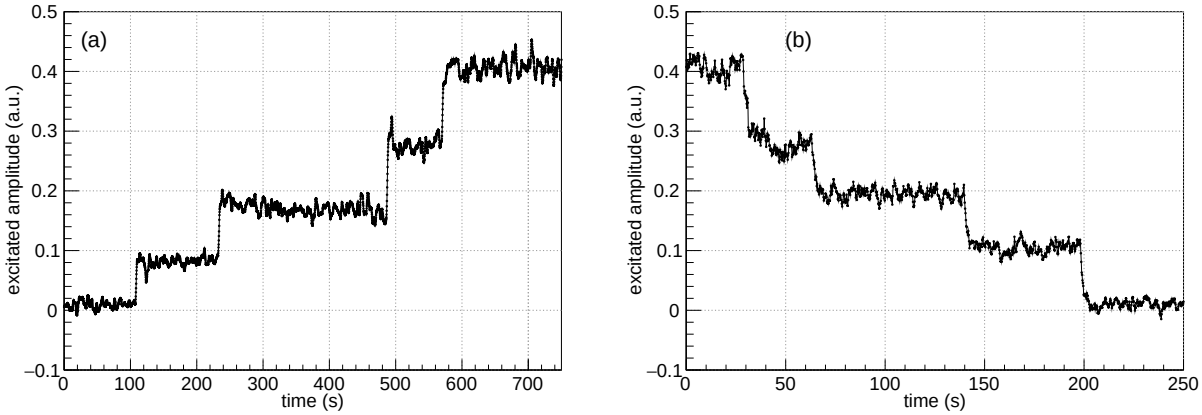


Figure 2.16: Counting the discrete loading of electrons using the parametric drive. (a) When loading electrons, the parametric drive at $2\nu_z$ is applied to the electrode, and the FEP is weakly biased. (b) When reducing the number of trapped electrons, a strong parametric drive is applied, and its response is monitored. Discrete jumps that correspond to electron loading or escaping are clearly visible.

parametric excitation can excite the electron to a very high amplitude that can be observed in the time domain. The electron is excited to high amplitude, and the parametric drive is turned off. The decay constant of excited oscillation power directly tells the axial damping rate γ_z. This method does not suffer from fast fluctuation of the axial frequency that can arise from any fast voltage noise, which would limit the linewidth in the dip detection or axial excitation methods.

Another feature of the parametric excitation is that it can drive the internal motion of a trapped cloud of electrons very efficiently. The trapped cloud of electrons is efficiently heated by the parametric drive, and it radiates energy by synchrotron radiation. The internal temperature can be used to probe the microwave cavity structure of the Penning trap. This feature will be discussed and used in detail in App. A.

Self-Excitation

A reliable and fast method to determine the electron's axial frequency is the self-excitation using positive feedback [67]. In this method, the signal from an electron is fed back to the drive electrode. By adjusting the phase, we set this feedback to be positive, leading to a large

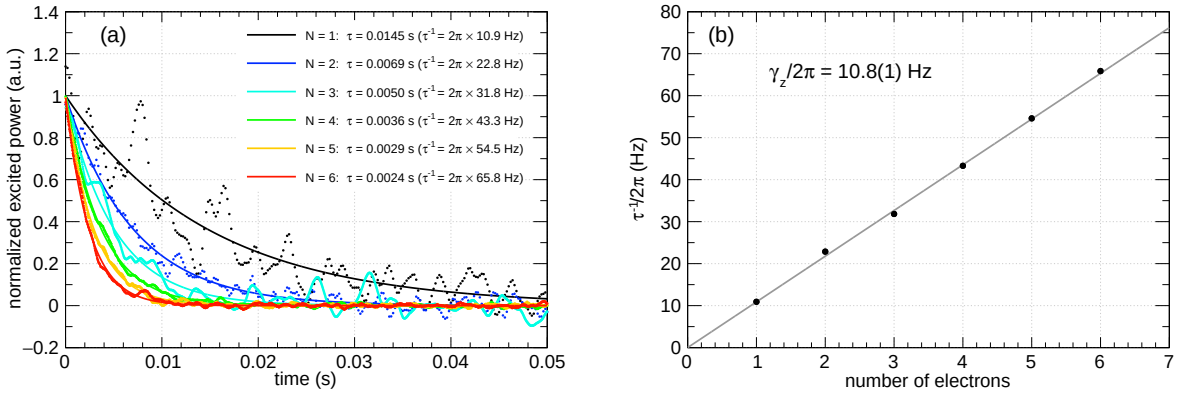


Figure 2.17: Measurement of the number of trapped electrons and its damping rate γ_z using the decay of parametrically excited motion. (a) The decay behavior of the excited power is fit with exponential curves. (b) The obtained time constant $\tau^{-1}/(2\pi) = \gamma_z$ shows discrete steps, with its coefficient given by the damping rate for a single electron $\gamma_z/(2\pi) = 10.8$ Hz. This data was taken at an axial frequency of 90 MHz.

excitation of electron by itself. To limit and control its excitation amplitude, a limiter based on DSP (Digital Signal Processor)[2] and voltage variable attenuator are used to limit the gain of the feedback loop [64]. Figure 2.18 shows the power spectrum of a self-excited electron. This method directly measures the oscillation frequency. We use this self-excitation method to measure the shift of the axial frequency to decipher cyclotron and spin transition. Details of the self-excitation are described in [64].

2.3.2 Measuring the Magnetron Frequency

The magnetron motion at ν_m can be measured by applying a cooling sideband drive at $\nu_z + \nu_m$. This drive couples the magnetron motion with the axial motion and cools the magnetron motion to

$$T_m = -\frac{\nu_m}{\nu_z} T_z. \tag{2.52}$$

The minus sign is necessary because the magnetron motion is meta-stable and higher orbit has less energy. In the limit that the magnetron motion is well cooled and equilibrated

[2]The highest n_c we can observe with this method is limited by the DSP. A new better limiting device needs to be developed.

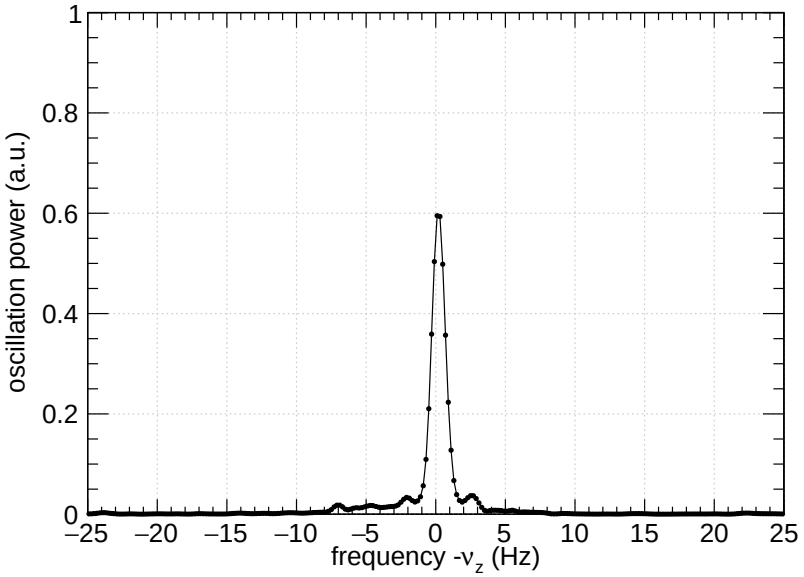


Figure 2.18: Frequency spectrum of the self-excited one electron. The width is limited by the resolution bandwidth of the spectrum analyzer, 1 Hz.

with the axial motion, the axial dip splits into two dips due to the drive (Fig. 2.19). For a given magnetron coupling drive at ν_d, the frequency of the left dip and right dip, ν_L and ν_R respectively, is related to the magnetron frequency as

$$\frac{\nu_L + \nu_R}{2} - \nu_z = \nu_d - (\nu_z + \nu_m). \tag{2.53}$$

Therefore, the dip splits symmetrically if the magnetron coupling frequency is exactly resonant with the cooling frequency, $\nu_d = \nu_z + \nu_m$. By sweeping the drive frequency and measuring the split dips, we can measure the magnetron frequency ν_m. With this method, the magnetron frequency is determined with a precision of about 0.1 Hz.

2.3.3 Magnetic Bottle Detection of the Cyclotron and the Spin States

Because of the low temperature of the trap, the cyclotron motion is always at its quantum ground state $n_c = 0$ unless an excitation drive is applied. Transitions between the quantum

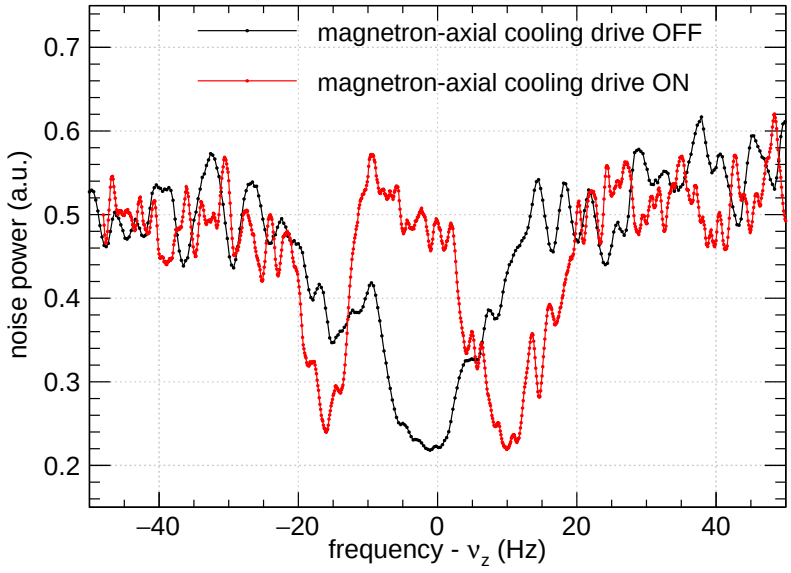


Figure 2.19: Split of electron's noise dip at axial frequency due to magnetron-axial sideband coupling.

states are detected using the magnetic bottle method [68, 69].

In the magnetic bottle method, a strong ferromagnetic material, in our case nickel, is placed near the center of the trap. The bottle alters the magnetic field and creates a quadratic gradient

$$\mathbf{B}(\rho, z) = B_0\hat{z} + B_2\left(z^2 - \frac{\rho^2}{2}\right)\hat{z} - B_2 z\rho\hat{\rho}. \tag{2.54}$$

The radial term $B_2 z\rho\hat{\rho}$ is used to drive the anomaly transition and will be discussed in the next section. We now focus on the magnetic field along the $\hat{z}$ direction. Since the electron's total magnetic moment in the z direction depends on the spin and cyclotron states,

$$\mu_z = -2\mu_B\left(n_c + \frac{1}{2} + \frac{g}{2}m_s\right) \tag{2.55}$$

the altered magnetic field couples the cyclotron state to the axial trapping potential by adding bottle term

$$H_z' = -\mu_z B(z) = 2\mu_B B_2 z^2\left(n_c + \frac{1}{2} + \frac{g}{2}m_s\right) + C. \tag{2.56}$$

The total confinement potential along the z axis is

$$\begin{aligned}\phi(z) &= \frac{1}{2}m\omega_z^2 z^2 + 2\mu_B B_2 z^2 \left(n_c + \frac{1}{2} + \frac{g}{2}m_s\right) \\ &\approx \frac{1}{2}m\left[\omega_z + \frac{2\mu_B B_2}{m\omega_z}\left(n_c + \frac{1}{2} + \frac{g}{2}m_s\right)\right]^2 z^2 \\ &= \frac{1}{2}m\left[\omega_z + \delta_c\left(n_c + \frac{1}{2} + \frac{g}{2}m_s\right)\right]^2 z^2,\end{aligned} \tag{2.57}$$

where the constant term is omitted, and

$$\delta_c \equiv \frac{2\mu_B B_2}{m\omega_z} = \frac{\hbar e B_2}{m^2\omega_z} \tag{2.58}$$

is the bottle shift for one quantum jump. Therefore, by monitoring the shift of the axial frequency, we can resolve the quantum state of the trapped electron. The axial frequency shift, with constant term subtracted, is

$$\delta\omega_z = \delta_c\left(n_c + \frac{g}{2}m_s\right). \tag{2.59}$$

Notice that the bottle shift expression in Eq. 2.59 also contains the spin quantum number m_s. The spin-flip $m_s = \frac{1}{2} \to m_s = -\frac{1}{2}$ shifts the axial frequency by $-(g/2)\delta_c \approx -1.001\delta_c$. This method is also used to detect spin-flip transition. The axial frequency shift by anomaly transition ($|n_c = 0, m_s = \frac{1}{2}\rangle \to |n_c = 1, m_s = -\frac{1}{2}\rangle$) is about $(g/2-1)\delta_c \approx 0.001\delta_c$, so is much smaller. Instead, we wait for the subsequent decay ($|n_c = 1, m_s = -\frac{1}{2}\rangle \to |n_c = 0, m_s = -\frac{1}{2}\rangle$) to detect the anomaly transition. Bottle jump parameter of $\delta_c/(2\pi) = 8.9$ Hz was used in commissioning, and $\delta_c/(2\pi) = 1.3$ Hz is used for the g-factor measurement.

The magnetic bottle gradient can be measured by shifting the electron along the z axis in the trap and measuring the change of the cyclotron frequency (Sec. 2.3.4). To shift the electron's position, an antisymmetric voltage of $V_A/2$ at top endcap electrode and $-V_A/2$ at bottom endcap electrode are applied. The displacement of the electron's position z_e is given

by [59]

$$\frac{z_e}{z_0} = \frac{1}{2}\left(\frac{d}{z_0}\right)^2 \frac{c_1}{1+C_2}\left(\frac{V_A}{V_R}\right). \tag{2.60}$$

Shifting the electron's position also shifts the axial frequency by shifting the electron's position,

$$\frac{\Delta\nu_z}{\nu_z} = -\frac{3}{4}\left(\frac{d}{z_0}\right)^4 \frac{c_1 c_3}{(1+C_2)^2}\left(\frac{V_A}{V_R}\right)^2. \tag{2.61}$$

Figure 2.20 shows the change of magnetic field and the axial frequency for a displacement of electron by applying the antisymmetric voltage. The magnetic field center shows about 17 μm of offset, and the axial frequency center shows about 8 μm of offset. The machining tolerance of our electrodes and spacers is 5 μm for each, which can explain this offset.

2.3.4 Measuring the Cyclotron Frequency

The cyclotron transition is excited by applying a drive at around $\nu_c = eB/(2\pi m)$. We need to send microwave drives between 80 GHz and 160 GHz. At this frequency range, the drive can be treated as a propagating electromagnetic wave. Figure 2.21 shows the schematic diagram of the microwave system. The microwave drive at ν_c is generated using a combination of a signal generator and a multiplier. Two signal generators are used, E8251A (Keysight) and SMA100B (Rohde & Schwarz). The frequency from the generator at 4–15 GHz is sent by a 2.92 mm cable to the multiplier and is multiplied to the desired drive frequency. Three generators are used to cover wide frequencies, IMPATT diode from ELVA-1 (140–152 GHz), WR6.5SGX from Virginia Diodes (110–170 GHz), and 934EF-20/387 from Millimeter Wave (60–90 GHz). The frequency and width of each combination of a generator and a multiplier is measured by beating the two sources and mixing down to RF range (Fig. 2.22). They all consistently give the right frequency and a width less than 1 Hz.

The maximum available power at multiplier's output is about 10 dBm, and the power is controlled by voltage variable attenuator for more than 100 dB dynamic range (Fig. 2.22). A

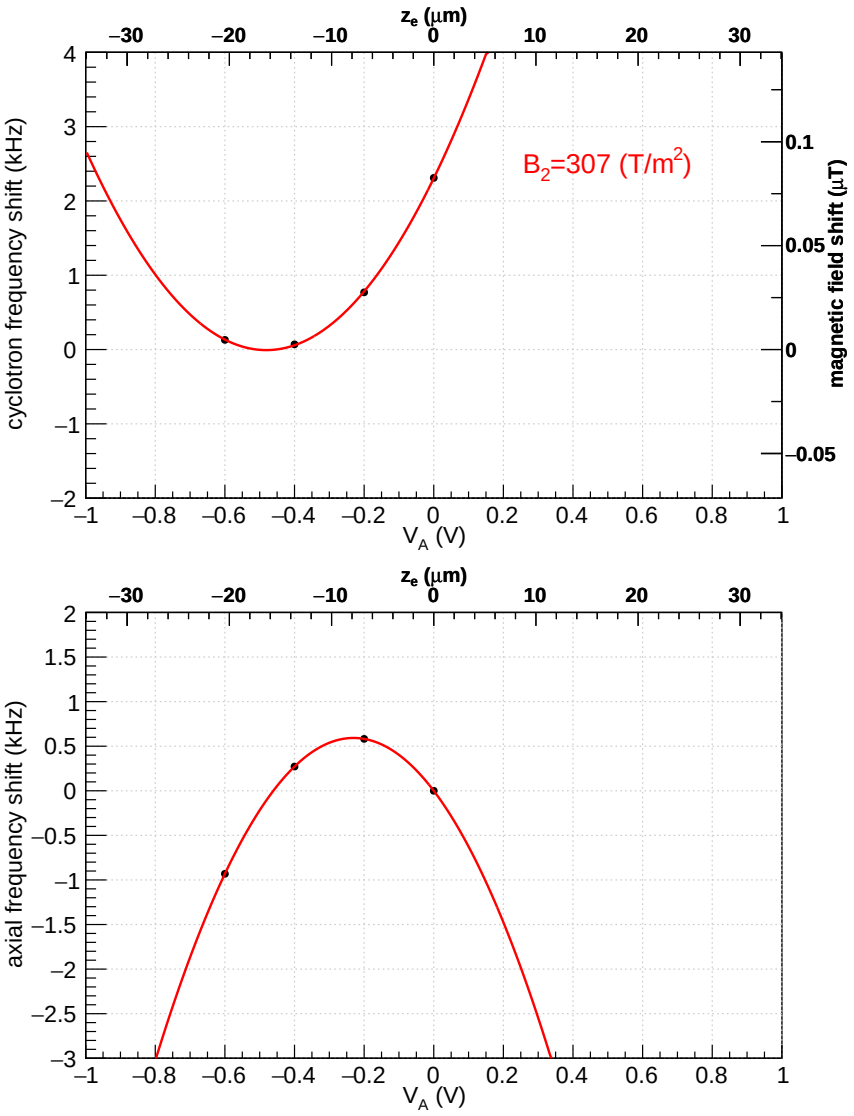


Figure 2.20: Shift of magnetic field (top) and axial frequency (bottom) when antisymmetric bias V_A is applied to shift electron's position.

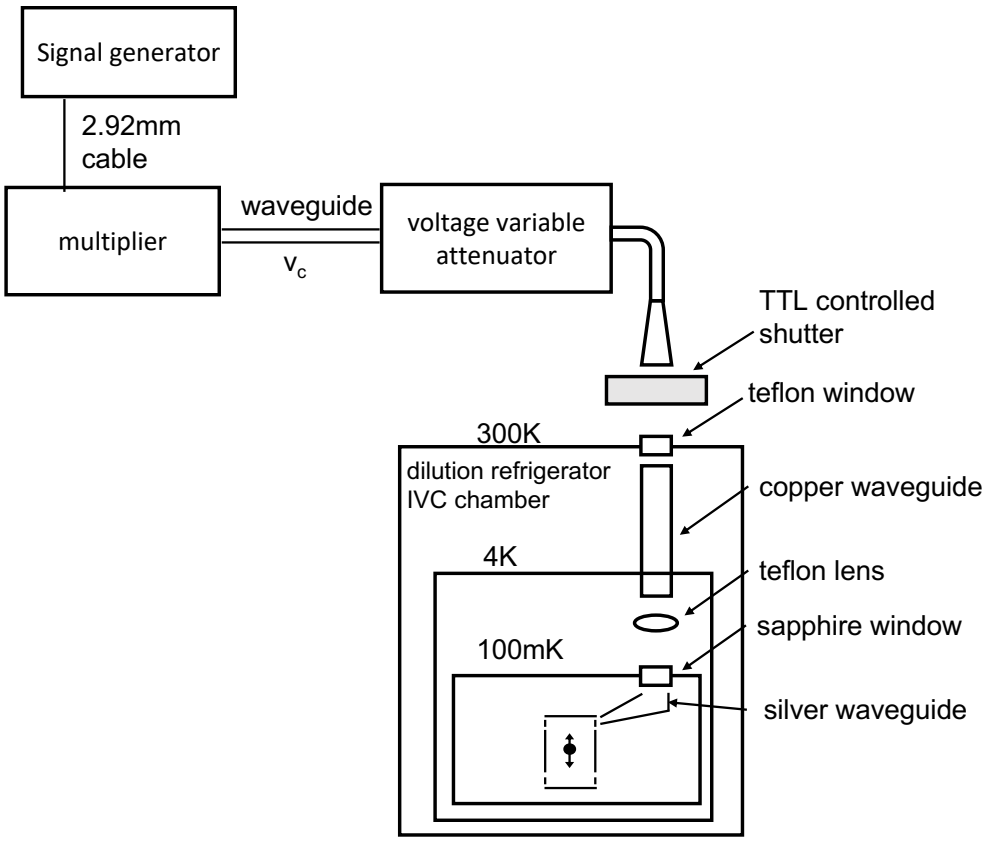


Figure 2.21: The system to generate and control cyclotron drive at microwave frequency ν_c.

TTL-triggered room temperature shutter is also installed to achieve clean attenuation. The drive is radiated from a horn at the top of the dilution refrigerator, guided through waveguides, collimated by PTFE lenses, and then radiated to the trap. Only about -200 dBm of power is required to induce one quantum cyclotron excitation.

Because the cyclotron transition is very narrow, it takes time to find the frequency initially. The cyclotron frequency is first estimated from ν_z and ν_m using the relation

$$\nu_c' = \frac{\nu_z^2}{2\nu_m}. \tag{2.62}$$

The actual cyclotron frequency, however, is usually different from the frequency determined by this method by about 10^{-4} due to the misalignment of the trap axis and magnetic field axis [55]. We use Eq. 2.62 to deduce the cyclotron frequency, and then sweep the cyclotron drive around its deduced value to find the actual cyclotron frequency in the trap.

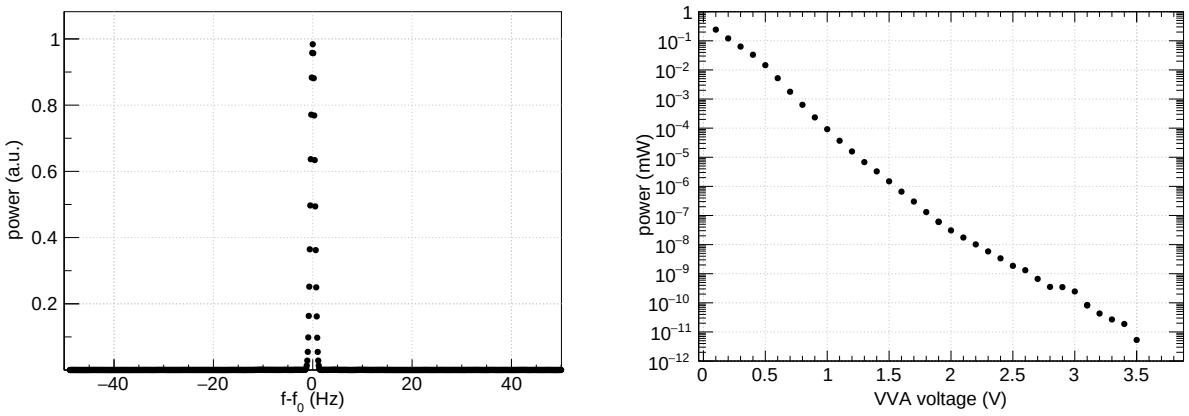


Figure 2.22: Measured microwave drive width (left) and attenuation on output power (right).

The cyclotron frequency can be found by monitoring the axial frequency and sweeping the drive frequency. Typically, the microwave drive is swept around the frequency deduced from Eq. 2.62 with the self-excitation is turned on. The self excited highly oscillating electron has larger cyclotron linewidth of about 50 kHz due to the magnetic bottle gradient (Eq. 2.54), compared to a few hundred Hz without axial excitation. When the drive is resonant with the cyclotron frequency, a quantum jump between cyclotron states is observed (Fig. 2.23).

The cyclotron frequency used for the g-factor measurement is measured when no axial excitation is applied. The resonant frequency without excitation is lower and much narrower than that measured when the self-excitation is on. Typically, an electron has an oscillation amplitude of about 100 μm by the self-excitation. This couples to the bottle gradient B_2 and shifts the magnetic field for the electron. To measure the cyclotron frequency when no excitation is applied, a microwave drive is applied with the self-excitation off, and then it is turned on to measure the axial frequency immediately after the drive. The axial frequency must be measured before the excited cyclotron state decays back with a timescale $1/\gamma_c = 5$ s. The exact procedure is discussed in Chap. 4.

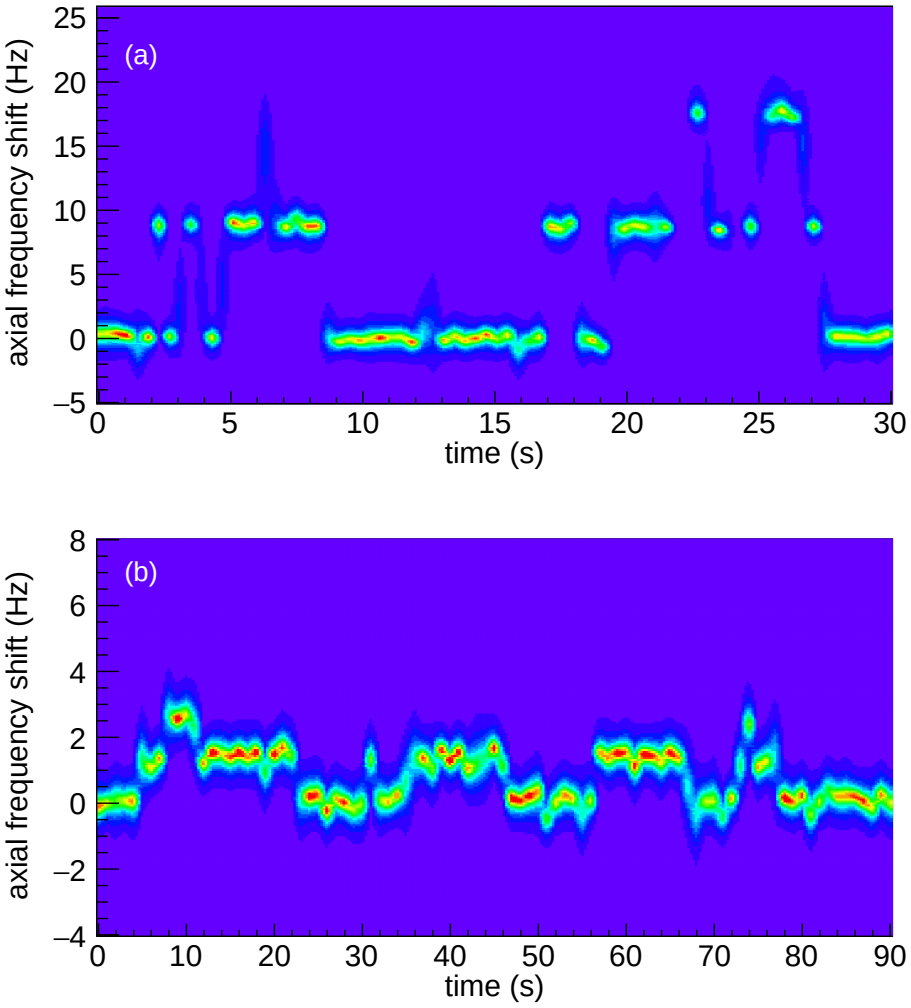


Figure 2.23: Quantum cyclotron transitions detected by monitoring axial frequency shift with self excitation. The colored z-axis is the Fourier transformed power, so a slice at particular time gives a Fourier spectrum similar to Fig. 2.18. (a) $\nu_z = 90$ MHz and $B_2 = 1500$ T/m^2, which gives $\delta_c/(2\pi) = 8.9$ Hz (b) $\nu_z = 115$ MHz and $B_2 = 300$ T/m^2, which gives $\delta_c/(2\pi) = 1.3$ Hz.

2.3.5 Measuring the Anomaly Frequency

The spin-flip is induced by driving the anomaly transition $|n_c = 0, m_s = +1/2\rangle \Leftrightarrow |n_c = 1, m_s = -1/2\rangle$. Since the lifetime of the spin transition is much longer than the typical experimental timescale $\gamma_s^{-1} \approx 5$ years, the spin state does not change unless an external drive is applied.

The anomaly transition is driven by applying an RF drive at the bottom endcap electrode. This drive modulates the electron's axial motion.

$$z(t) = z_a \cos(\omega_a t) \tag{2.63}$$

This modulation in the radial term of the magnetic bottle

$$B_\rho(\rho, z) = -B_2 z \rho \hat{\rho} \tag{2.64}$$

creates transverse modulation of the magnetic field $\mathbf{B}(t) = -B_2 z_a \rho \cos(\omega_a t)\hat{\rho}$. The radius ρ oscillates at its cyclotron frequency ω_c', which modulates the transverse magnetic field at $\omega_c' + \omega_a$. This has the right frequency and field direction to cause a spin-flip transition [54].

The spin state can be determined by applying a strong anomaly drive. When an electron is initially loaded, the spin state is unknown. After applying a strong anomaly drive, if the axial frequency shifts downward by $g/2 \times \delta_c \approx \delta_c$, it reveals that the electron was initially in the spin-up ($m_s = +1/2$) and now it is in the spin-down state ($m_s = -1/2$). When it is in the spin-down state, applying a strong resonant cyclotron drive and anomaly drive together and then waiting for a time longer than τ_c brings the spin-down state $|n_c = 0, m_s = -1/2\rangle$ back to the spin-up state $|n_c = 0, m_s = +1/2\rangle$ with 50 % of probability. Figure 2.24 demonstrates how we manipulate the spin state with this method. Strong cyclotron and anomaly drives are applied between the points. Clear manipulation of the spin states is demonstrated.

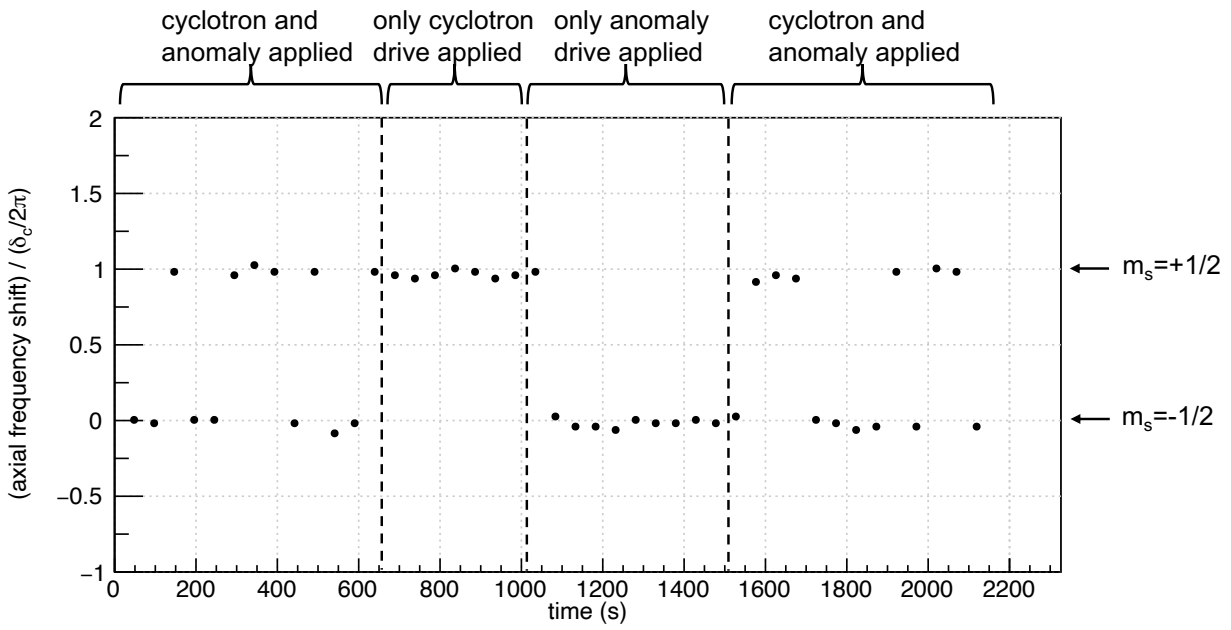


Figure 2.24: Manipulation of spin state using cyclotron and anomaly drive at $\nu_z = 90$ MHz and $B_2 = 1500$ T/m^2. Between each point, we apply a strong cyclotron or anomaly drive, or both, and then wait for 30 seconds to ensure that the cyclotron motion is in its ground state $n_c = 0$. The transition is clearly detected by the shift of axial frequency.

2.4 Summary

The setup for g-factor measurement has been described. The motion of an electron in a Penning trap has been illustrated, with cryogenic setup that allows quantum manipulation of the trapped electron's states. Several detection methods of the trapped electron using the axial motion has been described. All the oscillation frequencies of the trapped electron can be measured with the described procedure. The following studies are done by combining the methods listed in this chapter.

Chapter 3

Gaseous Helium-3 Cryogenic NMR Probe

Mechanical vibration was the largest systematic effect in the 2008 measurement [7]. We have moved to a cryogenic cold bore magnet to improve the mechanical stability of the apparatus. The bore of the magnet is filled with 4.2 K liquid helium. The homogeneity of the new cold bore magnet needs to be optimized for the best robustness against external mechanical perturbations. We have proposed and demonstrated a Helium-3 based Nuclear Magnetic Resonance (NMR) probe to achieve this. Part of the work here is summarized and published in [70].

NMR probes, such as water NMR probes, are used to optimize the homogeneity of typical warm bore magnets. However, these probes cannot be used to make high frequency resolution measurements in a cryogenic environment as they lose frequency resolution when the liquid sample in the probe freezes. A gaseous Helium-3 (^{3}He) NMR probe is designed and constructed to work naturally in such cryogenic environments, 4.2 K and 5.3 T [70]. This probe can achieve a frequency resolution better than 0.4 part per billion in less than 1 second. We use it to shim and study a superconducting solenoid with a cryogenic interior. The highly shimmed magnet produces a homogeneous magnetic field which reduces magnetic

field fluctuation due to the vibration of the probe.

An introduction to the pulsed-NMR measurement is given in Sec. 3.1. Design and construction of the ^{3}He NMR probe is described in Sec. 3.2. The observed signals are shown and discussed in Sec. 3.3. Measurements of the transverse and longitudinal time constants are reported in Sec. 3.4. The stability of the cold-bore magnet is characterized in Sec. 3.5. Sec. 3.6 discusses the possible future improvements.

3.1 Principle of Pulsed Fourier Transform NMR

Our technique to measure the homogeneity in a small region is to use pulsed Fourier transform NMR. In the pulsed Fourier transform NMR, a sample is placed in a volume with low magnetism. A strong magnetic field, $\vec{B} = B\hat{z}$ defines the initial spin quantization axis. Then an RF drive pulse is applied to tip the spin by 90 degrees. After that, each spin starts precession, whose frequency is defined by its local magnetic field value and is independent of the initial drive frequency. The spin precession induces a current on the same RF coil. The total induced signal is called the free induction decay (FID). Since the FID signal is a sum of all spins, its Fourier transformation gives the integral of the magnetic field sampled by each spin in the sample volume.

We first derive the essential features of the pulsed Fourier transform NMR from the first principle. The conclusions are the same in either the classical picture or the quantum picture. We use both classical and quantum picture and occasionally switch from one to the other to emphasize the essential feature. If necessary, any of the following conclusions can be derived using either classical or quantum picture only.

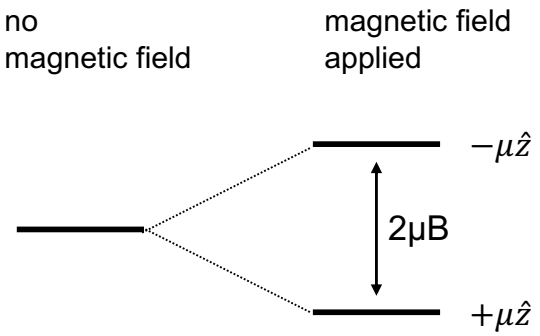


Figure 3.1: Two energy levels of a spin in a magnetic field B.

Spin Precession

Suppose a spin $\boldsymbol{S}$ (^{3}He in our case) is placed in a magnetic field $\mathbf{B} = B\hat{z}$, with a magnetic moment $\boldsymbol{\mu} = \gamma \boldsymbol{S}$, where γ represents the magnetic moment from the spin,

$$\gamma = \frac{g_n e}{2m_n}. \tag{3.1}$$

Here, g_n is the gyromagnetic ratio of the species, and γ for ^{3}He is known to be -32.434 MHz/T [71].

The Hamiltonian for the spin is then

$$H_0 = -\boldsymbol{\mu} \cdot \mathbf{B} = -\gamma \boldsymbol{S} \cdot \mathbf{B}. \tag{3.2}$$

Using the quantum picture, the magnetic moment has either up or down state along the magnetic field axis $\boldsymbol{\mu} = \pm\mu\hat{z}$, so the energy eigenvalues for up or down is (Fig. 3.1)

$$E_\pm = \mp\mu B = \mp\gamma\frac{\hbar}{2}B. \tag{3.3}$$

The torque from the magnetic field on the spin is given by

$$\frac{d\boldsymbol{S}}{dt} = \boldsymbol{\mu} \times \boldsymbol{B} = \gamma \boldsymbol{S} \times \boldsymbol{B} = \gamma B \boldsymbol{S} \times \hat{z}, \tag{3.4}$$

or explicitly,

$$\begin{aligned}\frac{d}{dt}S_x &= \gamma B S_y \\ \frac{d}{dt}S_y &= -\gamma B S_x \\ \frac{d}{dt}S_z &= 0.\end{aligned} \tag{3.5}$$

Define the complex transverse spin vector $S_{xy} \equiv S_x + iS_y$. Then the equation is simplified as

$$\begin{aligned}\frac{d}{dt}S_{xy} &= -i\gamma B S_{xy} \\ \frac{d}{dt}S_z &= 0.\end{aligned} \tag{3.6}$$

We can see that if the spin is pointing $\hat{x}$ direction at $t = 0$, $\boldsymbol{S} = (\hbar/2)\hat{x}$, then the time evolution is

$$\begin{aligned}S_{xy} &= \frac{\hbar}{2}e^{-i\gamma Bt} \\ S_z &= 0.\end{aligned} \tag{3.7}$$

or in vector form,

$$\boldsymbol{S} = \frac{\hbar}{2}\cos(\omega_{\mathrm{NMR}}t)\ \hat{x} - \frac{\hbar}{2}\sin(\omega_{\mathrm{NMR}}t)\ \hat{y}, \tag{3.8}$$

where

$$\omega_{\mathrm{NMR}} = \gamma B \tag{3.9}$$

is the NMR spin precession frequency. A spin in a magnetic field in the transverse direction rotates with this spin precession frequency defined by its local magnetic field.

External Drive, $\frac{\pi}{2}$-pulse, and π-pulse

Now we consider how the spin can be manipulated with an external drive. Suppose that the spin is initially in the spin-up state $\boldsymbol{S} = +(\hbar/2)\hat{z}$. An external RF magnetic field drive

with frequency ω is applied to the $\hat{x}$ direction

$$\boldsymbol{B}_1 = B_1 \cos(\omega t)\, \hat{x}. \tag{3.10}$$

The spin experiences a torque from the sum of the magnetic field. Using Eq. 3.4 with $\boldsymbol{B} = B\hat{z} + B_1 \cos(\omega t)\, \hat{x}$ gives

$$\begin{aligned} \frac{d}{dt}\boldsymbol{S} &= \gamma \left[\boldsymbol{S} \times (B\hat{z} + B_1 \cos(\omega t)\, \hat{x})\right] \\ &= \omega_{\mathrm{NMR}} \boldsymbol{S} \times \hat{z} + \gamma B_1 \cos(\omega t)\, \boldsymbol{S} \times \hat{x}. \end{aligned} \tag{3.11}$$

Define the Rabi frequency

$$\Omega_R = \frac{\gamma B_1}{2} \tag{3.12}$$

and move to the rotating frame

$$\begin{aligned} S_x &= \tilde{S}_x \cos(\omega t) + \tilde{S}_y \sin(\omega t) \\ S_y &= \tilde{S}_y \cos(\omega t) - \tilde{S}_x \sin(\omega t) \\ S_z &= \tilde{S}_z. \end{aligned} \tag{3.13}$$

In the rotating frame, Eq. 3.11 is now

$$\begin{aligned} \frac{d}{dt}\tilde{S}_x &= -\tilde{S}_y (\omega - \omega_{\mathrm{NMR}}) - 2\tilde{S}_z \Omega_R \cos(\omega t)\sin(\omega t) \\ \frac{d}{dt}\tilde{S}_y &= \tilde{S}_x (\omega - \omega_{\mathrm{NMR}}) + 2\tilde{S}_z \Omega_R \cos^2(\omega t) \\ \frac{d}{dt}\tilde{S}_z &= -2\tilde{S}_y \Omega_R \cos^2(\omega t) + 2\tilde{S}_x \Omega_R \cos(\omega t)\sin(\omega t). \end{aligned} \tag{3.14}$$

To solve this equation, we apply the rotating wave approximation, which drops the fast-changing terms in the time scale of 2ω. We also define the detuning $\delta \equiv \omega - \omega_{\mathrm{NMR}}$. The

equations above are now

$$\begin{aligned}
\frac{d}{dt}\tilde{S}_x &= -\delta\tilde{S}_y \\
\frac{d}{dt}\tilde{S}_y &= \delta\tilde{S}_x + \Omega_R\tilde{S}_z \\
\frac{d}{dt}\tilde{S}_z &= -\Omega_R\tilde{S}_y.
\end{aligned} \tag{3.15}$$

The solution of this equation with the spin initially in the up $(\tilde{S}_x, \tilde{S}_y, \tilde{S}_z) = (0, 0, \hbar/2)$ is

$$\begin{aligned}
\tilde{S}_x &= \frac{\hbar}{2}\frac{\Omega_R\delta}{\Omega_R^2+\delta^2}\left[\cos\left(\sqrt{\Omega_R^2+\delta^2}t\right) - 1\right] \\
\tilde{S}_y &= \frac{\hbar}{2}\frac{\Omega_R}{\sqrt{\Omega_R^2+\delta^2}}\sin\left(\sqrt{\Omega_R^2+\delta^2}t\right) \\
\tilde{S}_z &= \frac{\hbar}{2}\left[1 - \frac{2\Omega_R^2}{\Omega_R^2+\delta^2}\sin^2\left(\frac{\sqrt{\Omega_R^2+\delta^2}}{2}t\right)\right].
\end{aligned} \tag{3.16}$$

Of particular interest is when the drive frequency is equal with the NMR spin precession frequency $\omega = \omega_{\mathrm{NMR}}$, so $\delta = 0$. Eq. 3.16 then becomes

$$\begin{aligned}
\tilde{S}_x &= 0 \\
\tilde{S}_y &= \frac{\hbar}{2}\sin\left(\Omega_R t\right) \\
\tilde{S}_z &= \frac{\hbar}{2}\cos\left(\Omega_R t\right).
\end{aligned} \tag{3.17}$$

The amount of induced NMR signal is proportional to its transverse spin vector $|\tilde{S}_y|$. Figure 3.2 shows how the spin vector flips as a function of drive time and power $\Omega_R t$.

Two pulses are particularly interesting. One is the pulse that flips the spin vector by 90 degrees,

$$T_{\frac{\pi}{2}} = \frac{\pi}{2\Omega_R}. \tag{3.18}$$

This pulse length is called $\frac{\pi}{2}$-pulse and gives the largest observed transverse magnetization.

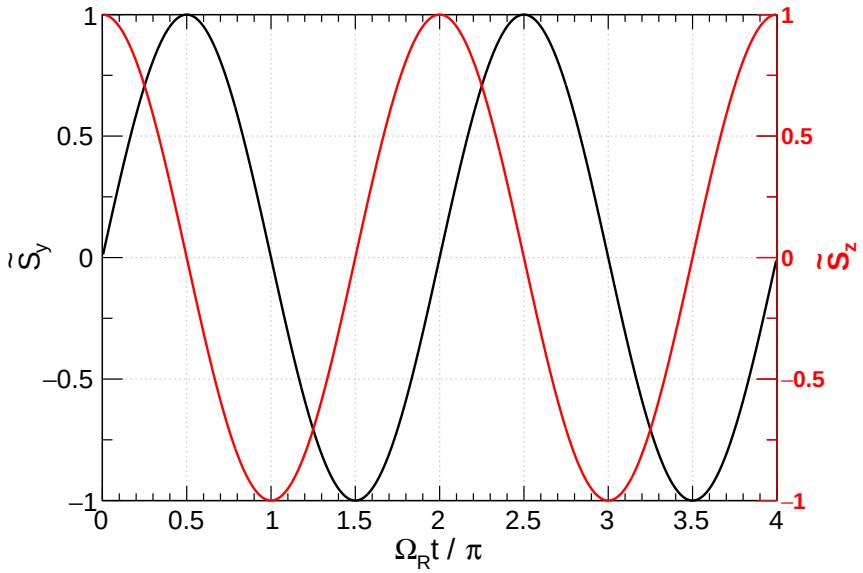


Figure 3.2: Change of spin vector $\tilde{S}_y$ and $\tilde{S}_z$ versus the product of drive power and time $\Omega_R t$.

Second, the pulse length that flips the spin vector 180 degrees is called π-pulse

$$T_\pi = \frac{\pi}{\Omega_R}. \tag{3.19}$$

The π-pulse flips the spin vector by 180 degrees. Small deviations from the ideal pulse length has negligible effects in the following measurements. We use these pulses to prepare the spin precession or to perform the spin echo measurement.

Measuring Homogeneity using Many Spins

The 90-degree flipped atom starts spin precession with its NMR frequency (Eq. 3.9). The frequency is determined by its local magnetic field B. If the spins distribute uniformly in a finite volume, their precession frequencies have a spread determined by the magnetic field inhomogeneity over the volume. In our case, we use a spherical glass bulb with a 1 cm diameter. We denote the variance of the magnetic field in the target volume as ΔB. The

spread of the free precession frequency is then,

$$\frac{\Delta\omega_{\mathrm{NMR}}}{\omega_{\mathrm{NMR}}} = \frac{\Delta B}{B}. \tag{3.20}$$

Due to the frequency-time uncertainty principle, as we measure the spin precession frequency with time, the spread in frequency domain Δ_{NMR} appears in the decay time constant of the total spin precession. As different spins precess with different angular frequencies, they acquire different phases. The net spin direction cancels with each other because of the decoherence of the phases. This is the so-called free-induction decay (FID) signal. By taking the Fourier transform of the FID signal, we measure the inhomogeneity $\Delta\omega_{\mathrm{NMR}}$. The decay constant of the FID signal due to the inhomogeneous field is called T_2^*. Because of the time-frequency uncertainty principle, T_2^* is related to $\Delta\omega_{\mathrm{NMR}}$ by

$$T_2^* \approx \frac{1}{\Delta\omega_{\mathrm{NMR}}}. \tag{3.21}$$

Therefore, the inhomogeneity can be measured as

$$\Delta B = B\frac{\Delta\omega_{\mathrm{NMR}}}{\omega_{\mathrm{NMR}}} = \frac{1}{\gamma T_2^*} \tag{3.22}$$

So far, we have only discussed decoherence among the spins due to magnetic field inhomogeneity. However, even in an ideal homogeneous magnetic field, the free induction signal has other decoherence effects, such as interactions among the spins. The physics behind this is very complicated and beyond the target of this thesis (for example, see [72]). Instead, in the practical application of NMR measurements, the decoherence time constant in an ideal magnetic field is labeled as T_2. This time constant T_2 limits the resolution of frequency resolution, so it needs to be long enough to make a useful measurement.

Magnitude of Signal from Thermal Imbalance

The maximum size of the FID signal is given by the net magnetic moment of N spins. To get a useful signal, the initial imbalance of the population between the spin states needs to be large. For room temperature ^{3}He NMR, optical pumping schemes are usually necessary to establish a large enough signal [72]. This requires a complicated system and time-consuming preparation. In our 4.2 K ^{3}He NMR, we demonstrate that no external pumping scheme is required because of the high density achieved by the low temperature.

In thermal equilibrium, each atom has spin-up or spin-down state. We assume $\mu > 0$ for simplicity, but the same discussion holds for $\mu < 0$ as well. The distribution of population between the two states (Fig. 3.1) is given by the Boltzmann distribution

$$\frac{N_{\mathrm{down}}}{N_{\mathrm{up}}} = \exp\left(-\frac{2\mu B}{k_B T}\right), \tag{3.23}$$

with the relation $N_{\mathrm{up}} + N_{\mathrm{down}} = N$. The imbalance is then

$$|N_{\mathrm{down}} - N_{\mathrm{up}}| = N\frac{1-\exp\left(-\frac{2\mu B}{k_B T}\right)}{1+\exp\left(-\frac{2\mu B}{k_B T}\right)} = N\tanh\left(\frac{\mu B}{k_B T}\right), \tag{3.24}$$

and the net magnetic moment M is

$$M = N\mu\tanh\left(\frac{\mu B}{k_B T}\right). \tag{3.25}$$

We will use this expression to estimate the magnitude of the signal in the next section.

The time constant to establish the thermal imbalance is called the longitudinal time constant T_1. For example, after an FID measurement, the spins point in different directions, and the net magnetic moment is $M = 0$. The spins need to be realigned with the magnetic field. For a completely randomized ensemble of spins, the time evolution of the net spin

$M(t)$ is given by

$$M(t) = M\left[1 - \exp\left(-\frac{t}{T_1}\right)\right]. \tag{3.26}$$

This T_1 needs to be short enough to repeat the NMR measurement is a realistic time scale. We measure the T_1 for ^{3}He using the saturation recovery method (Sec. 3.4).

Summary of Relaxation Time Constants

There are three important time constants that we have used to characterize the NMR signal:

- The longitudinal time constant T_1 is the time constant that establishes the initial spin alignment along the z axis. If T_1 is too long, it limits the repetition rate of the pulsed NMR measurement.

- The transverse time constant T_2 is the decoherence time of the horizontal net magnetism in an ideal homogeneous magnetic field. T_2 limits the smallest homogeneity that we can resolve.

- The time constant T_2^* is the decoherence time in the actual inhomogeneous magnetic field. T_2^* probes the inhomogeneity in the target volume and is made as long as possible by tuning the shim coils.

Typically there is a relation

$$T_2^* < T_2 < T_1. \tag{3.27}$$

Our target frequency broadening is about $1/(2\pi T_2^*) = 1$ Hz, so T_2 longer than 1 second is desired. On the other hand, to repeat measurement in a realistic time scale, T_1 needs to be shorter than, for example, $T_1 < 1000$ seconds.

3.2 Design and Construction of the Probe

In a warm bore magnet, a water sample is typically used as an NMR sample to characterize the homogeneity. However, in our 4.2 K cold bore magnet, a water sample cannot be used. When water freezes, it not only increases its volume and could break the glass sample bulb, but also loses its coherence time T_2. Constructing a vacuum chamber and attaching heaters to thermally isolate the water target from the 4.2 K liquid helium interior is not ideal because it requires additional large hardware and introduces additional magnetism. A natural approach is to use a gas sample instead. ^{3}He gas is chosen since it is the only species that exists as a gas at 4.2 Kelvin and still has a large nuclear magnetic moment. Our NMR probe is designed to work at $B = 5.3$ T magnetic field, generating a ^{3}He spin precession frequency of $\omega_{\mathrm{NMR}}/2\pi = 172.3$ MHz, but this frequency is widely tunable.

3.2.1 Estimate of NMR Signal Amplitude

We first estimate how much signal we can get from the ^{3}He NMR probe and compare it with the widely used water NMR probe. From Eq. 3.25, the NMR signal is approximated as

$$M = N\mu \tanh\left(\frac{\mu B}{k_B T}\right) \approx N\mu \frac{\mu B}{k_B T}, \tag{3.28}$$

where N is the number of spins, T is the temperature of thermal equilibrium, μ is the magnetic moment of each spin, and k_B is the Boltzmann constant. The hyperbolic tangent factor is the net fraction of the spins that are thermally aligned. As $\mu B/(k_B T)$ is very small, the approximation to the right in Eq. 3.28 suffices in all conditions considered here.

Since a room temperature water sample in a 1 cm diameter spherical volume (DSV) cell produces a large enough NMR signal to be useful, we compare the size of the water moment to that for ^{3}He gas in the same sample volume in Table 3.1. The magnetic moments, μ, are given in the unit of nuclear magneton μ_N. Since the ^{3}He moment is 76% that of water, the largest differences between the net moments come from the differing numbers of spins in the

	μ/μ_N	T (K)	$\mu B/(k_B T)$	N	M/μ_N
H_2O	2.8	300	1.8×10^{-5}	3.5×10^{22}	1.8×10^{18}
^{3}He only gas cell	2.1	4.2	9.8×10^{-4}	1.3×10^{19}	2.7×10^{16}
^{3}He with reservoir	2.1	4.2	9.8×10^{-4}	9.1×10^{20}	1.9×10^{18}

Table 3.1: Comparison of NMR samples at $B = 5.3$ T.

cell N and polarization fractions, $\mu B/(k_B T)$.

An atmosphere of ^{3}He in the same sample cell volume, after cooled from 300 K to 4.2 K, results in ~ 2700 times fewer spins than for the water sample (^{3}He only gas cell in the table). Even though the polarization factor increases by a factor of 54, the net magnetic moment M (and hence the size of the NMR signal) is only 1.5% that of the water sample.

Increasing the room temperature pressure inside a sealed bulb to match the water signal would require 60 atmospheres of pressure in the glass bulb at room temperature. Instead, we connect the 1 cm diameter (=0.5 cm^3) glass bulb through a capillary to a much larger (1200 cm^3) reservoir volume that stays at room temperature (Fig. 3.3). Gas atoms move from the reservoir into the bulb to keep approximately 1 atmosphere of pressure in the bulb as it cools to 4.2 K. The last line in the table (^{3}He with reservoir) shows that the number of nuclear spins in the bulb is still 38 times smaller than for the water sample. However, as the polarization fraction is 54 times larger, the net result (when the slightly different nuclear moments are also factored in) is that the magnetic moment of the gas sample is 1.1 times that of the water sample. The NMR signal size is thus 10% larger than a room temperature water sample would produce in the same volume.

This high-density condition also suppresses the effect of motional narrowing [73]. At 4.2 K and 1 atmospheric pressure, the diffusion coefficient of ^{3}He is as small as $D \approx 4 \times 10^{-7}$ m^2/s (Sec. 3.4 and [74]). With this slow diffusion rate, we are in the limit $D \to 0$, and motional narrowing does not occur. This ensures that the measured T_2^* reflects the inhomogeneity over the volume directly.

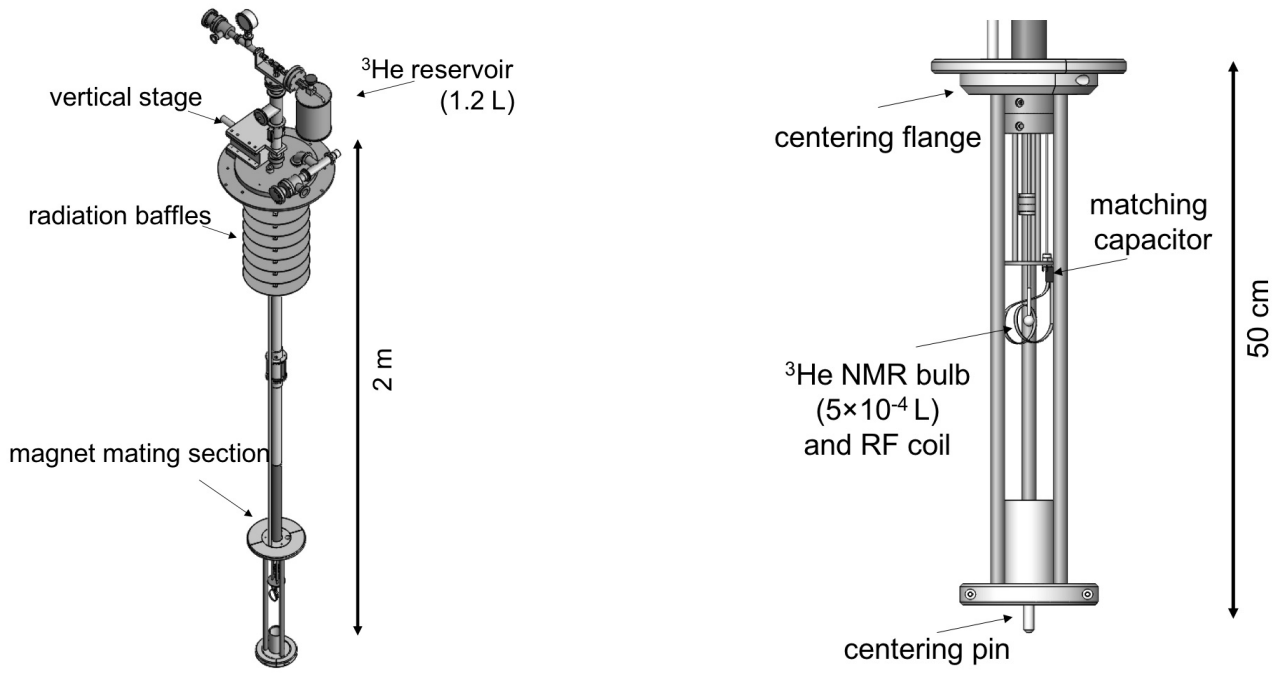


Figure 3.3: (left) Overview of an NMR probe and support. (right) Expanded view of the NMR sample bulb and its pickup coil.

3.2.2 The Helium-3 Probe

Figure 3.3 shows the constructed gaseous ^{3}He probe. It is designed to align the bulb with the axis of the superconducting solenoid. The large room temperature reservoir is connected to the NMR bulb via a capillary tube to ensure high density of ^{3}He target. The 1 cm diameter glass bulb (Type I, Class A borosilicate glass, 529-A-12 Wilmad-LabGlass) is produced for NMR use. The bulb is measured to have negligible magnetism at the level discussed here. All other probe components are also measured to have minimal magnetism and placed as far as possible from the bulb to avoid other magnetic perturbations. Special care is taken with the alignment parts in the magnet mating section, which are fabricated from only pure copper, aluminum, molybdenum, and titanium. The RF coil near the bulb is made from a 99.9999 % pure thin copper foil and is loosely wound around the bulb. The centering flange and centering pin ensure the radial alignment with our magnet. The ^{3}He line is mechanically fixed to the vertical translation stage at the hat and can be moved inside

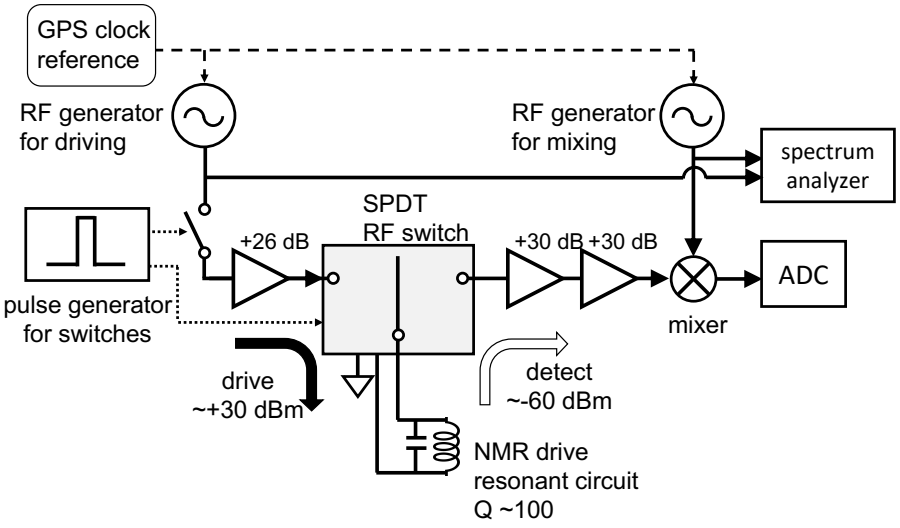


Figure 3.4: Circuit used to drive and detect the $\omega_{\mathrm{NMR}}/2\pi = 172.3$ MHz NMR signal.

the magnet bore that is filled with liquid helium. We can rotate the NMR bulb, capillary line, and the resonant circuit inside the magnet bore to check the residual magnetism of the probe.

The circuit used to produce and detect the NMR signal from the ^{3}He is a simple switching circuit shown in Fig. 3.4. Two RF frequency generators referencing a GPS clock signal are used. One drives the ^{3}He spin at the resonant frequency, and the other is used to mix the NMR signal down to 1.5 kHz. Then the signal is recorded by an Analog-to-Digital converter (ADC). Both frequencies are monitored by a spectrum analyzer. A pulse-controlled single pole, double throw (SPDT) RF switch is used to switch the driving side and the detection side. Since the signal isolation of the SPDT switch is not enough, another RF switch is used in the driving side to suppress direct feedthrough. Three RF amplifiers are used to drive and detect the NMR frequency. A matching capacitor is mounted near the NMR RF coil in the liquid helium to form a resonant circuit with a quality factor of about 100, which increases both driving and detection efficiency. The three applied pulse sequences with the circuit are shown in Fig. 3.5. Details of them are given in the following sections.

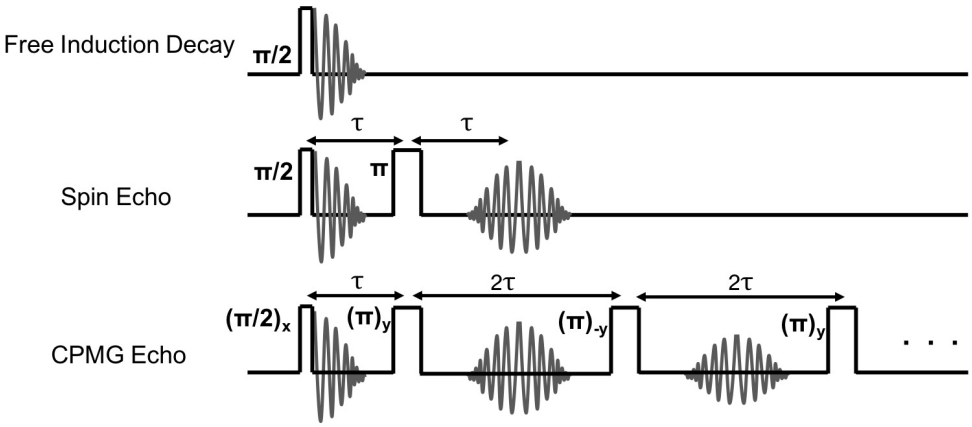


Figure 3.5: The drive pulse sequences for free induction decay (Sec. 3.3) and for both simple and CPMG spin echos (Sec. 3.4).

3.3 Spin Precession Signal

In a thermal equilibrium at temperature T, the population in the lower of the two spin states is slightly less, as described in Eq. 3.28. The ^{3}He bulb has the net magnetic moment given in the last line of Table 3.1. A nearly resonant drive pulse tips the resulting magnetic moment vector by an angle of $\pi/2$, as is typical in pulsed NMR measurements [75]. The size of the NMR signal depends upon the length of the drive pulse length and the intensity, as well as on the net magnetic moment. Figure 3.6 shows how the initial signal size varies as a function of the length of the drive pulse. Each peak in the graph corresponds to $\pi/2$, $3\pi/2$, $5\pi/2$, and so on. The decay constant is due to the inhomogeneity of the RF drive intensity. By taking this scan, we can measure the π-pulse drive length T_π.

The polarization, now tipped perpendicular to the magnetic field direction, rotates at the NMR angular frequency ω_{NMR} around the magnetic field direction. The changing flux through the pickup coils induces a signal across the coil, which is detected. Figure 3.7 shows how the free induction decay (FID) signal at 5.3 T, mixed down to about 1.5 kHz, decays with a time constant $T_2^* = 52$ ms, as field inhomogeneity in the sample causes the precessing nuclear spins to get out of phase with each other. A Fourier transform of this oscillating signal shows a sharp peak at the spin precession frequency (Fig. 3.8), with a signal-to-noise

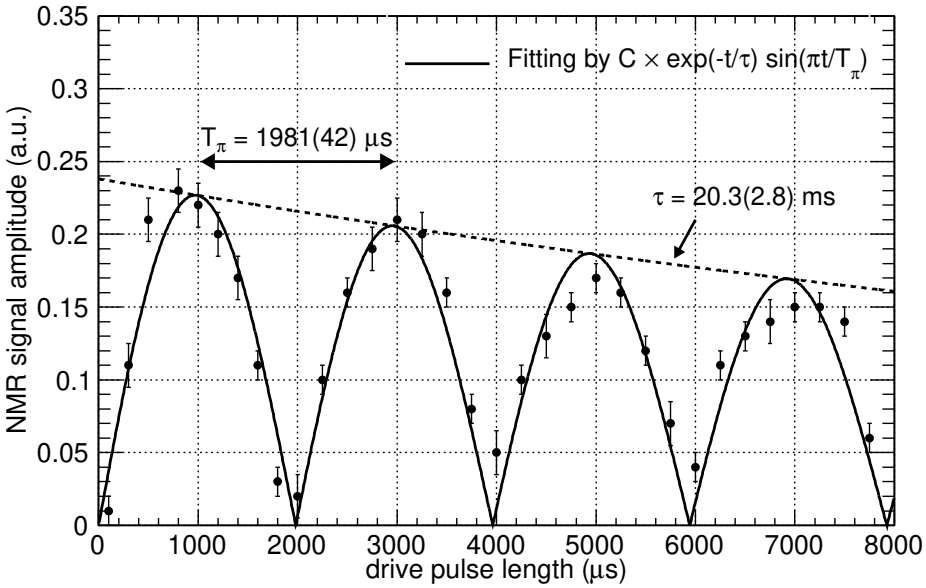


Figure 3.6: Dependence of the magnitude of the NMR precession signal upon the drive pulse's duration.

ratio of about 160. The width of this resonance divided by the drive frequency, $\omega_{\rm NMR}/2\pi =$ 172.3 MHz, gives the inhomogeneity of the field in the NMR bulb, 24 ppb. Figure 3.8 insert shows the Fourier transform, which has wider "tails". This is not surprising given that the ^{3}He gas in the glass capillary, just above the glass cell, contributes to the NMR signal, and the magnetic field in the capillary is different than in the center of the solenoid field. We thus concentrate on the width of the central feature, shown in the black line in the insert.

3.3.1 Possible Magnetism of the Probe

In the end, a measurement that requires a high field homogeneity will need to have the magnetic field shimmed to remove the unavoidable magnetism of the measurement apparatus. The magnetism of the NMR probe itself is one example. At the level of relative inhomogeneity we are interested in, $\mathcal{O}\left(10^{-9}\right)$, the magnetism of the probe is not necessarily negligible. To estimate the residual magnetism of the NMR probe, our NMR probe is designed so that the NMR bulb and its support structure can be rotated inside the magnet

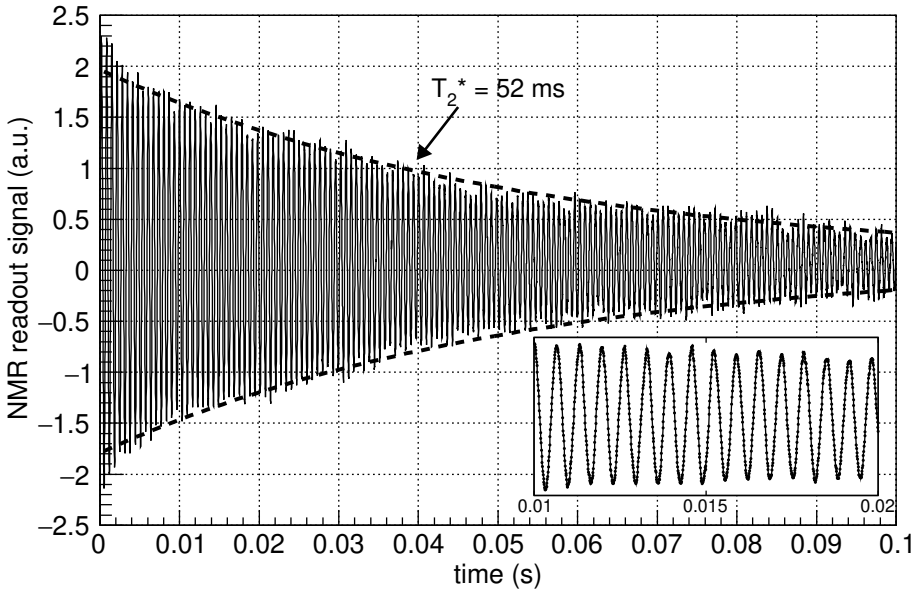


Figure 3.7: The NMR spin precession signal from the ^{3}He nuclei at 5.3 T, mixed down from 172.3 MHz to 1.5 kHz, decays with a time constant $T_2^* = 52$ ms in this example. The dashed lines represent the exponential decay with T_2^* obtained by a fitting. The inset shows an expanded view of the same plot from 0.01 s to 0.02 s.

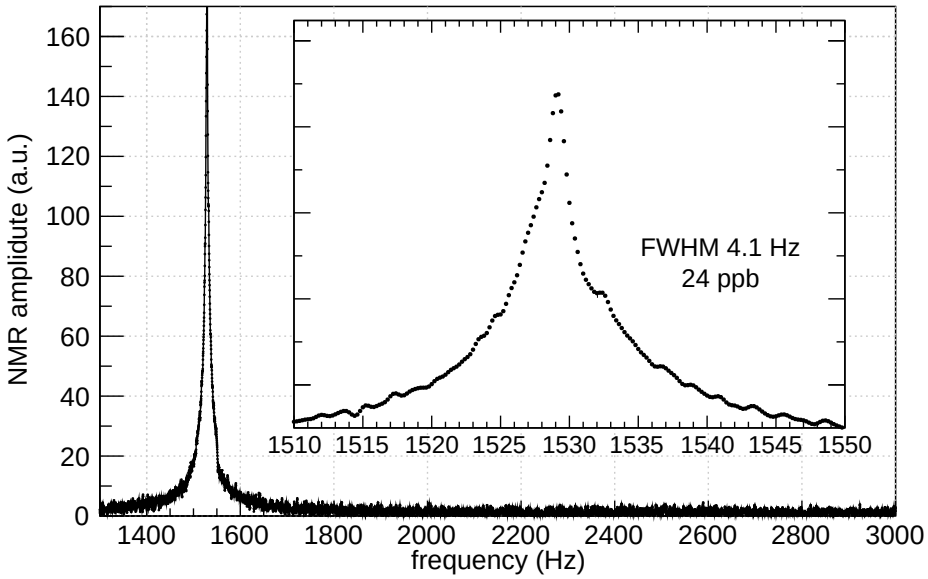


Figure 3.8: Fourier transform of the NMR spin precession signal shown in Fig. 3.7. The signal-to-noise ratio is about 160.

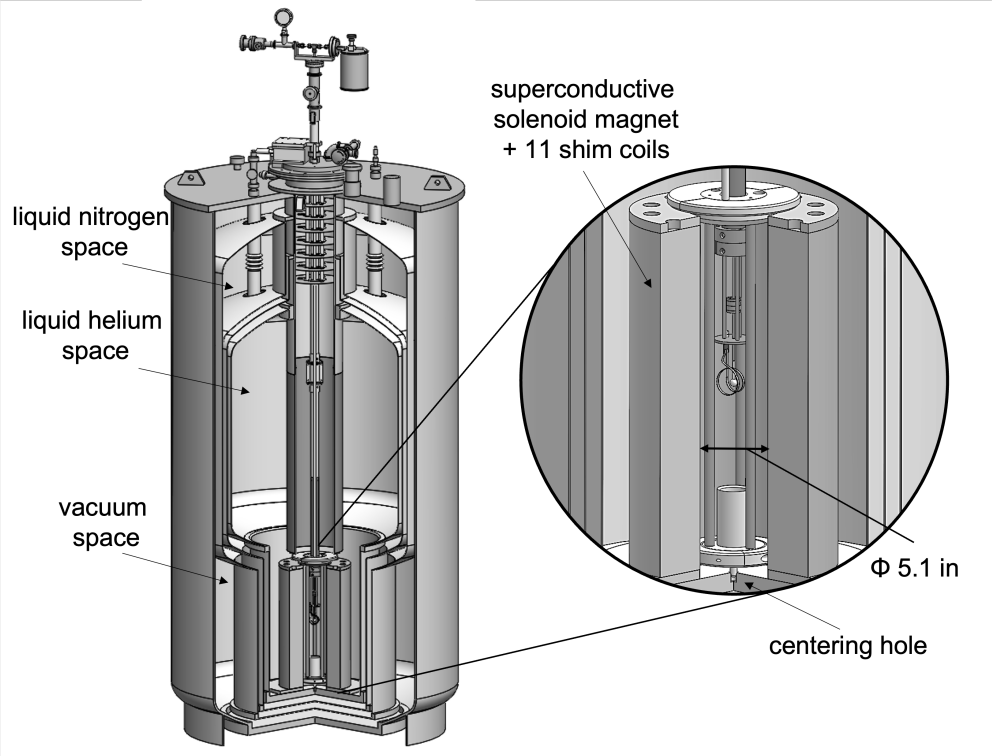


Figure 3.9: The superconducting solenoid system with the ^{3}He NMR probe inserted into the 4.2 K cold bore.

bore from the top of the dewar. Figure 3.9 shows our superconducting solenoid system with the NMR probe inserted into the cold bore. The bore size is 5.1 inches (130 mm) in diameter. It has 11 superconducting shim coils that can be used to optimize the homogeneity, in addition to the main 5.3 T solenoid magnet. The center rod that supports the NMR bulb is connected to the top. The NMR probe's centering plate and pin mate with the magnet structure as shown in the figure. We can rotate the NMR bulb, capillary line and its supports, the electronics circuit board, and the RF coil. Note that the magnet mating parts in Fig. 3.3 do not rotate, but they are made of pure copper and aluminum and much further away from the bulb. The rotatable parts are made of a variety of materials, and some of them are very close to the bulb. Thus the magnetism from the rotatable parts are much higher than that from others.

After shimming the magnet, the probe is rotated to check the residual magnetism, as shown in Fig. 3.10. The azimuthal angle of 0 degrees is defined as the initial position of

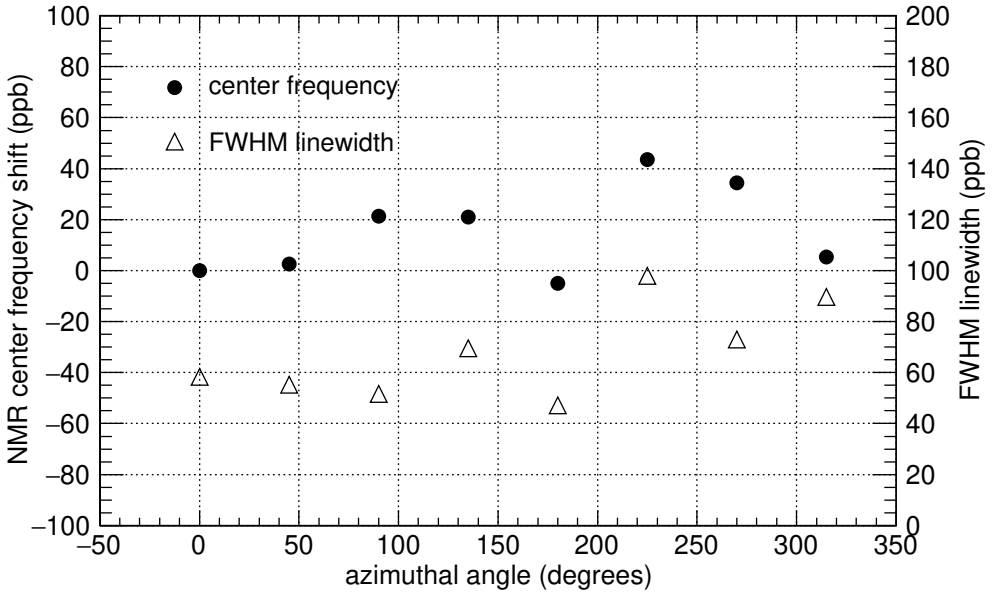


Figure 3.10: Dependence of the NMR center frequency and linewidth on the azimuthal angle of the probe. The initial orientation of the probe is defined to be 0 degrees.

the probe, and the initial center frequency is defined as 0 ppb shift on the left axis. Small dependence on the azimuthal angle can be seen. At the worst angle measured, 225 degrees, the linewidth increases to about 100 ppb, while the center frequency changes by about 50 ppb. Thus the effect of the residual magnetism is estimated to be 50 ppb.

Possible candidates for the residual magnetism in the probe have been investigated. The absolute value of the magnetic field produced by a dipole magnetization vector μ at distance r is $|B| \sim \mu_0/4\pi \times \mu/r^3$, where μ_0 is the vacuum permeability. The value varies by a factor of 2 at most, depending on the direction of the magnetization vector. As can be seen, the effect of residual magnetism is proportional to $1/r^3$. The closest part has the largest contribution to the magnetic field inhomogeneity.

In our case, the closest part is the RF drive coil made of copper. The magnetism of the 99.9999 % purity copper foil in the NMR probe is measured by a SQUID magnetometer (MPMS 3, Quantum Design Inc. [76]) to be $(5.0 \pm 1.2) \times 10^{-5}$ J/T cm^3 at 5.3 T. Our coil is made of a foil of cross-section 0.1 mm$\times$3 mm. Even with this small volume, an inhomogeneity would be seen. For example, if 1 cm of this foil is placed at 5 mm away from

the NMR bulb, it will induce about 40 ppb inhomogeneity. This is as large as the rotational dependence we have observed. Searches for high conductive metals with lower magnetism to replace the current copper coil are underway. Measurements using a small fragment of all other materials used (e.g., copper, tungsten, aluminum, circuit board, capacitor, SMA connector, glass of the bulb) suggest that these give negligible contributions.

3.4 Longitudinal and Transverse Time Constants

There are three time constants that are important in NMR measurements, T_1, T_2, and T_2^*. T_1 is the longitudinal relaxation time constant. T_2 is the decoherence time that would arise if the external magnetic field was perfectly homogeneous. It is the effect of the fluctuating magnetic field of the spins upon each other and limits the linewidth of an NMR probe. T_2^* is the decoherence time of the NMR signal because of the inhomogeneity of the magnetic field. The best T_2^* we have achieved is 52 ms, as shown in Fig. 3.7. Here we discuss the measurement of T_1 and T_2. Note that the RF field extends approximately 1cm into the 1.2 mm diameter capillary. The diffusion time through this centimeter length tube is estimated to be about 10^4 seconds [77], much longer than the T_1 and T_2 we measure.

3.4.1 Longitudinal Time Constant T_1

The time constant T_1 characterizes the time required for the initial thermal imbalance between the two spin states to be re-established. Some measurements report T_1 of ^{3}He to be as long as one day [78–81], and we were initially worried that this time constant was so long that it might be impossible to make repetitive measurements.

We measure the T_1 time of our ^{3}He sample by the saturation recovery method [82]. First, a very long pulse drive compared to the T_π is applied several times to randomize the spins of the ^{3}He atoms. Then we wait for a certain length of time for the total magnetization of ^{3}He to naturally "recover" back along the magnetic field axis. Finally, A $\pi/2$ pulse is applied to

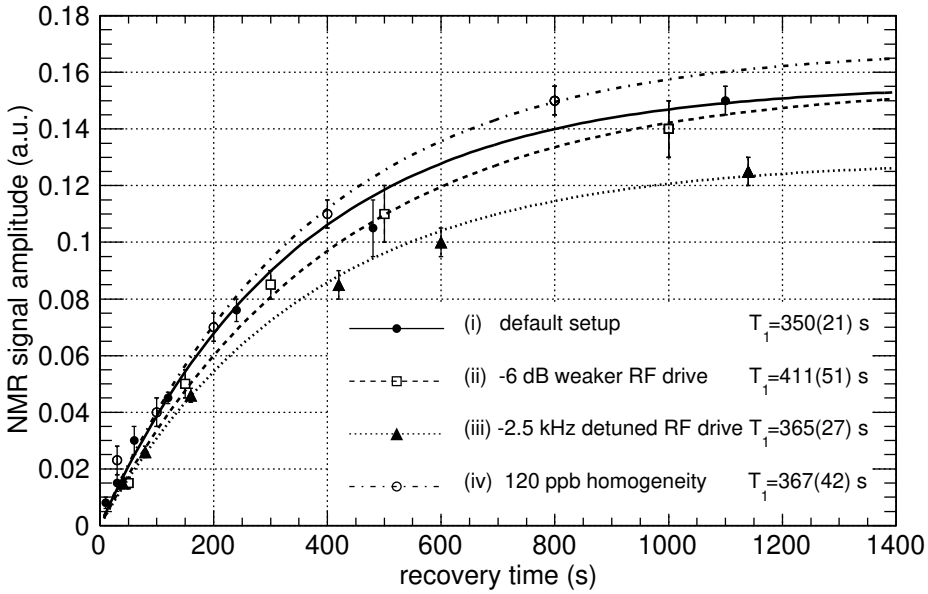


Figure 3.11: Measurement of the longitudinal relaxation time T_1 with saturation recovery method. The dots are measured data, and the lines are fittings by Eq. 3.26. Several parameters are varied to check the consistency.

measure the magnitude of the NMR signal after the recovery time. The time evolution of the magnetization $M(t)$ follows Eq. 3.26.

The T_1 measurements with this method are shown in Fig. 3.11. We also varied some parameters of the setup as systematic checks. In Fig. 3.11, (i) is the default setup as in Figs. 3.6, 3.7, and 3.8. As for the other measurements, (ii) a 6 dB RF attenuator is put in after the 26 dB amplifier on the drive side, (iii) the RF drive frequency is 2.5 kHz detuned from the resonant frequency, and (iv) the z shim coil is intentionally ramped to make the homogeneity worse. All the measurements are consistent within their error bars. By taking the weighted average and assigning the largest discrepancy as the systematic error, the longitudinal relaxation time is calculated to be $T_1 = 364$ (31) s. The time constants from magnetic dipole interaction and diffusion are much longer than this measured value [73, 78, 80, 81, 83, 84], and thus in our system, the wall relaxation effect is dominant. Similar results of T_1 measurements have been reported in [79, 85, 86].

Even though T_1 time is long, it does not limit the application of our NMR probe. Due to

the high signal-to-noise ratio achieved in our setup, as shown in Fig. 3.8, measurements with a recovery time of 20 seconds still give a signal-to-noise ratio of about 10. Usually, we spend about this much time changing the current on shim coils to avoid the magnet quenching. A signal-to-noise ratio of 10 is good enough to see the effect of changing the currents on the shim coils. When we monitor the drift of the superconducting magnet, we usually take the NMR signal every 60 seconds. The drift rate of the magnet is much slower than the longitudinal time constant T_1.

3.4.2 Transverse Time Constant T_2

T_2 is the relaxation time constant of the transverse magnetization even when the external magnetic field is perfectly homogeneous. This limits the coherence time of the NMR decay and thus sensitivity to the inhomogeneity of the magnetic field. Note that the ^{3}He atoms are moving at an average speed of

$$v_{\text{ave}} = \sqrt{\frac{8k_B T}{\pi m}} = 172 \text{ m/s}, \tag{3.29}$$

and the relaxation timescale of ^{3}He is on the order of 1 second. Therefore, even with the small diffusion coefficient, the effect is not negligible here.

A spin echo signal is widely used to measure T_2 [75]. Figure 3.12 shows the spin echo measurements performed with the probe. A $\pi/2$ pulse is applied at $t = 0$ second and a π pulse is applied at $t = 0.05$ second. A small FID signal after the π pulse arises from the imperfection of the π pulse. A clear spin echo signal is observed.

Figure 3.13 shows the spin echo measurements with different intervals. In the graphs, $\pi/2$ pulse and π pulses are applied at $t = -\tau$ and $t = 0$ respectively. In the top graph, the interval between the $\pi/2$ pulse and the π pulse, τ, is varied among 16 different values. Clear echos corresponding to each τ are observed. The bottom graph shows the amplitudes of the echos as a function of τ. As mentioned above, the effect of diffusion has to be considered

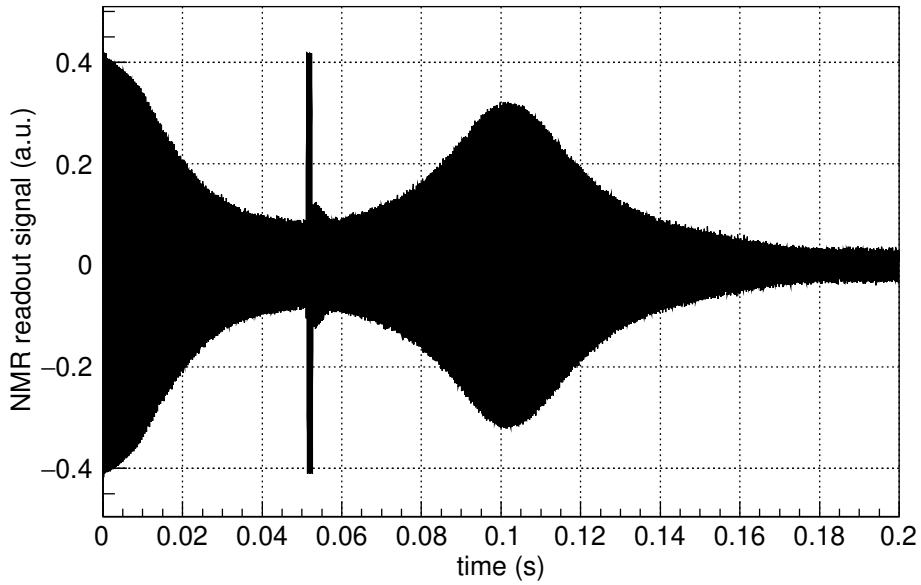


Figure 3.12: Spin echo signal observed with the ^{3}He NMR probe. A $\pi/2$ pulse is applied at $t = 0$ s and a π-pulse is applied at $t = 0.05$ s. A clear spin echo signal is observed after the π-pulse.

to explain the observed decay of the echo signals. Since the data was taken after shimming the magnet, we assume the largest source of inhomogeneity is the quadratic term of the magnetic field gradient. The amplitude of the first echo at $t = \tau$ as a function of the interval is given by [87, 88]

$$A(\tau) = \frac{\sqrt{\pi}}{2\beta\tau^{1.5}}\mathrm{Erf}\left(\beta\tau^{1.5}\right)\exp\left(\frac{-2\tau}{T_2}\right) \tag{3.30}$$

$$\beta = \sqrt{\frac{8}{3}D\gamma^2 b^2 L^2}, \tag{3.31}$$

where b represents quadratic magnetic field gradient $B_z(\mathbf{r}) = B_0 + bz^2$, D is the diffusion coefficient, γ is the gyromagnetic ratio, L is half of the typical size of the target volume, and T_2 is the intrinsic transverse decay constant. Figure 3.14 shows the echo signal is fitted by Eq. 3.30 assuming $\beta\tau^2 \gg 2/T_2$. The best fit result gives $\beta = 0.0023$ (ms)$^{-1.5}$.

The $\pm 2\sigma$ linewidth during these measurements is about 230 ppb. Based on the discussion of residual magnetism in Sec. 3.3, we conservatively assume the uncertainty of this value to

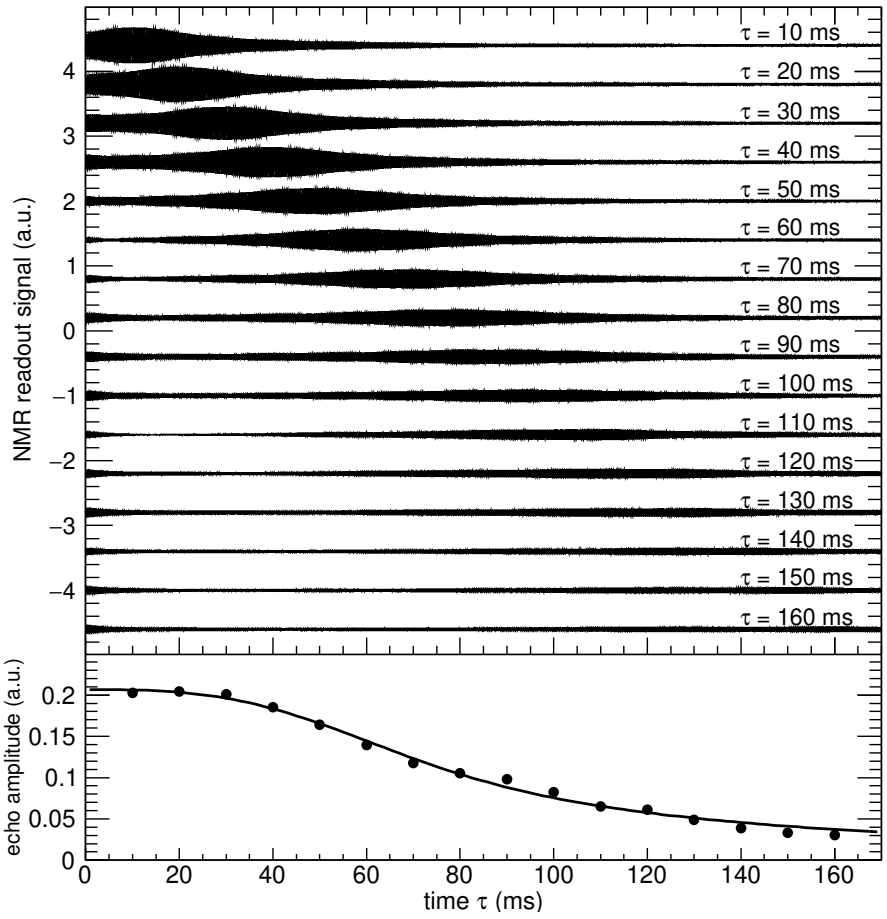


Figure 3.13: (top) Spin echo signals observed with the ^{3}He NMR probe. The horizontal axis is the time after applying π pulse. Measurements with 16 different echo times τ are shown. (bottom) Amplitudes of the echo are plotted as a function of echo time τ. Solid line is a fitting by Eq. 3.30 without the T_2 term.

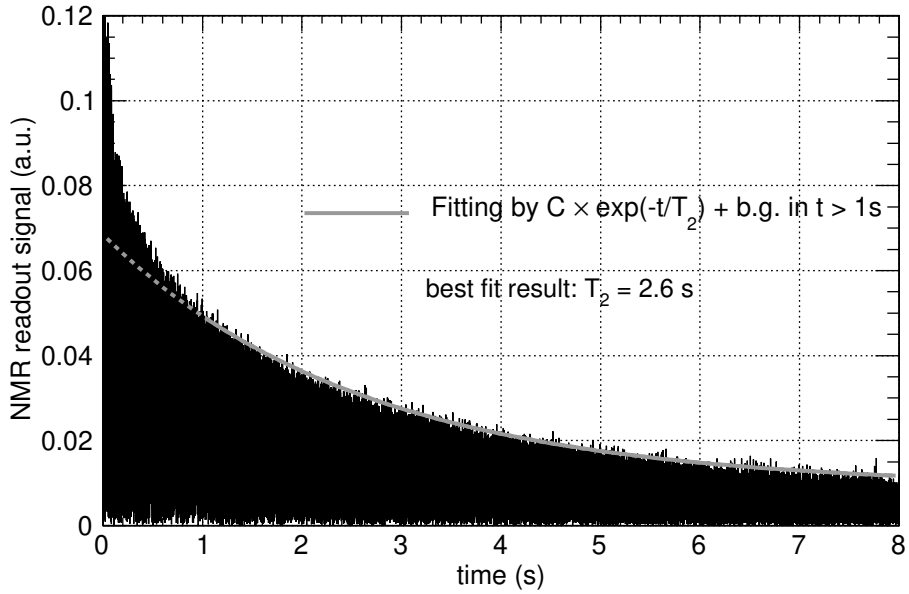


Figure 3.14: CPMG spin echo decay of ^{3}He measured by the probe with the echo time $\tau = 5$ ms.

be ± 50 ppb. The typical straight-line length of the bulb is $2L = \sqrt[3]{4\pi/3 \times (0.5\text{cm})^3} = 0.8$ cm. Thus we estimate $b = (7.6 \pm 1.7) \times 10^{-2}$ T/m^2. By using the gyromagnetic ratio of ^{3}He, $\gamma = 2\pi \times -32.434$ MHz/T, the diffusion coefficient is calculated to be $D = (5.9 \pm 2.6) \times 10^{-7}$ m^2/s. This agrees with a previous measurement [74] at a lower magnetic field that found $D = 3.6 \times 10^{-7}$ m^2/s. This small diffusion coefficient ensures that the motional narrowing effect is small in the T_2^* measurements [73].

To minimize the motional diffusion effects and measure T_2 accurately, we next employ the Carr-Purcell-Meiboom-Gill (CPMG) pulse sequence [89, 90]. As shown in Fig. 3.4, in a CPMG echo measurement, multiple π pulses are applied with 2τ intervals, with the first π pulse applied at τ after a $\pi/2$ pulse. The subscript x and y denote relative phases of the drive pulses. The interval between CPMG pulses is set to be $\tau = \tau_0 = 5$ ms. With this echo time, the effect of diffusion is negligible as long as $T_2 \ll 1/\beta^2\tau_0^2 = 7500$ s. Figure 3.14 shows the CPMG spin echo signal. The initial rapid decay is a combined effect of diffusion and the quadratic magnetic field [87,88]. The exponential decay at later times gives the time constant T_2. An exponential fitting in $t > 1$ s gives a transverse relaxation time constant $T_2 = 2.6$ s.

A similar value has been obtained by a room temperature NMR measurement [91].

We also performed this measurement with different π pulse lengths. The π pulse length is varied by $\pm 3\%$, and the measured T_2 values fluctuates between 2.56 s and 2.81 s. We take this spread as a systematic error and estimate $T_2 = 2.7(2)$ s. The corresponding relative inhomogeneity is $(1/T_2)/\omega_{\mathrm{NMR}} = 0.34(3)$ ppb. This is much smaller than the linewidth we have achieved, so does not limit the performance of our probe.

3.5 Stability of a Cold Bore Solenoid Magnet

For the magnetic moment measurement, the stability of the magnet is also an important parameter. We characterize the stability of the magnet using the probe. The NMR probe apparatus is inserted so that the bulb containing the ^{3}He gas is at the location that a single electron would be suspended. The solenoid magnet has a register at the top that centers the NMR probe and a hole at the bottom that centers the NMR probe.

The magnetic moment is measured from the spin and cyclotron frequencies. These frequencies are proportional to the magnetic field, and this field dependence cancels out to the lowest order. However, field variations are troublesome because the two frequencies are measured at slightly different times, separated by about 1 minute. For example, if we want to improve the limit by a factor of 10, the field needs to be stable or corrected for drifts better than 1.8 ppb/h.

Once a narrow NMR linewidth is determined, we measure this frequency repetitively to monitor the field stability. We are interested in the stability of times over which we make individual frequency measurements and the long-term stability over the time it takes to make the number of frequency measurements that must be averaged to get the desired uncertainty. The uncertainty in the NMR spin precession frequency in a single measurement is about 0.1 Hz, which corresponds to 0.5 ppb. By averaging the measurements over a long period, we can reduce the uncertainty of the drift rate.

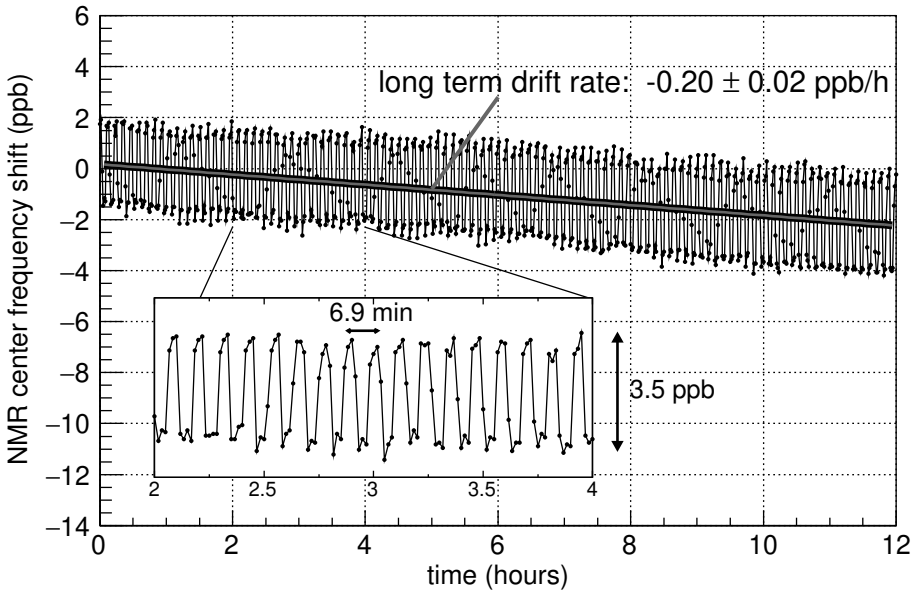


Figure 3.15: Measurement of the ^{3}He center frequency drift. ^{3}He NMR signal is taken every minute and fitted by a Lorentzian to acquire center frequency. Long term slow drift is slow enough for the g-factor measurement. The NMR signal identifies the 6.9 min oscillation, later also found in the single electron's axial frequency, to be from the temperature regulation heaters.

Figure 3.15 shows a sequence of measurements performed. The average pressure in the helium space and the nitrogen space of the solenoid system were well regulated during this measurement. The ^{3}He NMR signal is taken every minute and is fitted by a Lorentzian to get the center frequency. The center frequency is monitored for 12 hours, which shows a drift of about -0.20 ppb/h. The long-term drift rate is good enough to perform magnetic moments measurements. However, it also revealed a surprising periodic and non-negligible oscillation. Later, we discovered the same oscillation in the trapped electron's axial frequency. It turned out that an on-off heater at the top of the dewar was generating this periodic oscillation. Two observations from entirely different systems guided us to identify the source of the fluctuation. As demonstrated in this example, the ^{3}He probe works as an independent and fast way to diagnose our complicated system.

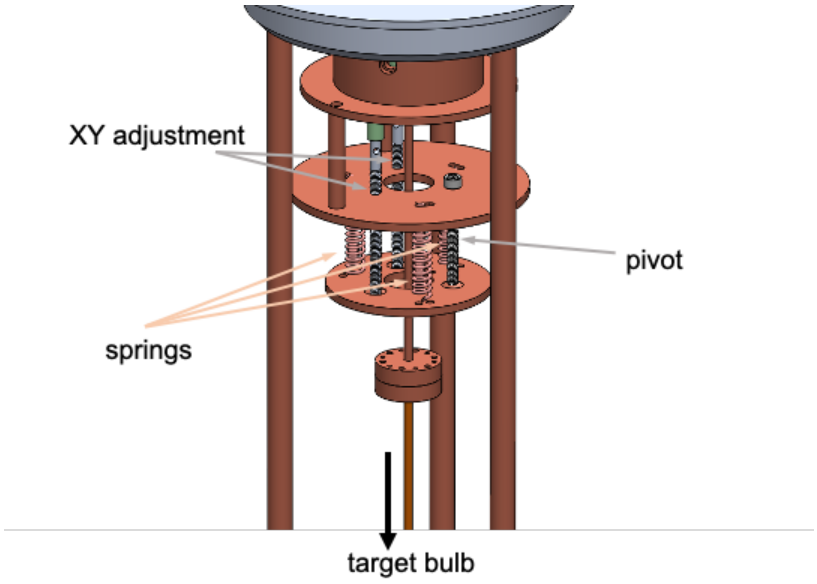


Figure 3.16: Design of the cryogenic XY stage. The top plate has three threaded holes. One is for pivot, and the other two are for X and Y adjustment.

3.6 Future Improvements

The accuracy of the probe is limited by how well the probe is radially aligned with the magnet. In the current probe, the vertical alignment can be changed *in-situ* inside the magnet. However, the radial alignment needs to be done at room temperature and cannot be changed in liquid helium. A new cryogenic XY stage is designed and implemented (Fig. 3.16). The top plate has three threaded holes. One is for a pivot, and the others are to adjust the XY plane. Turning the threaded rods pushes the bottom copper plate and tilts it. The bulb is connected at the bottom, and the capillary line is fixed to the bottom plate. Therefore, the position of the bulb can be adjusted in cryogenic environment by rotating the threaded rods. The threaded rod is connected all the way up to the room temperature feedthrough at the top. Although the two degree of freedom X and Y are not completely independent in this scheme, this adjustment does not take long time. We can always find the optimal point after several iterations.

Additionally, the inhomogeneity is limited by the magnetism of the RF coil. We have been using 99.999% purity copper. No conductive metal with lower magnetism has been

identified. A new coil with smaller material and larger diameter is also designed. The result will be presented in the future.

Chapter 4

Measurement of the Electron Magnetic Moment

A new measurement of the electron's magnetic moment is performed. Improved stability due to the new dedicated dilution refrigerator and superconducting magnet (Chap. 2) narrows the anomaly transition by a factor of 4. Careful shimming and optimization of the magnet (Chap. 3) allows measurement of g-factor at various fields, from 3.1 T to 5.3 T. Systematic errors are studied using a cloud of trapped electrons *in-situ*. The measurement principle is described in Sec. 4.1. The data-taking process, the analysis, and fitting methods are summarized in Sec. 4.2 The most critical systematic correction—microwave cavity correction—is studied in detail in Sec. 4.3. Other systematic effects are discussed in Sec. 4.4. Finally, the measured electron's magnetic moment is reported in Sec. 4.5.

4.1 Principle of Measurement

In principle, the g-factor can be determined by measuring the spin frequency and the cyclotron frequency of a trapped electron. However, small corrections from the electric field potential, imperfections of the trap, and microwave resonances need to be included. Shifts from the magnetic field misalignment, inhomogeneity, trap potential, and microwave

resonances are evaluated and summarized in this section.

4.1.1 Brown-Gabrielse Invariance Theorem

In an ideal Penning trap, a magnetic field $\mathbf{B} = B\hat{z}$ and a trap potential $V(x,y,z) = -\phi_0\left(z^2 - \frac{x^2+y^2}{2}\right)$ is applied to confine one electron. While the cyclotron motion in the trap shifts from the value in free space due to the applied electrostatic potential, the spin frequency does not (Chap. 2). The trap potential can have elliptic distortion $V(x,y,z) = -\varepsilon\phi_0\left(\frac{x^2-y^2}{2}\right)$ and misalignment angle θ with respect to the magnetic field. This imperfection is small, $\varepsilon \ll 1$ and $\theta \ll 1$, but shifts the measured frequencies $\bar{\nu}_c$, $\bar{\nu}_z$, and $\bar{\nu}_m$, from the ideal frequencies ν_c', ν_z, and ν_m. L. S. Brown and G. Gabrielse derived an invariance theorem that relates the measured frequencies to free space cyclotron frequency ν_c [55]

$$\nu_c = \bar{\nu}_c\left\{1 + \frac{1}{2}\left(\frac{\bar{\nu}_z}{\bar{\nu}_c}\right)^2 + \frac{9}{16}\left(\frac{\bar{\nu}_z}{\bar{\nu}_c}\right)^4\left[\left(\frac{\bar{\nu}_m}{\tilde{\nu}_m}\right)^2 - 1\right]\right\}, \tag{4.1}$$

where $\tilde{\nu}_m = \bar{\nu}_c/(2\bar{\nu}_z^2)$ is the calculated magnetron frequency from the measured cyclotron and the axial frequency. It is related to the measured magnetron frequency $\bar{\nu}_m$ by

$$\tilde{\nu}_m = \bar{\nu}_m\left(1 + \frac{1}{2}\varepsilon^2 - \frac{9}{4}\theta^2\right). \tag{4.2}$$

In general, the misalignment θ is larger than the elliptic distortion ε, and $\tilde{\nu}_m$ tends to be smaller than $\bar{\nu}_m$. By comparing $\tilde{\nu}_m$ and $\bar{\nu}_m$, we observe about $\theta = 1^\circ$ of misalignment. The third term in Eq. 4.1 is then about 10^{-15}. Therefore, the approximation

$$\nu_c = \bar{\nu}_c + \frac{\bar{\nu}_z^2}{2\bar{\nu}_c} \tag{4.3}$$

suffices for all conditions in this thesis.

The cyclotron frequency also shifts due to the relativistic increase of the electron's effective mass. At the precision level of parts-per-trillion, even a mass increase at meV scale

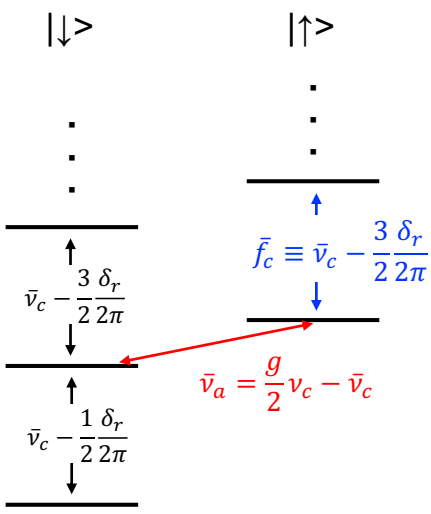


Figure 4.1: Quantum spin and cyclotron states of the trapped electron and the cyclotron (blue) and anomaly (red) transitions that are measured for g-factor measurement.

needs to be properly handled. The shift of cyclotron frequency (from n_c to n_c+1) is derived in [54],

$$\Delta\nu_c \;=\; -\frac{\delta_r}{2\pi}\left(n_c+1+m_s\right), \tag{4.4}$$

where

$$\frac{\delta_r}{2\pi} = \frac{h\nu_c^2}{mc^2} \approx 180\ \text{Hz} \times \left(\frac{B}{5.3\ \text{T}}\right)^2. \tag{4.5}$$

We measure the cyclotron transition $|n_c = 0, m_s = 1/2\rangle \rightarrow |n_c = 1, m_s = 1/2\rangle$ and the anomaly transition $|n_c = 0, m_s = 1/2\rangle \rightarrow |n_c = 1, m_s = -1/2\rangle$ to determine the g-factor. Figure 4.1 summarizes the quantum states and transitions used to determine the electron's g-factor. $\bar{f}_c$ is defined as relativistically shifted cyclotron frequency. The g-factor is determined from the measured frequency as

$$\frac{g}{2} = 1 + \frac{\bar{\nu}_a - \frac{\bar{\nu}_z^2}{2\bar{f}_c}}{\bar{f}_c + \frac{3}{2}\frac{\delta_r}{2\pi} + \frac{\bar{\nu}_z^2}{2\bar{f}_c}} + \Delta\frac{g}{2}|_{\text{cav}}, \tag{4.6}$$

where $\Delta\frac{g}{2}|_{\text{cav}}$ is the shift of cyclotron frequency due to microwave cavity resonances and

is discussed in details in Sec. 4.3. Importantly, all quantities $\bar{f}_c, \bar{\nu}_a$, and $\bar{\nu}_z$ are measured, and correction due to cavity shift $\Delta\frac{g}{2}|_{\text{cav}}$ is also applied based on the measured microwave resonances.

4.1.2 Line Shape

The line shape theory derived by L. S. Brown [92, 93] has been widely used in Penning trap experiments. We have derived an updated line shape that can also apply to the quantum regime [94, 95]. Both line shapes yield a consistent result when the axial motion is in the classical regime.

The ideal line shape is derived from the magnetic bottle and the axial oscillation amplitude. Since the electron is trapped in the magnetic bottle gradient $B_2 z^2$, the cyclotron or anomaly frequency, collectively ω_0, depends on z as

$$\omega(z) = \omega_0 \left(1 + \frac{B_2}{B} z^2\right), \tag{4.7}$$

where ω_0 is its oscillation frequency at $z = 0$. The electron's average axial amplitude $\langle z^2 \rangle$ is given by the average of the Boltzmann distribution.

$$\langle z^2 \rangle = \frac{k_B T_z}{m\omega_z^2} \tag{4.8}$$

Therefore, the scale of broadening is given by

$$\Delta\omega = \omega_0 \frac{B_2}{B} \langle z^2 \rangle = \omega_0 \frac{B_2}{B} \frac{k_B T_z}{m\omega_z^2} = \begin{cases} \frac{eB_2}{m} \frac{k_B T_z}{m\omega_z^2} & \text{(cyclotron)} \\ \frac{g-2}{2} \frac{eB_2}{m} \frac{k_B T_z}{m\omega_z^2} & \text{(anomaly)} \end{cases}. \tag{4.9}$$

Here, $\Delta\omega$ is called the bottle broadening parameter. The quantum description gives the same result from another perspective. The quadratic magnetic bottle adds a term in the

Hamiltonian

$$\mathcal{H}' = \hbar\delta_c \left(\hat{a}_c^\dagger \hat{a}_c + \tfrac{1}{2}\right)\left(\hat{a}_z^\dagger \hat{a}_z + \tfrac{1}{2}\right), \tag{4.10}$$

where δ_c represents the shift of axial frequency by one quantum cyclotron, as well as the shift of cyclotron frequency for an increase of axial quantum number. The average axial quantum number $\bar{n}_z$ at temperature T_z is

$$\bar{n}_z = \left[\exp\left(\frac{\hbar\omega_z}{k_B T_z}\right) - 1\right]^{-1} \approx \frac{k_B T_z}{\hbar\omega_z}. \tag{4.11}$$

The last approximation corresponds to the classical limit ($T_z \gg \hbar\omega_z/k_B$). In this limit, the bottle parameter for cyclotron transition is expressed by

$$\Delta\omega_c = \bar{n}_z\delta_c = \omega_c \frac{B_2}{B}\frac{k_B T_z}{m\omega_z^2}, \tag{4.12}$$

The same discussion holds for the anomaly transition. Since our axial quantum number is about $\bar{n}_z = 100$, we discuss the classical line shape below.

Line Shape in Classical Regime

The line shape in the classical regime is derived in [92, 93]. The line shape for general damping rate γ_z and bottle broadening parameter $\Delta\omega$ is given by

$$\chi(\omega) = \frac{4}{\pi}\mathrm{Re}\left[\frac{\gamma'\gamma_z}{(\gamma'+\gamma_z)^2}\sum_{n=0}^{\infty}\frac{(\gamma'-\gamma_z)^{2n}(\gamma'+\gamma_z)^{-2n}}{(n+\frac{1}{2})\gamma' + \frac{1}{2}(\gamma_c - \gamma_z) - i(\omega-\omega_0)}\right] \tag{4.13}$$

where

$$\gamma' \;=\; \sqrt{\gamma_z^2 + 4i\gamma_z\Delta\omega}, \tag{4.14}$$

Figure 4.2 shows the line shapes for several $\gamma_z/\Delta\omega$'s.

Two limits are instructive to discuss, (I) the loose coupling limit $\gamma_z \ll \Delta\omega$, and (II) the

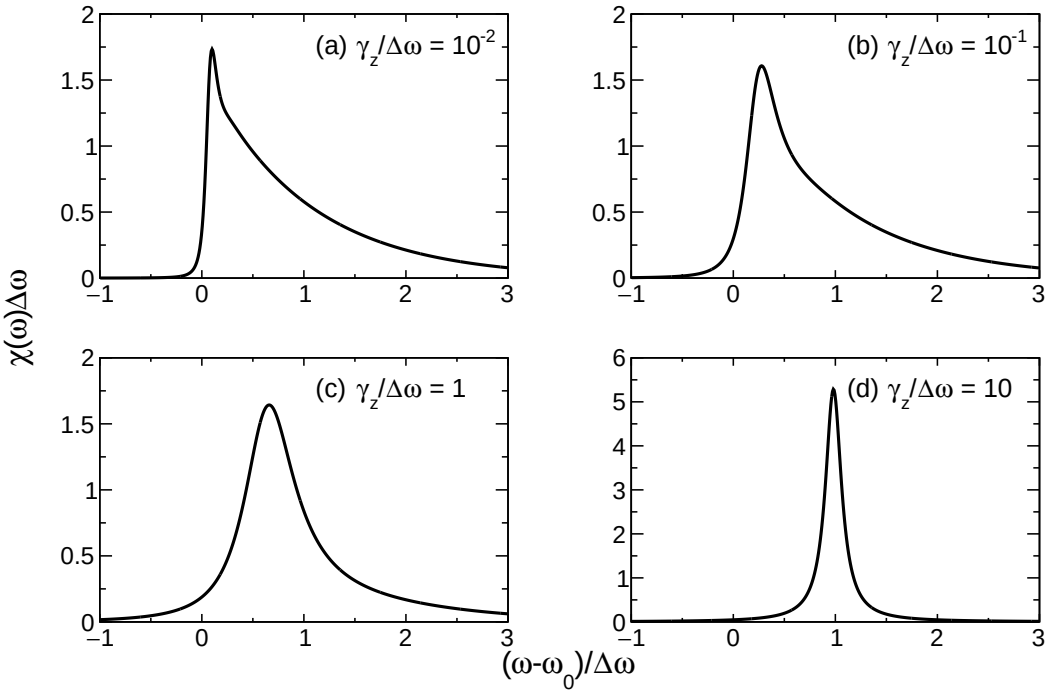


Figure 4.2: Line shapes in the classical limit for four different $\gamma_z/\Delta\omega$'s.

tight coupling limit $\gamma_z \gg \Delta\omega$.

$$\chi(\omega) = \begin{cases} \theta(\omega-\omega_0)\frac{1}{\Delta\omega}\exp\left(-\frac{\omega-\omega_0}{\Delta\omega}\right), & (\gamma_z \ll \Delta\omega) \\ \frac{1}{\pi}\frac{\Delta\omega^2/\gamma_z}{(\omega-\omega_0-\Delta\omega)^2+(\Delta\omega^2/\gamma_z)^2}, & (\gamma_z \gg \Delta\omega), \end{cases} \tag{4.15}$$

where $\theta(x)$ is the Heaviside step function. The cyclotron transition is described by (I), and the anomaly transition by (II).

(I) The loose coupling limit ($\gamma_z \ll \Delta\omega$)

In this limit, the rate of change of axial amplitude γ_z is slower than the transition's frequency scale $\Delta\omega$. The axial oscillation amplitude is constant during a transition. Therefore, the transition picks up the instantaneous magnetic field when the transition occurs. The instantaneous field is determined by the product of the bottle gradient

B_2 and the axial amplitude, following the Boltzmann distribution

$$P(\bar{z}^2) \propto \exp\left(-\frac{m\omega_z^2\bar{z}^2}{k_B T_z}\right). \tag{4.16}$$

In this regime, the line shape has a sharp rise-up edge and exponential decay [Fig. 4.2 (a)].

For our experimental parameters $\Delta\omega_c/(2\pi) = 200$ Hz and $\gamma_z/(2\pi) = 5$ Hz, the cyclotron transition is in this regime. We can use the exponential slope of the cyclotron transition's line shape to probe the axial temperature T_z.

(II) The tight coupling limit ($\gamma_z \gg \Delta\omega$)

In this limit, the rate of axial amplitude fluctuation γ_z is much faster than the time scale of transition $\Delta\omega$. As a result, the transition picks up the average of the magnetic field during its transition time scale $1/\Delta\omega$. The peak frequency of transition is given by its average amplitude $\langle z^2\rangle$. The magnetic field fluctuation during the transition is averaged, so the linewidth is narrowed to $(\Delta\omega)^2/\gamma_z$.

The anomaly transition is in this regime, $\Delta\omega_a/(2\pi) = 0.22$ Hz and $\gamma_z/(2\pi) = 5$ Hz. Therefore, the anomaly transition has a narrower linewidth, as shown in Fig. 4.2 (d).

Line Shape with Driven Axial Motion

In the actual measurement, an RF drive is applied at the bottom endcap electrode to excite the electron to an amplitude $z(t) = z_a\cos(\omega_a t)$ when driving the anomaly transition. The broadening parameter for the axially driven electron is defined as

$$\Delta_p\omega = \omega_0\frac{B_2}{B}\frac{z_a^2}{2} \tag{4.17}$$

The line shape of the axially driven electron is complicated and given in [92]. However, the shapes in two limiting coupling cases, loose coupling limit ($\gamma_z \ll \Delta\omega$) and tight coupling

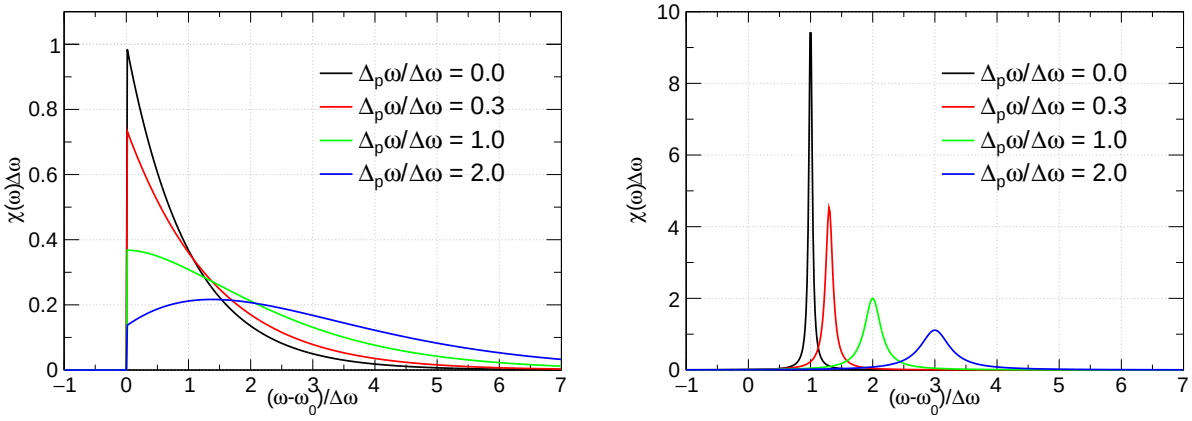


Figure 4.3: Line shape of axially driven electron for different drive broadening parameters $\Delta_p\omega/\Delta\omega$ in loose coupling limit (left) and tight coupling limit (right).

limit ($\gamma_z \gg \Delta\omega$), are instructive.

$$\chi(\omega) = \begin{cases} \theta(\omega-\omega_0)\frac{1}{\Delta\omega}\exp\left(-\frac{\omega-\omega_0+\Delta_p\omega}{\Delta\omega}\right) I_0\left(\frac{2\sqrt{(\omega-\omega_0)\Delta_p\omega}}{\Delta\omega}\right), & (\gamma_z \ll \Delta\omega) \\ \frac{1}{\pi}\frac{\Delta\omega'^2/\gamma_z}{(\omega-\omega_0')^2+(\Delta\omega'^2/\gamma_z)^2}, & (\gamma_z \gg \Delta\omega), \end{cases} \tag{4.18}$$

where $I_0(z)$ is the modified Bessel function of zero order with $\omega_0' = \omega_0 + \Delta\omega + \Delta_p\omega$ and $\Delta\omega' = \sqrt{\Delta\omega^2 + 4\Delta_p\omega\Delta\omega}$.

Figure 4.3 shows the line shape for the axially driven electron. We typically drive the amplitude to $z_a = 150$ nm to achieve 40% of transition probability. With the broadening parameter for 150 nm driven oscillation only being $\Delta_p\omega/\Delta\omega = 1.5 \times 10^{-4}$ and $\Delta_p\omega/\omega_0 = 5.6 \times 10^{-13}$, this shift is much smaller than the current experimental precision. Therefore, we do not include the effect of driven broadening $\Delta_p\omega$.

4.1.3 Drive-Time Broadening

Because of our narrow anomaly linewidth, the finite drive time is also important. For a sinusoidal drive with its drive length t_d, the line shape needs to be convoluted with

$$\chi(\omega) = t_d \left[\frac{\sin\left(\frac{\omega t_d}{2}\right)}{\frac{\omega t_d}{2}} \right]^2 . \tag{4.19}$$

Eq. 4.19 is the well-known sinc function and its FWHM is given by

$$\frac{\Delta\omega_{\text{FWHM}}^{\text{drive time}}}{2\pi} = \frac{0.886}{t_d}. \tag{4.20}$$

The FWHM of the anomaly line in this thesis is partly limited by the cyclotron lifetime. For example, a cyclotron lifetime of $\gamma_c^{-1} \approx 5$ s corresponds to FWHM of $\gamma_c/(2\pi) = 0.032$ Hz. Since the statistical sensitivity is limited by the broader cyclotron linewidth, we chose a drive time of $t_d = 30$ s, which corresponds to 0.03 Hz of drive-time broadening. With this drive time, the anomaly linewidth is still significantly narrower than the cyclotron line, and the measurement time is still reasonably short.

4.1.4 Other Smaller Broadenings from Anharmonicity and Magnetic Bottle

The anharmonicity C_4 and C_6, and B_2 also generate coupling between the oscillation frequencies. The results are summarized in [96–98], and we only cite its result here. The

shifts are summarized as

$$\begin{pmatrix} \Delta\omega_c/\omega_c' \\ \Delta\omega_z/\omega_z \\ \Delta\omega_m/\omega_m \\ \Delta\omega_s/\omega_s \end{pmatrix} = (\mathcal{M}_{B_2} + \mathcal{M}_{C_4}) \begin{pmatrix} E_c \\ E_z \\ E_m \end{pmatrix} + \mathcal{M}_{C_6} \begin{pmatrix} E_c^2 \\ E_z^2 \\ E_m^2 \\ E_c E_z \\ E_c E_m \\ E_z E_m \end{pmatrix}, \tag{4.21}$$

where

$$\mathcal{M}_{B_2} = \frac{1}{m\omega_z^2}\frac{B_2}{B} \begin{pmatrix} -\eta^2 & 1 & 2 \\ 1 & 0 & -1 \\ 2 & -1 & -2 \\ -\eta^2 & 1 & 2 \end{pmatrix} \tag{4.22}$$

$$\mathcal{M}_{C_4} = \frac{1}{m\omega_z^2}\frac{C_4}{(1+C_2)d^2} \begin{pmatrix} \frac{3}{2}\eta^2 & -3\eta^2 & -6\eta^2 \\ -3\eta^2 & \frac{3}{2} & 6 \\ -6\eta^2 & 6 & 6 \\ 0 & 0 & 0 \end{pmatrix} \tag{4.23}$$

$$\mathcal{M}_{C_6} = \frac{1}{m^2\omega_z^4}\frac{C_6}{(1+C_2)d^4} \begin{pmatrix} -\frac{15}{4}\eta^6 & -\frac{45}{4}\eta^2 & -45\eta^2 & \frac{45}{2}\eta^4 & 45\eta^4 & -90\eta^2 \\ \frac{45}{4}\eta^4 & \frac{15}{4} & 45 & -\frac{45}{2}\eta^2 & -90\eta^2 & 45 \\ \frac{15}{2}\eta^4 & \frac{45}{2} & 30 & -90\eta^2 & -90\eta^2 & 90 \\ 0 & 0 & 0 & 0 & 0 & 0 \end{pmatrix}, \tag{4.24}$$

with $\eta = \omega_z/\omega_c$. Our typical parameters are $B = 5.3$ T, $B_2 = 300$ T/m^2, $C_4 = 2 \times 10^{-4}$, $C_6 = -0.1$, and $\eta = \omega_z/\omega_c = 7 \times 10^{-4}$, together with $E_c = \hbar\omega_c'/2 = 5 \times 10^{-23}$ J, $E_z = k_B T_z = 7 \times 10^{-24}$ J, and $E_m = k_B T_z \times (\omega_m/\omega_z) = 2 \times 10^{-27}$ J. One can numerically prove that the broadening of cyclotron and spin frequency is dominated by the bottle term B_2

coupled with the energy of the axial motion E_z.

In addition, we experimentally observed additional broadening of the cyclotron transition line. The source of the broadening is still unknown. We fit the observed lineshape with various noise models and extract the center frequency to determine the g-factor. The discrepancy among different models is defined as line shape systematic uncertainty.

4.1.5 Measurement Cycle

The cyclotron and anomaly frequencies are the most important measured quantities. We measure them alternately to cancel the effect of long-term drift. The measurement cycle is automated and hardware-triggered. The measurement sequence can be categorized into three phases: cyclotron trial, anomaly trial, and spin initialization.

Cyclotron Trial

1. Turn off the self-excited oscillator and wait for 1 s.
2. Turn on the magnetron cooling drive for 1 s.
3. Turn off the magnetron drive and wait for 2 s.
4. Apply a cyclotron drive and a detuned anomaly drive for 5 s.
5. Turn on the self-excited oscillator and wait for 0.5 s to build up a steady axial oscillation.
6. Trigger the computer data-acquisition and measure the axial frequency.

Anomaly Trial

1. Turn off the self-excited oscillator and wait for 1 s.
2. Turn on the magnetron cooling drive for 1 s.
3. Turn off the magnetron drive and wait for 2 s.

4. Apply an anomaly drive and a detuned cyclotron drive for 30 s.

5. Wait for 60 s for the cyclotron state to decay to $n_c = 0$.

6. Turn on the self-excited oscillator and wait for 0.5 s to build up a steady axial oscillation.

7. Trigger the computer data-acquisition and measure the axial frequency.

When either cyclotron or anomaly drive is applied, the other drive is also applied with the same amplitude but far detuned from the resonance. Applying the detuned drive with the same power cancels any potential shift of the two frequencies due to the driven amplitude and heating from the drives.

Once the anomaly transition occurs, the quantum state changes as $|n_c = 0, m_s = 1/2\rangle \rightarrow |n_c = 1, m_s = -1/2\rangle$, and this state decays to $|n_c = 0, m_s = -1/2\rangle$. In order to repeat the measurement, a spin initialization drive is applied to drive the spin down cyclotron ground state back to the original state $|n_c = 0, m_s = -1/2\rangle \rightarrow |n_c = 0, m_s = 1/2\rangle$. In the spin initialization, both drives are applied with resonant frequencies and with a much stronger power.

Spin Initialization

1. Turn off the self-excited oscillator and wait for 1 s.

2. Turn on the magnetron cooling drive for 1 s.

3. Turn off the magnetron drive and wait for 2 s.

4. Apply a 10 dB stronger resonant anomaly drive and a 10 dB stronger resonant cyclotron drive for 10 s.

5. Wait for 60 s for the cyclotron state to decay to $n_c = 0$.

6. Turn on the self-excited oscillator and wait for 0.5 s to build up steady state axial oscillation.

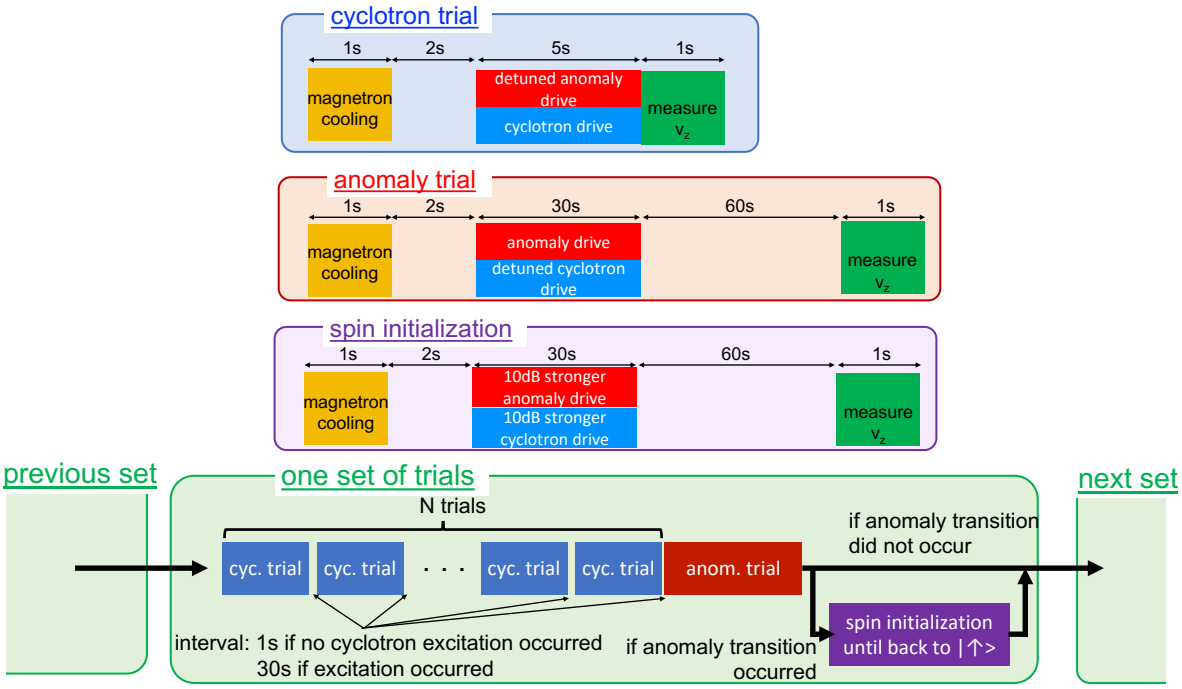


Figure 4.4: Cycle of the g-factor measurement. There are three main excitations, cyclotron trial, anomaly trial, and spin initialization. Cyclotron trials are repeated N times, followed by the anomaly trial. If we see an anomaly transition, the spin initialization excitation is applied until the spin is brought back to $|n_c = 0, \uparrow\rangle$. The sets of trials are repeated with different drive frequencies.

7. Trigger the computer data-acquisition and measure the axial frequency.

This spin initialization drive is repeated until we find that the spin is flipped back to the initial $|n_c = 0, m_s = 1/2\rangle$ state.

Because the cyclotron transition has a much wider linewidth, the cyclotron trial is repeated N times more often than the anomaly transition trial. We chose $N = 8$ for most of the runs but also checked that the result does not depend on N. Figure 4.4 illustrates the described measurement cycle. This cycle is repeated automatically; no manual adjustment is needed during the sequence.

4.1.6 Blinded Measurement

The measurement is performed "blindly". The actual value of the measured g-factor is not known during the data acquisition, analysis, and study of systematic effects. The blinding is done by adding a constant offset to the anomaly drive frequency,

$$\nu_{a;\mathrm{drive}}[\mathrm{actual}] = \nu_{a;\mathrm{drive}}[\mathrm{set\ in\ computer}] + X. \tag{4.25}$$

What the experimenters know is the frequency set in the computer, but the exact anomaly drive frequency from the RF generator had been unknown until after analysis and a comprehensive study of systematic effects. The random offset X is generated by software in the range

$$-1\ \mathrm{Hz} < X < 1\ \mathrm{Hz}, \tag{4.26}$$

which corresponds to ± 6 ppt in g-factor at 150 GHz. The range is chosen to be large enough to cover the previous error (0.28 ppt) and the discrepancy between the SM (0.5 ppt), but small enough so that the anomaly transition can be found within a few hours of sweeping. The offset X was generated on 8^{th} June 2021. After all the systematic studies were completed, the number was unblinded on 17^{th} August 2022, and it was $X = -0.100$ Hz.

4.2 Spectroscopy

With the constructed and optimized apparatus, a new measurement of the g-factor is performed. The cyclotron frequency $\bar{\nu}_c$ and the anomaly frequency $\bar{\nu}_a$ are measured using a single trapped electron. Data sets, drift correction, fitting, and analysis methods are summarized in this section.

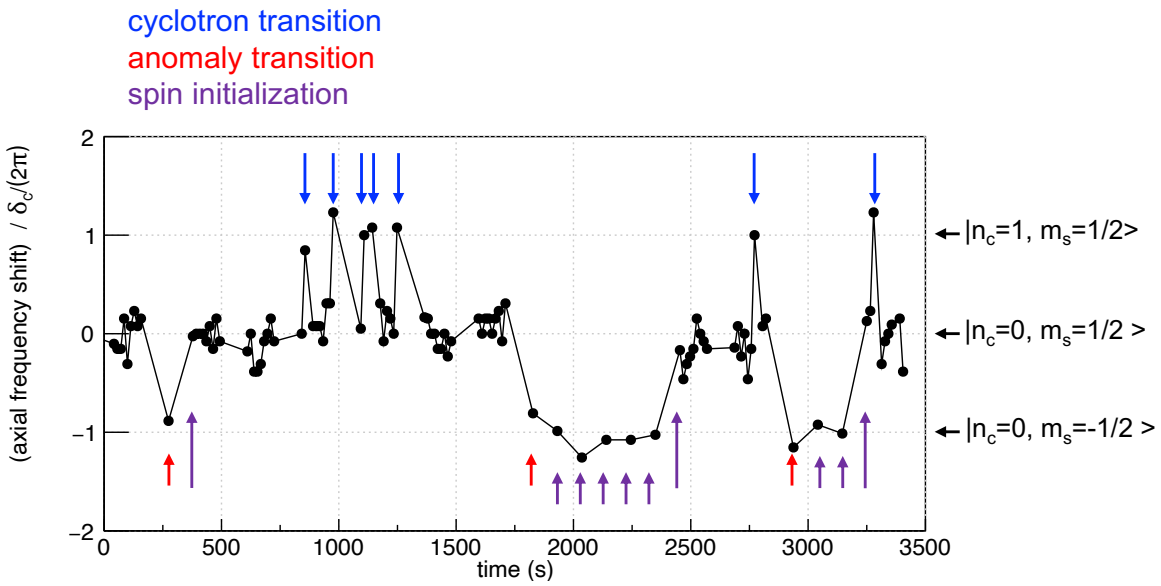


Figure 4.5: Change of axial frequency due to cyclotron and anomaly transitions. A cyclotron or anomaly drive is applied between the points. Observed cyclotron (anomaly) transitions are marked by blue (red) arrows. The measured axial frequencies after spin initialization drives are marked with purple arrows, with long arrows indicating successful excitation back to the spin-up state.

4.2.1 Data Acquisition

A series of measurements is conducted. Table 4.1 summarizes the data sets used for the g-factor determination. The measurement is done by repeating the sequence described in Sec. 4.1. What we actually measure is the change of axial frequency after applying cyclotron, anomaly, or spin initialization drives. Whether the corresponding transition occurred or not is judged by the shift of axial frequency.

Figure 4.5 shows the typical measured axial frequency during the measurement cycle. A cyclotron or anomaly drive is applied between the points. When the anomaly transition occurs, the spin initialization drive is repeated until the spin is moved back to the initial state $|n_c = 0,\ m_s = 1/2\rangle$. The corresponding cyclotron transition, anomaly transition, and spin initialization process are marked by colored arrows.

By repeating this process, we get a set of [*time*; *drive frequency*; *transition occurred or not*] for both anomaly and cyclotron transitions. From this data, we construct a graph of

run #	time	magnetic field (T)	cyclotron frequency (GHz)
1-1	2021-12-19-14:45 – 2021-12-20-13:46	5.373	150.411
1-2	2021-12-22-12:57 – 2021-12-23-10:37		
1-3	2021-12-26-13:33 – 2021-12-27-15:31		
2-1	2021-12-29-17:43 – 2021-12-30-17:37	5.300	148.361
2-2	2021-12-31-15:15 – 2022-01-01-23:18		
2-3	2022-01-02-16:46 – 2022-01-04-11:43		
2-4	2022-01-05-12:46 – 2022-01-06-10:49		
3-1	2022-01-31-21:47 – 2022-02-02-12:01	5.269	147.498
3-2	2022-02-03-11:02 – 2022-02-04-13:58		
3-3	2022-02-04-16:13 – 2022-02-05-19:17		
3-4	2022-02-06-15:44 – 2022-02-07-16:30		
3-5	2022-02-07-17:56 – 2022-02-08-21:15		
4-1	2022-02-11-18:13 – 2022-02-14-00:14	5.326	149.091
4-2	2022-02-15-19:47 – 2022-02-17-17:15		
4-3	2022-02-19-11:38 – 2022-02-21-09:50		
5-1	2022-04-07-19:37 – 2022-04-08-19:53	4.071	113.956
5-1	2022-04-09-12:24 – 2022-04-10-21:49		
5-1	2022-04-10-21:03 – 2022-04-11-14:04		
6-1	2022-04-12-17:58 – 2022-04-13-15:10	4.245	118.822
6-1	2022-04-13-16:13 – 2022-04-14-14:32		
6-1	2022-04-14-16:58 – 2022-04-15-13:38		
7-1	2022-04-17-19:26 – 2022-04-18-22:13	4.078	114.141
7-2	2022-04-18-22:16 – 2022-04-20-10:29		
8-1	2022-06-26-11:38 – 2022-06-27-14:28	4.969	139.097
8-2	2022-06-27-15:02 – 2022-06-28-13:48		
8-3	2022-06-28-14:59 – 2022-06-29-10:19		
8-4	2022-06-29-11:33 – 2022-06-30-13:38		
9-1	2022-07-01-16:05 – 2022-07-02-10:21	5.001	139.989
9-2	2022-07-02-10:27 – 2022-07-03-11:37		
9-3	2022-07-03-12:08 – 2022-07-04-11:33		
10-1	2022-07-05-09:07 – 2022-07-06-11:10	4.537	127.007
10-2	2022-07-06-12:56 – 2022-07-07-11:57		
10-3	2022-07-07-17:10 – 2022-07-08-14:04		
11-1	2022-07-11-10:59 – 2022-07-12-10:48	3.108	87.010
11-2	2022-07-13-09:45 – 2022-07-14-11:27		
11-3	2022-07-14-11:31 – 2022-07-15-13:02		
11-4	2022-07-15-13:07 – 2022-07-16-18:38		

Table 4.1: Data sets used for the g-factor determination.

transition probability versus drive frequency for both cyclotron and anomaly transitions and extract the g-factor.

4.2.2 Extracting Cyclotron and Anomaly Frequencies

The cyclotron and anomaly frequencies are extracted from the recorded data. To extract the resonant frequencies, the slow magnetic field drift must be first corrected for, and the obtained transition probability is fit using the maximum likelihood method.

Drift Correction

The drift of the magnetic field is as small as $\mathcal{O}(10^{-10})$/hour (Chap. 3), but is not negligible at our precision. The drift rate is measured and corrected *in-situ* using the recorded transition frequency. We first make a graph of *(drive frequency that transition occurred)* versus *(time)* for both transitions (Fig. 4.6). The drift rate of the magnetic field is now visible by the two different transitions. To correct the drift effect, we fit the cyclotron transition by a second-order polynomial function

$$\frac{\delta B}{B} = p_0 + p_1 \times t + p_2 \times t^2 \tag{4.27}$$

and extract the drift rate p_1 and p_2. The cyclotron transition is used because it has more data points. The drift is then corrected using the best-fit parameters. Whether the result changes if we use other fitting functions is studied in Sec. 4.4.

Obtained Line Shapes and Fitting

After correcting the drift of the magnetic field, we integrate the data over time and construct a histogram. Each bin in the histogram contains the probability of excitation at its drive frequency. The width of the bin is much smaller than the linewidth, and consistency by using different bin sizes is checked. The histogram illustrates the transition probability

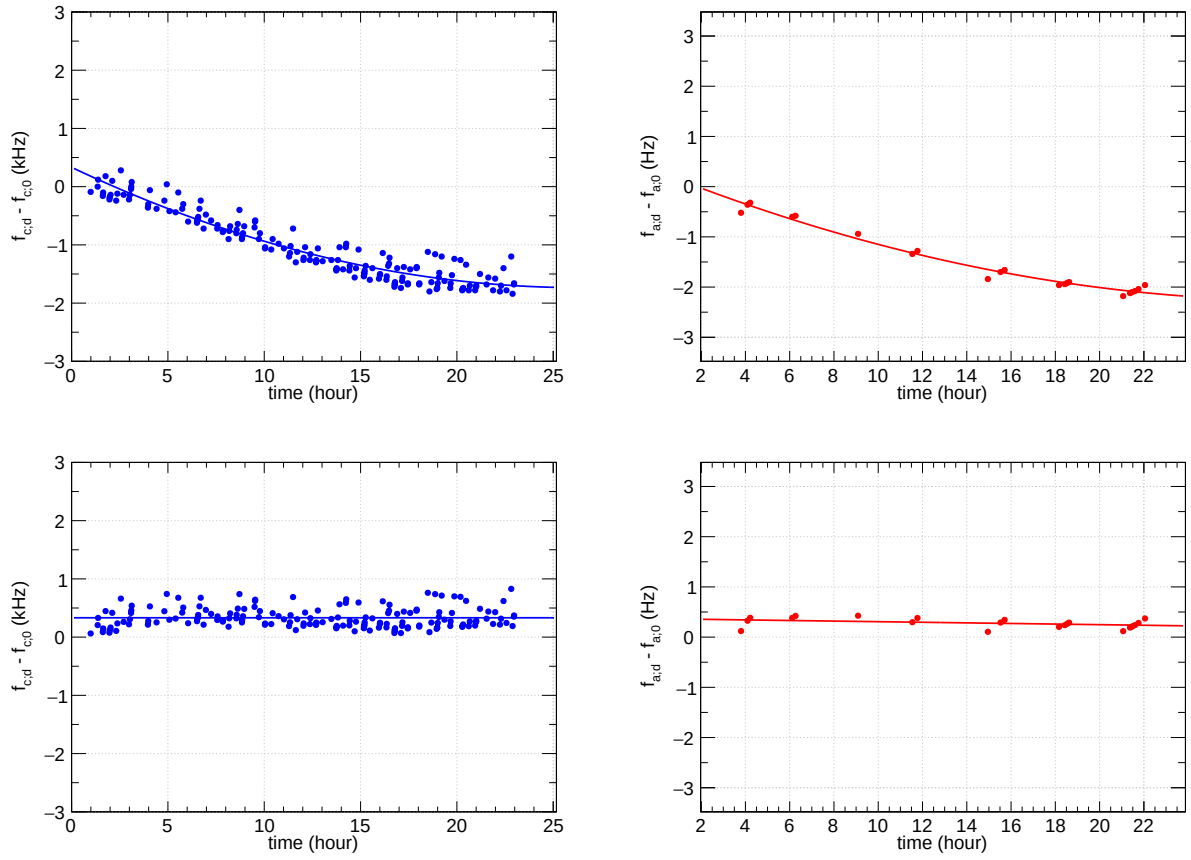


Figure 4.6: Correction of magnetic field drift. (top) Distribution of *drive frequency that transition occurred* versus *time* for cyclotron (blue) and anomaly (red) transitions. Second-order polynomial fitting is also shown to indicate the drift rate. (bottom) Distribution after correcting the drift rate by second-order polynomial fitting. Data with an especially bad drift rate is shown.

at each frequency.

To extract the frequencies, we use the maximum-likelihood method. Ideally, there are five parameters that we need to determine from the observed transition probabilities: cyclotron and anomaly frequencies $\bar{\nu}_c$ and $\bar{\nu}_a$, the axial temperature T_z, and the maximum transition probabilities $P_c^{\max}$ and $P_a^{\max}$. However, because of the asymmetric line shape, the determination of cyclotron frequency $\bar{\nu}_c$ is strongly correlated with its linewidth, so with the axial temperature T_z. In addition, as we explain later, we observed a broadening in the cyclotron line. The cyclotron frequency $\bar{\nu}_c$ also has a large correlation with the width of the broadening.

Therefore, instead of fitting with these five parameters, we extract the mean of the cyclotron $\bar{\nu}_c^* = \bar{\nu}_c + \Delta\nu_c$ and the mean of the anomaly frequency $\bar{\nu}_a^* = \bar{\nu}_a + \Delta\nu_a$. The cyclotron line is fitted with the classical line shape, convoluted with a broadening σ_c. The broadening model is discussed later. The anomaly line is fitted by a Lorentzian with width $\Delta\nu_a^*$, which includes cyclotron lifetime broadening γ_c and the transit time broadening. The effect of using $\bar{\nu}_c^*$ and $\bar{\nu}_a^*$ instead of $\bar{\nu}_c$ and $\bar{\nu}_a$ is very small. This can be proved by taking the partial derivative of Eq. 4.6

$$\delta\left(\frac{g}{2}\right) = \frac{\partial g}{\partial \bar{\nu}_a}\Delta\nu_a + \frac{\partial g}{\partial \bar{\nu}_c}\Delta\nu_c \approx \mathcal{O}(10^{-20}). \tag{4.28}$$

Therefore, the correction by using $\bar{\nu}_c^*$ and $\bar{\nu}_a^*$ instead of $\bar{\nu}_c$ and $\bar{\nu}_a$ is negligible.

Now the total number of fit parameters are seven: Four for the cyclotron transition $\bar{\nu}_c^*$, $\Delta\nu_c$, $P_c|_{\max}$, and σ_c, and three for the anomaly transition $\bar{\nu}_a^*$ $\Delta\nu_a^*$, and $P_a|_{\max}$. After applying the drift correction, we obtain a set of *transition occurred or not* versus *drive frequency* for both cyclotron and anomaly transitions. Notice that the time information is eliminated because it has been corrected in the drift correction. For a given i'th excitation trial at ν_i (either cyclotron or anomaly) and particular fit parameters $\bar{\nu}_c^*$, $\bar{\nu}_a^*$, $\Delta\nu_c$, σ_c, $\Delta\nu_a^*$, $P_c|_{\max}$,

$P_a|_{\max}$, the probability of obtaining a transition at the i'th trial is calculated as

$$p_i = P(\bar{\nu}_c^*, \bar{\nu}_a^*, \Delta\nu_c, \sigma_c, \Delta\nu_a^*, P_c|_{\max}, P_a|_{\max}). \tag{4.29}$$

The probability of not obtaining a transition is, of course, given by $1 - p_i$. Therefore for one excitation trial, the probability of observing that result for given fitting parameters is.

$$P_i(\bar{\nu}_c^*, \bar{\nu}_a^*, \Delta\nu_c, \sigma_c, \Delta\nu_a^*, P_c|_{\max}, P_a|_{\max}) = \begin{cases} p_i, & \text{if transition observed.} \\ 1 - p_i, & \text{if transition not observed.} \end{cases} \tag{4.30}$$

We define the product of this for all trials as the likelihood function

$$\mathcal{L}(\bar{\nu}_c^*, \bar{\nu}_a^*, \Delta\nu_c, \sigma_c, \Delta\nu_a^*, P_c|_{\max}, P_a|_{\max}) = \prod_i P_i(\bar{\nu}_c^*, \bar{\nu}_a^*, \Delta\nu_c, \sigma_c, \Delta\nu_a^*, P_c|_{\max}, P_a|_{\max}). \tag{4.31}$$

The most likely parameters are the ones that make this likelihood function $\mathcal{L}$ maximum. To handle it conveniently, we take its logarithm

$$M = \ln \mathcal{L} = \sum_i \ln \left[P_i(\bar{\nu}_c^*, \bar{\nu}_a^*, \Delta\nu_c, \sigma_c, \Delta\nu_a^*, P_c|_{\max}, P_a|_{\max}) \right]. \tag{4.32}$$

The uncertainties of the parameters are determined by the curvature near the best-fit parameters. If there is no correlation, for example, the uncertainty of parameter p is

$$\Delta p = \left(-\frac{\partial^2 M}{\partial^2 p} \right)^{-1/2}. \tag{4.33}$$

The actual correlation and uncertainty are handled by the covariance matrix, see e.g. [99].

Validity of Fitting Model

The validity of the fitting model can be checked using the obtained best-fit parameters. Using the best-fit parameters, we run a simulation experiment using the Monte-Carlo method

and check how likely it is to observe the data we actually took. The steps are listed below.

1. Using the best fit parameters, the lineshape function is recalculated $P^{\text{best fit}}(\nu)$.

2. For each drive frequency at ν_i among all trials, we generate "transition occurred" or "transition not occurred" based on the probability $P^{\text{best fit}}(\nu_i)$.

3. By doing this, we now get a simulated data set of [*drive frequency*; *transition occurred or not*] for all trials.

4. The likelihood function M is calculated for this simulated data set.

By repeating this, we get a distribution of simulated likelihood M. If the experimentally obtained data are well explained by the fitting model, its likelihood M should be within the distribution of the simulated likelihood M. The probability of obtaining a likelihood value worse than the experimentally obtained likelihood is called the p-value.

From its definition, the p-value ranges from 0 to 1. If p-value is too close to 1, that means the experimentally obtained data is fit too good to the model. This happens, for example, when the fitting model has too many parameters. If the p-value is too close to 0, that means the obtained data is not well explained by the fitting model. This is the case when there is some other source of broadening that is not included in the fitting model.

The observed anomaly line shape is consistent with the theoretical line shape, but the observed cyclotron line shape is broader than the ideal line shape. We fit the cyclotron line shape by the ideal line shape and also with curves convoluted with noise models: 30 Hz noise broadening, 60 Hz noise broadening, Gaussian noise broadening, and Lorentzian noise broadening. The validity of the model is tested by the p-value check (Fig. 4.7). One can clearly see that for the line shape with no broadening model, $-2M = -2 \times \ln \mathcal{L}$ is large and is not a good fitting model. Among them, we reject the model with p-value lower than 0.01 or higher than 0.99. Only 30 Hz, 60 Hz, and Gaussian noise models are accepted by this test (Fig. 4.8). We use the result from the Gaussian noise model as the primary result, and

take the largest discrepancy as a systematic uncertainty from the line shape model (Sec. 4.4).

Observed Line Shape and Fitted Line

Figure 4.9 shows the typical line shape for the cyclotron transition and the anomaly transition for one day of data. The anomaly linewidth is about 0.05 Hz (0.3 ppb at 5.3 T) at full width at half maximum (FWHM) and is about 4 times narrower than the linewidth in the 2008 measurement. However, the cyclotron linewidth is wider than the ideal line shape [92] by about 100 Hz (0.6 ppb at 5.3 T) in FWHM. This broadening was also observed in the 2008 measurement [7]. The transition probability of cyclotron transition is set approximately below 20 %, and that of anomaly transition is set higher to avoid the possibility of missing the narrow resonance. The measured line shapes, including the unexpected broadening, are consistent among all measured fields. Despite the observed broadening, from one day of data, we can typically determine cyclotron frequency $\bar{\nu}_c^*$ at 20 Hz (0.13 ppb at 5.3 T) and anomaly frequency $\bar{\nu}_a^*$ at 0.01 Hz (0.06 ppb at 5.3 T). The fitting is done for every run independently, and the g-factor for each run is extracted.

4.2.3 Statistical Distribution of the Measured g-factors

Using the extracted cyclotron frequency and anomaly frequencies, together with the monitored axial frequency (when the self-excitation is off), the g-factor can be extracted using Eq. 4.6. The reproducibility and reliability of measurement can be checked using the measured g-factors done in nearly the same magnetic fields. The measured g-factor, with the microwave cavity shift corrected (Sec. 4.3), should be distributed by statistical fluctuation. We studied the reliability of the measurement using data around 150 GHz.

Figure. 4.10 shows the distribution of measured data around 150 GHz. The center value is corrected using the microwave cavity shift (Sec. 4.3), but the error from the microwave cavity shift is not included in the error bar. The distribution shows good χ^2/(ndf) and

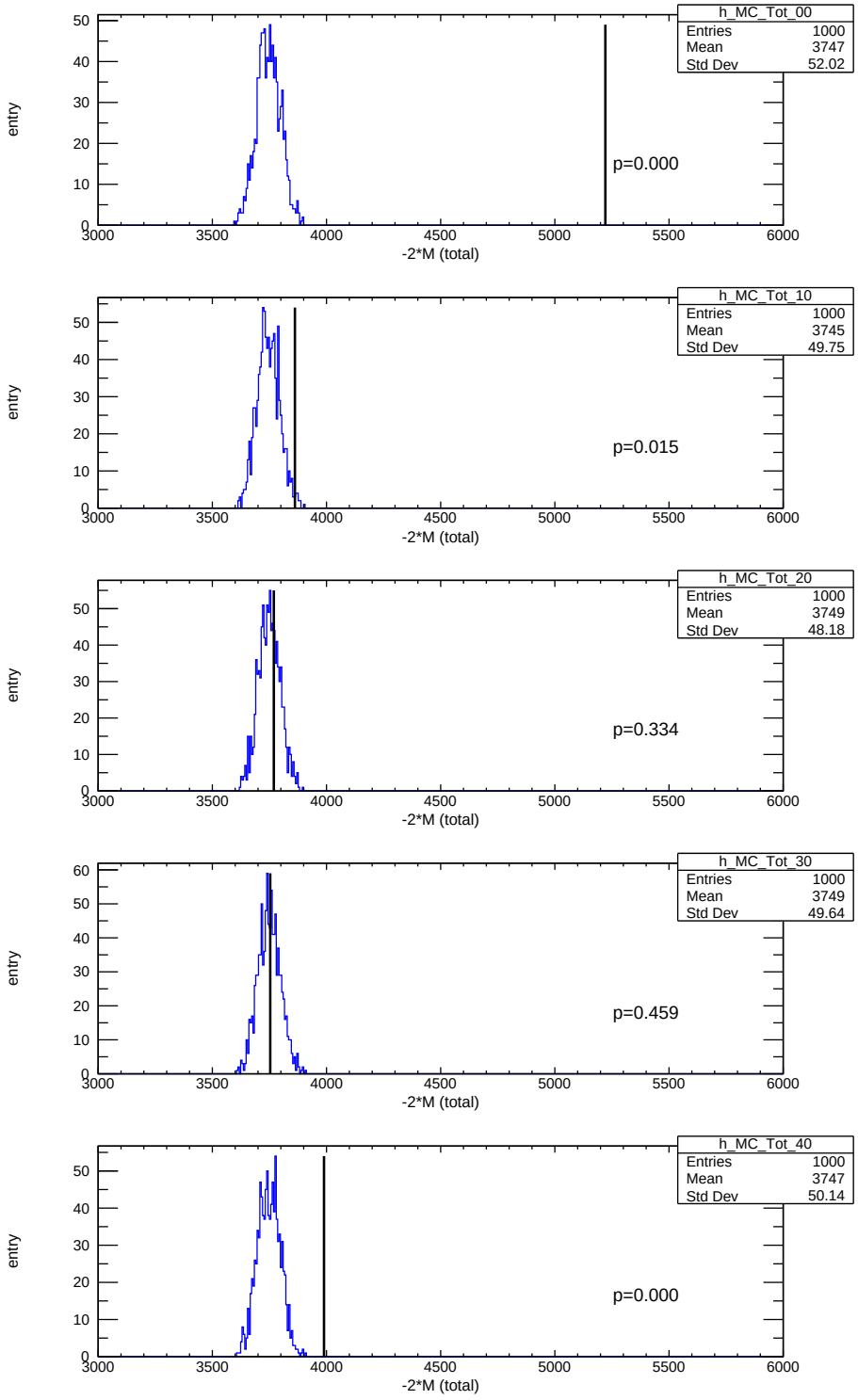


Figure 4.7: p-value of the fitting models. The experimentally observed p-value is shown by the solid line. From top to bottom, no broadening, 30 Hz noise, 60 Hz noise, Gaussian broadening, and Lorentzian shape broadening.

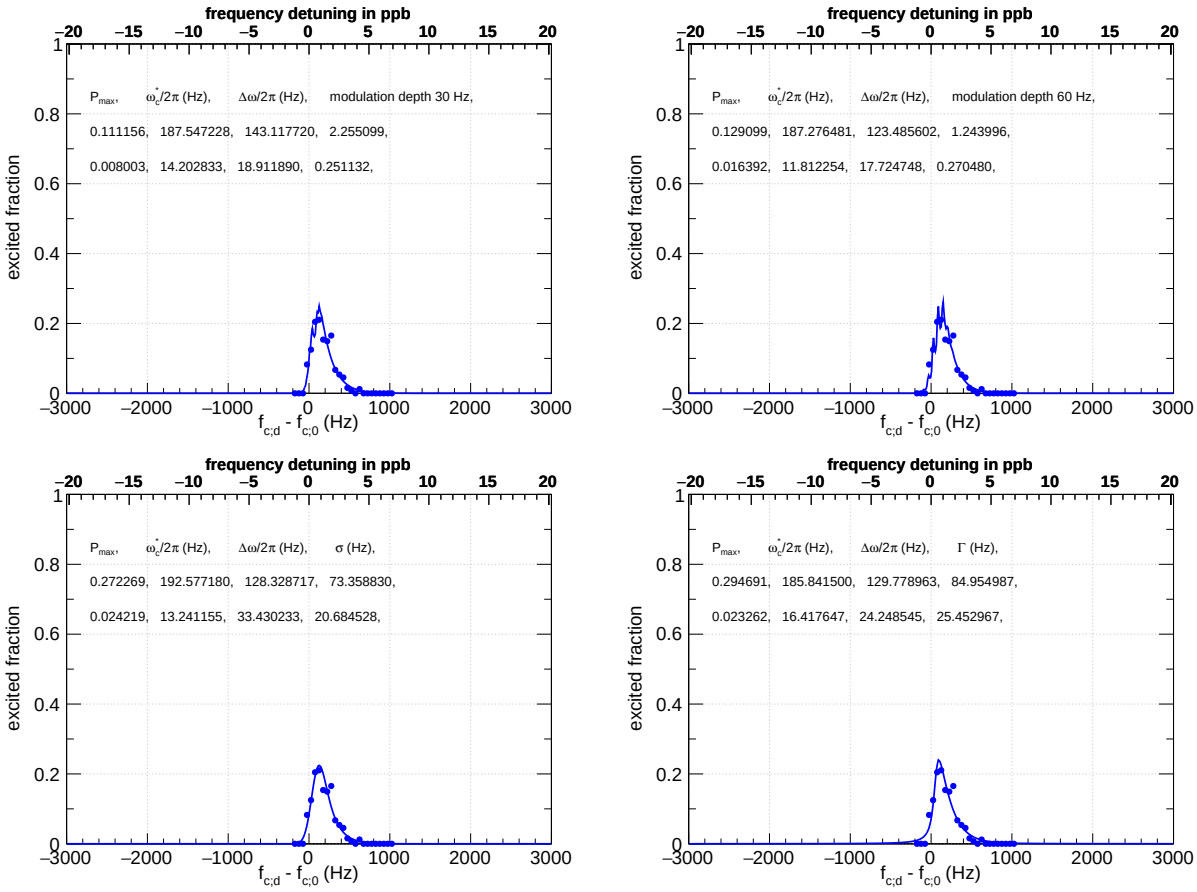


Figure 4.8: Different fitting of cyclotron line depending on the line shape model. Four models, 30 Hz noise (top left), 60 Hz noise (top right), Gaussian shape broadening (bottom left), and Lorentzian shape broadening (bottom right), are shown. The Lorentzian shape broadening (bottom right) is rejected after calculating the p-value of the fitting. One can see that the Lorentzian broadening has a long tail to the lower side.

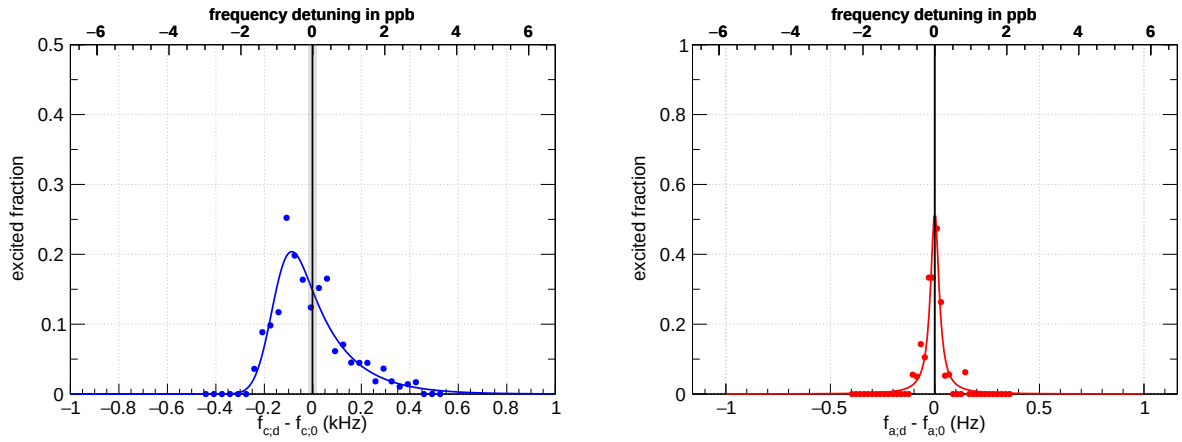


Figure 4.9: Typical line shape of cyclotron transition (left) and anomaly transition (right) for one day of data. Fitting with a Gaussian noise model is shown. The determined center frequencies $\bar{\nu}_c^*$ and $\bar{\nu}_a^*$ are shown by the black line, with the error indicated by the gray region.

p-value. The data here demonstrates that the measurement is consistent within a narrow range of magnetic fields. We also measure the g-factor at widely different magnetic fields to check the other systematic errors.

4.3 Microwave Cavity Correction

The conductive electrode surface of the Penning trap electrodes forms a microwave cavity that has resonances near the cyclotron frequency. In addition to the inhibited spontaneous emission, it also alters the measured cyclotron frequency in the trap cavity $\bar{\nu}_c^{\text{cav}}$ from $\bar{\nu}_c$ as [52, 53]

$$\bar{\nu}_c^{\text{cav}} = \bar{\nu}_c + \Delta\bar{\nu}_c^{\text{cav}} = \bar{\nu}_c \left(1 + \frac{\Delta\bar{\nu}_c^{\text{cav}}}{\bar{\nu}_c}\right) \tag{4.34}$$

The effect does not change the spin frequency, but the anomaly frequency—the difference of spin and cyclotron frequencies–shifts from the true anomaly frequency as

$$\bar{\nu}_a \to \bar{\nu}_a - \Delta\bar{\nu}_c^{\text{cav}}. \tag{4.35}$$

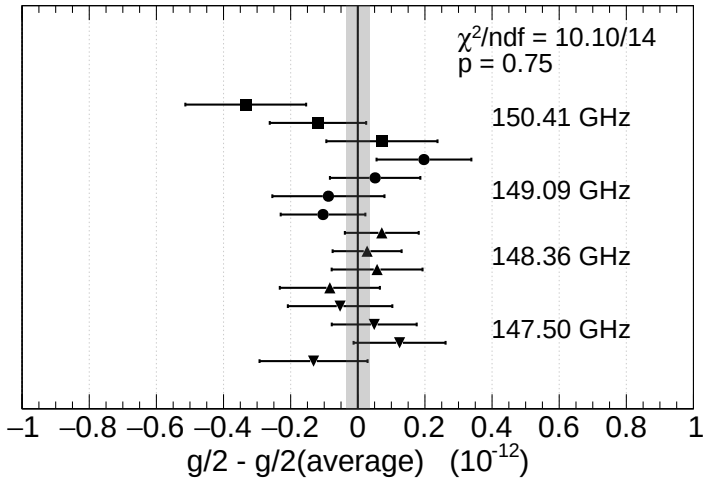


Figure 4.10: Statistical distribution of data around 150 GHz. The center value is corrected using the constructed microwave shift function, but the error from the microwave cavity shift is not included in the error bar.

Therefore, the measured g-factor (Eq. 4.6) needs to be corrected as

$$\Delta\frac{g}{2}|_{\rm cav} = \frac{\bar{\nu}_a + \Delta\bar{\nu}_c^{\rm cav} - \frac{\bar{\nu}_z^2}{2\left(\bar{f}_c+\Delta\bar{\nu}_c^{\rm cav}\right)}}{\bar{f}_c + \Delta\bar{\nu}_c^{\rm cav} + \frac{3}{2}\frac{\delta_r}{2\pi} + \frac{\bar{\nu}_z^2}{2\left(\bar{f}_c+\Delta\bar{\nu}_c^{\rm cav}\right)}} - \frac{\bar{\nu}_a - \frac{\bar{\nu}_z^2}{2\bar{f}_c}}{\bar{f}_c + \frac{3}{2}\frac{\delta_r}{2\pi} + \frac{\bar{\nu}_z^2}{2\bar{f}_c}} \approx \left(1+\frac{\bar{\nu}_a}{\bar{\nu}_c}\right)\frac{\Delta\bar{\nu}_c^{\rm cav}}{\bar{\nu}_c}, \qquad (4.36)$$

where the last approximation is valid up to $\mathcal{O}(10^{-15})$ level. To determine the cavity shift, we measure all the cavity modes and build the correction function.

4.3.1 Measuring the Microwave Resonances

There are two methods to measure the microwave cavity resonances: Using a cloud of electrons and using a single electron. A cloud of trapped electrons radiates its internal motion's energy by synchrotron radiation γ_c (App. A). A colder cloud of electrons shows a larger response to the axial excitation, so we can probe the change of γ_c by monitoring its axial oscillation amplitude. The parametric drive is used because it can excite the internal motion directly. The second method is to measure the cyclotron damping rate γ_c directly using a single electron. Although this method takes much longer time and gives less accuracy,

it relies on fewer assumptions. The single electron method is also more sensitive to the axial and radial misalignment of the microwave center and the trap center. Since we do not understand the detailed mechanism of the parametric drive method, we use the internal motion method to measure cyclotron resonances, and then confirm the mapped resonances with a single electron.

The physics behind the mapping of microwave modes is studied in detail in App. A. Figure 4.11 shows the full range of the measured cavity spectrum. The mapping is taken at four ranges, 60–90 GHz, 70–115 GHz, 100–140 GHz, and 134–160 GHz. The consistency is checked in the overlapped regions. We discuss the details and assigned the systematic error from this spectrum in the following. The mapping in 134–160 GHz is used as an example here, but all three maps are taken and checked with the same procedure.

Calibration of Mapped Spectrum

The mapping is taken by monitoring the axial oscillation amplitude and sweeping the current in the solenoid magnet. The exact cyclotron frequency that each resonance corresponds to needs to be calibrated. The current on the power supply is monitored, but it is not exactly the same as the current flowing in the magnet because of the large inductance of the superconducting solenoid (about 195 H). Calibration of the mapped spectrum is done by sending microwave drives of known frequencies and measuring the response from the cloud.

Figure 4.12 shows the circuit model of our superconducting magnet. In addition to the main coil's inductance $L = 195$ H, there is also a series resistance of the coil r_1, parallel resistance R that arises from the superconducting switch, and a series resistance r_2 that arises from the room temperature current leads. What we can monitor is the output voltage at the power supply $V(t)$ and the current flowing through the power supply $I(t)$. The actual

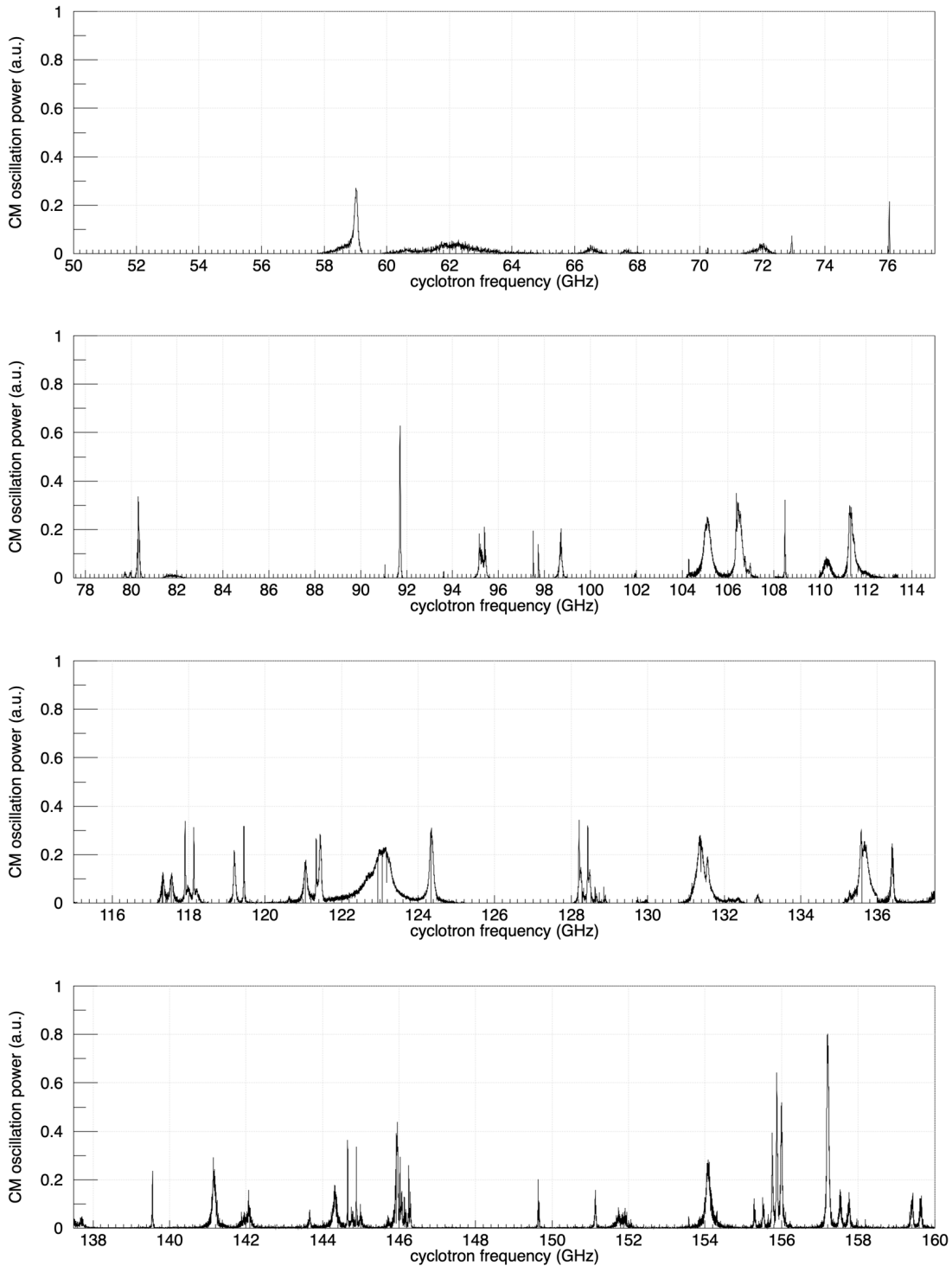


Figure 4.11: Mode mapping using parametrically driven electrons. Details of obtaining this mapping are described in the text.

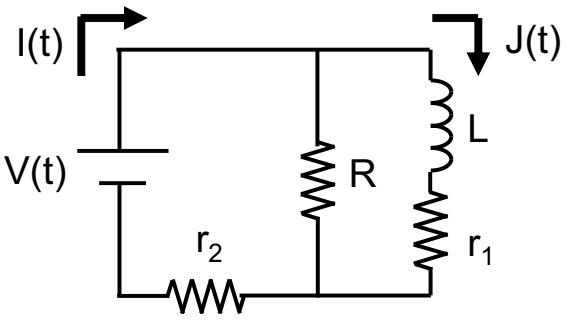


Figure 4.12: Circuit model of superconducting magnet and charging unit.

magnetic field at the center of the trap is proportional to the current on the coil

$$B(t) = KJ(t), \tag{4.37}$$

where K is later measured to be $K = 0.1327$ T/A. The relation between the quantities is

$$\begin{aligned} V(t) &= R[I(t) - J(t)] + r_2 I(t) \\ &= L\frac{dJ(t)}{dt} + r_1 J(t) + r_2 I(t). \end{aligned} \tag{4.38}$$

If the current on the power supply $I(t)$ is ramped linearly, $I(t) = I_0 + I_1 t$, then these equations give

$$J(t) = \frac{R}{R + r_1}\left(I_0 - \frac{L}{R + r_1} I_1 + I_1 t\right). \tag{4.39}$$

Therefore, as long as the current on the power supply is swept linearly, the current on the coil also changes linearly. Two scans with sweep-up and sweep-down are taken for each range. Figure 4.13 shows the change of the current on the power supply for two directions. By monitoring the current on the power supply, we guarantee that the sweep is done linearly. We only use the range where the current is more stable than 0.005 A. Using the conversion coefficient $K = 0.1327$ T/A, this corresponds to frequency fluctuation of 7×10^{-4} T = 18.5 MHz, which has negligible effects on the systematic error, as shown later. The temporal fluctuation of the current in the coil is even smaller than the fluctuation

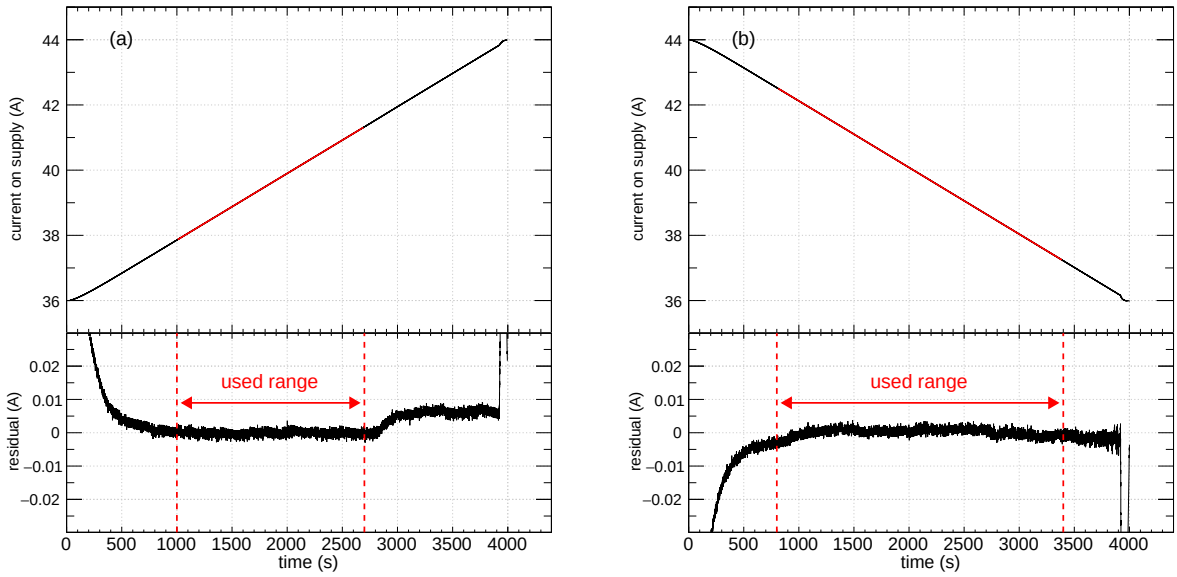


Figure 4.13: Change of current on the power supply when (a) swept up and (b) swept down.

at the power supply because of its large inductance. We verify this later by comparing the peak of resonances in the two scans.

Assuming the current is changing linearly, what we need to know is the cyclotron frequency at several points in the scan. The exact cyclotron frequency is calibrated by applying microwave drives with known frequencies. When the cloud of electrons is resonant with the drive frequencies, the microwave drive heats the internal motion to a much higher temperature, and the axial oscillation amplitude drops significantly. The result is a dip that appears exactly at the drive microwave frequency. An example of a dip from this calibration drive is shown in Fig. 4.14.

In the range 134–160 GHz, four calibration frequencies are used: 142.100 000 000 GHz, 145.925 000 000 GHz, 149.650 000 000 GHz, and 151.870 000 000 GHz. The frequency of the calibration drive is GPS locked and is better than 1 Hz. By fitting the dip with a Lorentzian, we get the conversion formula from the current on the power supply to the cyclotron frequency. The linearity of the calibration dip frequencies is also checked (Fig. 4.15).

For each range, two mode mappings with the sweep up and down are taken. To check the validity of the calibration method, we fit the modes in Fig. 4.11 and compare the center

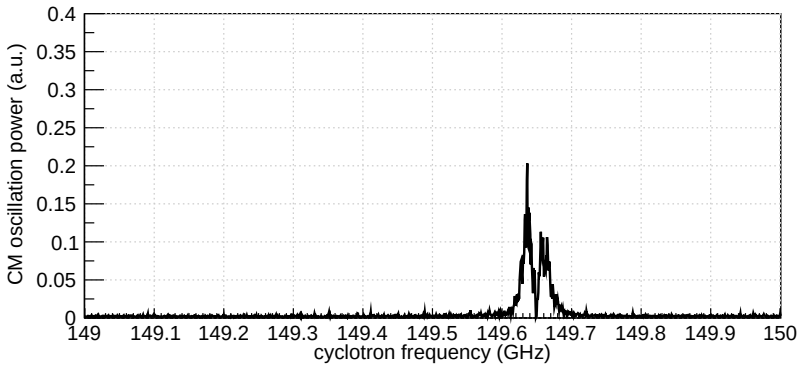


Figure 4.14: Calibration dip in the parametrically excited cloud of electrons' response on TE_{243} mode. The dip corresponds to a calibration drive at 149.650 000 000 GHz.

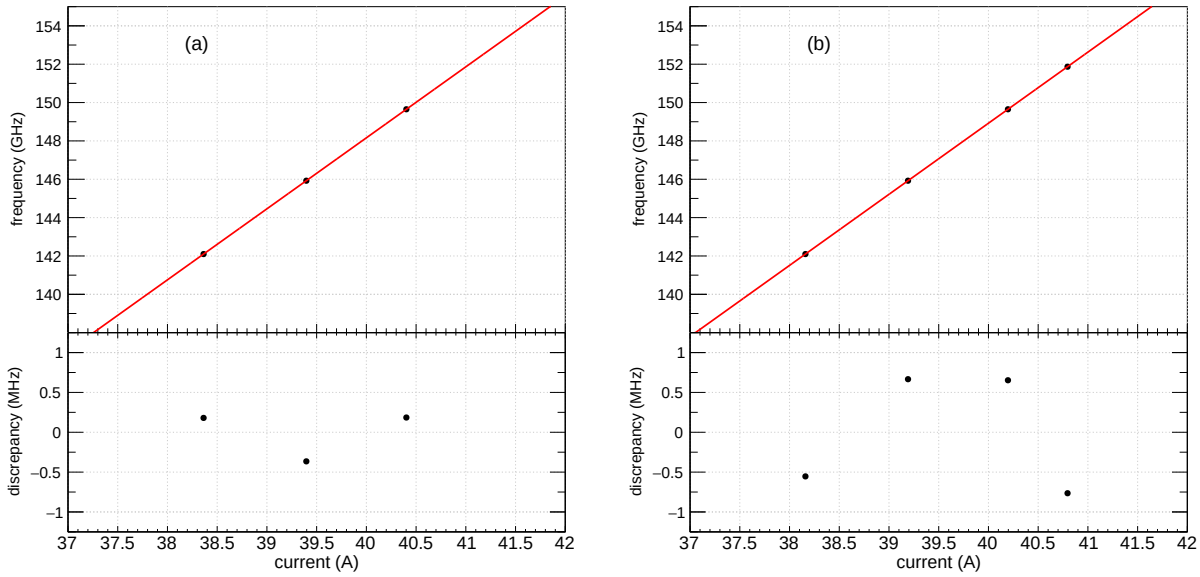


Figure 4.15: Fitting of measured dip frequency and current (a) in the sweeping up scan and (b) in the sweeping down scan.

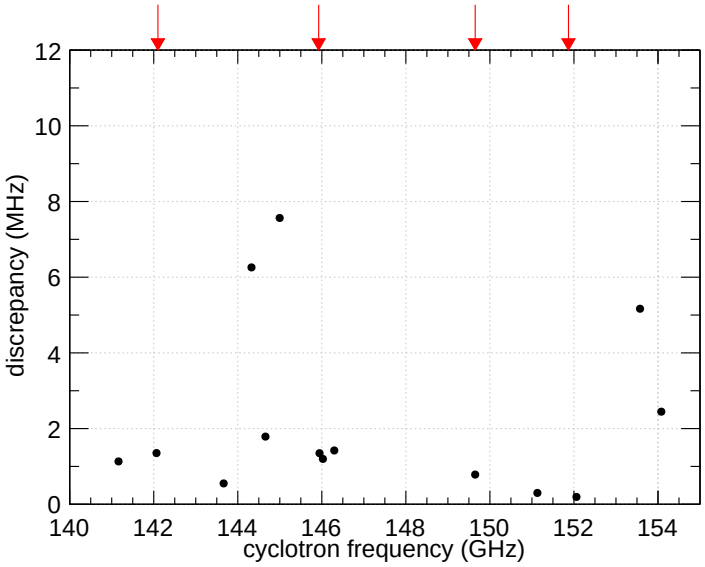


Figure 4.16: Discrepancies of obtained resonant frequencies between sweep up and down in the 135–160GHz range. The calibration frequencies are also shown with red arrows.

frequencies obtained in the sweep-up scan and in the sweep-down scan. Figure 4.16 compares the obtained center frequencies between the two scans. The discrepancy between the resonant frequencies is taken as the calibration error. This error is one of the systematic errors when calculating the microwave cavity correction to the g-factor.

All maps at different ranges are produced using the methods described here. They overlap with the adjacent map, and the consistency among them is checked. We then check the map with a single electron and fit the peaks with Lorentzian to extract the center frequencies. The measured resonant frequencies, with their coupling strength λ_M^2 for the strong coupling modes (will be introduced in Sec. 4.3.2) are summarized in Table. 4.2.

mode	calculated frequency (GHz)	measured frequency (GHz)	$(\lambda_M/2\pi)^2$ (10^8 Hz^2)
TE_{121}	59.236	59.015(11)	13.8
TM_{021}	61.115	60.655(20)	
TE_{113}	60.719	62.130(32)	6.7
TM_{013}	62.859	64.236(8)	
TE_{013}	70.247	70.253(8)	
TM_{113}	70.247	71.980(15)	6.6
TM_{121}	76.201	72.935(9)	1.1
TE_{021}	76.201	76.051(8)	
TE_{114}	79.139	79.846(10)	
TE_{123}	80.331	80.321(9)	13.8
TM_{023}	81.727	81.787(26)	
TM_{031}	92.968	91.054(8)	
TE_{131}	91.761	91.713(9)	21.6
TE_{023}	93.546	93.611(9)	
TM_{123}	93.546	95.282(18)	6.7
TE_{124}	95.023	95.280(9)	
TE_{132}	97.592	97.625(8)	
TE_{115}	97.853	98.717(10)	6.7
TM_{015}	99.196	101.959(9)	
TE_{015}	104.034	104.292(8)	
TM_{115}	104.034	105.101(16)	8.4
TM_{033}	107.644	106.361(8)	
TE_{133}	106.603	106.472(16)	21.6
TM_{124}	106.429	106.852(9)	
TE_{031}	108.650	108.481(8)	
TM_{131}	108.650	110.320(16)	0.8
TE_{125}	111.093	111.370(9)	13.8
TM_{132}	113.617	111.371(11)	
TE_{116}	116.720	117.441(10)	
TM_{016}	117.848	118.022(8)	
TE_{134}	118.070	118.095(10)	
TE_{225}	119.038	119.200(9)	
TE_{233}	119.561	119.447(8)	
TE_{331}	120.800	121.059(11)	
TE_{025}	120.993	121.338(8)	
TE_{033}	121.445	121.441(9)	
TM_{133}	121.445	122.994(149)	5.7
TM_{125}	120.993	123.143(149)[1]	11.1
TE_{141}	124.539	124.348(11)	29.5
TM_{232}	128.031	128.320(8)	
TE_{126}	128.023	128.365(15)	

[1] TM_{125} and TM_{133} overlap and it was impossible to distinguish them. Correction to the g-factor is calculated with two choices of mode assignment and the discrepancy is taken as a systematic error.

TM_{026}	128.903	128.737(8)	
TE_{142}	128.895	128.778(9)	
TM_{042}	129.754	129.844(9)	
TE_{135}	131.350	131.377(12)	21.6
TM_{035}	132.196	131.564(9)	
TE_{143}	135.846	135.646(13)	29.5
TE_{117}	135.676	136.372(10)	6.7
TM_{126}	136.703	137.572(11)	
TE_{017}	140.199	139.543(8)	
TM_{117}	140.199	141.161(10)	9.0
TM_{141}	141.365	141.968(21)	0.6
TE_{041}	141.365	142.066(9)	
TE_{035}	143.657	143.664(9)	
TM_{135}	143.657	144.329(10)	11.4
TE_{042}	145.218	144.773(8)	
TE_{144}	145.018	144.887(9)	
TM_{027}	146.289	145.728(9)	
TE_{127}	145.514	145.947(9)	13.8
TE_{136}	145.949	146.140(8)	
TM_{044}	145.782	146.183(9)	
TE_{243}	149.931	149.636(8)	
TE_{043}	151.421	151.130(8)	
TM_{143}	151.421	151.824(14)	4.8
TE_{027}	153.206	153.570(8)	
TM_{127}	153.206	154.077(11)	13.6
TE_{118}	154.688	155.380(9)	
TE_{145}	156.021	155.849(9)	29.5
TE_{151}	157.418	157.172(10)	37.4
TM_{136}	157.117	157.603(9)	
TM_{144}	159.701	159.467(9)	
TM_{052}	161.574	160.594(8)	
TE_{152}	160.886	160.654(8)	

Table 4.2: Summary of calculated and measured modes, with its calculated coupling strength λ_M^2 at the trap center (Sec.4.3.2).

Figure 4.17 shows the discrepancy between the measured frequencies and the calculated frequency using $\rho_0 = 4539$ μm and $z_0 = 3906$ μm. Immediately, two features are apparent. First, the discrepancy is smaller at high frequencies, 125–160 GHz. This is presumably from the implemented choke flanges that work at such frequencies. The RMS scatter is 1.3 % in the range 50–125 GHz, and 0.35 % at above 125 GHz. Second, the TE $m = 0$ modes (red)

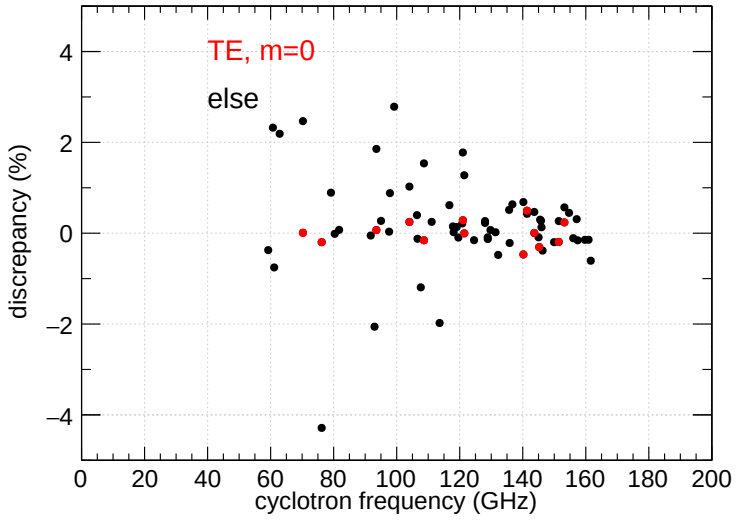


Figure 4.17: Discrepancy of measured resonant frequency from the calculated resonant frequency with $\rho_0 = 4539$ μm and $z_0 = 3906$ μm. The TE_{1np} modes are shown in red and other modes are shown in black.

show smaller discrepancies from the calculated resonant frequency. We use these modes to determine ρ_0 and z_0.

Determination of Trap Radius and Height

Among all the modes, the TE_{0np} modes do not generate current that cross the horizontal slits of the trap (but do generate current that crosses vertical slits on compensation electrodes). Therefore their measured resonant frequency agrees with the predicted resonant frequencies (Fig. 4.17). We use these modes to determine the trap radius ρ_0 and height z_0. We fit the resonant frequencies of all TE_{0np} modes by analytical resonant frequencies of a cylindrical trap with the least squares method. Figure 4.18 shows the calculated contour. Its minimum is normalized with the residual-mean-square (RMS) to be 1. The 68 % uncertainty of the ρ_0 and z_0 are indicated by the black contour. The best fit parameters yield the *in-situ* measured trap dimensions $\rho_0 = 4539$ (31) μm and $z_0 = 3906$ (35) μm.

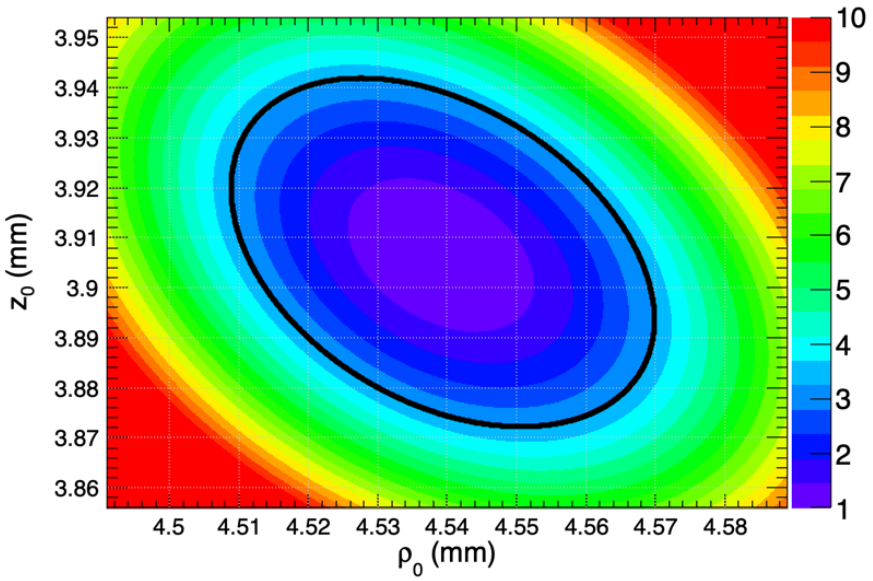


Figure 4.18: Determination of ρ_0 and z_0 using the TE_{0np} modes. The z-axis is the square-sum of the residual, normalized so that the minimum is equal to 1. The contour that corresponds to 68 % uncertainty is also shown by the black curve. The best-fit dimensions are $\rho_0 = 4539\ (31)\ \mu$m and $z_0 = 3906\ (35)\ \mu$m.

Measurement with a Single Electron

An alternative way to map microwave resonances is to use a single electron and measure γ_c at many different fields. The method using a cloud works reliably, but its mechanism is still not perfectly understood. The measurement using a single electron is very simple and well understood and confirms the map generated by the parametrically driven cloud. In addition, a single electron can be moved in the trap precisely to study the microwave center offset from the trap center. Three methods are used.

In the first method [Fig. 4.19 (a)], the electron is excited to $n_c = 1$ state with an external microwave drive with the self-excitation on, and the time it takes to decay back to $n_c = 0$ is measured. This process is repeated many times, and the dwell time at $n_c = 1$ is filled in a histogram. The dwell time distributes with an exponential shape, and the lifetime γ_c is measured by fitting its exponential slope. To accumulate enough data, one usually has to repeat the process for a few hours.

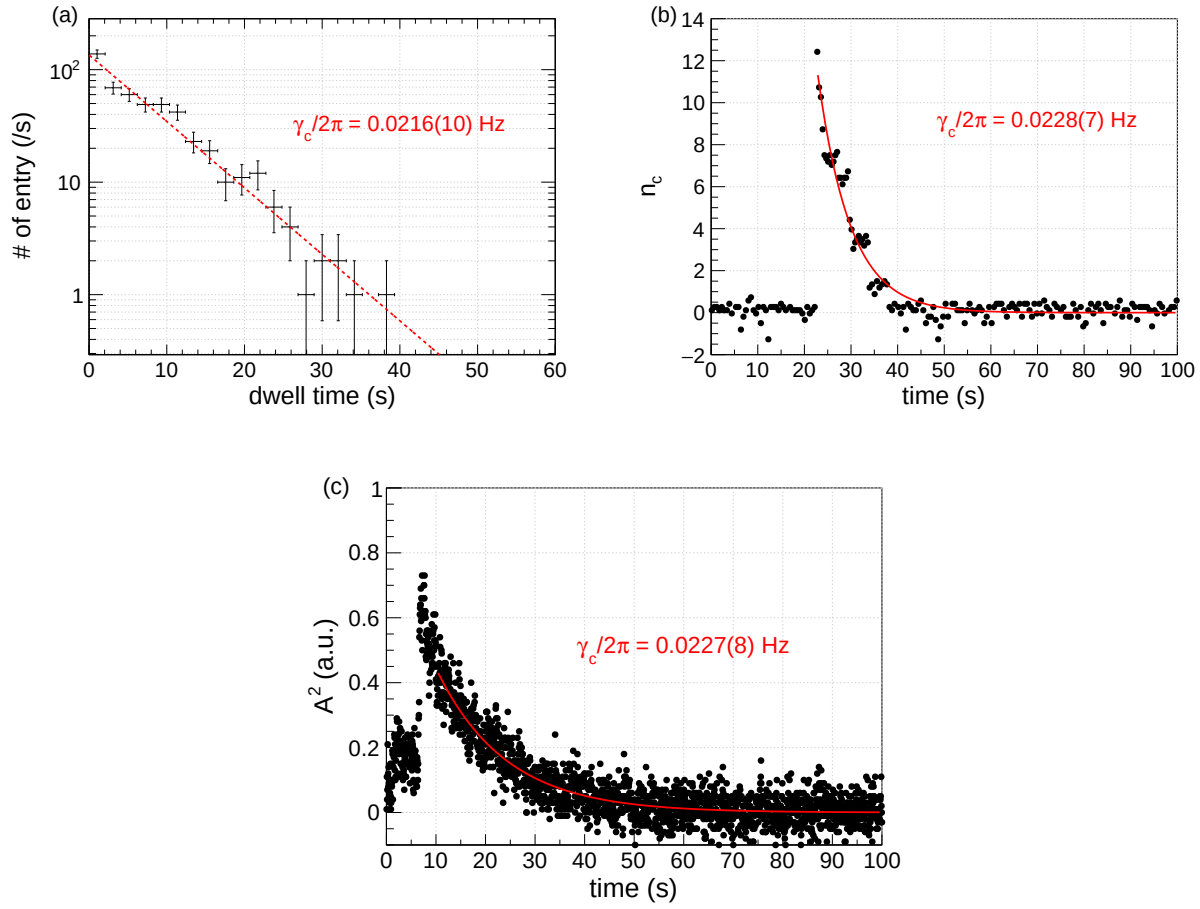


Figure 4.19: Three methods to measure γ_c using single electron: (a) dwell time measurement at $n_c = 1$, (b) exponential decay method, and (c) parametric excitation method.

Although this method works reliably, the fastest γ_c it can measure is limited by the averaging time to resolve one quantum transition. Even with the previous large magnetic bottle gradient B_2 [51], the highest measured γ_c was only $\gamma_c/(2\pi) = 0.3$ Hz. This limits the resolution of the center resonant frequency. Two new methods are developed to measure γ_c more quickly and with a larger dynamic range.

The second method is to excite the electron to a higher n_c state and measure the decay to the ground state by measuring the shift of self-excited axial frequency [Fig. 4.19 (b)]. The decay process is again fitted by an exponential curve and its time constant yields γ_c. Unlike the first method, this measurement in principle yields γ_c in one excitation. The average of γ_c and its error are obtained by repeating this measurement several times.

The third method is a completely different scheme. It uses the parametric drive in a tuned condition, $C_4 = 0$. In the tuned condition, the oscillation power of parametrically driven electron with $C_6 < 0$ is [100]

$$\begin{aligned} A^2 &= d^2 \sqrt{\frac{8}{15}\frac{1+C_2}{|C_6|}\left[\frac{1}{2}\sqrt{h^2-h_T^2} - \frac{2(\omega-\omega_z)}{\omega_z}\right]} \\ &= d^2 \sqrt{\frac{16}{15}\frac{1+C_2}{|C_6|\omega_z}\left(\omega_z + \frac{\varepsilon_+}{2} - \omega\right)}, \end{aligned} \tag{4.40}$$

where h is the modulation depth of the parametric drive, $h_T = 2\gamma_z/\omega_z$ is the parametric excitation threshold, and $\varepsilon_+ = \omega_z\sqrt{h^2 - h_T^2}/2$ is the rise-up frequency. Importantly, the response has a square-root shape of detuning $\omega_z + \varepsilon_+/2 - \omega$ (Fig. 4.20).

When the cyclotron state is excited, ω_z is a function of n_c

$$\omega_z = \omega_{z;0} + \delta_c n_c. \tag{4.41}$$

If we keep the drive frequency at its rise-up threshold $\omega = \omega_{z;0} + \varepsilon_+/2$, then the response is

$$A^2 = d^2 \sqrt{\frac{16}{15}\frac{1+C_2}{|C_6|\omega_z}\delta_c} \times \sqrt{n_c}. \tag{4.42}$$

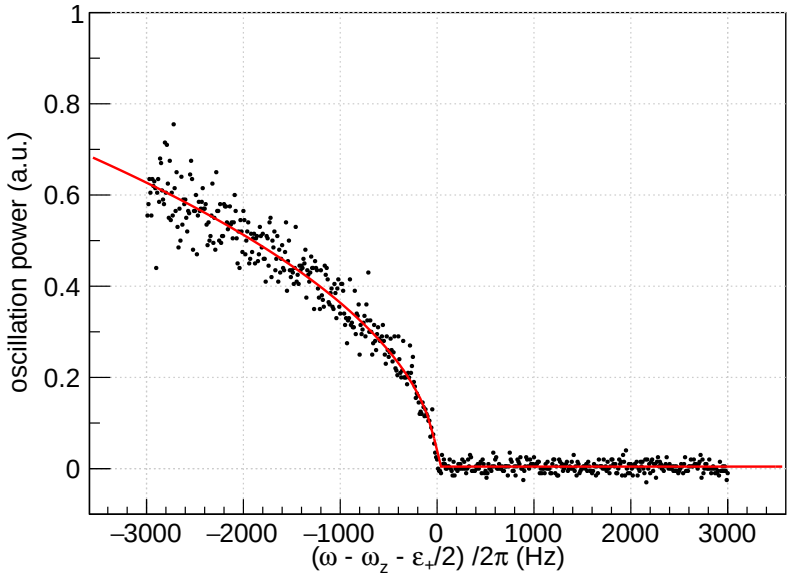


Figure 4.20: Oscillation power of a parametrically driven single electron with $C_4 = 0$ and $C_6 = -0.1$, with a square-root fitting function shown in red.

The cyclotron state n_c decays with exponential $n_c = n_{c;0} \exp(-\gamma_c t)$, so Eq. 4.42 yields

$$A^2 \propto \exp\left(-\frac{\gamma_c}{2}t\right). \tag{4.43}$$

The parametrically driven oscillation power can be monitored very quickly using an oscilloscope. The limit of this method is given by twice the axial decay time $2 \times \gamma_z/(2\pi) = 10$ Hz. Still, this method has about two orders of magnitude wider range than the previous methods. The γ_c can be measured closer to a cavity resonance using this method.

Although this method works for a much larger dynamic range, its uncertainty is also large near resonances because of the large oscillation amplitude. With a strong parametric drive, the electron can be axially excited up to a very high amplitude (sometimes 500 μm). The coupling to the off-center component of microwave resonances becomes very strong. The oscillation amplitude also changes while n_c decays back to 0. Large uncertainties need to be assigned to account for this effect. We fit the exponential decay with different time windows, and take the discrepancy as the uncertainty.

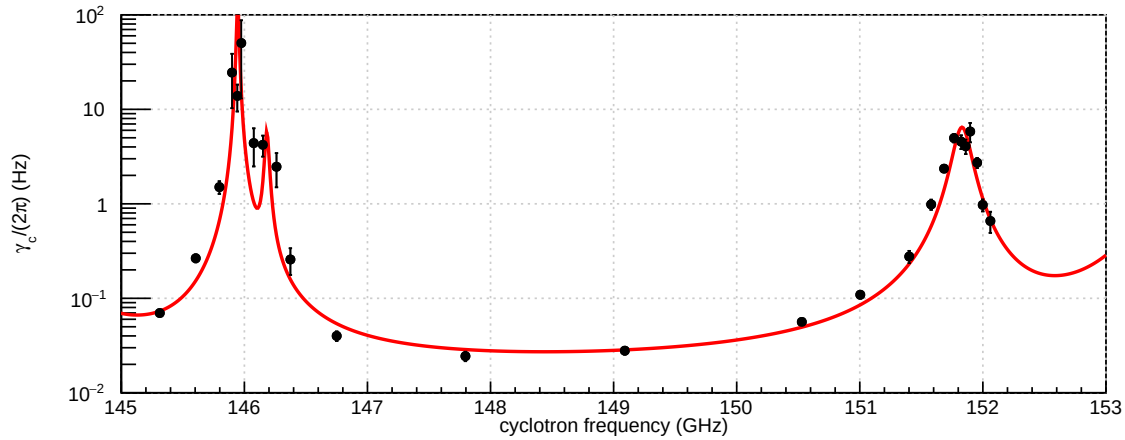


Figure 4.21: Confirmation of mode mapping by a cloud of electrons by the single electron measurements. The red line is the predicted γ_c using the fit parameters from the cloud mode mapping.

Despite its disadvantages, the parametric method is the only method that can measure γ_c near the resonances. We measure the off-resonance γ_c with the other two methods and the γ_c near resonances with the parametric method. Figure 4.21 shows the measured γ_c around 150 GHz. The red line is the theoretical prediction using the parameters measured using clouds of electrons. The consistency confirms our two methods.

4.3.2 Correction to the Cyclotron Frequency

Using the measured microwave resonances, we now construct the correction function to the g-factor. The method to construct the correction function and its uncertainty are discussed.

Renormalized Calculation

The coupling between the microwave resonant modes and trapped electron or electrons are studied in details in [51–53, 100–102]. We do not show the derivation again here. Instead, we only summarize the essential conclusions used in this thesis. For an electron at position z

and ρ with cyclotron frequency ${\omega_c}^2$, the shift of cyclotron frequency $\Delta\omega_c^{\rm cav}$ and the damping rate γ_c is given by

$$\Delta\omega_c^{\rm cav} - \frac{i}{2}\gamma_c = -\frac{i}{2}\gamma_{c;0} + \omega_c \left\{ \Sigma_S \left[\omega_c, z, \rho, Q^{(E)}, Q^{(M)} \right] + \Sigma_P \left[\omega_c, z, Q^{(E)}, Q^{(M)} \right] \right\}, \quad (4.44)$$

where $\gamma_{c;0} = \frac{1}{4\pi\epsilon_0}\frac{3mc^2}{4e^2\omega_c^2}$ is the free space synchrotron radiation rate, and $Q^{(E)}$ and $Q^{(M)}$ are the quality factors associated with TE modes and TM modes respectively. In the two terms, Σ_S contains the effect from the cylindrical surface, and Σ_P contains the effect from the top and bottom endcap surfaces. It is possible to assign different quality factors for TE and TM modes. However, it is not possible to assign quality factors for each mode. The correction to handle this limitation is given later.

The cylindrical surface part Σ_S is explicitly given by [102]

$$\begin{aligned}\Sigma_S(\omega, z, \rho, Q^{(E)}, Q^{(M)}) = -\frac{r_0}{z_0}\sum_{p=1}^{\infty} \sin^2\left[\frac{p\pi}{2}\left(\frac{z}{z_0}+1\right)\right] \\ \times \sum_{m=0}^{\infty}(1+\mathrm{sgn}(m))\left[\frac{K'_m(\mu_p^{(M)}\rho_0)}{I'_m(\mu_p^{(E)}\rho_0)} R_I(m;\mu_p^{(M)}\rho) \right. \\ \left. + \left(\frac{p\pi c}{2\omega z_0}\right)^2 \left(\frac{K_m(\mu_p^{(M)}\rho_0)}{I_m(\mu_p^{(M)}\rho_0)} R_I(m;\mu_p^{(M)}\rho) - \frac{K_m(\frac{p\pi\rho_0}{2z_0})}{I_m(\frac{p\pi\rho_0}{2z_0})} R_I\left(m;\frac{p\pi\rho}{2z_0}\right)\right)\right]\end{aligned} \quad (4.45)$$

with

$$\begin{aligned}\mu_p^{(E)} &= \sqrt{\left(\frac{p\pi}{2z_0}\right)^2 - \left[\frac{\omega}{c}\left(1+\frac{i}{2Q^{(E)}}\right)\right]^2} \\ \mu_p^{(M)} &= \sqrt{\left(\frac{p\pi}{2z_0}\right)^2 - \left[\frac{\omega}{c}\left(1+\frac{i}{2Q^{(M)}}\right)\right]^2}\end{aligned} \quad (4.46)$$

and

$$R_I(m;x) = \left(\frac{m}{x}\right)^2 I_m(x)^2 + I'_m(x)^2. \quad (4.47)$$

[2]In this section we denote cyclotron frequency in the trap as ω_c for conciseness. The difference between using $\bar{\omega}_c$, ω'_c and ω_c is negligible.

Here, r_0 is the classical radius of an electron $r_0 = e^2/(4\pi\epsilon_0 mc^2)$, $\mathrm{sgn}(x)$ is the signum function, $I_\nu(x)$ is the modified Bessel function of the first kind, and $K_\nu(x)$ is the modified Bessel function of the second kind. The parallel surface part Σ_P is explicitly given by

$$\Sigma_P(\omega, z) = -r_0 \left[2\sum_{j=1}^{\infty} F(4jz_0) - \sum_{j=1}^{\infty} F(2(2j-1)z_0 + 2z) - \sum_{j=1}^{\infty} F(2(2j-1)z_0 - 2z) \right] \tag{4.48}$$

with

$$F(z) = \frac{1}{|z|}\left[e^{\frac{i\omega|z|}{c}} \left(1 + \frac{ic}{\omega|z|} - \frac{c^2}{\omega^2 z^2} \right) + \frac{c^2}{\omega^2 z^2} \right] \tag{4.49}$$

Single Mode Lorentzian Approximation

In the renormalized calculation, Σ_S has poles at the right microwave resonant frequencies, where the denominators in Eq. 4.45 cross 0. The resonant frequencies are

$$\omega_{mnp}^{(E)} = c\sqrt{\left(\frac{x'_{mn}}{\rho_0}\right)^2 + \left(\frac{p\pi}{2z_0}\right)^2} \tag{4.50}$$

$$\omega_{mnp}^{(M)} = c\sqrt{\left(\frac{x_{mn}}{\rho_0}\right)^2 + \left(\frac{p\pi}{2z_0}\right)^2}, \tag{4.51}$$

where x_{mn} is the n-th zero of the order-m Bessel function $J_m(x)$, and x'_{mn} is the n-th zero of the derivative of order-m Bessel function $J'_m(x)$. The effect near the resonant frequencies can be approximated as

$$\Sigma_S(\omega, z, \rho) \approx \frac{\lambda_{mnp}^{2\ (E,M)}}{\left(\omega\left(1 + \frac{i}{2Q^{(E,M)}}\right)\right)^2 - \omega_{mnp}^{2\ (E,M)}}, \tag{4.52}$$

where $\lambda_{mnp}^{2\ (E,M)}$ characterizes the coupling strength from a mode. λ_M^2 represents the coupling of the electron and the cavity mode and is generally given by

$$\lambda_M^2 = \frac{e^2}{m\epsilon_0} \frac{|\vec{E}_M(\rho, z)_x|^2 + |\vec{E}_M(\rho, z)_y|^2}{\int_V |\vec{E}_M(\mathbf{r})|^2 d\mathbf{r}} \tag{4.53}$$

for the electron at ρ and z, where $\vec{e}_x$ is the unit vector along the x-axis. For each TE or TM mode, λ_M^2 is explicitly given by

$$\lambda_{mnp}^{2\ (E)} = \frac{2r_0c^2}{z_0\rho_0^2}\frac{-(1+\mathrm{sgn}(m))}{J_m''(x'_{mn})J_m(x'_{mn})}\sin^2\left[\frac{p\pi}{2}\left(\frac{z}{z_0}+1\right)\right]R_J\left(m;x'_{mn}\frac{\rho}{\rho_0}\right) \tag{4.54a}$$

$$= \frac{2r_0c^2}{z_0\rho_0^2}\frac{-1}{J_m''(x'_{mn})J_m(x'_{mn})} \qquad (\text{at } \rho=0 \text{ and } z=0 \text{ for } m=1 \text{ and } p\text{-odd})$$

$$\lambda_{mnp}^{2\ (M)} = \frac{2r_0c^2}{z_0\rho_0^2}\frac{1+\mathrm{sgn}(m)}{J'_m(x_{mn})^2}\left(\frac{p\pi}{2z_0}\frac{c}{\omega_{mnp}^{(M)}}\right)^2\sin^2\left[\frac{p\pi}{2}\left(\frac{z}{z_0}+1\right)\right]R_J\left(m;x_{mn}\frac{\rho}{\rho_0}\right) \tag{4.54b}$$

$$= \frac{2r_0c^2}{z_0\rho_0^2}\frac{1}{J'_m(x_{mn})^2}\left(\frac{p\pi}{2z_0}\frac{c}{\omega_{mnp}^{(M)}}\right)^2 \quad (\text{at } \rho=0 \text{ and } z=0 \text{ for } m=1 \text{ and } p\text{-odd}).$$

Here, $R_J(m;x)$ is defined by

$$R_J(m;x) = \begin{cases} \frac{m^2}{x^2}J_m(x)^2 + J'_m(x)^2 & (x\neq 0), \\ \frac{1}{2} & (x=0,\ m=1), \\ 0 & (x=0,\ m\neq 1). \end{cases} \tag{4.55}$$

One can prove that λ_M^2 has non-zero value at the trap center $\rho = z = 0$ only for $m = 1$ and p-odd modes. These modes are called the strong coupling modes. This approximation using the coupling strength is called the single-mode approximation. The correction to cyclotron frequency and the modified damping rate from a single mode ω_M with strength λ_M is

$$\Delta\omega_c^{\mathrm{cav}} - i\frac{\gamma_c}{2} = \frac{\omega\lambda_M^2}{\omega^2 + i\omega\Gamma_M - \omega_M^2} \quad (\text{single mode}), \tag{4.56}$$

where Γ_M is the full-width at half maximum of the coupling of the mode, and is related to the quality factor Q_M by

$$\Gamma_M = \frac{\omega_M}{Q_M} \tag{4.57}$$

This single mode approximation allows to assign different quality factors for different modes.

Notice that the correction Δ_c^{cav} is independent of Γ_M when off-resonance

$$\Delta\omega_c^{\text{cav}} \approx \frac{\omega\lambda_M^2}{\omega^2 - \omega_M^2} \quad (|\omega - \omega_M| \gg \Gamma_M) \tag{4.58}$$

and only the resonant frequency ω_M and the coupling strength λ_M^2 are important.

Divergence and Suppression with Hybrid Calculation

The reason we do not entirely use the single mode Lorentzian approximation for all modes is that the sum of Eq. 4.65 for all resonant modes yields ultraviolet divergence. The divergence arises from the electron's self-energy. The renormalized calculation takes off this divergence [53]. We first construct the renormalized function using the best fit of ρ_0 and z_0. From the renormalized function, each mode is subtracted using its ideal frequency and added back with the measured resonant frequencies using the Lorentzian approximation.

We use this hybrid method to suppress infinite divergence and assign the measured resonant frequency and Q-factor to each mode. We found that to subtract the original resonance perfectly, $Q^{(E)}$ and $Q^{(M)}$ in the renormalized calculation need to be same

$$Q^{(E)} = Q^{(M)} = Q^{(0)}. \tag{4.59}$$

Since the shift $\Delta\omega_c^{\text{cav}}/\omega_c$ is independent of Q off resonance, assigning only one Q-factor does not affect the result. In addition, we will assign the measured Q to each mode independently after subtraction, so the original input $Q^{(0)}$ in the renormalized calculation only changed modes far from resonances, and its effect is completely negligible.

The exact procedure is summarized as

$$\Delta\omega_c^{\mathrm{cav}} - \frac{i}{2}\gamma_c = -\frac{i}{2}\gamma_{c;0} + \omega_c \left\{\Sigma_S\left[\omega_c, z, \rho, Q^{(0)}, Q^{(0)}\right] + \Sigma_P\left[\omega_c, z, Q^{(0)}, Q^{(0)}\right]\right\} + \sum_{\substack{\text{all measured} \\ \text{modes}}} \left(-\frac{\omega_c \lambda_M^{2\ (\mathrm{calc.})}}{\omega_c^2 + i\omega_c \Gamma_M^{(\mathrm{calc.})} - \omega_M^{2\ (\mathrm{calc.})}} + \frac{\omega_c \lambda_M^{2\ (\mathrm{est.})}}{\omega_c^2 + i\omega_c \Gamma_M^{(\mathrm{meas.})} - \omega_M^{2\ (\mathrm{meas.})}} \right), \tag{4.60}$$

where the quantities with the superscript (calc.) are the calculated ideal values, those with (meas.) are the measured values, and the $\lambda_M^{2\ (\mathrm{est.})}$ is the estimated values discussed later. We construct the renormalized function Σ_S and Σ_P with the typical quality factor $Q^{(0)} = 3000$, subtract each mode using the ideal resonant frequencies (Eq. 4.50 and Eq. 4.51) and coupling strength (Eq. 4.54), and then add the Lorentzian function back with the measured Q-factor and resonant frequencies. By doing this, we suppress infinite divergence, and can still assign Q-factor and resonant frequency to each mode.

We know that the simple sum of the Lorentzian function diverges. To check if the divergence occurs for the subtraction and re-adding method, we study the correction as a function of the number of included modes. We calculate the correction from the second line in Eq. 4.60 to the g-factor at 115 GHz. Figure. 4.22 shows the effect of Lorentzian subtraction and re-addition on the g-factor at 115 GHz. The number of included modes is changed from two nearest modes to all the measured strongly coupled modes in 60 GHz–160 GHz (25 in total). Even with all measured modes included, the change of the correction from two nearest modes to all 25 modes is only 0.04×10^{-12}. Some portion of the correction by including more modes is real. It is difficult to judge if the small increase by including more modes is because of the imperfection of the method, but the validity of the Lorentzian subtraction and re-adding method is at least better than 0.04×10^{-12}.

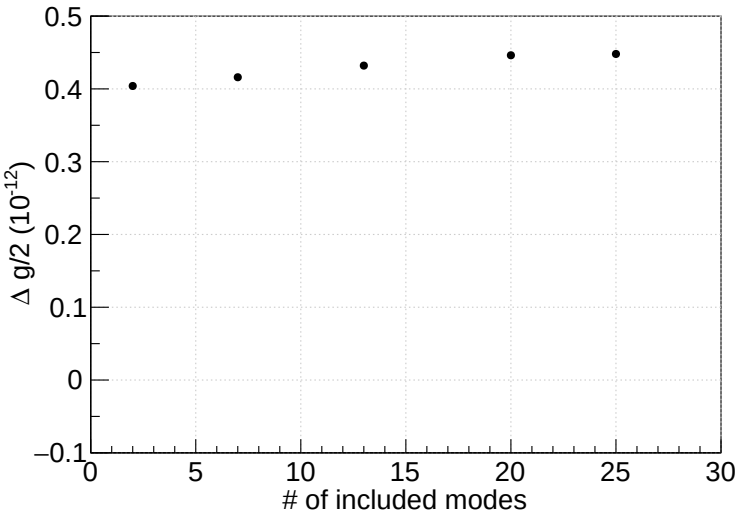


Figure 4.22: Dependence of the correction $\Delta g/2$ at 115 GHz as a function of the number of included modes. The number of included modes in the second line of Eq. 4.60 is varied, and the correction at 115 GHz is calculated.

Measurement of Microwave Center Offset

In the 2008 measurement, the center of microwave cavity modes was found to be inconsistent with the center of the electrostatic field using the TE_{136} mode [7]. The observed offset was about 165 μm, much larger than any tolerances. An offset of $z_{\mathrm{offset}} = 165$ μm is used for all modes. In this measurement, we study many more modes and observe different discrepancies between the trap center and the microwave center depending on the modes. The misalignment induces more systematic corrections because the coupling of an electron to microwave modes depends on the misalignment.

There are two ways to measure the center of the microwave cavity modes. First, the magnitude of axial sideband $\omega_M \pm \omega_z$ of a microwave mode is given by [51]

$$\frac{P_{\omega_M \pm \omega_z}}{P_{\omega_M}} = \left[\frac{\cos\left[\frac{p\pi}{2}\left(\frac{z_{\mathrm{offset}}}{z_0}+1\right)\right]\frac{p\pi A}{2z_0}}{\sin\left[\frac{p\pi}{2}\left(\frac{z_{\mathrm{offset}}}{z_0}+1\right)\right]\left[1-\left(\frac{p\pi A}{4z_0}\right)^2\right]} \right]^2 \approx \begin{cases} \left(\frac{A}{z_{\mathrm{offset}}}\right)^2 & (p\text{-even}) \\ \left(\frac{p\pi}{2z_0}\right)^4 A^2 z_{\mathrm{offset}}^2 & (p\text{-odd}) \end{cases}. \quad (4.61)$$

The last approximation is valid when the offset is small $\frac{p\pi}{2}\frac{z_{\mathrm{offset}}}{z_0} \ll 1$.

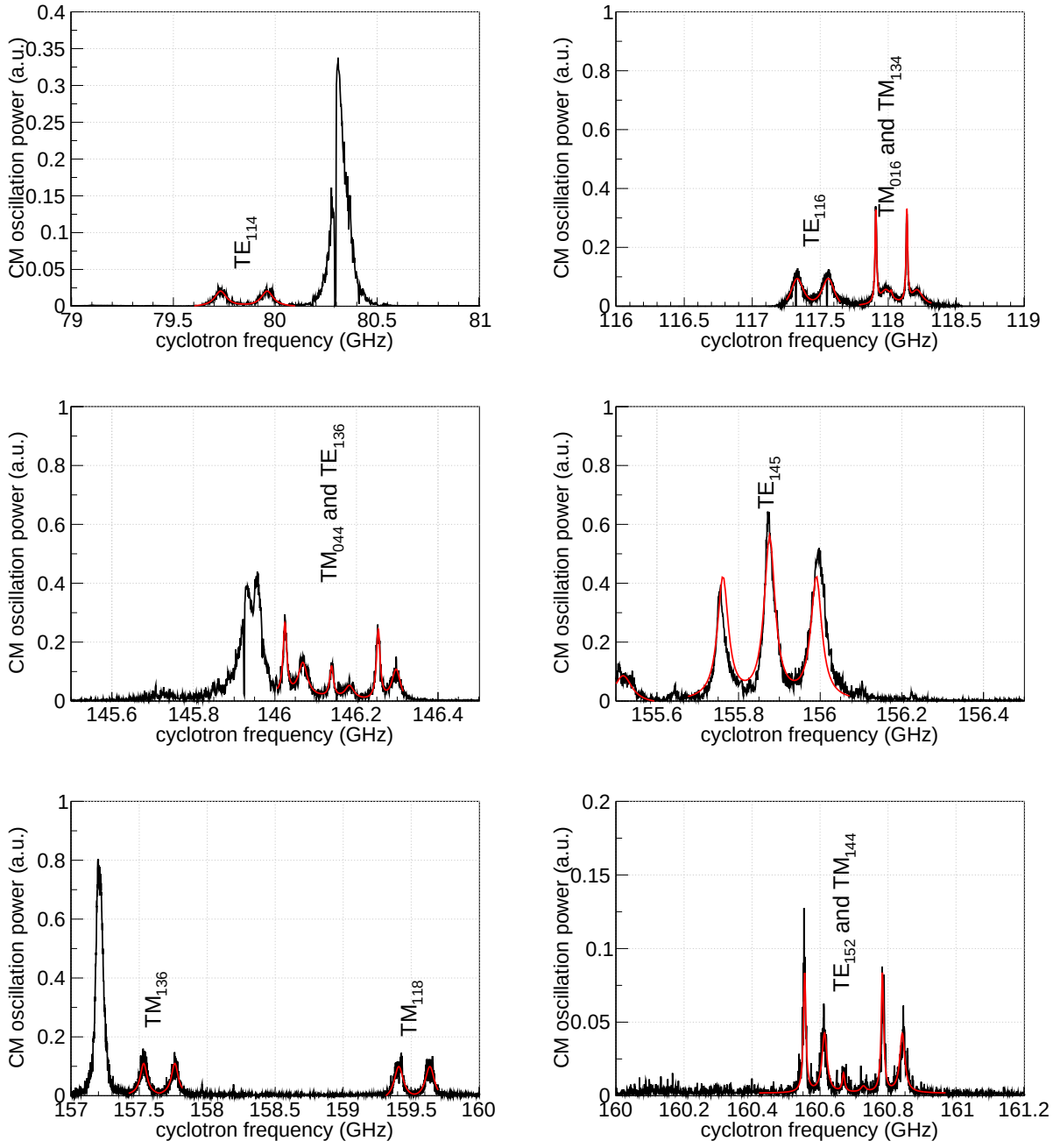


Figure 4.23: Examples of measurement of microwave offset using p-even modes. The axial excitation amplitude in the mode mapping scan is fitted with Lorentzian.

Figure 4.23 shows the spectrum around several modes. The amplitudes at $\omega_M \pm \omega_z$ sidebands and the one at ω_M are fit by the Lorentzian function to extract the misalignment factor. The misalignment is observed mostly in the p-even modes, but also observed for the strong coupling p-odd mode, TE_{145}. We notice that TE_{145} is the only mode that shows non-zero z_{offset} among the p-odd modes.

To determine the offset z_{offset}, the parametric oscillation amplitude A needs to be known precisely. We determine A based on the measurement from a single electron. First, the detected power on the spectrum analyzer is recorded when an electron is self-excited. The amplitude of the self-excitation A_{SXO} can be measured by measuring the cyclotron frequency shift and using the known bottle size $B_2 = 300\ \mathrm{T/m^2}$. The oscillation power of a parametrically driven cloud is proportional to the square of the number of electrons and its amplitude.

$$P_{\mathrm{cloud}} = P_{\mathrm{SXO}} \times N^2 \left(\frac{A}{A_{\mathrm{SXO}}}\right)^2 \tag{4.62}$$

For P_{cloud}, we use the peak of center ω_M for p-even modes and $\omega_M \pm \omega_z$ for p-odd modes. The observed non-zero z_{offset} is summarized in Table. 4.3.

mode	z_{offset} (μm)	mode	z_{offset} (μm)
TE_{114}	< 3	TE_{124}	< 32
TE_{132}	< 3	TE_{116}	< 10
TM_{016}	< 19	TM_{134}	15(10)
TM_{232}	148(50)	TM_{126}	30(23)
TM_{026}	190(40)	TE_{142}	60(40)
TM_{042}	< 5	TM_{126}	< 30
TE_{042}	< 5	TE_{144}	< 10
TM_{044}	120(40)	TE_{136}	55(33)
TE_{118}	28(15)	TE_{145}	89(53)
TM_{136}	< 6	TM_{118}	< 3
TE_{152}	< 10	TM_{144}	$< 44(10)$

Table 4.3: Observed z_{offset} and its uncertainty. The uncertainty is dominated by the determination of the ratio $P_{\omega_M \pm \omega_z}/P_{\omega_M}$ and is worse when there are other modes nearby.

Another method to measure microwave offset is to directly measure γ_c near a p-even microwave mode. By setting the cyclotron near to a p-even mode, the synchrotron radiation

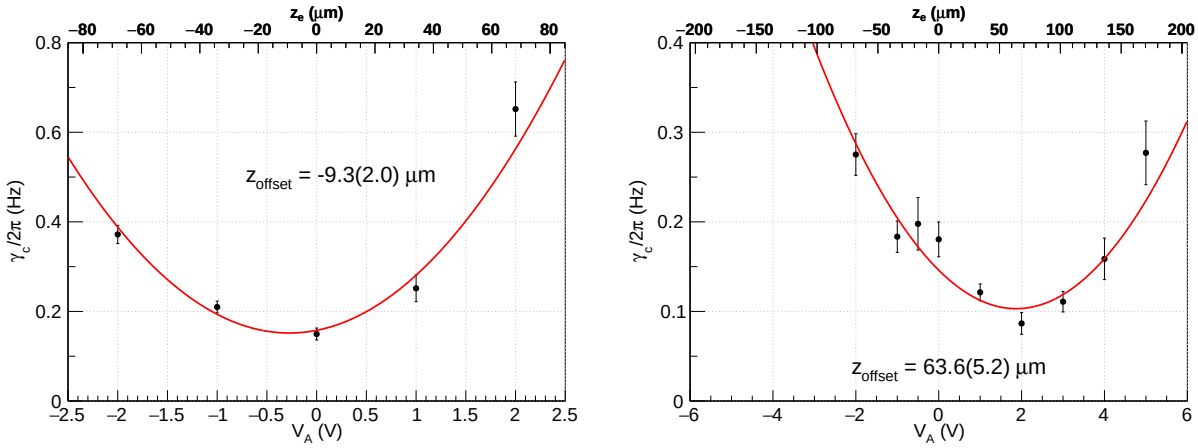


Figure 4.24: Measured microwave resonant mode's offset using an electron near TE_{116} (left) and TE_{136} (right).

rate γ_c depends on the position of the trapped electron. The position of the electron can be shifted by applying an antisymmetric bias to the endcap electrodes (Chap. 2). Figure 4.24 shows the measured microwave center offset using an electron near TE_{116} and TE_{136}. The results are consistent with the values in Table. 4.3 and verify the assigned error.

The radial misalignment ρ_{offset} is measured by setting the cyclotron frequency at exactly on resonance with the modes with $m \neq 1$. The damping rate γ_c at its resonance and at a detuned frequency from that mode is measured. The change of γ_c is compared with the theoretical model. Using Eq. 4.65, the synchrotron radiation rate at resonance of ω_M mode is

$$\gamma_c = \frac{2Q_M\lambda_M^2}{\omega_M}. \tag{4.63}$$

This comparison is made for four modes, TE_{035}, TE_{243}, TE_{043}, and TE_{025}. Table 4.4 summarizes the measured radial misalignment using several $m \neq 1$ cavity modes. Radial mis-

mode	change of $\gamma_c/(2\pi)$ (Hz)	ρ_{offset} (μm)
TE_{035}	< 0.049	< 5.8
TE_{243}	< 0.010	< 19.8
TE_{043}	< 0.016	< 3.3
TE_{025}	< 0.030	< 14.8

Table 4.4: Measurement of radial offset, upper limit of $\gamma_c/(2\pi)$ and calculated ρ_{offset}.

alignment has not been observed for any modes. Based on this measurement, we assign

$$\rho_{\text{offset}} < 3.3\ \mu\text{m}. \tag{4.64}$$

Splitting of Degenerated Modes

All modes with $m \neq 0$ are doubly degenerate. The degeneracy corresponds to two possible directions of rotation of the photon in the cavity. The two degenerated modes should have the same resonant frequency and Q-factor in an ideal cylindrical cavity, but the slits, holes, and loss in the real cavity remove the degeneracy.

Large splitting of degeneracy is observed only in the TM_{143} [Fig. 4.25 (a)]. The splitting can be handled by assuming two Lorentzian peaks, each with half of the coupling constant

$$\Delta\omega_c^{\text{cav}} - i\frac{\gamma_c}{2} = \frac{\omega_c\lambda_M^2/2}{\omega_c^2 + i\omega_c\Gamma_M - \omega_{M;\text{low}}^2} + \frac{\omega_c\lambda_M^2/2}{\omega_c^2 + i\omega_c\Gamma_M - \omega_{M;\text{high}}^2}, \quad \text{(for split mode)} \tag{4.65}$$

The effect of using two Lorentzians with $\lambda_M^2/2$ instead of one Lorentzian with λ_M^2 is very small if ω_c is away from the resonance. Figure 4.25 (b) shows the difference of correction $\Delta\omega_c^{\text{cav}}/\omega_c$ if only one Lorentzian with λ_M^2 is used or two split Lorentzians with $\lambda_M^2/2$ are used. The effect is less than 0.003×10^{-12} even in the closest frequency that we measure the g-factor.

Uncertainty of the Coupling Strength λ_M^2

In the single mode approximation function (Eq. 4.65), the resonant frequency ω_M and the width Γ_M can be determined from the measured spectrum. However, the remaining parameter, the coupling strength λ_M^2 cannot be directly measured. Since we do not know the mechanism of the mapping, we cannot determine λ_M^2 precisely from the parametric oscillation power. In addition, for most of the strong coupling mode, the peak of strong coupling resonances are likely saturated.

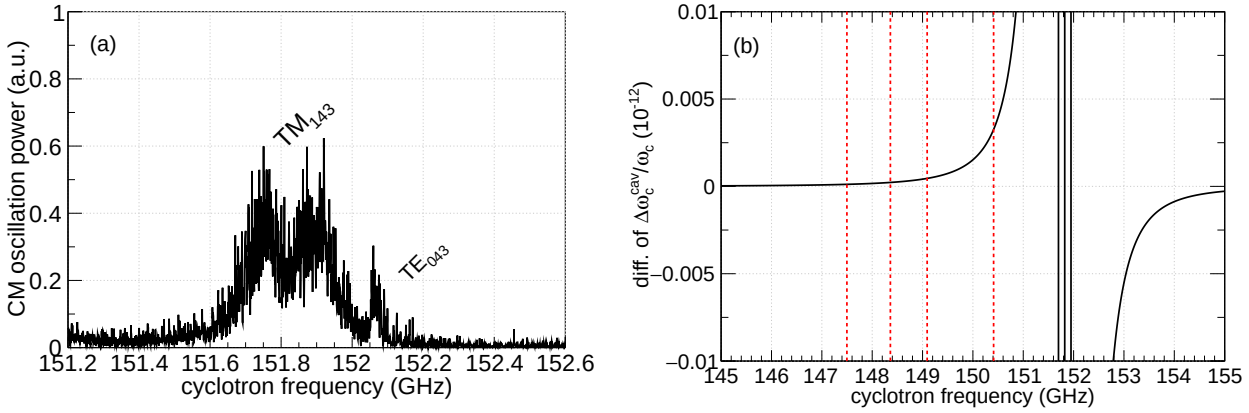


Figure 4.25: (a) Observed splitting of the degeneracy of TM_{143} mode. The small resonance at 152.06 GHz is TE_{043} mode. (b) Effect of splitting on the measured g-factor. The difference between assuming one Lorentzian at the center of two split peaks with $\lambda^2_{TM_{143}}$ and two Lorentzians with $\lambda^2_{TM_{143}}/2$ is shown. The frequencies that the g-factor is measured at are also shown.

We estimate the uncertainty of λ^2_M comes from its original expression (Eq. 4.53). The coupling strength λ^2_M represents the normalized energy density at the center, which is proportional to $(\text{length})^{-3}$. Since the resonant frequency scales as $(\text{length})^{-1}$ and λ^2_M scales as $(\text{length})^{-3}$, a natural estimate is that the λ^2_M can be different three times larger than the discrepancy of resonant frequency. The observed discrepancy between the calculated and measured resonant frequencies is shown in Fig. 4.17. The RMS scattering of the strongly coupled modes is 1.7 %, which corresponds to 5.1 % RMS scatter in λ^2_M. The uncertainty from λ^2_M is calculated as follows. For each mode, the correction function Eq. 4.60 is reconstructed with that mode's λ^2_M 5.1 % varied. The difference between using not-varied λ^2_M and varied λ^2_M is taken as a systematic error[3].

Different mode shifts the g-factor measured at different fields. For example, the uncertainty of TE_{145} (156 GHz) affects the measurements around 150 GHz a lot, but does not shift the measurement at 87 GHz so much. The correlation between the uncertainties and their averaging method is discussed in Sec. 4.5.

[3]An improved method to calculate the uncertainty of λ^2_M using a finite-element-analysis method is being discussed within the group. The uncertainty might be revised before publication.

mode	ideal frequency (GHz)	$\lambda_M^2/(2\pi)^2$ (10^8 Hz^2)	$\Delta g/2$ by 1 GHz shift (10^{-12})	$\Delta g/2$ by 5.1% λ_M^2 change (10^{-12})
TE_{137}	161.510	21.6	0.053	0.032
TE_{153}	166.507	37.4	0.045	0.037
TM_{145}	169.755	10.7	0.009	0.009
TM_{137}	171.669	15.6	0.011	0.012
TE_{119}	173.738	6.7	0.004	0.005
TM_{151}	174.197	0.5	0.000	0.000
TM_{119}	177.293	9.3	0.004	0.005
TE_{129}	181.525	13.8	0.005	0.007
TE_{147}	182.141	29.5	0.009	0.014
TM_{153}	182.452	4.1	0.001	0.002
TE_{155}	183.339	37.4	0.011	0.017
TM_{129}	187.747	15.0	0.003	0.006
TE_{161}	190.347	45.2	0.009	0.017
TM_{147}	194.035	16.0	0.003	0.005
TE_{139}	194.582	21.6	0.004	0.007
TE_{163}	197.929	45.2	0.006	0.014
TM_{155}	197.933	9.7	0.001	0.003

Table 4.5: Estimated uncertainty from the unmeasured higher frequency resonances at 150.411 GHz. The modes between 160 GHz and 200 GHz are considered.

Microwave Cavity Shift from the Unmeasured Modes

We have explored correction and uncertainties from the measured modes between 60 GHz and 160 GHz. There are also more modes below 60 GHz or above 160 GHz, which could shift the measured g-factor. The modes below 60 GHz are not measured because our current waveguide is not designed to deliver a strong microwave drive below 60 GHz. The modes above 160 GHz are not measured because of the limitation of the niobium-titanium magnet.

On the higher side, the next several strong coupled modes are summarized in Table. 4.5. The effect on the g-factor result at 150.411 GHz is also shown if their resonant frequency is shifted by ± 0.5 GHz or if λ_M^2 differs by 5.1 %. This effect is largest in the measurements around 5.3 T and is negligible for the measurements at the lower fields.

The modes below 60 GHz are also summarized in Table. 4.6. The effect is the largest in the 87.010 GHz measurement and is negligible for the other measurements at higher frequencies. Notice that unlike the higher side, there are only two modes that were not

mode	ideal frequency (GHz)	$\lambda_M^2/(2\pi)^2$ (10^8 Hz^2)	$\Delta g/2$ by 1 GHz shift (10^{-12})	$\Delta g/2$ by 5.1% λ_M^2 change (10^{-12})
TM_{111}	44.614	1.8	0.001	0.002
TE_{111}	27.251	6.7	0.001	0.005

Table 4.6: Estimated uncertainty from the unmeasured lower frequency resonances on measured g-factor at 87.010 GHz. Notice that unlike the high frequency modes, there are only two modes that were not measured.

measured. The coupling strength λ_M^2 is also much smaller than the modes on the higher side. The correction and uncertainty on the 87.010 GHz measurement are much smaller than the modes above 160 GHz.

4.3.3 Applied Microwave Cavity Correction and Uncertainty

Using the described methods, the cavity mode correction is calculated. We first construct the renormalized function (Eq. 4.44) with the best fit ρ_0 and z_0 (Fig. 4.18). To include the actual measured resonant frequencies, the resonance in the renormalized function is subtracted with the Lorentzian approximation (Eq. 4.52) and added back with measured resonant frequency and Q-factor(Eq. 4.60).

The uncertainty of measured radius, height, microwave resonant frequencies, offsets, Q-factor, and coupling strength is taken into account by recalculating the correction function with the shifted value and taking the difference. The square sum of all uncertainties yields the uncertainty of microwave correction.

The applied cavity correction is shown in Fig. 4.26 (a), and its uncertainty is shown in Fig. 4.26 (b) The major uncertainty comes from the uncertainty of λ_M^2. We now have taken a much wider range of microwave resonances, which allows estimating the uncertainty properly. The studies here emphasize the importance of the microwave cavity correction. The difficulty of the microwave correction motivates the measurement of g-factor at lower fields than the traditional 5–6 T.

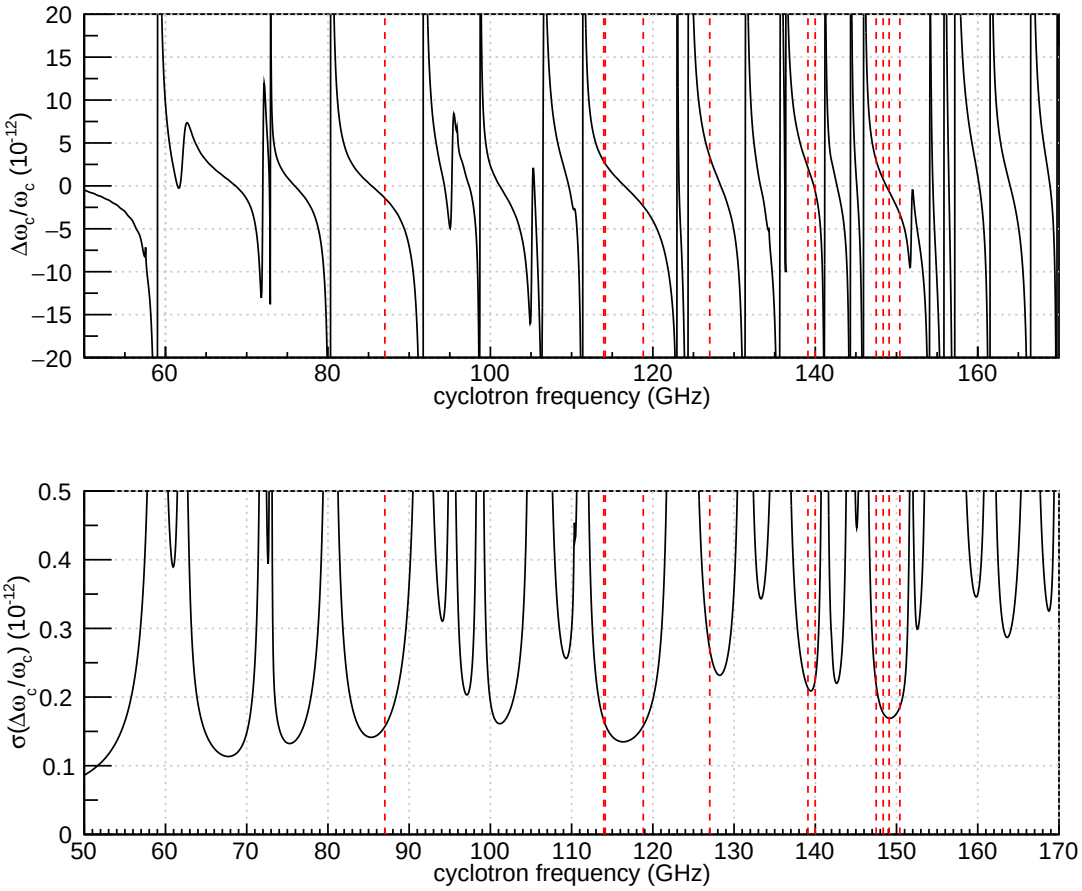


Figure 4.26: (top) Applied Cavity correction from the measured resonances. Notice that the correction at nearby fields is correlated. (bottom) Uncertainty of the cavity correction. The frequencies that g-factor measurement is performed are indicated by the red dotted lines.

4.4 Other Systematic Effects

In addition to the microwave cavity shift, other systematic effects are also investigated. Several experimental parameters are also varied to search for possible shifts and broadening effects. These other systematic shifts and uncertainties are discussed in this section.

4.4.1 Cyclotron Power Shift

The drive power to induce one cyclotron transition is only about -200 dBm. The temperature of the mixing chamber stage increases by only 1 mK by a drive with 30 dB stronger power. The shift from cyclotron drive power is first studied by measuring the anomaly frequency's shift when a strong detuned cyclotron drive is applied. Measuring the shift of cyclotron frequency for a strong power is rather challenging because of excitation to higher cyclotron states and the relativistic cyclotron frequency shift (Sec.4.1). Figure 4.27 shows the measured anomaly frequency with different cyclotron drive power. The x-axis is the relative drive power compared to the maximum power used in the spectroscopy. Even with the 100 times stronger cyclotron drive, the shift of anomaly frequency is less than 1 ppb. We fit the result with a linear line, and extract the possible shift that the cyclotron drive for spectroscopy can induce (relative cyclotron power = 1 in the x-axis). The actual effect on g-factor is even smaller by a factor of $(g-2)/2 \approx 0.00115$.

The drive power dependence can also be studied using the measured g-factors. Figure 4.28 shows the measured g-factor as a function of peak cyclotron transition probability. Only the data around 150 GHz are used because they are shifted with the same amplitude if there are any unaccounted cavity corrections. The linear fitting gives a slope consistent with zero.

Based on these estimates, we take the product of $(g/2-1)$ and the one sigma of anomaly

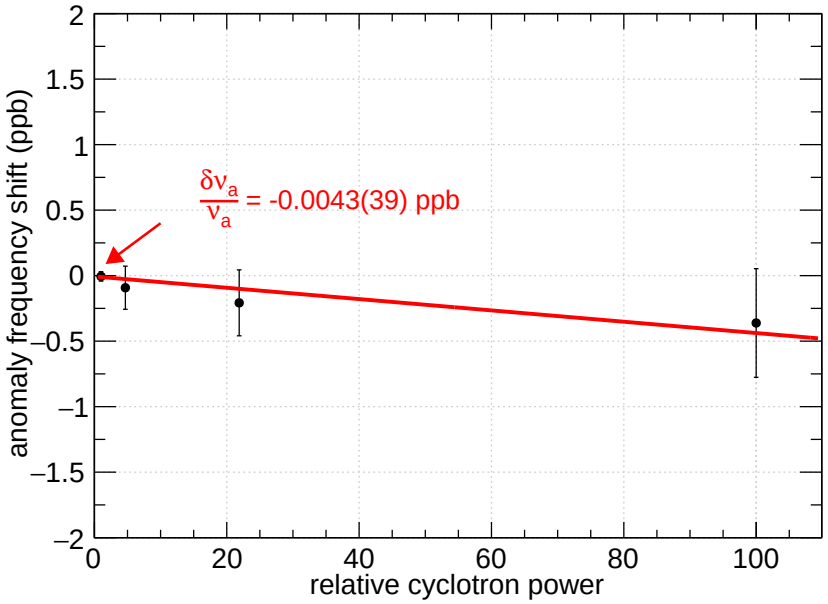


Figure 4.27: Measurement of cyclotron drive induced anomaly frequency shift.

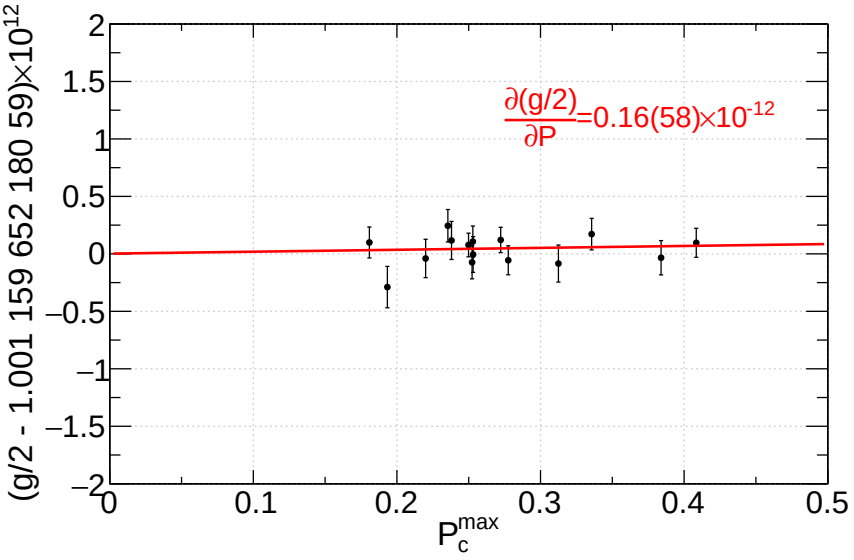


Figure 4.28: Dependence of measured g-factor on the peak cyclotron transition probability.

frequency shift and assign the systematic shift due to cyclotron power as

$$\Delta\left(\frac{g}{2}\right) < 4.9 \times 10^{-15}. \tag{4.66}$$

4.4.2 Anomaly Power Shift

The anomaly drive is relatively stronger than the cyclotron drive. What we measure is the cyclotron or anomaly frequency of an electron under axial modulation from the anomaly drive. Since a detuned anomaly drive is also applied during the cyclotron drive, the effect anomaly drive should cancel when calculating the g-factor.

The 1987 experiment that used a smaller magnetic bottle (150 T/m^2) suffered from frequency shift due to a strong anomaly drive [103]. We reduced the magnetic bottle size by a factor of 5 from the 2008 measurement, but it is still larger than the 1987 measurement.

The anomaly drive with voltage amplitude V_a at the bottom endcap electrode excites the electron to an amplitude [104]

$$z_a = \frac{c_1 d^2}{2 z_0}\left[\left(\frac{\omega_a}{\omega_z}\right)^2 - 1\right]^{-1}\frac{V_a}{V_R}. \tag{4.67}$$

The Rabi frequency for anomaly transition is

$$\Omega_a = \frac{g}{2}\frac{e\hbar}{2m}B_2 z_a\sqrt{\frac{2}{m\hbar(\omega_c' - \omega_m)}}. \tag{4.68}$$

The probability of making a transition with drive length T in the weak drive limit is

$$P(\omega) = \frac{\pi}{2}T\Omega_a^2\chi(\omega), \tag{4.69}$$

where $\chi(\omega)$ is the lineshape function that is given in Sec. 4.1.2. Its maximum value, $\chi(\omega_{\max})$

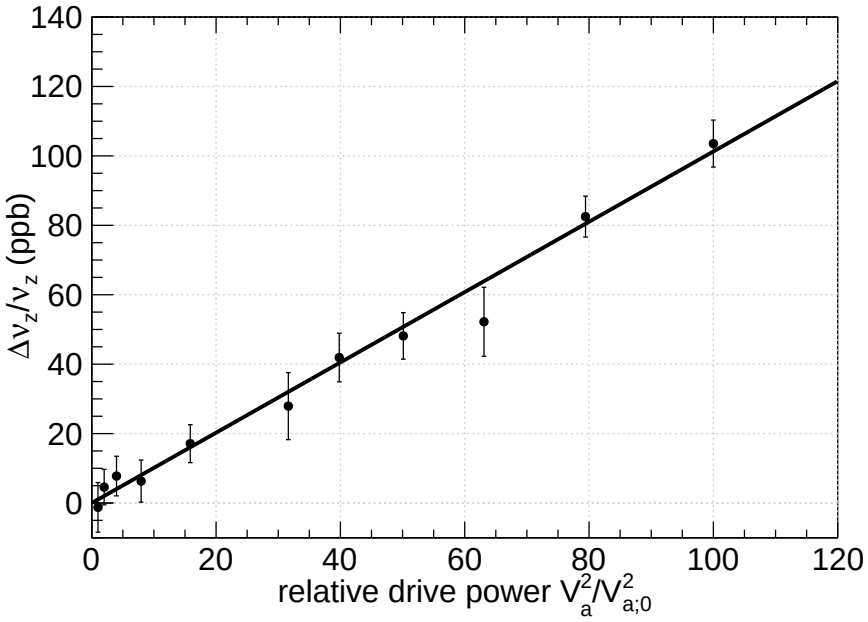


Figure 4.29: Observed shift of axial frequency from much stronger anomaly drive power.

is inversely proportional to the linewidth.

$$\chi(\omega_{\max}) = \frac{2}{\pi}\left(\frac{2\Delta\omega_a^2}{\gamma_z} + \gamma_c\right)^{-1} \tag{4.70}$$

Using our typical parameters, $B_2 = 300$ T/m^2, $\omega_c'/(2\pi) = 150$ GHz, $\omega_m/(2\pi) = 43$ kHz, $\gamma_z/(2\pi) = 5$ Hz, and $\gamma_c/(2\pi) = 0.04$ Hz, we estimate the drive amplitude of $z_a = 150$ nm to account for the observed 40% of peak transition probability.

Another way to calibrate the actual modulation amplitude is to measure the shift of the axial frequency. The shift of axial frequency due to anomaly drive is [104]

$$\frac{\Delta\nu_z}{\nu_z} = \frac{V_a^2}{V_R^2}\left\{\frac{3c_1c_3}{8}\left[\left(\frac{\omega_a}{\omega_z}\right)^2 - 1\right]^{-1} + \frac{(1+C_2)^2}{16}\left[\left(\frac{\omega_a}{\omega_z}\right)^2 - 4\right]^{-1}\right\}. \tag{4.71}$$

Here, all the parameters other than the anomaly drive amplitude V_a are known with much better uncertainty. We can measure the axial frequency shift and calibrate the anomaly drive amplitude V_a at the electrode that is actually applied.

Figure 4.29 shows the observed shift of axial frequency by anomaly drives. Much stronger anomaly drives than the power used in the spectroscopy are applied to make a visible axial frequency shift. The x-axis is the ratio of applied anomaly drive power here and the maximum power used in the spectroscopy $V_a^2/V_{a;0}^2$. From this measurement, the maximum drive amplitude used for spectroscopy is $V_{a;0}^2 = (6.5\ (3)\ \mathrm{mV})^2$ at 150 GHz. The corresponding oscillation amplitude is $z_a = 190\ (9)$ nm. The corresponding shift from at $z_a = 190$ nm is only

$$\frac{\Delta_p \omega}{\omega_0} = 1.1 \times 10^{-12}, \tag{4.72}$$

and the uncertainty on the g-factor is smaller by a factor of $(g/2 - 1)$.

The shift can also be directly measured by applying a detuned anomaly drive and measuring the cyclotron shift (Fig. 4.30). A much stronger detuned anomaly drive is applied, and the change of cyclotron frequency is measured. The x-axis is again the relative drive power compared to the maximum power used in the spectroscopy. Even with the 31 times stronger anomaly drive, the shift of cyclotron frequency is less than 1 ppb. We fit the result with a linear line and extract the possible shift that the anomaly drive for spectroscopy can induce (relative anomaly power = 1 in the x-axis). The actual effect on g-factor is even smaller by a factor of $(g-2)/2 \approx 0.00115$ than the measured $\delta\nu_a/\nu_a = 8.8 \times 10^{-15}$.

The drive power dependence can also be studied using the measured g-factors. Figure 4.31 shows the measured g-factor as a function of peak anomaly transition probability. Only the data around 150 GHz are used because they are shifted with the same amplitude if there are any unaccounted cavity corrections. The linear fitting gives a slope consistent with zero.

From these estimates, we take the product of $(g/2-1)$ and the one sigma of the cyclotron frequency shift as the anomaly drive's power shift

$$\Delta\left(\frac{g}{2}\right) < 10 \times 10^{-15}. \tag{4.73}$$

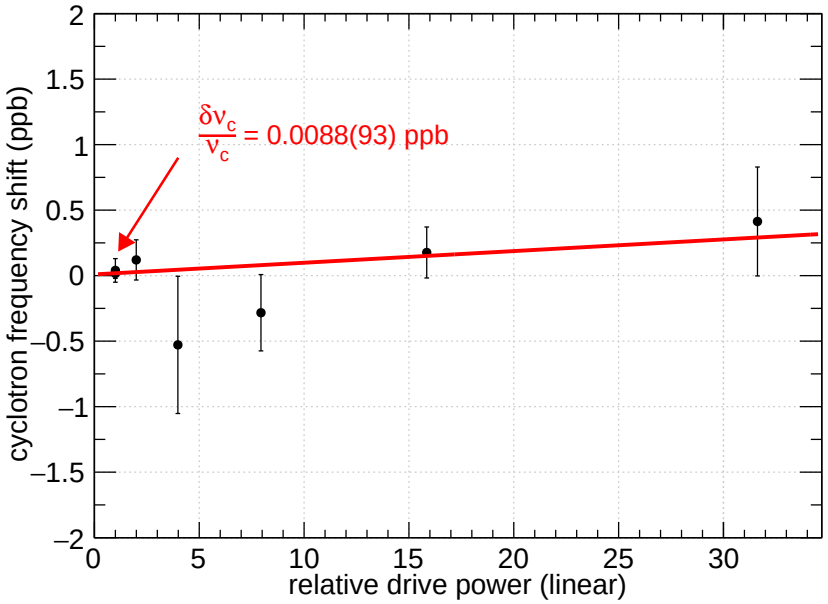


Figure 4.30: Power shift from the anomaly drive.

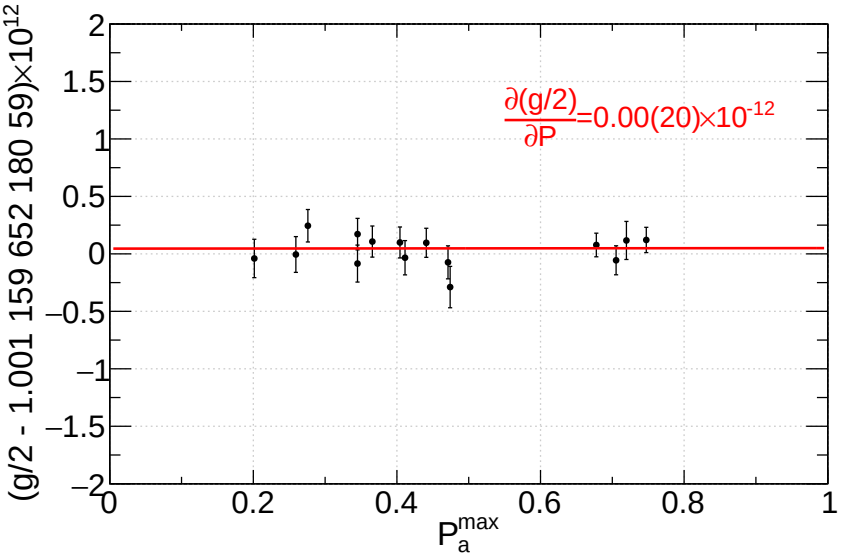


Figure 4.31: Dependence of measured g-factor on the peak anomaly transition probability.

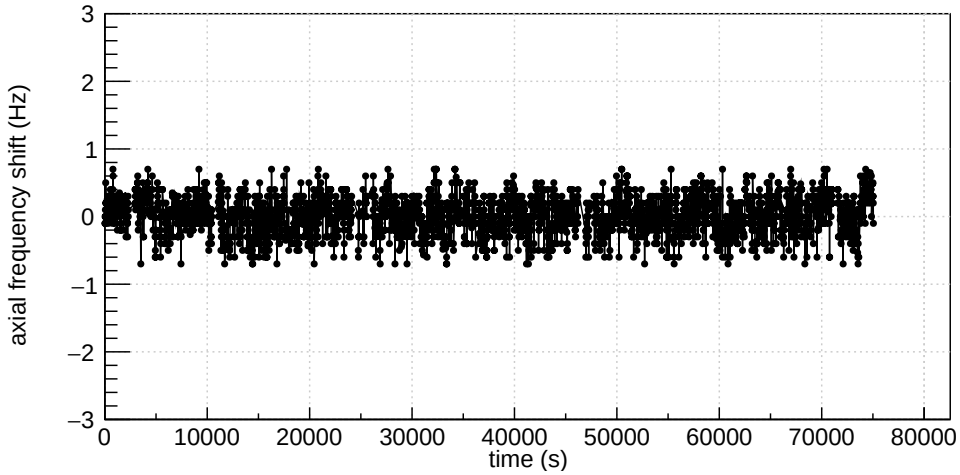


Figure 4.32: Fluctuation of axial frequency during a run. The frequency fluctuation is less than 1.3 Hz.

4.4.3 Fluctuation of Axial Frequency

The axial frequency is continuously monitored and regulated during the measurement. Figure 4.32 shows the measured axial frequency during the measurement when the electron is in $|n_c = 0, m_s = 1/2\rangle$. The axial frequency fluctuation is less than 0.6 Hz. Using Eq. 4.6, the shift of axial frequency propagates as

$$\begin{aligned}\Delta\left(\frac{g}{2}\right) &= -\frac{\frac{\bar{\nu}_z}{\bar{f}_c}\delta\bar{\nu}_z}{\bar{f}_c + \frac{3}{2}\delta + \frac{\bar{\nu}_z^2}{2\bar{f}_c}} - \frac{\bar{\nu}_a - \frac{\bar{\nu}_z^2}{2\bar{f}_c}}{\left(\bar{f}_c + \frac{3}{2}\delta + \frac{\bar{\nu}_z^2}{2\bar{f}_c}\right)^2}\frac{\bar{\nu}_z}{\bar{f}_c}\delta\bar{\nu}_z \\ &\approx -\left(\frac{g}{2} - 1\right)\frac{\frac{\bar{\nu}_z}{\bar{f}_c}\delta\bar{\nu}_z}{\bar{\nu}_a - \frac{\bar{\nu}_z^2}{2\bar{f}_c}}\left(1 + \frac{\frac{\bar{\nu}_z}{\bar{f}_c}\delta\bar{\nu}_z}{\bar{f}_c + \frac{3}{2}\delta + \frac{\bar{\nu}_z^2}{2\bar{f}_c}}\right) \\ &\approx -\left(\frac{g}{2} - 1\right)\frac{g}{2}\frac{\frac{\bar{\nu}_z}{\bar{f}_c}\delta\bar{\nu}_z}{\bar{\nu}_a - \frac{\bar{\nu}_z^2}{2\bar{f}_c}}\end{aligned} \tag{4.74}$$

This approximation is valid up to 10^{-15} precision. Therefore, the induced systematic shift from axial frequency fluctuation is

$$\Delta\left(\frac{g}{2}\right) < 3.2 \times 10^{-15}. \tag{4.75}$$

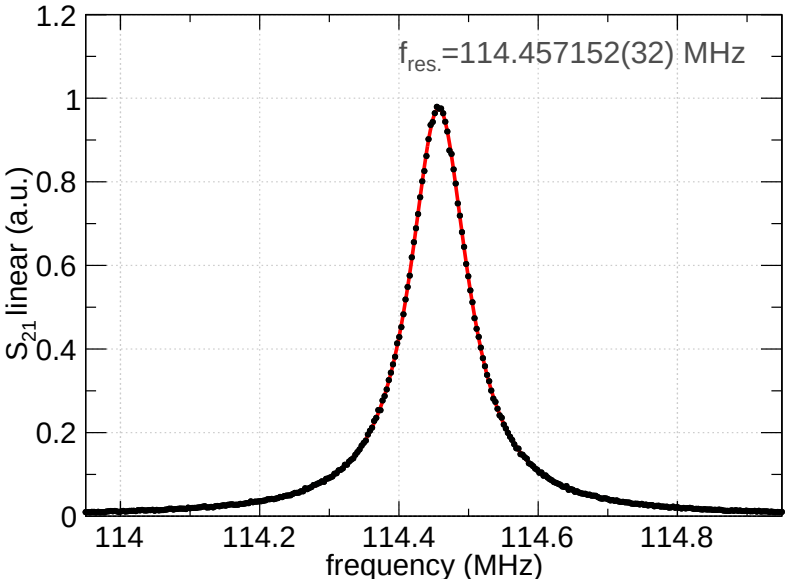


Figure 4.33: S_{21} measurement of the axial detection resonator.

4.4.4 Axial Frequency Shift by the Resonator

The measured axial frequency slightly shifts from coupling to the resonant circuit (Eq. 2.47). The resonant circuit's center frequency and parallel resistance are measured precisely from its driven resonance. Figure 4.33 shows the measured resonance of the detection circuit. The electron's axial frequency is 114.4365665 (1) MHz. The discrepancy of 20.585 (32) kHz causes an axial frequency shift of

$$\Delta\bar{\nu}_z = -0.8738\ (10)\ \text{Hz} \tag{4.76}$$

from its value if the resonator were not there.

This shift changes the axial frequency that we use to calculate the g-factor using Eq. 4.74. The shift and uncertainty on the g-factor is

$$\Delta\left(\frac{g}{2}\right) = -4.4\ (1) \times 10^{-15}. \tag{4.77}$$

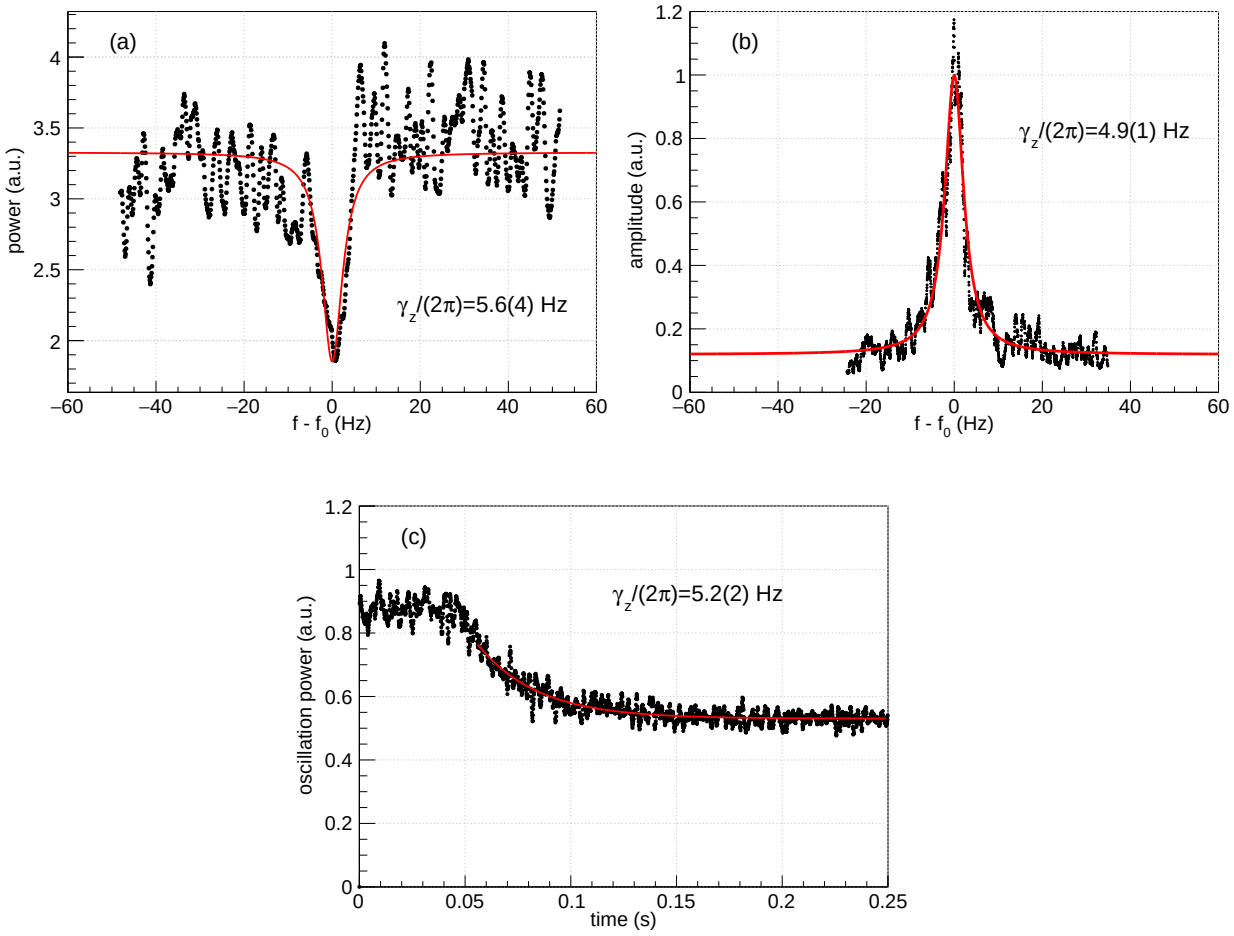


Figure 4.34: The axial damping rate γ_z measured in three different methods, (a) dip detection, (b) axial driven scan, and (c) free decay method.

4.4.5 Uncertainty of the Axial Damping Rate γ_z

The axial damping rate γ_z was not measured in the previous 2008 measurement [102]. We improved the stability of the apparatus and invented new methods to measure the axial damping rate γ_z in three ways. It can be measured from the width of the dip on noise resonance, the width of the axially driven response, and the decay constant of the largely excited motion. γ_z is a parameter that determines the fitting line. Uncertainty of γ_z causes uncertainty of fitting shape, and thus the extracted cyclotron and anomaly frequencies.

Figure 4.34 shows the three independently measured axial damping rate γ_z's. The damping rate is consistent among the three measurements. To be conservative, we take the

weighted mean of the three measurements as mean γ_z and assign the discrepancy among the three measurements as its one standard deviation uncertainty.

$$\frac{\gamma_z}{2\pi} = 5.0\ (4)\ \text{Hz} \tag{4.78}$$

We construct the fitting function using different γ_z's and extract the g-factor. The center value of the measured g-factor changes less than 3×10^{-15}, so the estimated systematic error is

$$\Delta\left(\frac{g}{2}\right) < 3 \times 10^{-15}. \tag{4.79}$$

4.4.6 Magnetic Field Drift

In the primary analysis, the magnetic field drift is corrected by the second-order polynomial function. The change of the result using different correction models is studied. Since both cyclotron frequency and anomaly frequency are proportional to the magnetic field, the drift of the magnetic field should not change the measured g-factor to the first order approximation.

To check the systematic shift related to magnetic field correction, the long-term drift is fit by the third and fourth order polynomial functions. The extracted g-factor is compared with the result using the second order drift correction function. By taking its largest discrepancy, the systematic error from drift correction is estimated to be

$$\Delta\left(\frac{g}{2}\right) < 9 \times 10^{-15}. \tag{4.80}$$

4.4.7 Fluctuation of Temperature

The magnetic field changes when the physical temperature of the trap changes. The dominant effect comes from the nuclear paramagnetism, which has a very large temperature dependence at low temperature [60].

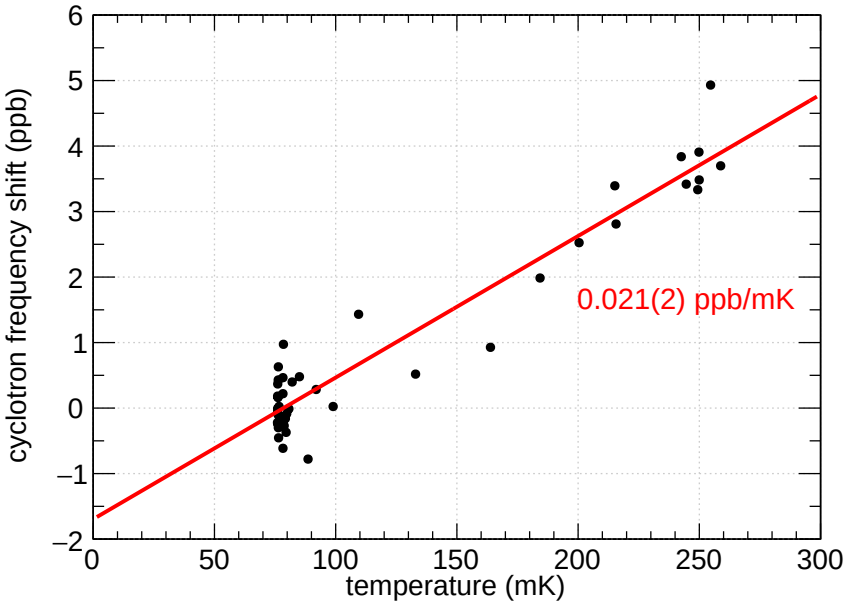


Figure 4.35: Dependence of cyclotron frequency on the temperature of trap can.

The temperature fluctuation during a measurement run is $\Delta T = 0.5$ mK at maximum during one run. The dependence of cyclotron frequency on trap temperature is measured as Fig. 4.35. The fluctuation of temperature should cancel to the first order because the ratio of cyclotron and anomaly frequency is measured. By calculating the change of magnetic field by 0.5 mK fluctuation and multiplying by $(g/2 - 1)$, the systematic error is

$$\Delta\left(\frac{g}{2}\right) < 12 \times 10^{-15}. \tag{4.81}$$

4.4.8 Line Shape Model of Residual Broadening

The anomaly linewidth agrees with the theoretical linewidth within its uncertainty, but the cyclotron linewidth is broader than the theoretical line shape. To extract the cyclotron frequency, we have constructed fitting lines with several noise models (Sec. 4.1). Figure 4.36 shows the dependence of the extracted g-factor on the three fitting models: 30 Hz sinusoidal

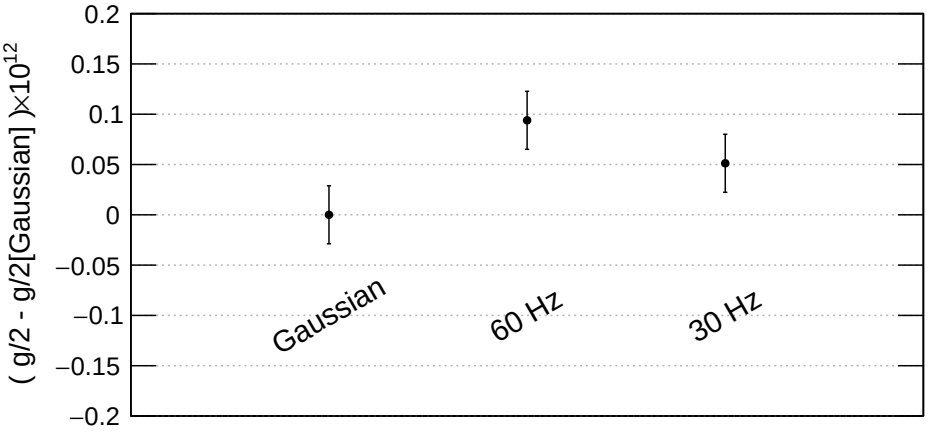


Figure 4.36: Dependence of g-factor on line shape model. The largest discrepancy among the three models is taken as the line shape systematic error. Notice that the models with no broadening and Lorentzian shape broadening have been rejected by the p-value test (Sec. 4.1).

noise, 60 Hz sinusoidal noise, and Gaussian shape noise. Notice that from the p-value argument in Sec. 4.1, the Lorentzian broadening model has been rejected. By taking the largest discrepancy among the three accepted models, we assign an uncertainty of

$$\Delta\left(\frac{g}{2}\right) < 0.094 \times 10^{-12}. \tag{4.82}$$

4.4.9 Higher-Order Correction from the Invariance Theorem

There are higher-order corrections from the invariance theorem. The expression for the free space cyclotron frequency ν_c from measured frequencies $\bar{\nu}_c$, $\bar{\nu}_z$, and $\bar{\nu}_m$ are

$$\frac{\nu_c}{\bar{\nu}_c} \approx 1 + \frac{1}{2}\left(\frac{\bar{\nu}_z}{\bar{\nu}_c}\right)^2 + \frac{1}{8}\left(\frac{\bar{\nu}_z}{\bar{\nu}_c}\right)^4 \left[\left(\frac{\bar{\nu}_m}{\bar{\nu}_z^2/(2\bar{\nu}_c)}\right)^2 - 1\right] \tag{4.83}$$

This expression is valid up to $(\bar{\nu}_z/\bar{\nu}_c)^6 \approx 10^{-19}$. The third term is the correction from the imperfection of the trap, which causes a mismatch of measured magnetron frequency $\bar{\nu}_m$ and the calculated magnetron frequency measured cyclotron and anomaly frequencies $\bar{\nu}_z^2/(2\bar{\nu}_c)$.

We measured these to be $\bar{\nu}_m = 43.835(1)$ kHz and $\bar{\nu}_z^2/(2\bar{\nu}_c) = 43.808$ kHz. Using these frequencies, the correction to the g-factor is

$$\Delta\left(\frac{g}{2}\right) = -5.3(2) \times 10^{-20}. \tag{4.84}$$

Therefore, this effect is negligible in the current precision.

4.5 Determination of g-factor

Table 4.7 summarizes the raw g-factor, statistical uncertainties, and shift from the microwave cavity effect. The microwave cavity effect has various sources, as listed in the table. For example, the z_{offset} of TE_{145} mainly affects the measurements at around 150 GHz. TM_{125} and TM_{133} overlap so well that it was impossible to identify the center frequencies precisely, so they add uncertainty to the measurements near 120 GHz. Among them, the uncertainty from the cavity modes' coupling strength λ_M^2 is the largest.

magnetic field (T)	3.108	4.071	4.078	4.245	4.537	4.969	5.001	5.269	5.300	5.326	5.373
frequency (GHz)	87.010	113.956	114.141	118.822	127.007	139.097	139.989	147.498	148.361	149.091	150.411
raw $g/2$ (10^{-12})	1.34(16)	−3.41(13)	−2.91(15)	2.27(15)	−3.21(12)	−1.84(9)	1.09(19)	−2.80(7)	−0.58(6)	0.83(7)	3.35(9)
correction (10^{-12})	−1.43(16)	2.86(17)	2.57(16)	−2.38(16)	3.41(27)	2.11(22)	−0.63(23)	2.96(23)	0.76(19)	−0.65(19)	−3.30(21)
source	uncertainty (10^{-12})										
uncertainty of λ_M^2	0.157	0.165	0.159	0.154	0.266	0.211	0.219	0.208	0.173	0.166	0.182
freq. uncertainty	0.009	0.019	0.017	0.018	0.043	0.030	0.053	0.039	0.018	0.014	0.026
$\omega_{\mathrm{TM}_{125}}$ and $\omega_{\mathrm{TM}_{133}}$	0.000	0.005	0.005	0.028	0.005	0.001	0.001	0.000	0.000	0.000	0.000
Q-factor	0.000	0.000	0.000	0.003	0.005	0.001	0.001	0.000	0.000	0.000	0.003
z_{offset} of TE_{145}	0.002	0.003	0.003	0.003	0.004	0.006	0.006	0.012	0.013	0.014	0.018
z_{offset} of TE_{136}	0.001	0.002	0.002	0.003	0.004	0.010	0.011	0.048	0.029	0.022	0.015
modes $>$ 160 GHz	0.021	0.027	0.028	0.030	0.034	0.048	0.050	0.075	0.080	0.085	0.097
modes $<$ 60 GHz	0.005	0.003	0.003	0.003	0.002	0.002	0.002	0.002	0.002	0.002	0.002

Table 4.7: Summary of measured $g/2 - 1.001\ 159\ 652\ 180\ 59$, microwave cavity correction and its dominant errors.

To extract the g-factor, the correlation of the uncertainties are considered. The uncertainty of microwave cavity correction comes from several different sources, such as calibration error, z_{offset}, the uncertainty of unmeasured modes, and uncertainty of λ_M^2. For example, the error from a mode near 150 GHz (e.g., TM_{127}) shifts all the measured g-factors at 147.498 GHz, 148.361 GHz, 149.901 GHz, and 150.411 GHz approximately the same amount. To estimate the correlation and uncertainty correctly, we construct the covariance matrix V_{ij} and the correlation matrix C_{ij}.

A covariance matrix for each uncertainty in Table. 4.7 is constructed, and they are summed.

$$V_{ij} = \sum_{k \in \{\text{all uncertainties}\}} \delta \left(\frac{g}{2}\right)_i^k \delta \left(\frac{g}{2}\right)_j^k, \tag{4.85}$$

where i and j represent the measurement at different fields (i.e. i and j runs for the 11 run numbers). The total covariance matrix is then normalized to get the correlation table

$$C_{ij} = \frac{V_{ij}}{\sqrt{V_{ii} V_{jj}}} \tag{4.86}$$

Figure 4.37 shows the constructed correlation matrix for the microwave cavity shift. One can see that the nearby modes have large correlations, for example, among the measurements around 150 GHz. One can also notice that two measurements across modes have a negative correlation. For example, the 4.245 T measurement and the 4.537 T measurement have a negative correlation. This is because they are across the modes at around 123 GHz—TM_{133}, TM_{125}, and TE_{141}. The correction of the g-factor from these modes is negative on the lower frequency side and positive on the higher frequency side. As a result, the two measurements have a negative correlation.

The error studied in Sec. 4.4 are mostly common to all measured fields: such as the line shape model, power shift, and determination of axial frequency. For example, the line shape model uncertainty have 100 % correlation among all measurements. This can also be treated by the covariance matrix method and added to the microwave shift covariance matrix. The

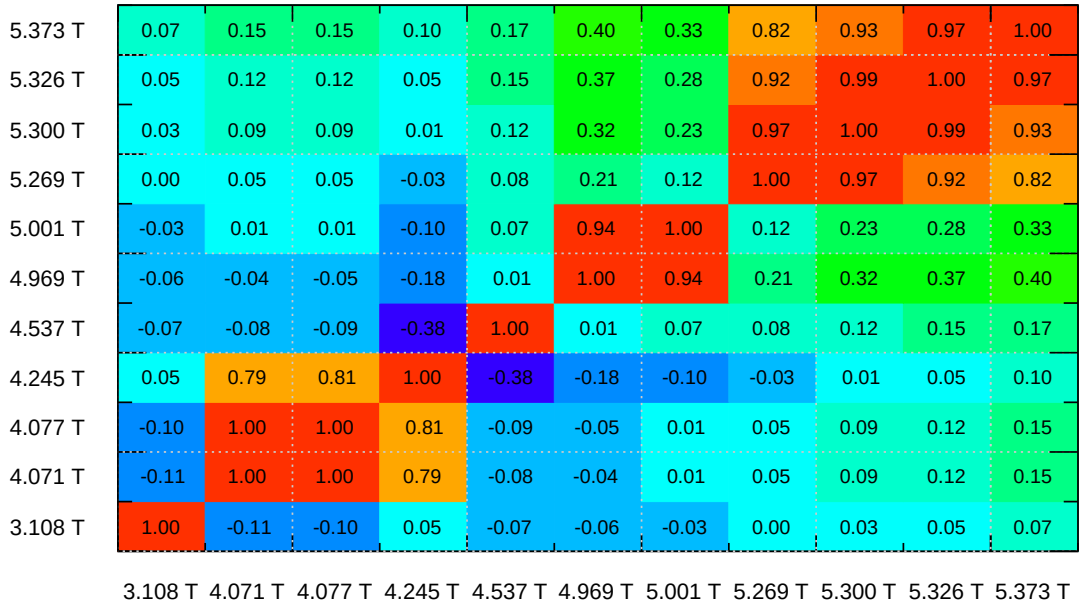


Figure 4.37: Correlation matrix C_{ij} of the microwave cavity correction uncertainty. Strong correlations among the measurements at nearby fields are visible.

common-mode uncertainties are summarized in Table. 4.8.

After constructing the total covariance matrix, we follow the standard procedure to obtain an average of the g-factor [105]. The weight for each measurement at i'th field is defined by the inverse of the covariance matrix

$$w_i = \frac{\sum_j (V^{-1})_{ij}}{\sum_{ij} (V^{-1})_{ij}}. \tag{4.87}$$

The average of the measured g-factor and its uncertainty are then given by

$$\begin{aligned} \frac{g}{2} &= \sum_i w_i \left(\frac{g}{2}\right)_i \\ \Delta\frac{g}{2} &= \left(\sum_{ij} (V^{-1})_{ij}\right)^{-1/2}, \end{aligned} \tag{4.88}$$

name	shift (10^{-12})	uncertainty (10^{-12})
statistical	—	0.029
microwave cavity correction	—	0.090
line shape model	0.000	0.094
cyclotron power shift	0.000	0.005
anomaly power shift	0.000	0.010
fluctuation of axial frequency	0.000	0.003
axial frequency shift by resonator	−0.004	0.000
uncertainty of axial damping rate	0.000	0.003
magnetic field drift	0.000	0.009
temperature fluctuation	0.000	0.012
correction from the invariance theorem	0.000	0.000
total	−0.004	0.134

Table 4.8: Summary of statistical and systematic uncertainties. The shift from microwave cavity correction depends on the field and is listed in Table. 4.7.

with its chi-square χ^2 given by

$$\chi^2 = \sum_{ij} \left\{ \left(\frac{g}{2}\right)_i - \frac{g}{2} \right\} \left(V^{-1}\right)_{ij} \left\{ \left(\frac{g}{2}\right)_j - \frac{g}{2} \right\} \tag{4.89}$$

The measured g-factor, with the correction and systematic error is shown in Fig. 4.38. The short error bars represent statistical uncertainty only, and the long error bars include the systematic uncertainties. The newly measured g-factor, including all the correlated and uncorrelated errors, is

$$\frac{g}{2} = 1.001\ 159\ 652\ 180\ 59\ (03)\ (13), \tag{4.90}$$

where the uncertainties are statistical uncertainty and systematic uncertainty, respectively. The χ^2/(ndf) of the measurements are 13.04/10, with p-value of $p = 0.22$. Using the result in Eq. 1.3 yields a new value of the fine structure constant

$$\alpha^{-1} = 137.035\ 999\ 166\ (16). \tag{4.91}$$

The electron's g-factor is measured in a wide range of magnetic fields for the first time.

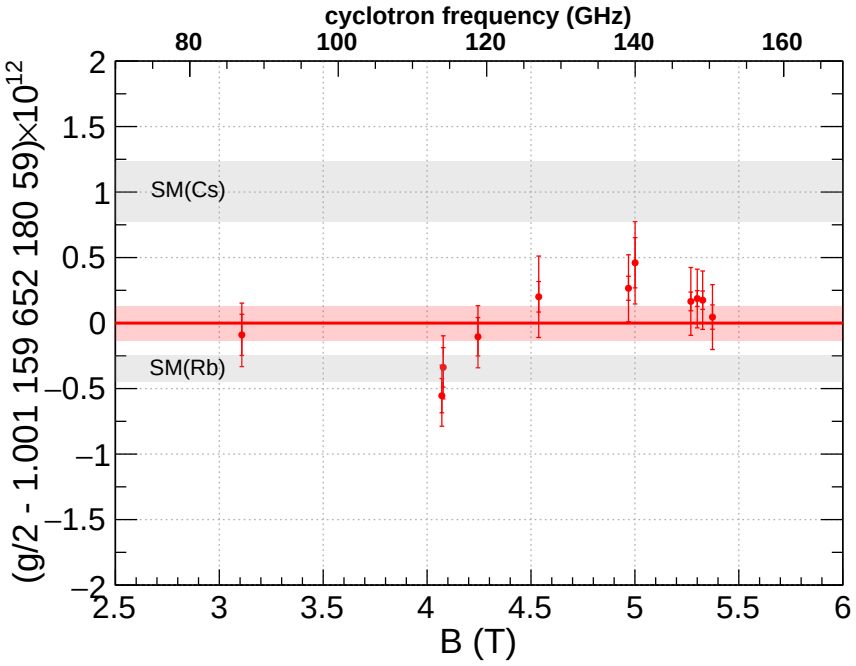


Figure 4.38: Measured g-factor as a function of the magnetic field. The short error bars represent statistical uncertainty only, and the long error bars include the systematic uncertainties. The SM predictions are also shown with the two gray bands.

The newly constructed system narrows the anomaly transition by a factor of 4. All techniques here can be applied to the positron's g-factor measurement. Despite all the efforts, further improvements are still possible. The following chapters discuss improvements and an application of the developed system for the dark matter search.

Chapter 5

Towards Relativistic Bottle Detection with a Quantum Limited Detector

We discuss possible future directions of the magnetic moment measurement. The linewidth is dominated by the magnetic bottle broadening

$$\Delta\omega_c = \frac{eB_2}{m}\frac{k_B T_z}{m\omega_z^2} \tag{5.1a}$$

$$\Delta\omega_a = \frac{g-2}{2}\frac{eB_2}{m}\frac{k_B T_z}{m\omega_z^2}. \tag{5.1b}$$

The expressions are the same except for the initial factor $(g-2)/2$[1]. To improve the precision of g-factor determination, the linewidth $\Delta\omega_c$ needs to be narrowed. We have seen the additional broadening, but the study of the broadening will also be easier if the magnetic bottle linewidth becomes narrower.

The parameters we have control are the magnetic bottle gradient B_2, the axial temperature T_z, and the axial frequency ω_z. In future measurements, T_z should be reduced as much as possible as it is independent of other parameters. However, ω_z and B_2 are correlated. B_2 should be made as small as possible, but it needs to be large enough that the axial frequency

[1]In this chapter we denote cyclotron frequency in the trap as ω_c for conciseness. The difference between using $\bar{\omega}_c$, ω_c' and ω_c is negligible.

shift for one quantum cyclotron jump $\delta_c = \hbar e B_2/m^2\omega_z$ is larger than the resolution of the axial frequency σ_{ω_z}

$$\delta_c \gg \sigma_{\omega_z}. \tag{5.2}$$

Higher ω_z is desired, but it is constrained as the Q-factor of the detection resonator drops sharply at higher frequencies. As a result, γ_z and σ_z also decrease at higher frequencies.

Reducing B_2 and increasing ω_z are both beneficial, as long as the condition Eq. 5.2 is satisfied. To run a long-term measurement, we require δ_c to be larger than σ_{ω_z} with a margin factor $\mathcal{C}$

$$\delta_c = \frac{\hbar e B_2}{m^2\omega_z} = \mathcal{C}\sigma_{\omega_z}. \tag{5.3}$$

Typically, a margin of $\mathcal{C} \approx 3$ is required. Then, the expression for bottle broadening becomes

$$\Delta\omega_c = \mathcal{C}\frac{k_B T_z}{\hbar\omega_z}\sigma_{\omega_z}. \tag{5.4}$$

Since the quality factor of the resonator depends on its frequency, σ_{ω_z} is also a function of ω_z. Therefore, it is difficult to characterize their relation quantitatively. Qualitatively, σ_{ω_z} gets worse when the quality factor of the detection circuit gets low. In the past, $\omega_z/(2\pi) =$ 200 MHz has been used at maximum. In this thesis, we chose $\omega_z/(2\pi) = 115$ MHz for better axial frequency resolution and reduced B_2 by a factor of 5.

To summarize, in order to reduce the linewidth $\Delta\omega_c$, one has to

- Reduce magnetic bottle B_2 as much as possible. Our goal is to reduce B_2 to 0 to use the relativistic bottle effect (Sec. 5.1). Although this requires a much improved axial frequency resolution σ_{ω_z}, we propose two new schemes to improve σ_{ω_z}: a new trap with $C_6 = 0$ (Sec. 5.2) and using spin-flip transition instead of cyclotron transition (Sec. 5.3)

- Reduce axial temperature T_z as much as possible. Lower axial temperature directly narrows the linewidth. We have developed a new quantum limited detector with Superconducting Quantum Interference Device (SQUID) to replace the traditional

HEMT amplifier to achieve this (Sec. 5.4).

In this chapter, we propose a new experimental scheme that uses a relativistic bottle with a newly developed SQUID detector. The other concerns are also addressed in Sec. 5.5

5.1 Relativistic Bottle

The magnetic bottle causes axial frequency shift for one cyclotron jump, $\delta_c = \hbar e B_2/m^2\omega_z$. However, as we have seen, this also induces frequency broadening $\Delta\omega_c$. A long ambition in electron's magnetic moment experiment [54, 106, 107] is to eliminate the magnetic bottle completely and to use relativistic mass increase to detect one quantum jump.

One cyclotron transition increases the energy of the electron by $\hbar\omega_c$. This energy increase causes a shift in the effective mass of the electron due to the relativistic effect $m \to m + \hbar\omega_c/c^2$. Since the axial frequency depends on the mass $\omega_z \propto m^{-1/2}$, the increase of mass changes axial frequency by

$$\delta_{rel} \equiv -\frac{\hbar\omega_c}{2mc^2}\omega_z. \tag{5.5}$$

The relativistic shift δ_{rel} is very similar to the physical magnetic bottle B_2. It is effectively a magnetic bottle with

$$B_{2;rel} = -\frac{m\omega_z^2\omega_c}{2ec^2}. \tag{5.6}$$

Our measurement parameters $\omega_z/(2\pi) = 115$ MHz and $\omega_c/(2\pi) = 150$ GHz yield $\delta_{rel}/(2\pi) = -0.07$ Hz and $B_{2;rel} = -15$ T/m^2. This value is about 20 times smaller than the current axial frequency shift δ_c in this thesis. Therefore, 20 times better axial frequency resolution is required. In the following sections, two new ideas are proposed to achieve this regime.

5.2 Orthogonalized and Compensated $C_6 = 0$ Trap

The axial frequency is measured using the self-excitation of the trapped electron (Sec. 2.3). Its fluctuation is determined by the trap's anharmonicity, coupled with fluctuation of the

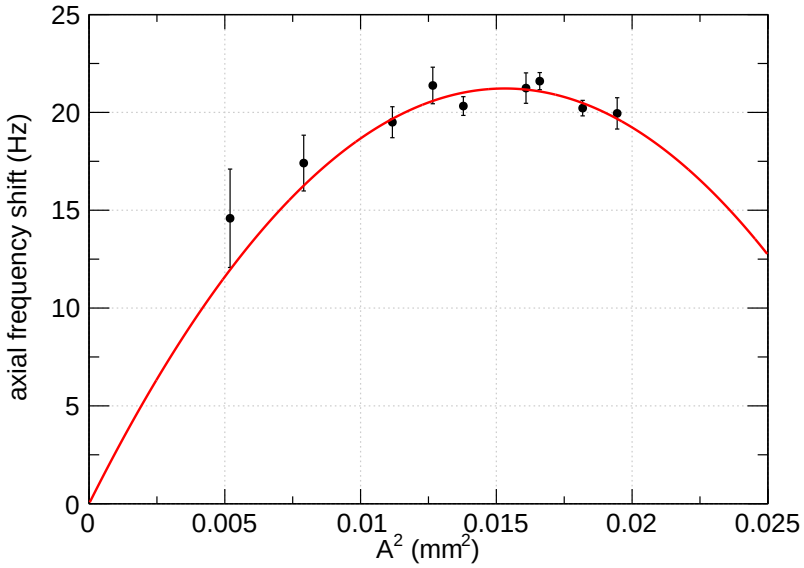


Figure 5.1: Dependence of self-excitation frequency on oscillation amplitude [67]. The error bar is the RMS scattering of the frequency at each amplitude.

axial oscillation amplitude. The amplitude dependence of axial frequency follows the anharmonicity of the trap

$$\omega_z(A^2) = \omega_z \left[1 + \frac{3C_4}{4(1+C_2)} \frac{A^2}{d^2} + \frac{15C_6}{16(1+C_2)} \left(\frac{A^2}{d^2} \right)^2 \right] \tag{5.7}$$

Fig. 5.1 shows the measured axial frequency dependence. Excitation amplitude is tuned so that it comes to the flat top of the curve.

At its optimal $d\omega_z(A^2)/dA^2 = 0$, the fluctuation of oscillation amplitude σ_{A^2} results in the fluctuation of axial frequency as

$$\Delta\omega_z = \omega_z \frac{15C_6}{16(1+C_2)d^4} \left(\sigma_{A^2}\right)^2 . \tag{5.8}$$

σ_A^2 can arise, for example, from axial temperature or T_z, fluctuation of gain of amplification chain, imperfection of amplitude limiting device (DSP) [64]. We design a new trap geometry that achieves smaller C_6.

There are three parameters when designing a five-electrode cylindrical trap, ρ_0, z_0, and

z_c. The electrostatic properties are determined by their relative dimensions, so we take z_0, ρ_0/z_0, and z_c/z_0 as three independent parameters. The trap height z_0 only changes the relative size of the trap, but not its electrostatic property (in a relative scale). Therefore the anharmonicity is determined by two parameters ρ_0/z_0 and z_c/z_0.

First, for a given ρ_0/z_0, Eq. 2.33 and Eq. 2.34 are used to find the ratio z_c/z_0 that D_2/D_4 vanishes. This yields the orthogonality condition that C_4 can be changed without changing the axial frequency [59]. Figure 5.2 shows the required z_c/z_0 to make $D_2/D_4 = 0$ for given ρ_0/z_0. The voltage ratio V_c/V_R to achieve $C_4 = 0$ is also shown.

Now we have one constraint that relates z_c/z_0 to ρ_0/z_0. We can still adjust ρ_0/z_0 without breaking the $D_2/D_4 = 0$ condition. For each ρ_0/z_0, z_c/z_0 and V_c/V_R are determined from Fig. 5.2, and then C_6 with the orthogonal condition is calculated. Figure 5.3 shows that we can get both $C_4 = 0$ and $C_6 = 0$ at $\rho_0/z_0 = 0.9684$, $z_c/z_0 = 0.6888$, and $V_c/V_R = 0.7992$.

How small C_6 we can realize depends on machining tolerance and imperfection of the trap. To estimate the realistic value of C_6, we use $z_0 = 2540$ μm (we will see that this gives a suitable microwave cavity structure), vary each trap geometry by 25 μm, four times larger than the machining tolerance, and calculate C_6 again. By calculating C_6 with 25 μm tolerance, we estimate that the achievable C_6 is

$$|C_6| < 4.6 \times 10^{-3}, \tag{5.9}$$

which is still a factor of 20 smaller than the C_6 of the current trap ($C_6 = -0.1$). The dominant anharmonicity axial fluctuation (Eq. 5.8) will be reduced by a factor of 20.

Now we have fixed z_c/z_0 and ρ_0/z_0. The remaining question is whether we can get a good microwave cavity structure. The only free parameter now is z_0, which only changes the size of the cavity, but not the relative dimension. The distribution of the microwave cavity modes cannot be changed, but its frequency scale is still variable.

A smaller trap is better for the microwave cavity structure. Practically, the smallest

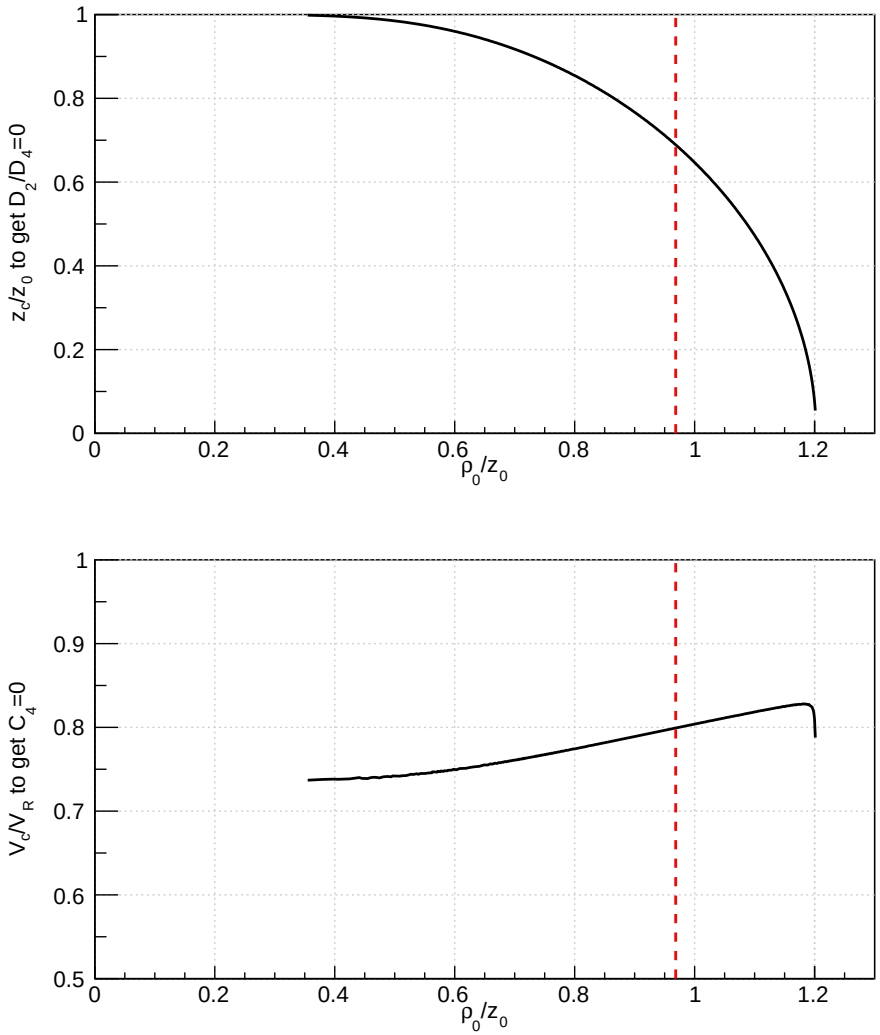


Figure 5.2: z_c/z_0 to make $D_2/D_4 = 0$ for given ρ_0/z_0. The voltage ratio V_c/V_R to get $C_4 = 0$ is also shown. The ideal ρ_0/z_0 to get $C_6 = 0$ is shown by the red dotted line (derived later).

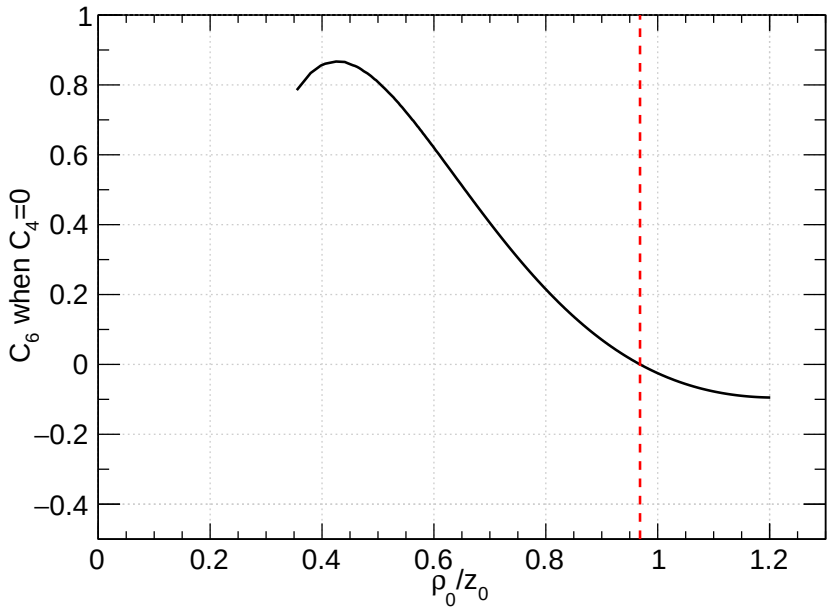


Figure 5.3: C_6 for given ρ_0/z_0. For a given ρ_0/z_0, the compensation electrode's length z_c/z_0 and the voltage ratio V_c/V_R are determined from Fig. 5.2. The ideal ρ_0/z_0 to get $C_6 = 0$ is shown by the red dotted line.

possible size is limited by the machining capabilities. In the current trap, the smallest dimension is the height of the compensation electrode, 766 μm. The smallest dimension in the $C_6 = 0$ trap is the height of the ring electrode $z_R = 2(z_0 - z_c) \approx 0.6224 z_0$. For a realistic assumption, we set half of the trap height to be $z_0 = 2540$ μm. The height of z_c and z_R with this condition are 1750 μm and 1579 μm, respectively, and is still two times larger than the current trap. The trap dimension in this condition is summarized in Table 5.1.

Figure 5.4 shows the microwave resonance structure for a z_0=2540 μm cavity as an example. The red lines are the resonant modes that strongly couples to the electron at the center (TE_{mnp} mode or TM_{mnp} mode with $m = 1$ and p-odd). The blue lines are the modes that have z-node at the center (TE_{mnp} mode or TM_{mnp} mode with $m = 1$ and p-even). With this geometry, there are many attractive regions for a g-factor measurement. Notice that the interval is much larger than the trap used in this thesis (Chap. 4). The larger spacing is because of the reduced trap size, which is possible because of the longer compensation electrode length z_c.

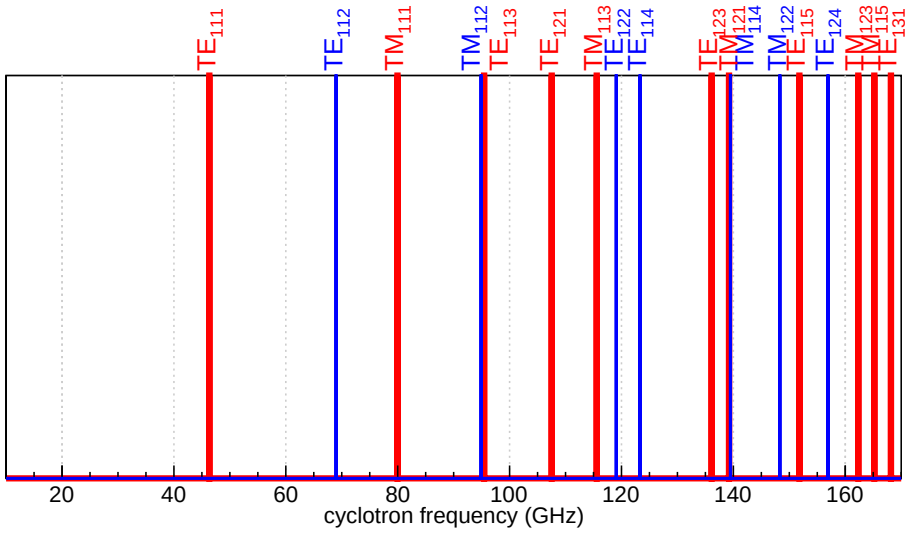


Figure 5.4: Microwave resonant modes of the newly designed $C_6 = 0$ trap. A trap height of $z_0 = 2540$ μm is assumed. Red lines are the strong coupling modes to the electron at the center, and blue lines are the modes that have a node at the trap center.

The systematic uncertainty for g-factor measurement scales as

$$\Delta\frac{g}{2}|_{\rm cav} \propto (\text{interval of modes})^{-1} \propto (\text{trap size}) \tag{5.10}$$

The newly designed trap is about 40 % smaller than the trap used in this thesis (Chap. 2). Additionally, by going to the lower cyclotron frequency, the spacing between the modes becomes significantly larger than in the current measurement (12 GHz at maximum). More than a factor of 3 reduction of systematic uncertainty from the microwave cavity correction is expected.

Table 5.1 summarizes the trap parameters for the $C_6 = 0$ trap. All parameters are promising, and we should be able to get 20 times better anharmonicity and 3 times smaller microwave cavity correction.

parameter	value
half of trap height: z_0	2540 μm
trap radius: ρ_0	2460 μm
height of compensation electrode: z_c	1750 μm
height of ring electrode: z_R	1579 μm
trap length parameter: d	2177 μm
image charge parameter: c_1	0.630
asymmetry parameter: c_3	0.492
optimal voltage ratio: V_c/V_R	0.7992

parameter	value	parameter	value at $V_c/V_R = 0.7992$
C_2^0 D_2	0.046 0.000	C_2	0.046
C_4^0 D_4	-0.258 -0.863	C_4	0
C_6^0 D_6	0.147 0.490	C_6	0
C_8^0 D_8	-0.074 -0.109	C_8	-0.042

Table 5.1: Designed parameters for the $C_6 = 0$ trap.

5.3 Directly Driven Spin Flip

Even with the same amplitude of axial frequency fluctuation, the resolution can be increased by averaging for a longer time. The averaging time is currently limited by the cyclotron lifetime τ_c = 5–10 s. This limit can be avoided if we measure spin frequency ω_s instead of cyclotron frequency. The g-factor can be obtained similarly with a slightly different expression

$$\frac{g}{2} = \frac{\nu_s}{\nu_c} = \frac{\nu_s}{\nu_s - \nu_a} = \left(1 - \frac{\nu_a}{\nu_s}\right)^{-1} = \left(1 - \frac{\bar{\nu}_a - \frac{\bar{\nu}_z^2}{2(\bar{\nu}_s - \bar{\nu}_a)}}{\bar{\nu}_s + \frac{1}{2}\frac{\delta_r}{2\pi}}\right)^{-1} + \Delta\frac{g}{2}|_{\text{cav}}, \tag{5.11}$$

where $\delta_r/2\pi = \hbar\nu_c^2/mc^2$ is the relativistic cyclotron frequency shift (Eq. 4.5), and the quantities with bar are the measured quantities.

The largest challenge is to drive the spin-flip transition directly. The Rabi frequency for

the spin-flip is smaller by

$$\frac{\Omega_s}{\Omega_c} = 3 \times 10^{-5}. \tag{5.12}$$

Therefore, being able to drive the spin transition without heating the trap is not trivial. In this section, the directly driven spin-flip is demonstrated, and the heating from the spin-flip drive is measured.

5.3.1 Observation of Directly Driven Spin Flip

Spin-flips by directly applied microwave drive are achieved. The same microwave drive source as in Chap. 2 is used, but with about 100 dB higher drive power. The cyclotron frequency is set at 148.047 GHz, where the cyclotron lifetime is $\tau_c = 7.2$ (2) s. This is far from any of the microwave resonances, and thus the correction is small enough to perform g-factor measurement.

Figure 5.5 shows the measured axial frequency shift after applying a resonant spin-flip drive. A strong spin-flip drive is applied between each point, and the axial frequency is measured after 60 seconds. An averaging time of 16 seconds is used to determine the axial frequency shift. Clear jumps in the axial frequency are only visible when the drive is resonant. The clear resolution of quantum jump demonstrates that reduction of bottle size is possible with a longer averaging time.

The spin resonance can be measured similarly to the cyclotron resonance. The drive frequency is swept and the probability of make a transition is measured (Fig. 5.6). The lineshape fits well with the theoretical line convoluted with Gaussian broadening, which is also observed in the cyclotron line (Chap. 4). Although unfortunate, observation of the same broadening implies that the cyclotron and spin transitions are consistent.

The temperature increase by the spin-flip drive is also measured. The HEMT amplifier is turned off to let the pinbase reach about 32 mK. The temperature increase of the pinbase is monitored when a strong drive is applied (Fig. 5.7). The drive power that corresponds to

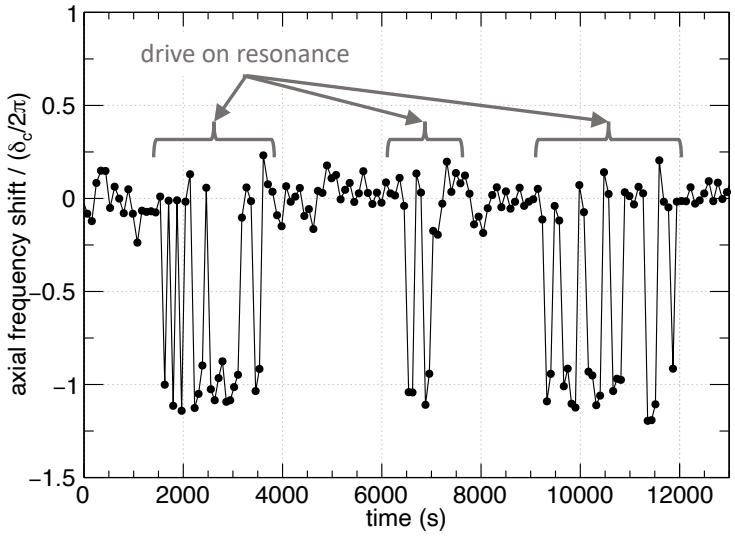


Figure 5.5: Observation of directly driven spin-flip transition. Between each point, resonant drives are applied during the time indicated by the arrows, and off-resonance drives are applied elsewhere. The axial frequency is measured with an averaging time of 16 seconds.

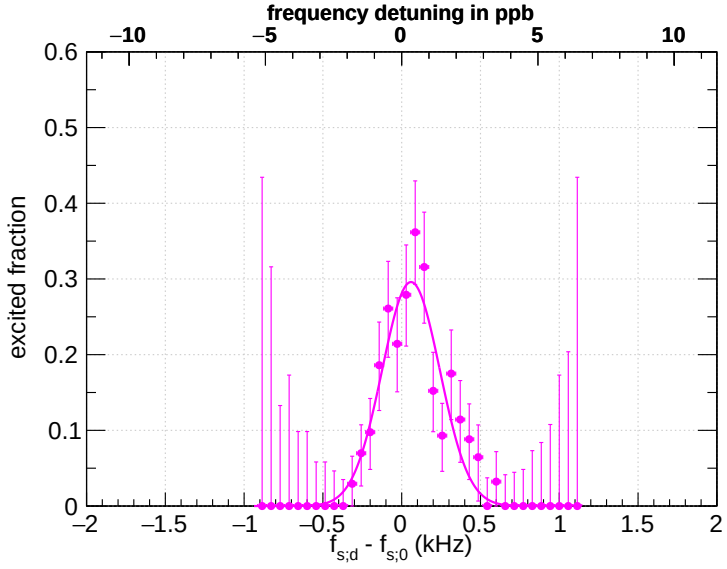


Figure 5.6: Measured lineshape of the spin-flip transition.

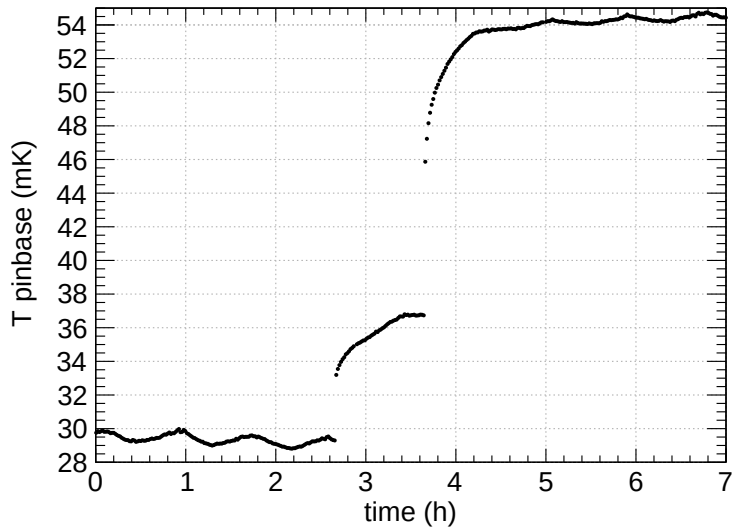


Figure 5.7: Temperature increase of pinbase by spin-flip drives. A drive power that can induce 30 % transition probability is applied first, then a 10 times stronger drive is applied later. The increase that corresponds to the first step implies a heat load of 2.5 μW.

30 % of transition probability is first applied, and then a ten times stronger drive is applied. The heating from the first drive is estimated to be 2.5 μW using the cooling curve of the dilution refrigerator. The heating is much lower than the power dissipation of the amplifier and can be made significantly better with a dedicated microwave guide.

Averaging Time and Axial Frequency Resolution

Longer averaging time helps only if the drift of axial frequency is small. We measure the axial frequency resolution as a function of averaging time. The shift of axial frequency between successive two measurements

$$\Delta\nu_z = \nu_{z;i+1} - \nu_{z;i} \tag{5.13}$$

is recorded for different averaging times. Measurement of $\Delta\nu_z$ is sequentially repeated to construct a histogram. The histogram is fitted by a Gaussian function to obtain its 1σ standard deviation. Measured histograms with three different time constants are shown in

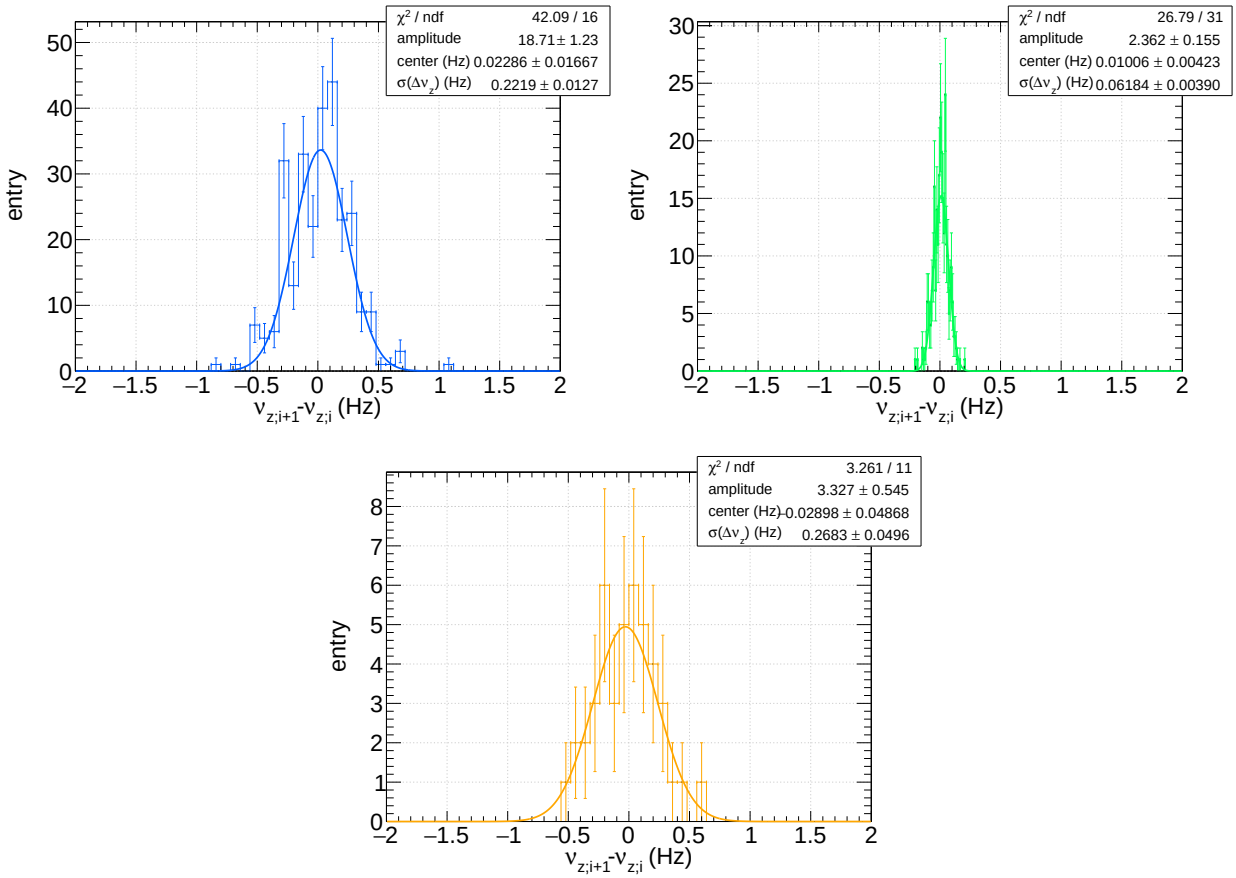


Figure 5.8: Measure axial frequency stability for averaging time of 2 s (blue), 64 s (green), and 1024 s (orange).

Fig. 5.8. As can be seen, the scatter of axial frequency $\Delta\nu_z$ depends on the averaging time and is the best with 64 s among the three histograms.

The axial frequency stability for a wider range of averaging time is shown in Fig. 5.9. Each point corresponds to the fitted 1σ width in Fig. 5.8. The relativistic shift $|\delta_{rel}/(2\pi)| = 0.07$ Hz is shown with the red line. With the current apparatus, the relativistic shift regime is barely reachable, with a margin of only about 1.7. About 3σ of margin is required to make a stable measurement of g-factor. The gain from $C_6 = 0$ trap can lower the $t_{\rm ave}^{-0.5}$ line. These two improvements will make the relativistic detection possible.

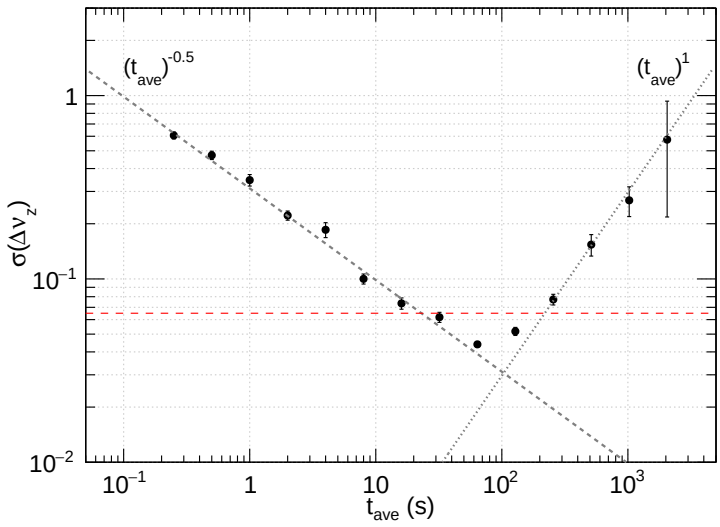


Figure 5.9: Measured axial frequency fluctuation $\sigma(\Delta\nu_z)$ for different averaging times. The short time range is dominated by random scatter, and the long time range is dominated by the drift from the bias voltage supply. The relativistic bottle size $\delta_{rel}/(2\pi)$ is shown by the red dashed line.

5.4 Quantum Limited Detector With a New Magnet

Reducing T_z will narrow the linewidth $\Delta\omega_c$ directly. In the current measurement, the axial temperature T_z is limited by the used HEMT amplifier. The dilution refrigerator can reach 25 mK if the amplifier is off, but the temperature increases to 80 mK when the amplifier is on. Additionally, heating of electron's T_z depending on the bias power is observed. Therefore, the HEMT amplifier must be replaced to achieve lower T_z.

We have developed a new quantum limited detector to achieve lower T_z. The detector is based on a Superconducting Quantum Interference Device (SQUID). A SQUID is a very sensitive magnetic field sensor, having sensitivity at a level of $\sim$fT/$\sqrt{\text{Hz}}$. It is so sensitive that it can be used as an amplifier of an electric signal by detecting the induced magnetic field. Moreover, we employ a SQUID with a resonant input coupling coil, called Microstrip SQUID amplifier (MSA), which can operate in the RF range. The typical bias power of the HEMT amplifier is about 50 μW. An MSA can achieve the same gain with about 1 nW of bias power.

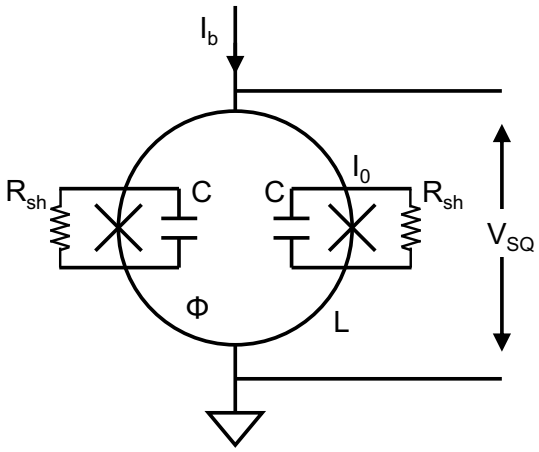


Figure 5.10: The schematics of a DC SQUID.

5.4.1 Superconducting Quantum Interference Device

A SQUID consists of two Josephson junctions connected in parallel (Fig. 5.10). Each junction has a parasitic capacitance C and is shunted by a resistor $R_{\rm sh}$. The SQUID loop has a geometrical inductance of L. When it is biased by a constant current $I_{\rm b}$, the voltage drop across the loop is a periodic function of the magnetic flux through the loop Φ

$$V_{\rm SQ} = R_{\rm sh}\sqrt{I_{\rm b}^2 - 4I_0^2\cos^2\left(\frac{\pi\Phi}{\Phi_0}\right)}, \tag{5.14}$$

where $\Phi_0 = h/2e = 2\times10^{-15}$ T/m^2 is the flux quantum.

In the typical operation parameter, $I_b = 2I_0$ and $\Phi = \frac{2n+1}{4}\Phi_0$, the sensitivity to flux change is

$$\left|\frac{dV_{\rm SQ}}{d\Phi}\right| = \sqrt{2}\frac{\pi R_{\rm sh}I_0}{\Phi_0} \tag{5.15}$$

For example, with $R_{\rm sh} = 10\ \Omega$ and $I_0 = 10\ \mu$A, the slope is $dV/d\Phi = 2\times10^{11}$ V/(Tm^2). This estimate illustrates the SQUID's sensitivity if flux is efficiently coupled to its loop. The concept of the MSA is to couple the magnetic field from RF input current to the SQUID loop by a resonant coil and detect the output voltage $V_{\rm SQ}$.

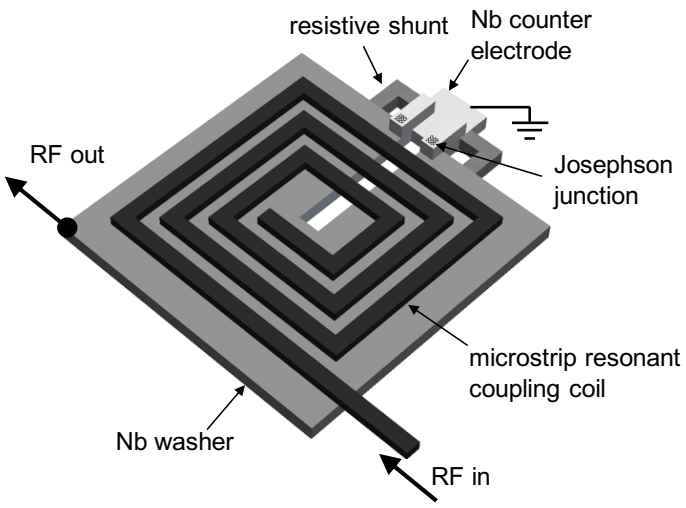


Figure 5.11: Schematic diagram of a microstrip SQUID amplifier.

5.4.2 Microstrip SQUID Amplifier

In traditional DC SQUIDs, the input current is coupled to the SQUID loop by winding coils on top of the loop. The current flowing through the loop generates magnetic flux through the loop. This coupling works well at low frequencies below a few 10 MHz, but the gain drops significantly at higher frequencies because of the capacitive coupling between the input coil and the SQUID washer [108].

An alternative approach to operate at higher frequencies is to feed the input signal from one end and leave the other end open. The inductance and capacitance of the input coil and SQUID plane form a resonant circuit. When the microstrip line's length is equal to half of the input signal's wavelength $\lambda/2$, resonance is formed and the SQUID has a high gain. This coupling scheme and the resulting amplifier is called microstrip SQUID amplifier, MSA (Fig. 5.11) [109].

MSA is known to have gain higher than 20 dB up to a few GHz. The noise temperature is typically below the ambient physical temperature and limited by the standard quantum-limited (SQL) at high frequency. The standard quantum limited temperature at 200 MHz

is

$$T_{\mathrm{SQL}} = \frac{\hbar\omega_z}{k_{\mathrm{B}}} = 9.6\ \mathrm{mK} \times \frac{\omega_z/(2\pi)}{200\ \mathrm{MHz}}. \tag{5.16}$$

Our ambient temperature is 25 mK, very close to the SQL temperature.

Our MSA is fabricated by ez-SQUID [110]. The microstrip SQUID amplifier has been mainly used at higher frequencies [109, 111–113]. Our MSAs are designed for the trapped electron's axial frequency $\omega_z/2\pi = 100$–200 MHz. We test an MSA optimized for 230 MHz operation. Figure 5.11 shows the schematics of the MSA. It consists of a dc SQUID and a microstrip resonant input coupling circuit resonant at around 200 MHz. The SQUID consists of a niobium washer, Josephson junctions, resistive shunts, and a niobium counter electrode. The washer is made of 600 μm $\times$ 600 μm niobium on an oxidized silicon substrate. It has a slit with width of $d = 10$ μm and length of $l = 300$ μm to form a SQUID loop. The Josephson junctions are made of about 3 $\mu\mathrm{m}^2$ of Nb-Al-$\mathrm{Al}_x\mathrm{O}_y$-Nb with a critical current of about $I_0 = 10$ μA. Each junction is shunted by a resistor $R_{\mathrm{sh}} = 10\ \Omega$ made by palladium. The other side of the junction and the shunt is connected to a grounded niobium counter electrode. The inductance of the SQUID loop is estimated to be $L_{\mathrm{SQUID}} = 100$ pH based on [114].

An RF signal is coupled to the SQUID by a niobium microstrip resonator printed on the SQUID washer (Fig. 5.11). The microstrip line and the SQUID washer are insulated by $t = 300$ nm of SiO, whose permittivity is $\epsilon/\epsilon_0 \approx 5$. The microstrip line has spacing and width of both 5 μm and is wound for $N = 33$ turns. The end of the microstrip line is left open to form a resonant circuit. The microstrip line's distributed inductance and the capacitance between the SQUID washer form a resonant circuit at around 200 MHz.

The RF output signal is coupled through a large capacitor. The Josephson junctions are biased by a constant current source with a low pass filter. A flux bias coil is also placed beneath the SQUID washer to adjust DC flux Φ through SQUID. These DC and RF filters and bias coils are designed not to affect each other.

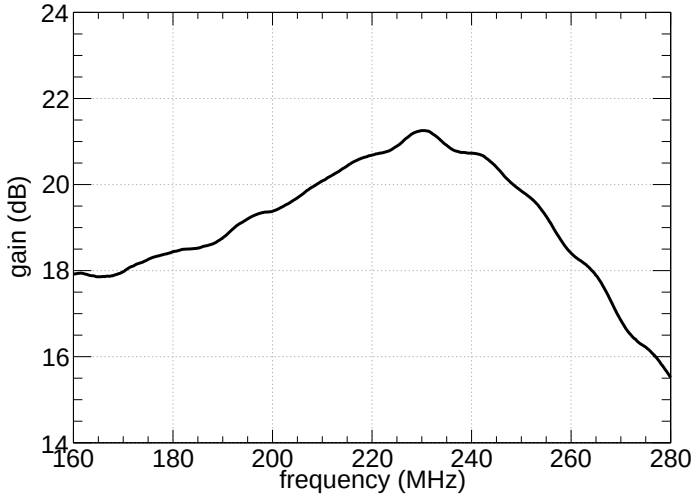


Figure 5.12: The gain of our fabricated microstrip SQUID amplifier. $I_b = 11$ μA and $P_{\rm in} = -120$ dBm.

Power Gain

The first figure of merit of the MSA is its power gain. A power gain of more than 20 dB is desired to replace the HEMT. The input and output impedance are close to 50 Ω, so we measure the power gain with the standard 50 Ω cables. Figure 5.12 shows the measured gain of the fabricated MSA. As designed, our SQUID has a maximum gain higher than 20 dB at around 230 MHz. The axial oscillation frequency can be tuned to this maximum frequency. The bias current is only $I_b = 11$ μA, which corresponds to a power dissipation of $I_b^2 R_{\rm sh} = 1.2$ nW.

Noise Temperature

The theoretical noise temperature of MSA is about half of the bath temperature (25 mK) [109]. The quantum-limited temperature $T_Q = \hbar\omega/k_{\rm B}$ at 200 MHz is about 10 mK, so comparable with the expected noise temperature.

We measure the noise temperature of the MSA at 3.6 K with a pulse tube refrigerator. The noise temperature can be measured from the detected noise power on a spectrum analyzer. The noise temperature of the following stage amplifiers is designed to be negligible.

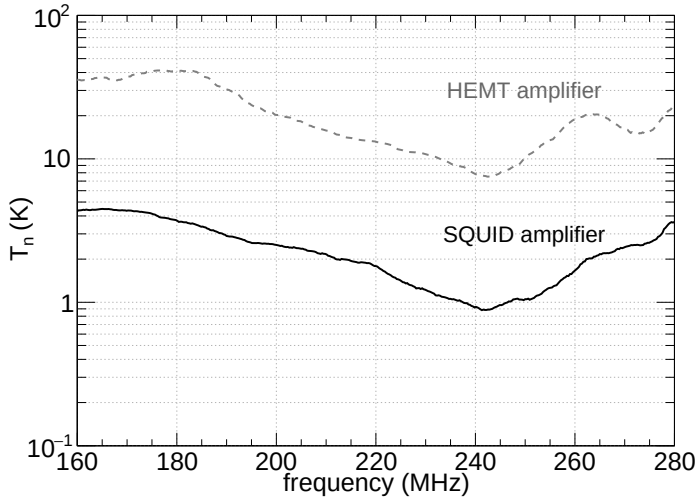


Figure 5.13: Measured noise temperature of the MSA at 3.6 K. The conventional HEMT amplifier used for the best measurement [7] is also shown.

Therefore, the noise temperature T_n of the MSA is measured by

$$T_n = \frac{P^{\text{on}} - P^{\text{off}}}{G_{\text{tot}}} - T_{\text{load}}, \tag{5.17}$$

where P^{on} and P^{off} are the measured power on the spectrum analyzer when the MSA is biased on and off, respectively, G_{tot} is the total gain of the MSA and its following stage amplifiers including the losses, and T_{load} is the Johnson noise temperature of the SQUID input load.

The noise temperature of the MSA is measured as in Fig. 5.13. The noise temperature of the conventional HEMT amplifier used in the current measurement is also measured and shown. The MSA has the lowest noise temperature of about 0.8 K at its resonant frequency. Compared to the conventional HEMT amplifier, the SQUID amplifier will reduce the noise temperature by about a factor of 10 even with an operation temperature of 3.6 K. The noise temperature will be lower by about another factor of 10 when cooled below 100 mK by a dilution refrigerator.

Saturation Input Power

The SQUID output voltage responds linearly only near its operation point $\Phi = \Phi_0 \left(\frac{2n+1}{4}\right)$. If the magnetic field modulation from the input RF coupling coil is too large, the SQUID will be out of the linear response range, and the gain will decrease dramatically. Figure 5.14 shows the peak gain of the MSA for different RF input power. The gain at its resonant frequency of 230 MHz is taken at each input power. The gain drops rapidly at around -105 dBm input.

The electron in the Penning trap is sometimes driven very strongly to characterize its behavior. Especially when a self-excitation scheme is applied, the electron has a peak-to-peak amplitude of 1 mm [67]. The induced power from the electron can be calculated based on the geometry of the trap and electronics to be -140 dBm [54], as in Fig. 5.14, thus much lower than the saturation threshold.

When the electron is not driven by an external drive, the signal from the Penning trap is much smaller. The only input power is the Johnson noise from the detection resonator at 25 mK, whose bandwidth is typically 0.3 MHz [51]. The input power can be calculated from the well-known Johnson noise $P = k_{\mathrm{B}} T \Delta f$ and is only about -160 dBm, again much smaller than the saturation threshold.

Impedance Matching to the Single Electron

One of the most challenging part is to couple the MSA to the Penning trap. Conventionally, the first stage amplifier is placed as close as possible to the Penning trap to avoid additional RF losses. The MSA must be placed about 50 cm away from the trap to operate in a low magnetic field (Sec. 5.4.3). Therefore, we implement a new RF impedance matching circuit and couple the electron's signal to the amplifier.

Figure 5.15 shows the equivalent RF electronics diagram of the Penning trap. Typically, the electrode has a parasitic capacitance of about $C_{\mathrm{p}} = 8.2$ pF. A tune-out inductor $L = L_1 + L_2 = 80$ nH is attached in parallel so that their impedance at $\omega_z/2\pi \approx 200$ MHz

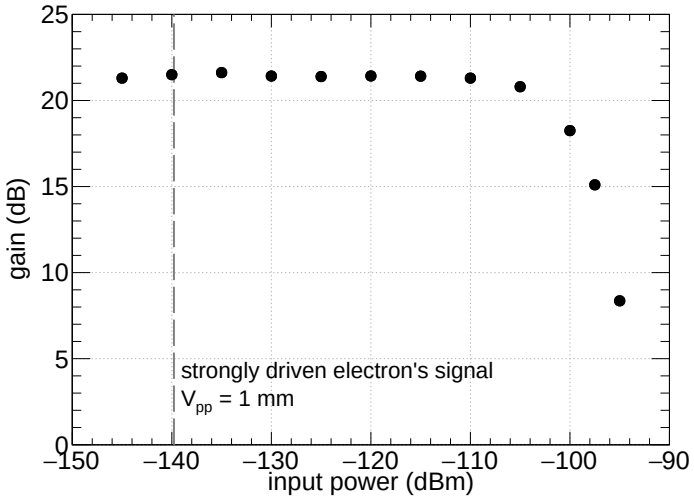


Figure 5.14: Measurement of saturation of the MSA gain. The gain at the resonant frequency is measured for different input power P_{in}. The signal from a strongly driven electron is also shown [67].

cancel each other. The effective parallel resistance between the electrodes at resonance is approximately $R_{\text{eff}} = 60$ kΩ at 230 MHz. This value is made to be as high as possible. At its resonant frequency, the resonator is effectively represented as a power source with an output impedance of R_{eff}.

The signal needs to be efficiently transferred to the MSA at about 50 cm away. For flexibility, we use a conventional 50 Ω coaxial cable to transmit the signal. RF impedance matching was achieved by two stages tap scheme; the inductive tap L_1 and L_2 and capacitive

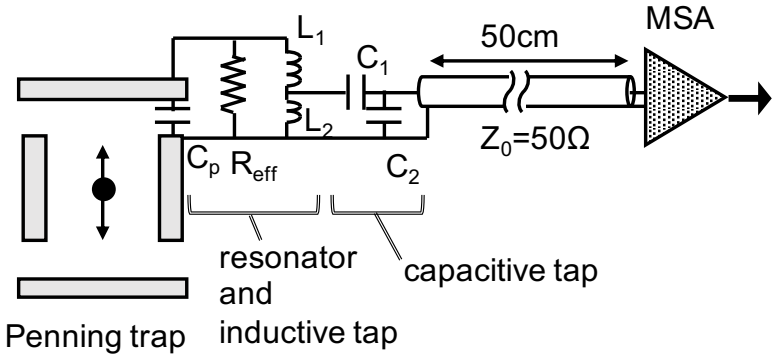


Figure 5.15: RF electronics to detect and impedance match the particle to the MSA amplifier.

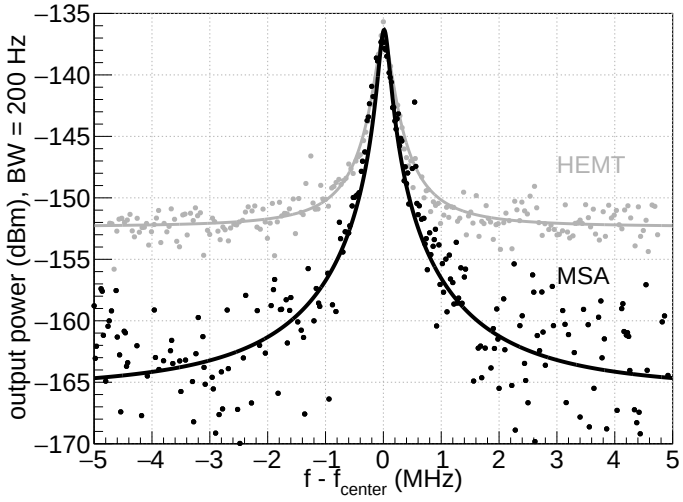


Figure 5.16: Noise resonance observed with the MSA compared to HEMT amplifier.

tap C_1 and C_2. They are designed so that each can be treated as an independent tap-down scheme near the frequency of interest. The inductor is tapped at $L_1 = 60$ nH and $L_2 = 20$ nH, and the capacitors are $C_1 = 2.0$ pF and $C_2 = 20$ pF respectively. Theoretically, the net transformed impedance of the resonator is

$$R_{\text{eff}} \left(\frac{L_2}{L_1 + L_2} \right)^2 \left(\frac{C_1}{C_1 + C_2} \right)^2 \approx 31\ \Omega. \tag{5.18}$$

Since the particle's dip width is also proportional to the effective parallel resistance, the amplifier is undercoupled to keep the particle's dip width large enough to be observed. In the actual experiment, the value of C_2 is adjusted to get the highest loaded R_{eff} and signal-to-noise ratio.

The noise resonance from the RLC circuit with an MSA is measured in Fig. 5.16. All electronics and amplifiers are cooled to 3.6 K. The noise signal is also compared with a conventional HEMT-based amplifier. The quality factor is about 750 with the HEMT amplifier and 720 with the MSA. Both of them are large enough to detect a single electron.

The figure of merit is the amplitude of the resonance compared to the broad baseline noise, SNR. The MSA shows nearly a factor of 10 improved signal-to-noise ratio compared

to the conventional HEMT amplifier even at 3.6 K. This result is also consistent with the measured noise temperature in Fig. 5.13. By using a dilution refrigerator and cooling down to 100 mK or below, the MSA noise temperature and thus the signal-to-noise ratio will be improved by another order of magnitude.

Based on the measured characteristics, a factor of 20 reduction of T_z, from 0.5 K to 25 mK, should be possible. The following section describes the shielding of the magnetic field, a crucial development required for operation of a SQUID amplifier in our apparatus.

5.4.3 Magnet with low fringe field and its shielding

To operate the developed MSA with the Penning trap, a new magnet is designed. The Penning trap's magnetic field is about 5.3 T. On the other hand, the SQUID is sensitive to fT scale magnetic field variation. The SQUID needs to be attached to the mixing chamber of the dilution refrigerator. The mixing chamber stage is only 50 cm away from the magnet center. The field at this point needs to be low and stable enough for the operation of the SQUID. A new superconducting magnet and a superconductor-based magnetic shield are designed and manufactured to overcome this challenge.

Superconducting Magnet with a Cancellation Coil

A new solenoid magnet with a much faster drop of the fringe field than ordinary solenoid magnets is designed and fabricated (Fig. 5.17). Its principle is to have an inner small main solenoid magnet, about 7 T, and an outer large counteracting solenoid, about -1.7 T together. Two solenoids are connected in series, but the direction of the magnetic field is opposite. At the center of the trap, the subtracted field value of the two is $B = 5.3$ T. However, as one goes away from the center, the field from the inner solenoid drops more sharply than the outer larger solenoid. As a result, cancellation of the fringe field can be achieved at short distance.

The mixing chamber stage is about 50 cm away from the center the trap. If an ordinary

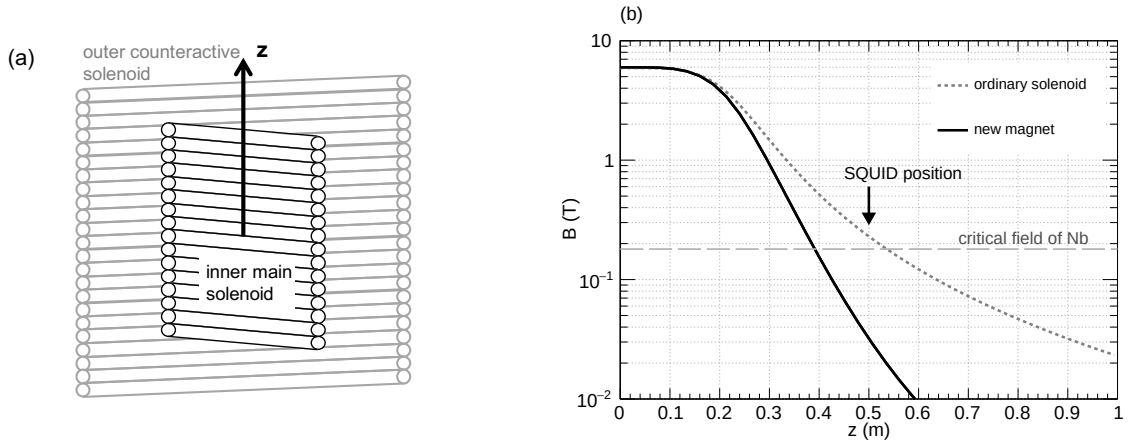


Figure 5.17: (a) The schematic of the newly designed magnet. The inner small coil applies about 7 Tesla to $+z$ direction, and the outer larger coil applies -1.3 Tesla to $-z$ direction. (b) The magnetic field of the newly designed magnet. A typical magnetic field from the same size magnet without the cancellation coil are also shown. The SQUID will be placed at about $z = 50$ cm. The lower critical field of niobium is also shown.

solenoid magnet with the same size were used, the field at the mixing chamber would be about 0.25 T. Due to the newly designed cancellation coil, the magnetic field value at the mixing chamber stage becomes about an order of magnitude smaller, 0.03 T. This order of magnitude improvement allows using a niobium superconducting shield, whose lower critical field is 0.19 T. Niobium single layer magnetic shield suffices for MSA operation. We also implement an outer higher temperature shield, discussed in the next section.

Double Layer Superconducting Magnetic Shield

The new magnet allows us to use a niobium superconducting shield. Ideally, if the shield is cooled first and the magnetic field is ramped later, a single layer niobium shield is sufficient to shield the ambient field of 0.03 T at the mixing chamber. However, discharging and ramping the superconducting magnet every time is inefficient. Therefore, for an operation without changing the magnetic field, we implement a Bi-2223-based outer magnetic shield (CST-22/100, CAN superconductor) in addition to the niobium inner superconducting shield (Fig. 5.18).

The inhomogeneity of the field at the center of the trap caused by the niobium and the Bi-

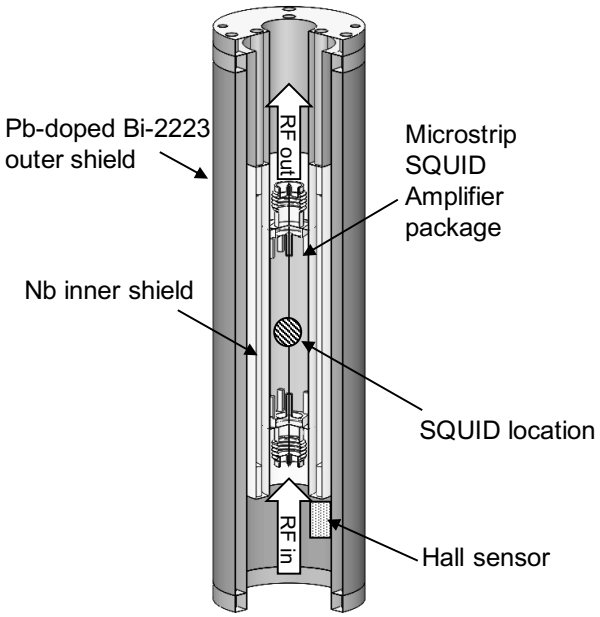


Figure 5.18: Superconducting double layer magnetic shield by niobium and Bi-2223.

2223 shield is calculated to be about 2.5 ppb for 1 cm diameter spherical volume (DSV) using the finite element analysis method (ANSYS). This is much smaller than the superconducting magnet's inhomogeneity, 24 ppb for 1 cm DSV [70]. Bi-2223's purpose is to shield the magnetic field during the cooling process. It becomes superconducting at $T = 110$ K at around 1.5 m away from the center, where the ambient magnetic field is 0.3 mT. At that location, the Bi-2223 shield traps this 0.3 mT field, but also shields further increase of the magnetic field inside until the inner niobium shield reaches its transition temperature. Once the niobium shield becomes superconducting, it works as the primary magnetic shield. With this double layer design, we can operate SQUID in a low enough field without turning off the magnet every time.

idea	effect	improvement on $\Delta\omega_c$
new trap with $C_6 = 0$	$\times 20$ more harmonic trap	20
direct spin flip	$\times 10$ longer averaging time	3
SQUID detector	$\times 50$ smaller T_z	50

Table 5.2: List of possible improvements for g-factor measurement.

5.5 Summary of Improvements and Remaining Developments

We have proposed three methods to improve the precision of g-factor measurement. The methods and improvements are summarized in Table 5.2. Better anharmonicity will result in smaller fluctuation of ν_z (Eq. 5.8). Longer averaging time allows better resolution of axial frequency shift (Fig. 5.9). Lower axial temperature narrows the linewidth drastically (Eq. 5.4). Improvements of the axial frequency resolution σ_{ω_z} allow for a smaller magnetic bottle B_2 and narrower linewidth (Eq. 5.4).

Notice that the improvements here are estimates based on the achieved parameters. In the following section, we summarize other important developments and challenges and propose possible solutions.

5.5.1 Driving Anomaly Transition without a Magnetic Bottle

One concern in the relativistic bottle scheme is that we cannot use the magnetic bottle gradient to drive the anomaly transition (Sec. 2.3). In the current method, the electron is axially modulated by an RF drive, and the ρ direction magnetic field from the magnetic bottle induces the anomaly transition. If the magnetic bottle is completely eliminated, this drive scheme will not work.

We now go back to the first principles calculation and estimate the possibility of driving from a split compensation electrode. When an alternating transverse magnetic field

$$\mathbf{B}(t) = b_1 \boldsymbol{\rho} \cos(\omega_a t) \tag{5.19}$$

is applied, the Rabi frequency for anomaly transition is [104]

$$\Omega_a = \frac{egb_1}{4m}\sqrt{\frac{2\hbar}{m\omega_c}} \tag{5.20}$$

The transition probability also depends on the anomaly transition's linewidth $\Delta\omega_a$. The required drive power is lower for a narrower line. The transition probability is approximately given by

$$P = \frac{\pi}{2}\frac{\Omega_a^2}{\Delta\omega_a}\Delta T, \tag{5.21}$$

where ΔT is the drive length. The linewidth $\Delta\omega_a$ will be limited by the synchrotron radiation rate in the relativistic bottle regime, and a realistic value with current trap at $\nu_c = 150$ GHz is $\Delta\omega_a/(2\pi) = 0.02$ Hz.

To get a transition probability of 50% with $\Delta T = 30$ s drive, a Rabi frequency of $\Omega_a/(2\pi) = 0.006$ Hz is required. From Eq. 5.20, the required b_1 gradient to achieve this value is $b_1 = 2.6 \times 10^{-5}$ T/m. Our traditional excitation scheme achieves this size of modulation by modulating the axial amplitude to about $z_a = 100$ nm with $B_2 = 300$ T/m^2.

In the proton's experiment, a split compensation electrode has been used to drive the spin-flip transition [115, 116]. The current flowing through the split compensation electrode generates the $b_1\boldsymbol{\rho}$ field. The magnetic field gradient from current I flowing through a split compensation electrode with radius a and distance l (Fig. 5.19) is given by

$$b_1 = \frac{3\mu_0 I}{4}\frac{a^2 l}{(a^2+l^2)^{5/2}}. \tag{5.22}$$

Taking the designed values of the new trap (Table 5.1), $a = \rho_0 = 2.5$ mm and $l = z_0 - z_c = 0.8$ mm, then one needs $I = 0.58$ mA to achieve $b_1 = 2.6 \times 10^{-5}$ T/m. Assuming it is driven through a 10 Ω load, then the dissipated power is about 3.3 μW.

This power dissipation is manageable in the dilution refrigerator, but is still much larger than the drive we currently use for spectroscopy. The drive power for the current spec-

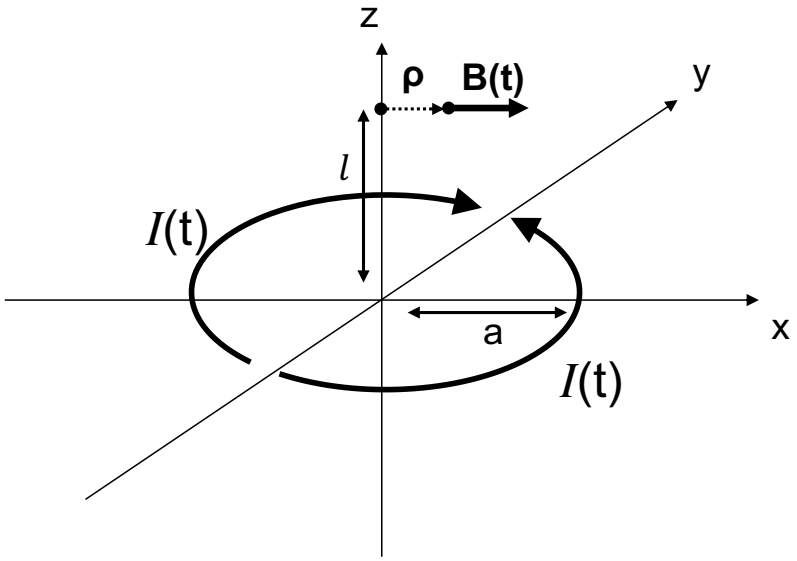


Figure 5.19: Current model for generating transverse magnetic field drive B_1 by split compensation electrode.

troscopy is about 0.6 μW. The drive power when anomaly power shift is studied is 18 μW at maximum. We did not observe the shift of cyclotron frequency, but its effect needs to be studied carefully.

One possibility to reduce the required drive power is to narrow the linewidth $\Delta\omega_a$. In the relativistic bottle regime, the linewidth will be limited by the synchrotron radiation rate γ_c. The radiation rate roughly scales with the square of the magnetic field, so the proposed measurement at 100 GHz or below also helps. Research about trap material and coating is also ongoing to improve the quality factor of the cavity. Any improvement of γ_c will help this anomaly drive scheme.

5.5.2 Microwave Cavity Shift

Once the transition linewidth is narrowed, the largest systematic error is the shift from the microwave cavity. Ideally, one wants to construct a much smaller trap, but then the effect from the gaps will be more dominant. Another way to reduce the cavity effect is to move to lower cyclotron frequencies. In the past, the cyclotron frequency was chosen to be

as high as possible because the linewidth from the magnetic bottle has been the dominant linewidth

$$\frac{\Delta\omega_c}{\omega_c} \propto \frac{B_2}{B}. \tag{5.23}$$

Higher magnetic field (and thus cyclotron frequency) is preferred because the relative uncertainty is smaller.

Once the B_2 is reduced enough that it is not the dominant error anymore, we can reduce the magnetic field B and lower ω_c to suppress the cavity effect. The density of cavity mode scales as

$$(\text{density of cavity modes}) \propto \omega_c. \tag{5.24}$$

Therefore, for example, a three times lower cyclotron frequency will suppress cavity shift by a factor of 3.

5.5.3 Other Challenges

The broadening of cyclotron frequency needs to be studied. The fact that it only appears in the cyclotron transition but not in the anomaly transition suggests that the timescale of the noise is between $\Delta\omega_a/(2\pi) = 0.2$ Hz and $\Delta\omega_c/(2\pi) = 200$ Hz. The relativistic bottle scheme with SQUID detector will reduce the linewidth to $\Delta\omega_c/(2\pi) = 1$ Hz. This should improve the robustness of the cyclotron line against the noise..

Once the cyclotron broadening is made as narrow as $\Delta\omega_c/(2\pi) = 1$ Hz, then its linewidth will be limited by the axial damping rate γ_z. In the current measurement, the damping rate is $\gamma_z/(2\pi) = 5$ Hz. A new RF switch has been developed to further narrow down this linewidth [94, 95, 117].

The requirement for axial frequency stability will become more stringent. We are now using the Stahl UM-LN1-14 power supply with a 2000 s cryogenic low pass filter. The hour scale drift is about 0.5 Hz, and the 10 s scale short-term fluctuation is smaller than 0.2 Hz. Currently, the short-term stability is not very precisely measured because it is limited by the

axial frequency resolution of the self-excitation. The proton's experiments achieved better long-term stability [115, 118–120]. Based on Fig. 5.9, the drift is negligible for averaging time less than 100 seconds. If better long-term stability is needed, a low pass filter with a longer time constant can be used.

The drift and stability of the magnetic field will be more critical. The target linewidth in the relativistic bottle is $\Delta\omega_c/\omega_c = 6 \times 10^{-11}$. The magnet has a drift rate of about $\mathcal{O}(10^{-10})$ per hour. If we spend longer time to improve axial frequency resolution, the effect of drift also becomes more significant. For example, if we spend 100 seconds to resolve one quantum transition, then a drift rate of 10^{-10}/hour corresponds to broadening of $\Delta\omega_c/\omega_c = 3 \times 10^{-12}$. This is still manageable, but needs to be monitored and compensated carefully.

Despite all the challenges listed here, there are no fundamental reasons that limit the proposed scheme. A significantly improved magnetic field homogeneity and lower temperature will improve the precision at least by another order of magnitude.

Chapter 6

Search for Dark Photon using a Single Electron

The established cylindrical Penning system with a single electron quantum cyclotron is so well understood and controlled that it can also be used for searches of dark photon dark matter. The electron quantum cyclotron, trapped at its ground state, is completely background-free due to the ultracold ambient temperature achieved by the dilution refrigerator. In this chapter, the physics of dark matter and dark photon is first reviewed in Sec. 6.1. The idea of a dark photon search using the single electron quantum cyclotron is explained in Sec. 6.2. The actual measurement and obtained limit are shown in Sec. 6.3, and future prospects in such a search are described in Sec. 6.4. The results presented here are in collaboration with Peter Graham, Harikrishnan Ramani, Samuel S. Y. Wong, and Yawen Xiao from Stanford University, and Roni Harnik from Fermi National Accelerator Laboratory. Part of the work here is summarized and published in [121]

6.1 Dark Matter and Dark Photon

Dark matter is one of the most important mysteries of the standard model of particle physics. Despite an abundance of evidence [122–127], its interaction remains a mystery

except for the gravitational force. Its direct detection will open a new path for physics. The dark photon is a promising candidate for dark matter and motivated particle from many theories beyond the Standard Model. The nature of DM and DP is summarized in this section.

6.1.1 Dark Matter

Cosmological observations revealed that the Standard Model's particles only consist of 4.9 % of the total energy in the universe [128]. The remaining 26.8 % consists of dark matter (DM), and 68.3 % consists of dark energy. The existence of dark matter has also been confirmed by many observations, such as the rotation speed of galaxies and the gravitational lens effects [129].

Over the past decades of observations, several constraints have been set. The most important features are that the DM is made of non-SM particles which interact weakly with the SM particles and that it must be moving at non-relativistic speeds to be gravitationally bound to a galaxy (so called cold dark matter, CDM) [130, 131]. Especially for the DM bound to our galaxy, the fact that the earth is moving in the same gravitational potential yields that the DM has a velocity of about $v/c = 10^{-3}$ [132]. In this non-relativistic limit, the Doppler shift of a massive particle yields linewidth of the DM signal

$$\frac{\Delta\omega_{\mathrm{DM}}}{\omega_{\mathrm{DM}}} \approx \left(\frac{v}{c}\right)^2 = 10^{-6}. \tag{6.1}$$

The candidate particles beyond the SM can be classified into two categories: weakly-interacting massive particles (WIMPs) that have a mass range of GeV–TeV [133], and weakly-interacting slim particles (WISPs) with μeV–eV mass range [130, 134]. WIMPs have been extensively searched with the recoil experiments, but so far, they have not been detected [135–139]. Efforts to search for WISPs, such as sterile neutrinos, axions, axion-like particles, and dark photons (DPs), have also been explored [140]. WISPs at $\sim$meV range

are especially motivated by the dark energy density of the universe $\rho_\Lambda \sim (\text{meV})^4$, the energy scale of the neutrinos, and the minimal dark photon dark matter model with purely gravitational production [141].

Because of its light mass, the best methods to search for WISPs are low-energy experiments using lasers, microwave cavities, or optomechanical systems [134]. Several experiments have been proposed to explore this parameter space, but there is a gap in the limit at the 10–200 GHz range. Below 10 GHz, the limits are mostly from the sensitive dark matter haloscope experiments using a high-Q resonant cavities (e.g. ADMX [142,143], CAPP [144–146], and HAYSTAC [147,148]) . However, its Q-factor drops sharply at above 10 GHz (or 0.04 meV). At the same time, the technology for single photon detection is not widely available below 200 GHz [149].

The method proposed and demonstrated here explores this gap using a trapped electron. The cyclotron motion of the electron is used as a background-free detector of CDM. Using this highly controlled and well-understood system, we demonstrate a background-free search of dark photon dark matter.

6.1.2 Dark Photon

The target in our search using the trapped electron is the dark photon (DP). The DP is the gauge boson of a new $U(1)$ symmetry added in the extended SM theory [150]. It is analogous to the SM ordinary photon, except that the added DP field A'_μ can have mass $m_{A'}$ and kinetic mixing parameter χ with the ordinary electromagnetic field A_μ. The extended Lagrangian (in natural units) includes

$$\mathcal{L} \supset -\frac{1}{4}F'_{\mu\nu}F'^{\mu\nu} - \frac{\chi}{2}F_{\mu\nu}F'^{\mu\nu} + \frac{m^2_{A'}}{2}A'_\mu A'^\mu, \tag{6.2}$$

where $F_{\mu\nu}$ and $F'_{\mu\nu}$ are the field strength for the SM photon and the DP, respectively. The mixing parameter χ yields conversion from the DP to the ordinary photon (Fig. 6.1). The

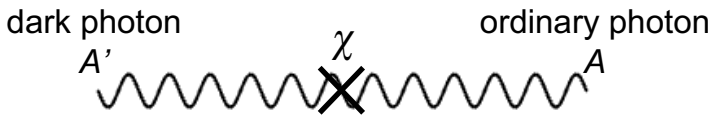


Figure 6.1: Feynman diagram showing the kinetic mixing of DP field and the ordinary electromagnetic field.

value of χ ranges widely depending on the model. For the model that the DP arises from superstring theory, $10^{-12} < \chi < 10^{-3}$ is predicted [134]. There are stringent limits on allowed $m_{A'}$ and χ, for example from cosmological observation [130] and solar lifetime [151], but in general, wide range of $m_{A'}$ and χ, especially around $m_{A'}$ ∼meV and $\chi < 10^{-9}$, is allowed for dark photon dark matter(DPDM).

The equation of motion for the DP follows the Proca equation

$$\left[\frac{\partial^2}{\partial t^2} - \nabla^2 + \left(\frac{m_{A'}c^2}{\hbar}\right)^2\right] A'_\mu = 0. \tag{6.3}$$

The explicit solution of its spatial component is

$$\vec{A'}(\vec{x},t) = A' e^{i\omega_{A'}t}\vec{n}(\vec{x},t)e^{i\phi(\vec{x},t)}, \tag{6.4}$$

where $\vec{n}(\vec{x},t)$ is the unit vector of pointing direction, $\phi(\vec{x},t)$ is the phase, and $\omega_{A'}$ is angular oscillation frequency [152]

$$\omega_{A'} = \frac{m_{A'}c^2}{\hbar}. \tag{6.5}$$

The direction vector $\vec{n}(\vec{x},t)$ and the phase term $\phi(\vec{x},t)$ varies with a coherence length of $\lambda = c^2/(v\nu) = 2\text{ m} \times (150\text{ GHz}/\nu)$. In our experiment, the typical length of the trap is about a centimeter, so the position dependence of DPDM can be assumed to be constant. The coherence time is given by $\tau_{\text{coherence}} = c^2/(v^2\nu)$. This arises from the Doppler broadening of the DPDM and is included as the linewidth of DPDM (Eq. 6.1). Therefore, an alternative

way to express Eq. 6.4 is to assume a spatially uniform field

$$\vec{A}'(\vec{x},t) = \vec{n}A'e^{i\omega_{A'}t}, \tag{6.6}$$

and assume that $\omega_{A'}$ has a spread of $\Delta\omega_{A'}/\omega_{A'} = 10^{-6}$. In this picture, $\vec{n}$ is now a position-independent unit vector.

The local density of the DM is measured to be $\rho_{\rm DM}c^2 = (0.4 \pm 0.1)$ GeV/cm^3 [153]. We use a conservative value $\rho_{\rm DM}c^2 = 0.3$ GeV/cm^3 in this thesis. Assuming the DM is entirely made of DP, the energy density is associated with the DP field as

$$\rho_{\rm DM}c^2 = \frac{\epsilon_0}{2}\omega_{A'}^2 A'^2. \tag{6.7}$$

The electric field from the DPDM is then

$$\begin{aligned} \vec{E}_{\rm DPDM}(\vec{x},t) &= \chi\frac{\partial\vec{A}'(\vec{x},t)}{\partial t} \\ &= i\chi\vec{n}\omega_{A'}A'e^{i\omega_{A'}t} \\ &= i\chi\vec{n}\sqrt{\frac{2\rho_{\rm DM}c^2}{\epsilon_0}}e^{i\omega_{A'}t}. \end{aligned} \tag{6.8}$$

The exact value using $\rho_{\rm CM}c^2 = 0.3$ GeV/cm^3 is

$$|\vec{E}_{\rm DPDM}| = \chi\sqrt{\frac{2\rho_{\rm DM}c^2}{\epsilon_0}} = \chi \times 33 \text{ V/cm}. \tag{6.9}$$

We use the trapped electron's cyclotron motion as a probe of this electric field $|\vec{E}_{\rm DPDM}|$. The DPDM signal is manifested as an excitation of cyclotron motion from the ground state to the first excited state. Our demonstration search here probes to about $\chi \sim 3 \times 10^{-11}$ at a single frequency. Future experiments using the demonstrated method can reach $\chi \sim 10^{-10}$ for a wide range of frequencies.

6.2 Principle of the Search

In the method proposed here, we employ the single electron in the Penning trap as the "detector" for DPDM. The idea is to look for the excitation of cyclotron transition $n_c = 0 \to 1$ driven by the DPDM electric field. Here, we revisit several advantages. Some of them overlap with the other sections, but we rephrase them here in terms of the DPDM search. Importantly, all features and advantages can be measured *in-situ* by the trapped electron itself.

6.2.1 Quantum Cyclotron as a Probe of Dark Photon

The electric field associated with DPDM (Eq. 6.9) can excite the cyclotron state from $n_c = 0$ to $n_c = 1$ in the absence of any drives. To search for DPDM, we leave the cyclotron state at $n_c = 0$ and monitor the state without applying an external drive. Resolution of the quantum states n_c has been clearly demonstrated, for example, in Fig. 2.23. A single quantum transition $n_c = 0 \to 1$ can be detected with a very high fidelity, especially when a large magnetic bottle is used.

One of the unique advantages is the complete suppression of background. Because of the low temperature achieved by the dilution refrigerator, the quantum cyclotron "detector" is completely background-free. With the typical experiment parameters, $T = 50$ mK, $B = 5.3$ T and $\gamma_c = 0.14$ s^{-1}, excitation from ordinary blackbody radiation is

$$\begin{aligned} \Gamma_{\rm SM} &= \bar{n}_c \gamma_c \\ &= \left[\exp\left(\frac{\hbar\omega_c}{k_B T} - 1 \right) \right]^{-1} \gamma_c \\ &= 1.9 \times 10^{-62}\ \text{s}^{-1} \approx 0. \end{aligned} \tag{6.10}$$

In this background free limit, the electron is always at the $n_c = 0$ state. If no excitation event is detected, the upper limit on the DPDM excitation rate $\Gamma_{A'}$ is set. In the background

free regime, the upper limit scales as the inverse of the time

$$(\text{upper limit on } \Gamma_{A'}) \propto T_{\text{obs}}^{-1}, \tag{6.11}$$

where T_{obs} is the total observation time. The background-free search provides a big advantage compared to ordinary detectors that have a non-zero background rate, where the sensitivity scales as $T_{\text{obs}}^{-1/2}$.

Another feature is that the required power to drive one quantum cyclotron is very low, $\hbar\omega_c = 10^{-22}$ J at $\omega_c/2\pi = 150$ GHz. The electron is very sensitive to the small field from DPDM. As we will see later, the electron's cyclotron motion is narrower than the DPDM linewidth, so the drive force is modeled by an incoherent source. The excitation rate of $n_c = 0 \to 1$ by an incoherent electric field at the center $E_0(t)$ is [154, 155]

$$\Gamma_{A'} = \frac{\pi e^2 |X_{12}|^2}{\hbar^2} \int S_E(\omega)\chi(\omega, \omega_c, \Delta\omega_c)d\omega = \int \frac{\pi e^2}{2m\hbar\omega_c} S_E(\omega)\chi(\omega, \omega_c, \Delta\omega_c)d\omega, \tag{6.12}$$

where $X_{12} = \langle n_c = 0|\hat{x}|n_c = 1\rangle = \sqrt{\frac{\hbar}{2m\omega_c}}$, $\chi(\omega, \omega_c, \Delta\omega_c)$ is the normalized cyclotron lineshape function, and $S_E(\omega)$ is the power spectrum density of $E_0(t)$ defined in angular frequency space. The lineshape $\chi(\omega, \omega_c, \Delta\omega_c)$ is determined by the cyclotron frequency ω_c and its linewidth $\Delta\omega_c$. When we monitor the cyclotron state n_c, the electron is excited to a high axial amplitude z_A along the z axis. This excited amplitude, coupled with the magnetic bottle gradient $B(z) = B_2 z^2$, determines the linewidth $\Delta\omega_c = eB_2 z_A^2/m$. The lineshape function arising from this broadening is given by the Gaussian function

$$\chi(\omega, \omega_c, \Delta\omega_c) = \frac{1}{\sqrt{2\pi}\Delta\omega_c} \exp\left[-\frac{1}{2}\left(\frac{\omega - \omega_c}{\Delta\omega_c}\right)^2\right]. \tag{6.13}$$

For the DPDM field, the power spectrum density $S_E(\omega)$ can be approximated as

$$\begin{aligned} S_E(\omega) &= \int_{\infty}^{\infty} E[E_{0;x}(\vec{0},t)\overline{E_{0;x}(\vec{0},t+\tau)}]e^{-i\omega\tau}d\tau \\ &= \begin{cases} \frac{|E_{0;x}|^2}{2\Delta\omega_{A'}}, & \text{if } \omega_{A'} < \omega < \omega_{A'} + \Delta\omega_{A'}. \\ 0, & \text{otherwise.} \end{cases} \end{aligned} \tag{6.14}$$

Here, $E[X(t)\overline{X(t+\tau)}]$ is the auto-correlation function and $E_{0;x}(\vec{0},t)$ is the x-component of the electric field at the center of the trap generated by the DPDM. Notice the factor 2 in the denominator because we are calculating the average power spectrum density. The excitation field at the center of the trap $E_{0;x}(t)$ is not exactly equal to $E_{\text{DPDM}}(t)$ because of the Penning trap cavity and random polarization of the DPDM field. They are related by a coefficient κ as

$$\begin{aligned} |\vec{E}_{0;x}(\vec{0},t)| &= \kappa \times |\vec{E}_{\text{DPDM}}|e^{i\omega_{A'}t} \times \sqrt{\langle \sin^2\theta \rangle} \\ &= \kappa \times \chi\sqrt{\frac{2\rho_{\text{DM}}c^2}{\epsilon_0}}e^{i\omega_{A'}t} \times \sqrt{\langle \sin^2\theta \rangle}. \end{aligned} \tag{6.15}$$

Here, κ represents the enhancement from the geometry of the Penning trap, and $\sqrt{\langle \sin^2\theta \rangle} = \sqrt{2/3}$ is the expectation value of DPDM's random direction $\vec{n}$ (pointing at polar angle θ) projected to the cyclotron motion's plane (xy-plane). We now calculate κ in detail in the following subsection.

6.2.2 Enhanced Sensitivity by the Cylindrical Penning Trap

The cylindrical microwave trap electrode not only increases the cyclotron lifetime, but also enhances the DPDM signal amplitude. We will see that the correction coefficient κ is larger than 1 in a broad range even away from any cavity resonance. The electric field at the trap center $E_{0;x}(\vec{0})$ driven by the DPDM field $\vec{E}_{\text{DPDM}}$ (Eq. 6.15) is calculated as follows.

The DPDM field can be treated as an electric field drive source of the cavity. The electric

field of the driven cavity at the location $\vec{x}$ is given by [156]

$$\vec{E}_0(\vec{x}) = \sum_M \frac{\omega^2}{\omega^2 - \omega_M^2} \frac{\int d\boldsymbol{r} \vec{E}_M^*(\boldsymbol{r}) \cdot \vec{E}_{\mathrm{DPDM}}(\boldsymbol{r})}{\int d\boldsymbol{r} |\vec{E}_M(\boldsymbol{r})|^2} \vec{E}_M(\vec{x}), \tag{6.16}$$

where M runs all the resonant microwave modes (TE_{mnp} and TM_{mnp} for the cylindrical cavity), and $\vec{E}_M(\boldsymbol{r})$ is the electric field of the corresponding resonant mode. Since the coherence length is much larger than the cavity size, the DPDM field is treated as a uniform field. The random polarization factor $\langle \sin^2 \theta \rangle$ (Eq. 6.15) allows us to assume that the direction of the DPDM field is along x-axis $\vec{E}_{\mathrm{DPDM}} = |\vec{E}_{\mathrm{DPDM}}| \vec{e}_x$. These two conditions simplify Eq. 6.16 as

$$\vec{E}_0(\vec{x}) = \sum_M \frac{\omega^2}{\omega^2 - \omega_M^2} \frac{|\vec{E}_{\mathrm{DPDM}}| \int d\boldsymbol{r} \vec{E}_M^*(\boldsymbol{r}) \cdot \vec{e}_x}{\int d\boldsymbol{r} |\vec{E}_M(\boldsymbol{r})|^2} \vec{E}_M(\vec{x}). \tag{6.17}$$

The κ from Eq. 6.15 is defined by the ratio of the amplitude of field at the center $\vec{x} = \vec{0}$,

$$\kappa = \frac{\vec{E}_{0;x}(\vec{0})}{|\vec{E}_{\mathrm{DPDM}}|} = \sum_M \frac{\omega^2}{\omega^2 - \omega_M^2} \frac{\int d\boldsymbol{r} \vec{E}_M^*(\boldsymbol{r}) \cdot \vec{e}_x}{\int d\boldsymbol{r} |\vec{E}_M(\boldsymbol{r})|^2} E_M(\vec{0})_x, \tag{6.18}$$

The resonant modes and the frequencies are mapped using a cloud of electrons. For DPDM search, we use $\rho_0 = 4.527$ mm and height $2z_0 = 7.790$ mm by fitting only the resonances around 150 GHz. We calculate κ using this ideal cavity geometry and then correct the actually measured frequency for the modes between 130 GHz and 160 GHz. Figure 6.2 shows the obtained κ^2, with the line indicating the DPDM measurement frequency in this thesis.

κ represents the enhancement of the DPDM field at the center of the trap. In a free space with no cavity, κ is equal to 1. The excitation rate scales as $\Gamma_{A'} \propto |\vec{E}_0|^2 \propto |\kappa|^2 |\vec{E}_{\mathrm{DPDM}}|^2$. Therefore, to perform a sensitive search of the DPDM field, higher $|\kappa|^2$ is desired. The enhancement $|\kappa|^2$ is obviously high near resonant modes, but it is also high even off resonance (Fig. 6.2). The cylindrical cavity wall focuses the converted electric field at the center of the cavity and yields higher $|\kappa|^2$. The ordinary photons, driven by DPDM and

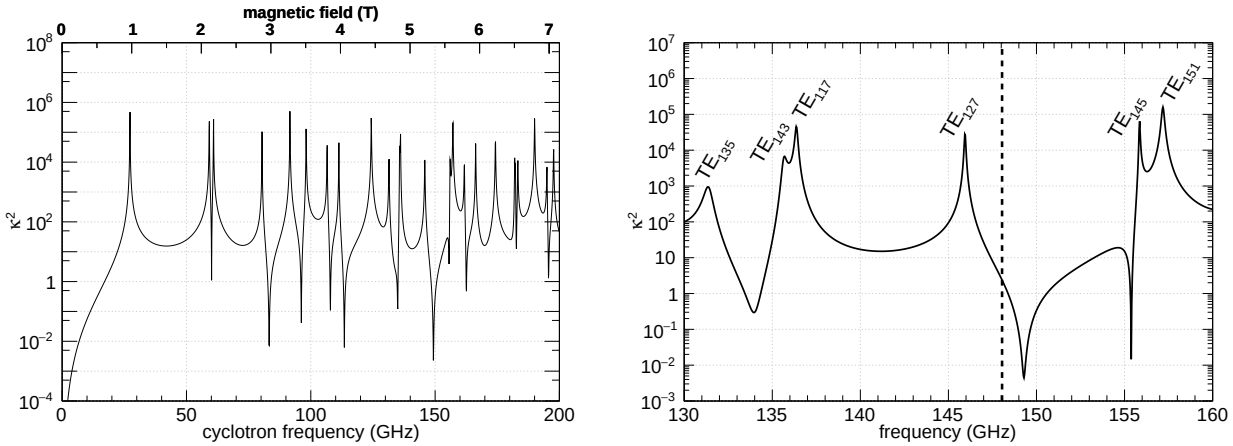


Figure 6.2: Calculation of κ for wide range (left) and for the range around this search (right). The frequency demonstrated in this thesis, $\omega_c/(2\pi) = 148$ GHz, is indicated by the dash line.

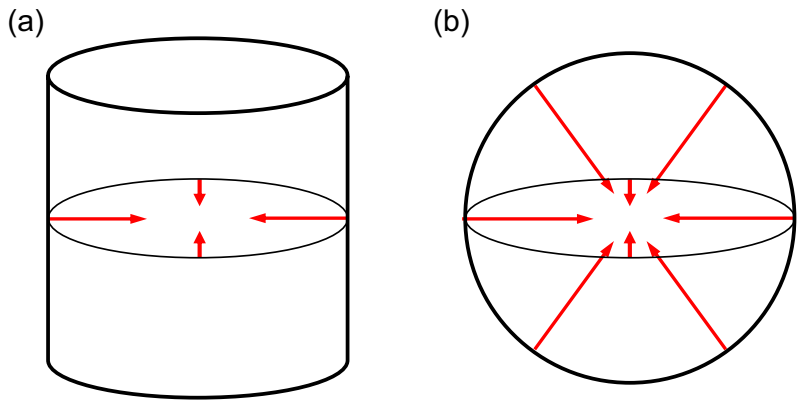


Figure 6.3: Enhancement of DP induced electric field (red arrow) by a cylindrical trap (a) and a spherical trap (b). DP induced field (red arrow) is emitted perpendicularly from the wall and is focused at the center of the trap.

emitted from the cylindrical circumference $2\pi\rho_0$, are focused at the center to its wavelength $\lambda = 2\pi c/\omega$,. Therefore, for a cylindrical cavity, the power is approximately enhanced by [Fig. 6.3(a)].

$$|\kappa|^2 \simeq \frac{\rho_0 \omega}{c} \tag{6.19}$$

We later see that this focusing effect is even higher for spherical cavity [Fig. 6.3(b)] in Sec. 6.4, which is consistent with the intuitive description here.

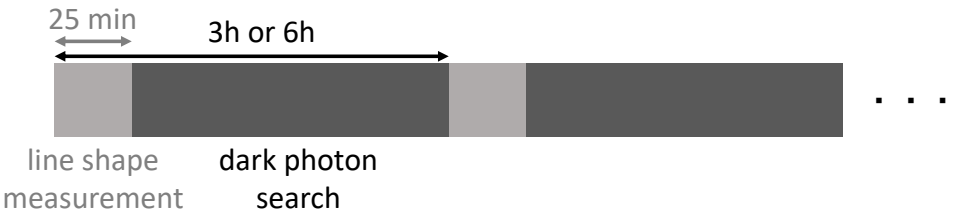


Figure 6.4: Measurement cycle for the DPDM search. The cyclotron resonance line shape $\chi(\omega, \omega_c, \Delta\omega_c)$ is measured in period. In the dark photon search period, no external drive is applied, and the electron is kept at $n_c = 0$. Excitation to $n_c = 1$ from DPDM is searched.

6.3 Search for Dark Photon Dark Matter

With the method described above, a search for DPDM is performed with the same trap used for the g-factor measurement. The measurement sequence and the result of the search are described in this section.

6.3.1 Measurement Sequence

The measurement sequence is shown in Fig. 6.4. It consists of two periods, (I) lineshape measurement and (II) DPDM search period. The lineshape measurement period is to map the cyclotron lineshape $\chi(\omega, \omega_c, \Delta\omega_c)$, and the search period is to look for cyclotron excitation of the electron from DPDM field. The lineshape measurement is repeated regularly, typically every 3 or 6 hours. The axial self-excitation is used to resolve the cyclotron state quickly and is kept on with the same amplitude in both periods.

(I) In the lineshape measurement period, a microwave drive is deliberately applied to measure cyclotron line shape $\chi(\omega, \omega_c, \Delta\omega_c)$. The average quantum number n_c is measured as the drive frequency is swept. Because of the self-excited axial oscillation, the line shape is broader than the one in the g-factor measurement (Chap. 4) . Due of the coupling with the magnetic bottle $B_2 z^2$, the linewidth is given by $\Delta\omega_c/\omega_c = B_2 z_A^2/B$. This width is set to be

$$\frac{\Delta\omega_c}{\omega_c} = 2.2 \times 10^{-7} \tag{6.20}$$

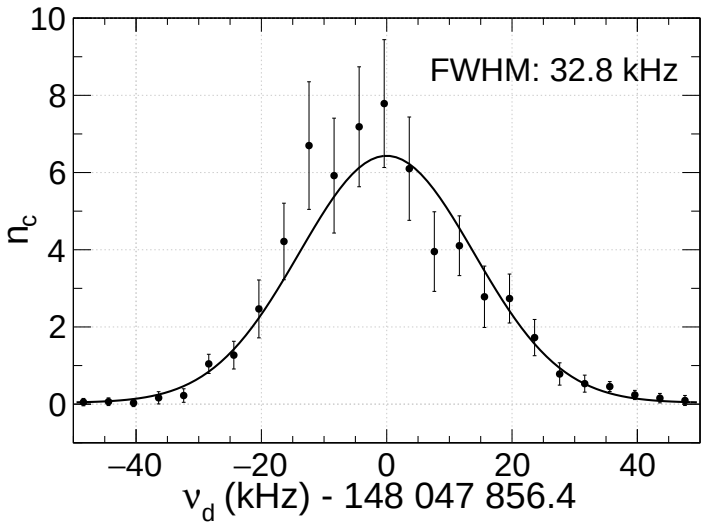


Figure 6.5: Measured line shape with the axial self-excitation on. The quantum number n_c is measured as a function of the microwave drive frequency.

and is comparable with the DPDM field $\Delta\omega_{A'}/\omega_{A'} = 10^{-6}$, which yields the widest sensitivity (Fig. 6.5).

The line shape mapping is repeated to measure the drift rate of the magnet. The drift rate is measured to be less than 1 ppb per hour by the ^{3}He NMR probe (Chap. 3) and one electron's cyclotron frequency (Chap. 4). Both measurements already guarantee that the drift is much smaller than the linewidth here. This repeated line shape measurement is still necessary to prove that $\chi(\omega, \omega_c, \Delta\omega_c)$ stays the same during the search. Figure 6.6 shows the repeated measurement of $\chi(\omega, \omega_c, \Delta\omega_c)$. The plot shows time in the x-axis, drive frequency in the y-axis, and the average quantum number n_c is plotted in the z-axis with color. The result confirms the expected low drift rate during the whole measurement.

(II) During the search period, the cyclotron quantum state n_c is monitored without any external drive. The axial frequency averaged for $t_{\text{ave}} = 2$ seconds is repeatedly measured. The drift of the axial frequency longer than 600 s is regulated by PID control of the ring voltage. The axial oscillation amplitude is set to be the same throughout the whole measurement. The first 24 hours of the result is shown in Fig. 6.7. We define the measured

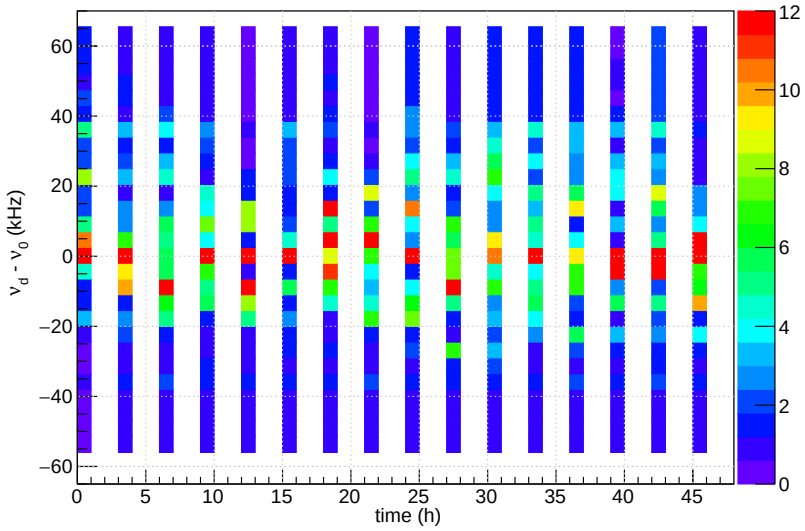


Figure 6.6: Measured n_c every 3 hours. The color represents measured n_c.

run #	time (day/hour:minute)	observation length (s)
1	11/ 12:46 – 13/ 13:15	148058
2	14/ 18:26 – 15/ 11:33	58162
3	15/ 11:50 – 17/ 17:22	179698
4	17/ 18:38 – 18/ 18:40	80640
5	19/ 12:15 – 21/ 15:43	172312
total	—	638870

Table 6.1: Data sets for DPDM search in March 2022. Each run consists of the repeated measurement cycle in Fig. 6.4.

quantum number as

$$\tilde{n}_c \equiv (\nu_z \text{ shift})/(\delta_c/2\pi). \tag{6.21}$$

Notice that $\tilde{n}_c$ is now a continuous number because it is defined from the measured axial frequency shift. No evident excitation to $n_c = 1$ is observed during this period.

The data sets for the DPDM search are summarized in Table 6.1. The search is split because of practical reasons such as cryogen fill, ramping of a nearby magnet, and maintenance of the helium pressure system. The limits to excitation rate $\Gamma_{A'}$ and DP parameters χ and $m_{A'}$ are calculated quantitatively in the next section.

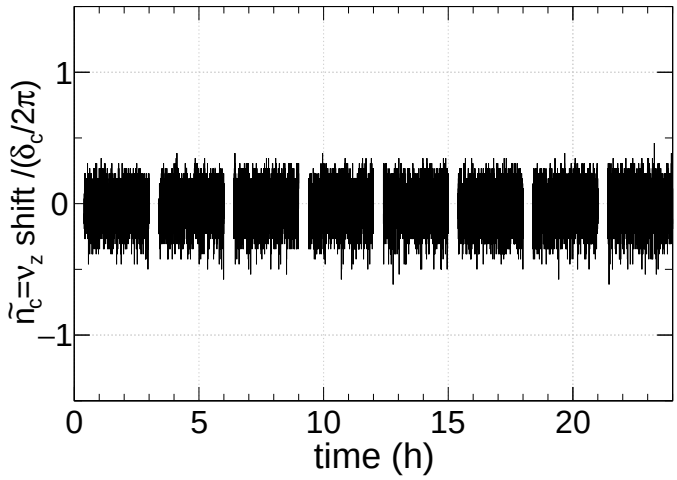


Figure 6.7: Monitored quantum state $\tilde{n}_c$ for the first 24 hours. Breaks that correspond to line shape measurements are visible.

6.3.2 Limit on Dark Matter Dark Photon

The measured quantum state $\tilde{n}_c$ scatters with $\sigma = 0.13$ standard deviation (Fig. 6.8). We define event with $\tilde{n}_c > 5\sigma = 0.65$ as an excited event. Conversion to the DPDM excitation rate $\Gamma_{A'}$ requires careful estimate of detection efficiency ζ. Even if there is an excitation, if it immediately decays back to the $n_c = 0$ state, we will not detect it. The quantitative estimate is as follows.

An excited event $n_c = 1$ has lifetime of $\tau_c = 7.2$ (2) s. If there is an excitation at $t = 0$, the probability that it decays back to $n_c = 0$ between t and $t + dt$ is given by

$$P(t)dt = \frac{1}{\tau_c} \exp\left(-\frac{t}{\tau_c}\right) dt. \tag{6.22}$$

The detection efficiency of DPDM excitation ζ is estimated by calculating the probability that an excited event stays longer than $5\sigma \times t_{\text{ave}}$=1.3 seconds and is recorded above the detection threshold

$$\zeta = \int_{1.3\text{s}}^{\infty} \frac{1}{\tau_c} \exp\left(-\frac{t}{\tau_c}\right) dt = 83\ \%. \tag{6.23}$$

The conversion to $\Gamma_{A'}$ is now straightforward. Using the standard estimate of an upper

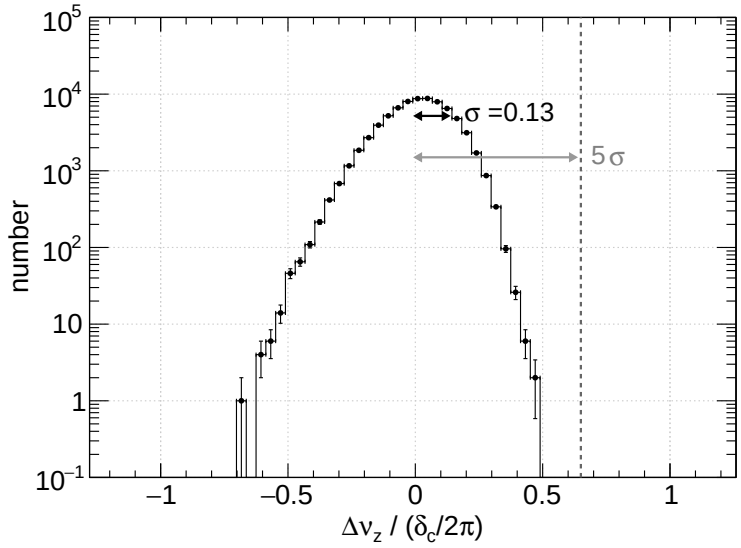


Figure 6.8: Distribution of measured $\tilde{n}_c$. It has standard deviation of $\sigma = 0.13 \times \delta_c/(2\pi)$. The 5σ detection threshold is also shown.

limit of a null measurement [157], the upper limit on the DPDM excitation rate with $CL = 90\%$ confidence level is

$$\Gamma_{A'} < -\frac{1}{\zeta T_{\rm tot}} \log\left(1 - CL\right) = 4.33 \times 10^{-6}\ \mathrm{s}^{-1} \tag{6.24}$$

The conversion to DPDM mass $m_{A'}$ and mixing parameter χ can be done using Eq. 6.12. $|\kappa|^2$ is calculated to be 2.37 at $\omega_c/(2\pi) = 148.047\ 856$ GHz. The obtained limit, compared with other experiments, is shown in Fig. 6.9. The limit for solar DP search from XENON1T [158–160] and the limit from DM cosmology [130] are also shown.

6.4 Future Improvements

The DPDM search with the quantum cyclotron has been demonstrated in the previous sections. In this section, we discuss how to improve the sensitivity drastically. Some of the ideas and developments in this section are especially attributed to the collaborators listed at the beginning of this chapter.

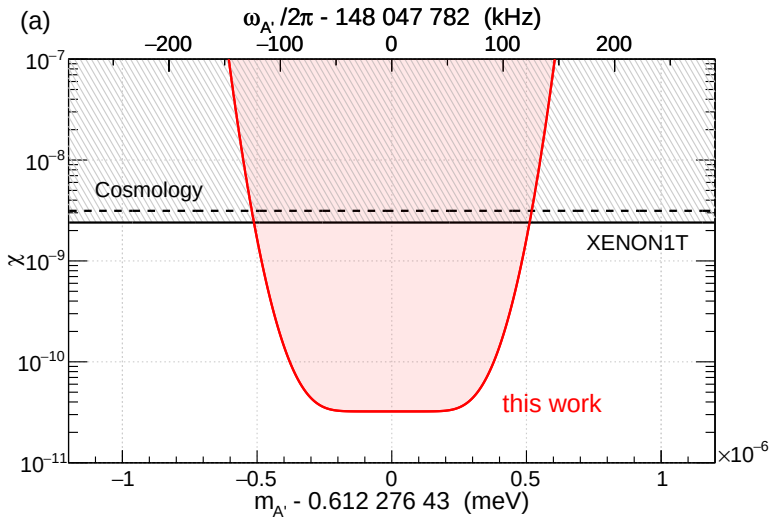


Figure 6.9: Obtained limit on dark photon dark matter. The limit from XENON1T [158–160] and DM cosmology [130] are also shown.

6.4.1 Wide Range Search

An important advantage of using the Penning trap is that the detection frequency can be easily swept by changing the magnetic field, $\omega_c = eB/m$. The magnetic field can be swept for wide range, as long as the background photon $\bar{n}_c = \left[\exp\left(\frac{\hbar\omega_c}{k_B T}\right) - 1\right]^{-1}$ is not dominant. With a typical dilution refrigerator, $T = 10$ mK, frequency range from 20 GHz to 200 GHz can be covered. This range is very large compared to the conventional cavity resonant type search such as ADMX [161].

The axial frequency (so the cyclotron state n_c) can be monitored while sweeping the field. The sweep rate of the magnetic field is very smooth and slow because of the large inductance of the solenoid coil, ~ 200 H. The magnet for this purpose does not require high homogeneity and stability as needed for g-factor measurement, so a cryogen-free magnet with a pulse-tube refrigerator is the most promising choice. Trap and detection of a single electron cyclotron transition in such a magnet have been demonstrated with a cryogen-free magnet in the lab (C2204M, Cryomagnetics, inc.). The magnetic field can be swept while maintaining the high fidelity detection of cyclotron state n_c.

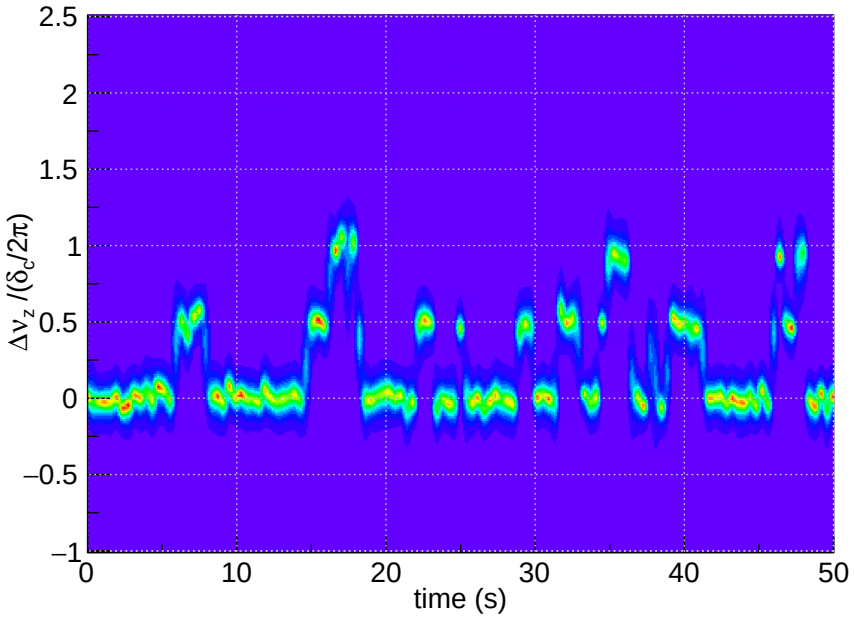


Figure 6.10: Observed axial frequency shift by cyclotron transition for $n_e = 2$ trapped electrons. The shift of axial frequency by one electron is half of the original shift $\delta_c/(2\pi)$.

6.4.2 Detecting Single Cyclotron Excitation from Many Trapped Electrons

An ideal way to improve the sensitivity is to trap n_e (≥ 2) electrons all at $n_c = 0$ state, and look for single electron's excitation to $n_c = 1$. If this succeeds, we gain a factor of n_e higher sensitivity in the DPDM search.

With n_e trapped electrons, the axial frequency shift from one electron's cyclotron transition will be n_e times smaller $\delta_c/(2\pi n_e)$. We have observed this for two electrons (Fig. 6.10), and in the past, the same phenomenon with three electrons has been observed [162]. We assume that detecting one transition from n_e electrons is reliably possible if B_2 is also increased by n_e. The bottle used in this search, $B_2 = 300$ T/m^2, is made as small as possible for the g-factor measurement. Much larger bottles are widely used in the proton's experiments; for example 1000 times larger bottle has been used in [115, 116, 118–120]. We conservatively assume that detecting one transition from $n_e = 10$ electrons should be possible if the bottle is made larger.

6.4.3 Large Spherical Cavity

The enhancement factor κ^2 from the Penning trap's boundary condition can be increased further if we use a spherical Penning trap. The enhancement κ qualitatively comes from the focusing of emitted photon on the surface of the trap at the center of the trap (Fig. 6.3). For a cylindrical trap with radius ρ_0, the emitted power from the circumference $2\pi\rho_0$ is focused to $\lambda = 2\pi c/\omega$. For a spherical trap with the same radius ρ_0, the emitted power from the surface $4\pi\rho_0^2$ is focused to $\lambda^2 = (2\pi c/\omega)^2$. Therefore the focusing is approximately proportional to

$$|\kappa|^2 \propto \begin{cases} \omega\rho_0, & \text{for cylindrical trap.} \\ (\omega\rho_0)^2, & \text{for spherical trap.} \end{cases} \tag{6.25}$$

The analytically calculated κ^2 can be calculated using the analytic solution of spherical cavity [163]. We only quote the result,

$$\kappa = \sum_{p=1}^{\infty} \frac{4}{3} \frac{\omega^2}{\left(\frac{u'_p c}{\rho_0}\right)^2 - \omega^2} \frac{{u_p}^5 j_1(u_p)}{{u_p}^4 + (2u_p - \frac{1}{2}{u_p}^3)\sin(2u_p) - \left[1 + \cos(2u'_p)\right] {u'_p}^2 - 1 + \cos(2u_p)}, \tag{6.26}$$

where $j_n(x)$ is the spherical Bessel function and u_p is p-th zero of $j_n(x) + xj'_n(x)$. The calculated κ^2 is shown in Fig. 6.11, with $\rho_0 = 4.5$ mm and $\rho_0 = 25$ mm. The κ^2 for the current cylindrical trap is also compared with the black line. The enhancement over a wide range is visible.

Spherical cavities have not been used, but there is no obvious technical difficulty. The spherical cavity can be split into 5 electrodes in the same way as the cylindrical cavity for anharmonicity tuning [163]. Microwave cavity mode should be much better because of its higher degree of symmetry. The magnetic bottle can be implemented in the same way, although a much larger bottle is preferred for large cavity, because γ_z scales as ρ_0^{-2}. However, more than two orders of magnitude larger bottle has been used in proton and antiproton experiments [115, 116, 118–120]. The only concern is that machining of the spherical trap is

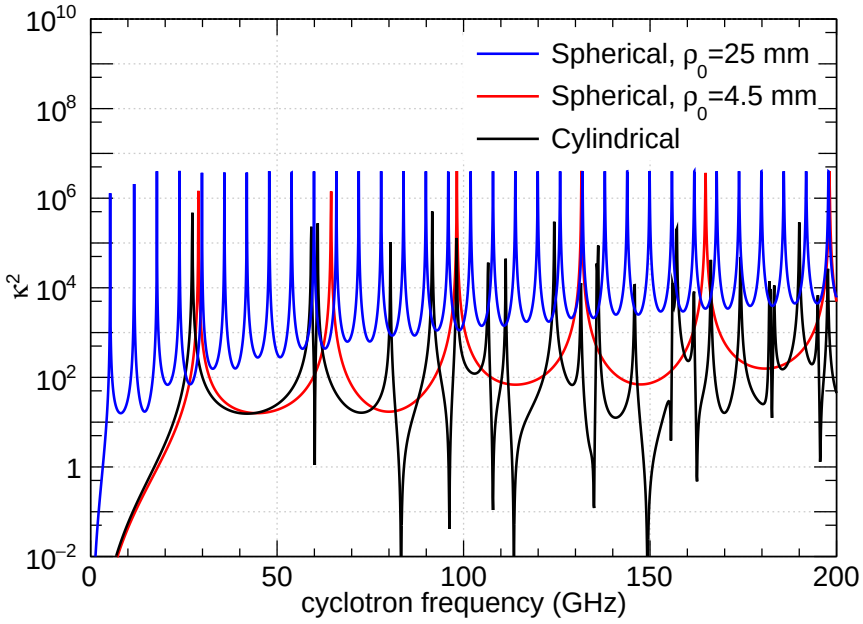


Figure 6.11: Calculation of the enhancement factor κ^2 for a spherical trap with radius $\rho_0 = 4.5$ mm (red) and $\rho_0 = 25$ mm (blue), compared with the cylindrical cavity used in this thesis (black).

more challenging, but extreme machining precision is not required for the DPDM search, so this should be possible. From the estimate here, the spherical cavity is a promising direction for the DPDM search.

6.4.4 Remaining Challenges and Future Limit

The use of n_e electrons and a larger trap with radius ρ_0 decrease the axial frequency shift for one electron's cyclotron transition as

$$\Delta\nu_z \text{ (from one cyclotron jump)} \propto B_2\, n_e^{-1}. \tag{6.27}$$

The bottle size scales as

$$B_2 \propto \rho_0^{-2} \tag{6.28}$$

and the detected power also drops as

$$P \propto \gamma_z z_A^2 \propto \rho_0^{-2} z_A^2. \tag{6.29}$$

Since the detected axial oscillation power is a product of γ_z and oscillation amplitude z_A, the decrease of the axial signal can be compensated to some extent. If the current ring electrode is replaced by a cobalt-iron electrode, B_2 will be 400 times larger than the B_2 in this thesis. Using $n_e = 10$ electrons decrease jump size by 10, and making the trap larger by 5 decreases by another factor of 25. The axial damping rate γ_z also decreases by a factor of 25, but exciting to 5 times larger amplitude should compensate for this. We assume a 5 times larger $\rho_0 = 25$ mm spherical trap is possible.

Future expected limit, with $n_e = 10$ electrons and 1 year total sweep time, using $\rho_0 = 25$ mm spherical cavity is shown in Fig. 6.12. One year of ramping is unrealistic with our magnet that consumes liquid helium, but is possible with a cryogen-free magnet. A dedicated apparatus for DPDM search yield much wider sensitivity and open a new method of DPDM searches.

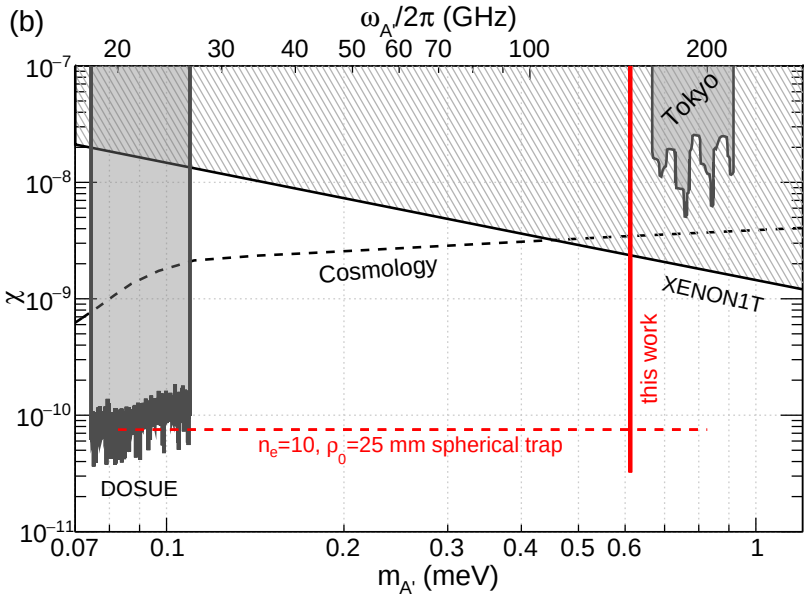


Figure 6.12: Expected DPDM limit with $n_e = 10$ electrons using a cavity of radius $\rho_0 = 25$ mm, with 1 year scan between 20 GHz and 170 GHz (red dash). The limit obtained by the search here (red solid) and limits from DM cosmology [130], XENON1T [158–160], DOSUE [164], and Tokyo dish antenna experiment [165] are also shown.

Chapter 7

Conclusion

A single isolated electron in a Penning trap yields a new measurement of the electron magnetic moment

$$g/2 = 1.001\ 159\ 652\ 180\ 59\ (13). \tag{7.1}$$

Combined with the Standard Model calculation, this yields an independent determination of the fine structure constant

$$\alpha^{-1} = 137.035\ 999\ 166\ (16). \tag{7.2}$$

Comparison of the measured g-factor and the predicted g-factor using an independent measurement of the fine structure constant yields the most stringent test of the Standard Model.

A new dilution refrigerator–superconducting solenoid system with significantly improved stability has been constructed. The new system has a more robust mechanical joint, which improves the long-term stability of the magnetic field. A Helium-3-based cryogenic NMR probe has been invented and used to optimize the homogeneity and the drift rate of the cryogenic bore magnet. The achieved low drift rate and robustness enables measurement of the g-factor at many widely different fields for the first time.

The statistical uncertainty has been improved by a factor of 4 because of the newly

developed system. The large systematic shift—microwave cavity correction—is studied in an eight times wider parameter range. A new correction model and characterization methods have been proposed. The g-factor is measured at 11 fields to confirm the new systematic correction method.

Three developments to improve the systematic error and precision for future measurements have been proposed and demonstrated. A new trap with an order of magnitude better anharmonicity is proposed and designed. The new trap is smaller than the current trap to suppress the microwave cavity correction. A new scheme to measure g-factor with direct measurement of the spin frequency is proposed and demonstrated. A superconducting quantum limited detector has been also developed to achieve 20 times narrower linewidth. All developments promise an improved measurement of the electron's g-factor.

The constructed system has been also used to search dark photon dark matter. The single trapped electron is used as a background-free detector at 0.6 meV. A new limit on dark photon is set with a week of data. The search demonstrates the sensitivity of the single electron and guarantees a future search in the 0.1–1 meV range.

The newly constructed system and a better understanding of the systematic error allow tests of the Standard Model and theories beyond it in many aspects. The same technique can be applied for the positron's g-factor measurement, which will be the most precise test of CPT in the lepton sector.

Appendix A

Microwave Resonances Probed by a Cloud of Electrons

The shift of the electron's cyclotron frequency due to the coupling between the cyclotron motion and Penning trap's microwave resonances is the largest systematic shift in the g-factor measurement (Chap. 4). A cloud of many trapped particles has been used to map the microwave resonances *in situ* [51, 166]. The resonances are mapped using the amplitude of parametrically pumped electron oscillators [100, 101, 167], but the detailed mechanism behind this method was not fully understood.

Here, we report another observation of coupling between microwave resonances and the axial oscillation—the oscillation of directly axially pumped electrons also depends on the microwave resonances. In addition to the traditional parametric drive, two different direct axial pumping schemes are compared: axial drive and magnetron sideband cooling drive. Although a complete understanding of the coupling has not been established yet, we summarize the observed couplings of axial oscillation and the cyclotron motion here.

A.1 Mapping Penning Trap Microwave Resonances

The microwave properties of the trap are approximated by an ideal cylindrical cavity with radius $\rho_0 = 4.539$ mm and height $2z_0 = 7.812$ mm. The characteristics of an ideal cylindrical microwave cavity are discussed in detail, for example, in [156]. The resonant modes are classified in two groups: transverse-electric modes TE_{mnp} and transverse-magnetic modes TM_{mnp}, where each mode is labeled by three integers: $m = 0, 1, 2, ...$, $n = 1, 2, 3, ...$, and $p = 1, 2, ...$ for TE modes and $p = 0, 1, 2, ...$ for TM modes. The complete expression of the electric field and magnetic field are:

$$\mathbf{E} = E_0 \frac{{}^{(E)}\omega_{mnp}}{c} \left(\frac{\rho_0}{x'_{mn}}\right)^2 \sin\left[\frac{p\pi}{2}\left(\frac{z}{z_0}+1\right)\right] \left[\mp\hat{\boldsymbol{\rho}}\frac{m}{\rho}J_m\left(x'_{mn}\frac{\rho}{\rho_0}\right)\cos\left({}^{(E)}\omega_{mnp}t \mp m\phi\right) - \hat{\boldsymbol{\phi}}\frac{x'_{mn}}{\rho_0}J'_m\left(x'_{mn}\frac{\rho}{\rho_0}\right)\sin\left({}^{(E)}\omega_{mnp}t \mp m\phi\right)\right] \tag{A.1}$$

$$\mathbf{B} = \frac{E_0}{c}\Bigg\{\hat{\boldsymbol{z}}J_m\left(x'_{mn}\frac{\rho}{\rho_0}\right)\sin\left[\frac{p\pi}{2}\left(\frac{z}{z_0}+1\right)\right]\cos\left({}^{(E)}\omega_{mnp}t \mp m\phi\right) + \frac{p\pi}{2z_0}\left(\frac{\rho_0}{x'_{mn}}\right)^2\cos\left[\frac{p\pi}{2}\left(\frac{z}{z_0}+1\right)\right] \left[\hat{\boldsymbol{\rho}}\frac{x'_{mn}}{\rho_0}J'_m\left(x'_{mn}\frac{\rho}{\rho_0}\right)\cos\left({}^{(E)}\omega_{mnp}t \mp m\phi\right) \pm \hat{\boldsymbol{\phi}}\frac{m}{\rho}J_m\left(x'_{mn}\frac{\rho}{\rho_0}\right)\sin\left({}^{(E)}\omega_{mnp}t \mp m\phi\right)\right]\Bigg\} \tag{A.2}$$

for TE_{mnp} modes, and

$$\mathbf{E} = E_0\Bigg\{\hat{\boldsymbol{z}}J_m\left(x_{mn}\frac{\rho}{\rho_0}\right)\cos\left[\frac{p\pi}{2}\left(\frac{z}{z_0}+1\right)\right]\cos\left({}^{(M)}\omega_{mnp}t \mp m\phi\right) - \frac{p\pi}{2z_0}\left(\frac{\rho_0}{x_{mn}}\right)^2\sin\left[\frac{p\pi}{2}\left(\frac{z}{z_0}+1\right)\right] \left[\hat{\boldsymbol{\rho}}\frac{x_{mn}}{\rho_0}J'_m\left(x_{mn}\frac{\rho}{\rho_0}\right)\cos\left({}^{(M)}\omega_{mnp}t \mp m\phi\right) \pm \hat{\boldsymbol{\phi}}\frac{m}{\rho}J_m\left(x_{mn}\frac{\rho}{\rho_0}\right)\sin\left({}^{(M)}\omega_{mnp}t \mp m\phi\right)\right]\Bigg\} \tag{A.3}$$

$$\mathbf{B} = \frac{E_0}{c}\frac{{}^{(M)}\omega_{mnp}}{c}\left(\frac{\rho_0}{x_{mn}}\right)^2 \cos\left[\frac{p\pi}{2}\left(\frac{z}{z_0}+1\right)\right] \left[\pm\hat{\boldsymbol{\rho}}\frac{m}{\rho}J_m\left(x_{mn}\frac{\rho}{\rho_0}\right)\cos\left({}^{(M)}\omega_{mnp}t \mp m\phi\right) + \hat{\boldsymbol{\phi}}\frac{x_{mn}}{\rho_0}J'_m\left(x_{mn}\frac{\rho}{\rho_0}\right)\sin\left({}^{(M)}\omega_{mnp}t \mp m\phi\right)\right], \tag{A.4}$$

for TM_{mnp} modes. The corresponding resonant frequencies are

$$\begin{aligned} {}^{(E)}\omega_{mnp} &= c\sqrt{\left(\frac{x'_{mn}}{\rho_0}\right)^2 + \left(\frac{p\pi}{2z_0}\right)^2} \\ {}^{(M)}\omega_{mnp} &= c\sqrt{\left(\frac{x_{mn}}{\rho_0}\right)^2 + \left(\frac{p\pi}{2z_0}\right)^2}. \end{aligned} \tag{A.5}$$

Here, x_{mn} is the nth zero of the order-m Bessel function $J_m(x)$, and x'_{mn} is the nth zero of the derivative of the order-m Bessel function $J'_m(x)$. All but $m = 0$ modes are doubly degenerate, indicated by the $\pm$ sign.

Only TM_{1np} and TM_{1np} modes have non-vanishing transverse electric field at $\rho = 0$. Those with odd p have anti-node at the center $z = 0$ and thus couple to the trapped electrons strongly. Those with even p have a node at $z = 0$, but finite axial oscillation amplitude creates coupling. A large cloud of electrons also generates coupling between trapped electrons and the modes other than TM_{1np} and TM_{1np}.

Coupling of the microwave resonances and the axial oscillation of driven electrons is observed in three axial drives: (a) parametric drive, (b) axial drive, and (c) magnetron sideband drive (Fig. A.1). The details of the drives are explained in Chap. 2. The frequency of the resonant modes agree with the analytical resonant frequencies within a few percent of relative uncertainty (Chap. 4).

The vertical axis of Fig. A.1 is the integral of the shaded region in Fig. A.2. Figure A.2 shows the output from the axial amplifier in the frequency domain measured by a spectrum analyzer. The gray curve shows the spectrum when cyclotron frequency is off-resonant from any cavity mode, and the black curve is the spectrum when on resonance. For the parametric

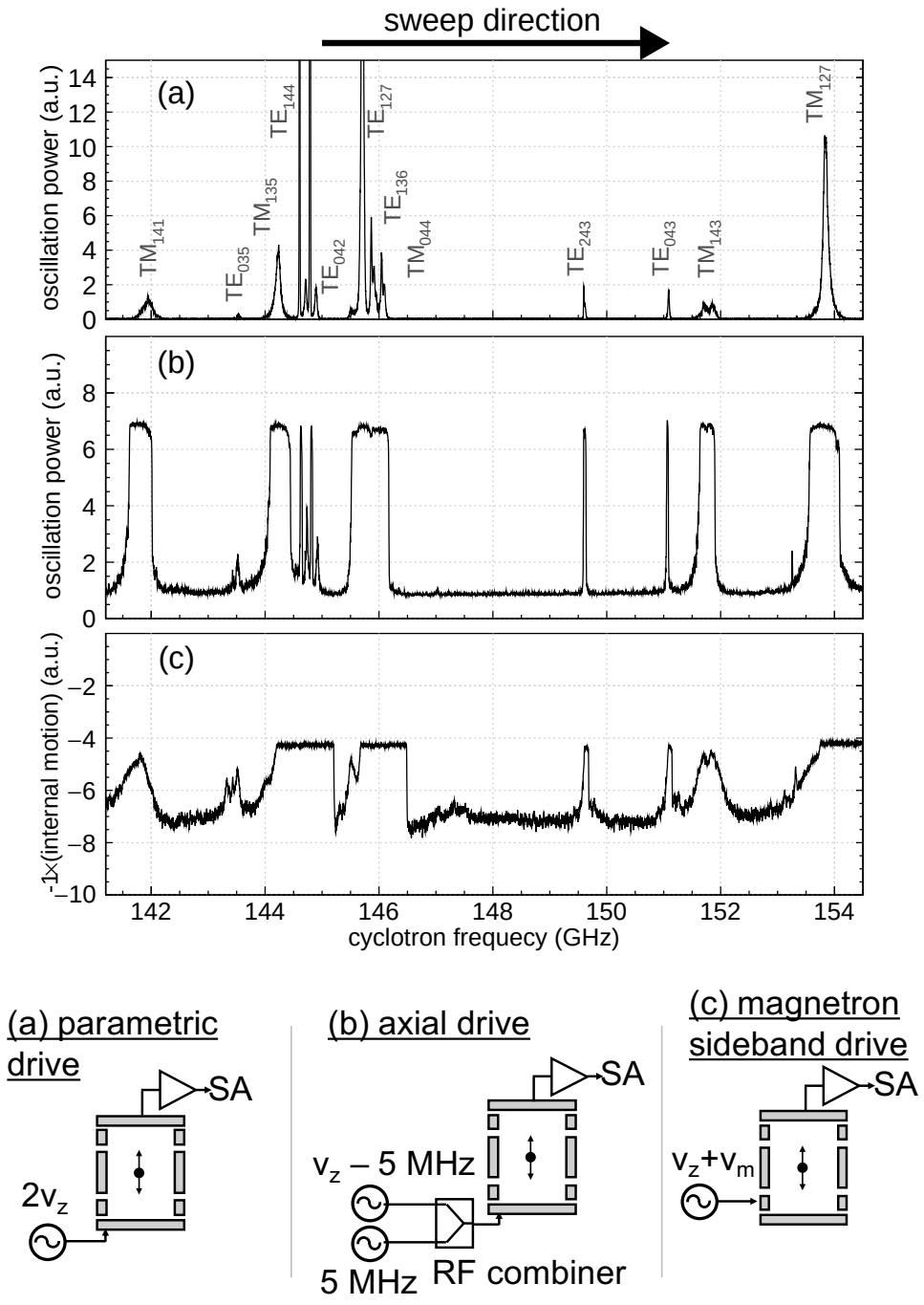


Figure A.1: Mapping the microwave cavity resonances with (a) parametric drive (b) axial drive and (c) magnetron sideband drive. The vertical axis is the integral of the Fourier spectrum for the shaded range in Fig. A.2.

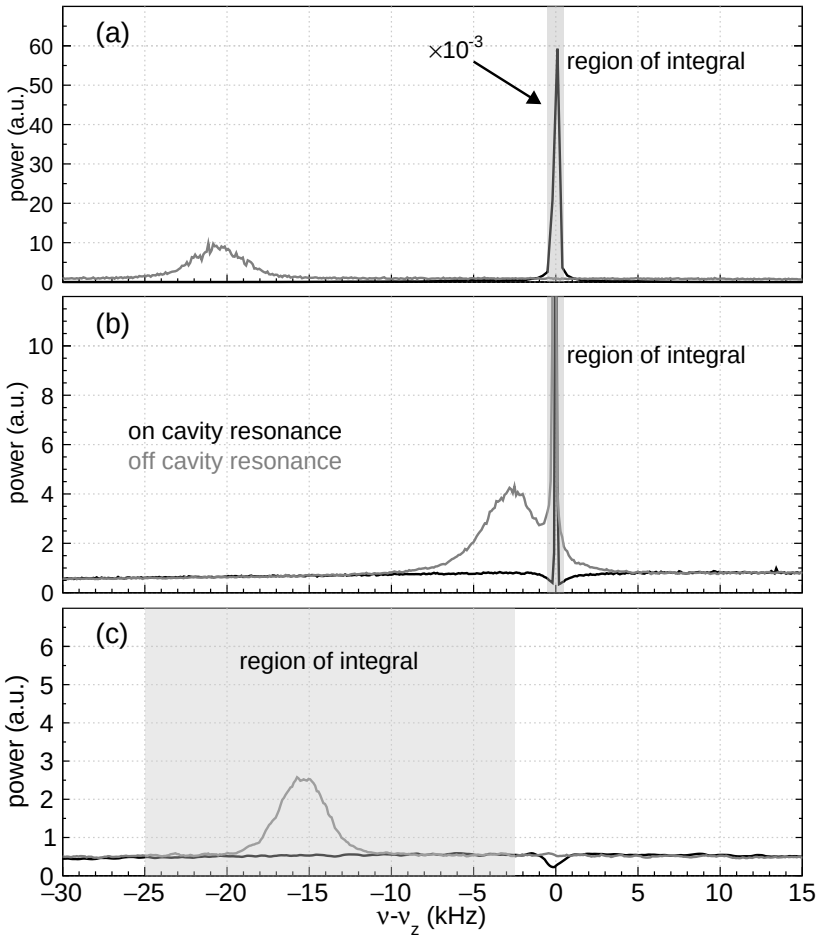


Figure A.2: Fourier spectrum around the axial frequency ν_z when cyclotron frequency is on cavity resonance (black) and off cavity resonance (gray) for (a) parametric drive (b) axial drive and (c) magnetron sideband drive. The anharmonicity of the trap is set at $C_4 = -0.036$.

drive (a) and the axial drive (b), the region is defined to cover the center of mass oscillation power. For the magnetron drive (c), the region is defined to cover the "bump", which we interpret as the excitation of the electron cloud's internal motion. The y-axis in Fig. A.1 (c) is multiplied by -1 to compare the resonance with the other two plots.

A couple of important features need to be emphasized.

- Emergence of small "bump" is visible for all three excitation schemes when off-resonance. We interpret this as the excitation of the internal motion of the trapped electrons. The internal motion is cooled by high γ_c near resonances.

- The signal-to-baseline ratio of the parametric drive is much better than the other two schemes. The black line in Fig. A.2 (a) is scaled by 10^{-3} to show in the same vertical scale, so the actual amplitude is three orders of magnitude larger than the height in Fig. A.2 (a).

- The mapping in the axial drive and magnetron sideband drive clearly shows saturation [Fig. A.1 (b) and (c)]. The black lines in Fig. A.2 (b) and (c) are the spectrum when this saturation occurs. They show dips at the axial frequency, which suggests that the electrons' internal motion is completely cooled, and they behave as one rigid sphere in the saturated condition.

The consistency of three different excitation schemes suggests an underlying simplicity. The small "bump" disappears near the cavity resonances, which suggests that it is related to the efficiency of cooling of cyclotron motion. It is known that the transfer of energy between the transverse cyclotron motion and axial internal motion is very efficient for the high number of electrons [168, 169]. What is unique here is that the well-cooled internal motion results in a higher axial center of mass amplitude, even if the axial drive amplitude is constant. The extremely better signal-to-baseline ratio for the parametric drive also suggests that the parametric drive has a unique feature compared to the other two methods.

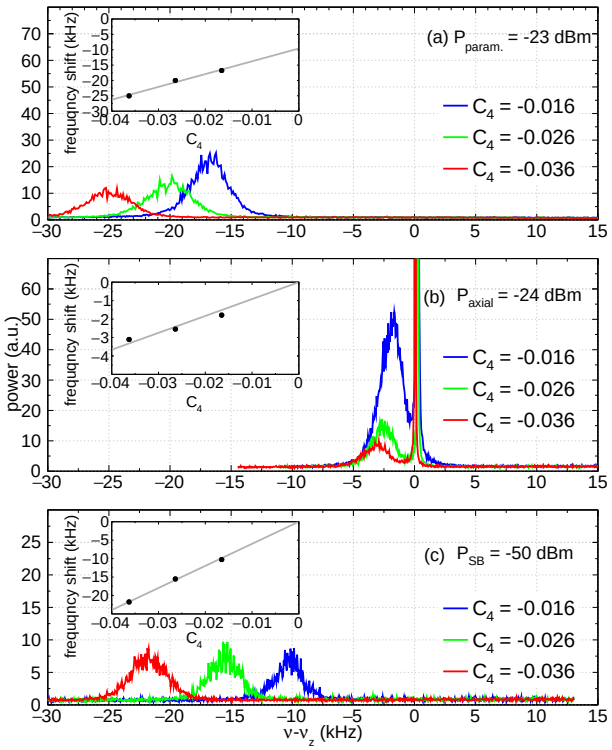


Figure A.3: Excitation of internal motion of $N = 100$ electrons for different anharmonicity C_4 by (a) parametric drive (b) axial drive, and (c) sideband drive.

A.2 Characterizing the Internal Motion

Observations about the coupling between the axial signal and microwave resonances are summarized here. Based on these observations, We interpret the "bump" that appears at off-resonance as the axial internal motion of electrons.

A.2.1 Exciting and Detecting the Internal Motion

We first find that the internal motion is more efficiently excited for larger C_4 (Fig. A.3). The excited small internal motion shifts further away from the main peak at ν_z for all three drives, which suggests that the excitation of internal motion is related to the nonlinearity C_4. The frequency shift of the internal motion is plotted as a function of C_4 for each drive scheme in the insets of Fig. A.3. A linear line fits well with axial and magnetron sideband drives, but has offset for the parametric drive.

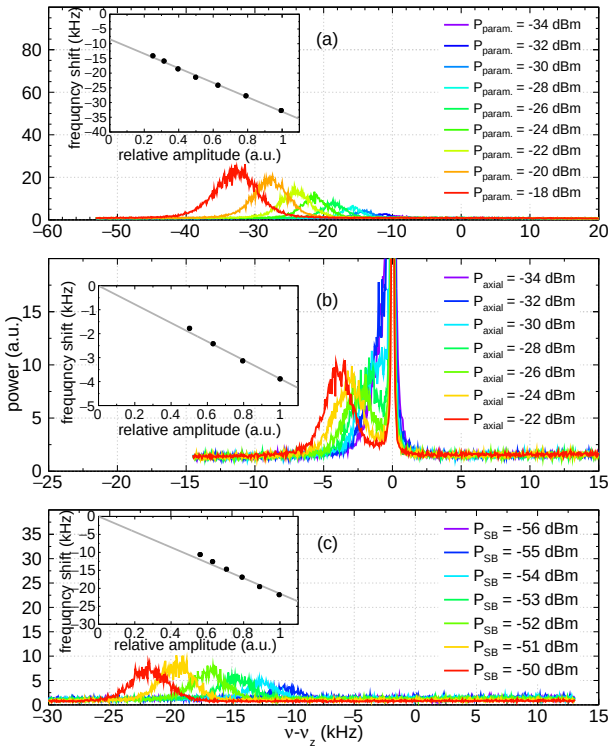


Figure A.4: Excitation of internal motion of $N = 100$ electrons for different drive power by (a) parametric drive (b) axial drive, and (c) sideband drive with $C_4 = -0.036$.

Figure A.4 shows the output signal for different drive power with $C_4 = -0.036$. The stronger excitation of the internal motion can be observed for all three drives for high drive power. The peak frequency of the internal motion shifts downward for higher drive power. We plot the shift of the peak frequency for different drive amplitudes in the insets of Fig. A.4. The x-axis is the linear drive power normalized by the maximum drive amplitude for each drive. A linear line fits well for axial and magnetron excitations, but has an offset for the parametric excitation. The internal motion is excited more for a stronger axial drive.

The internal motion also should be excited if the cyclotron motion is heated. A strong microwave drive excites the cyclotron motion, which transfers energy to the axial internal motion through collisions. The excited microwave motion also heats the magnetron motion if the drive is too strong and is applied for a long time. We tune our drive power to be weak enough that the magnetron heating is negligible. Figure A.5 shows the Fourier spectrum at $C_4 = -0.036$ with different powers of resonant microwave drives. The shift of the dip is

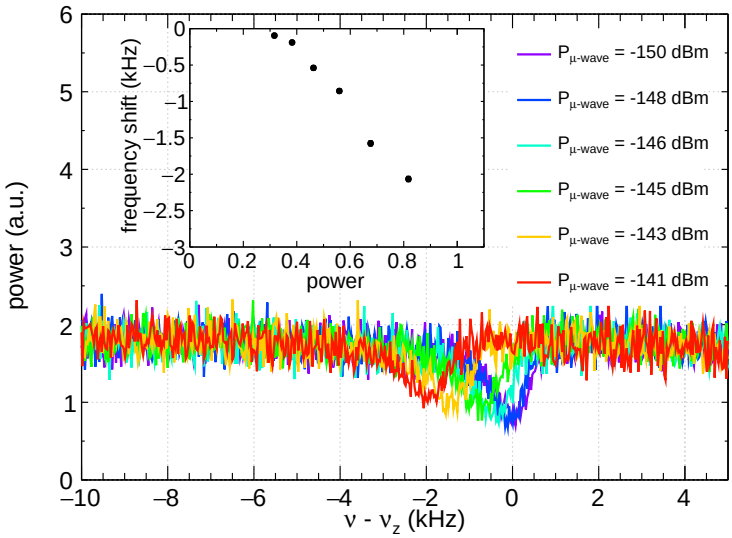


Figure A.5: Exciting the internal motion of $N = 100$ electrons by a microwave drive with anharmonicity parameter $C_4 = -0.036$.

visible as the microwave power increases.

Another indication of the heating and cooling of internal motion is observed when the microwave drive is turned off. Figure A.6 (a) shows the relaxation of the dip frequency to the original axial frequency when the microwave drive is turned off. Measurements at the opposite sign of C_4 and at different cyclotron damping rates γ_c are shown. The dip frequency exponentially drifts back to the original axial frequency with a time constant τ'. The cyclotron lifetime τ_c is measured from the lifetime of the first excited quantum cyclotron state [51] using the quantum non-demolition measurement [69]. Relaxation of the dip frequency to the initial axial frequency with different time constants is observed. Figure A.6 (b) plots the measured relaxation time constant τ' versus the cyclotron lifetime τ_c. The data fit well with a linear function, with the coefficient 3/2. This factor of 3/2 has been observed for the cooling rate of non-neutral plasma [166]. It originates from the cooling of internal motion, which has three degrees of freedom, by cyclotron damping, which has transverse two degrees of freedom [168, 169].

In the completely cooled limit, all electrons move together as a rigid body and the behavior is described by the center of mass motion of N electrons. We can observe the

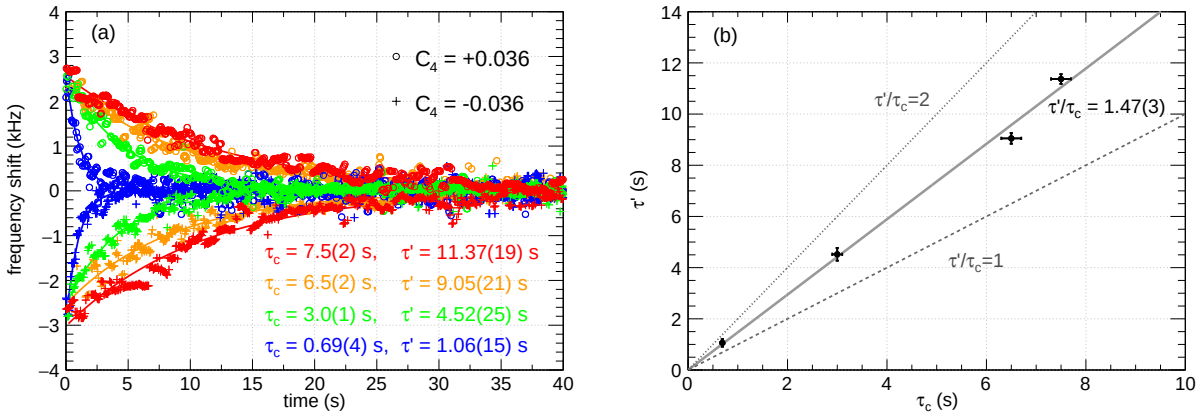


Figure A.6: Relaxation of the dip frequency after microwave drive is turned off. Measurements with different C_4 and γ_c are shown in time domain (a) and in two dimensional plot (b).

deviation from the rigid body limit by comparing the driven signal at different cyclotron damping γ_c. Figure A.7 shows the driven CM amplitude of $N = 100$ electrons at two different cyclotron frequencies with $C_4 = -0.01$. All parameters are the same except for the cyclotron frequency. The black line is taken at a strong microwave resonance, where the oscillation amplitude is "saturated" in Fig. A.1. The grey line is taken with the cyclotron frequency far away from any microwave mode.

The vertical axis is the absolute amplitude of the center of mass motion of the cloud. When the cyclotron damping γ_c is high enough that the internal motion is efficiently cooled, the electrons behave as a rigid body, and the driven amplitude is exactly described by an anharmonic oscillator (black line in Fig. A.7). The emergence of internal motion is observed in the gray line, where the oscillation amplitude falls suddenly, but not all the way to zero, and the driven response becomes much less stable. A long tail exists after the amplitude drops, resulting from the excited internal motion. The Fourier spectrum on a spectrum analyzer when the internal motion is excited has the "bump" shown in Fig. A.2, Fig. A.3, and Fig. A.4

All the observations in this section suggest that the internal motion is excited for a strongly driven cloud through anharmonicity C_4. The observation of internal motion is

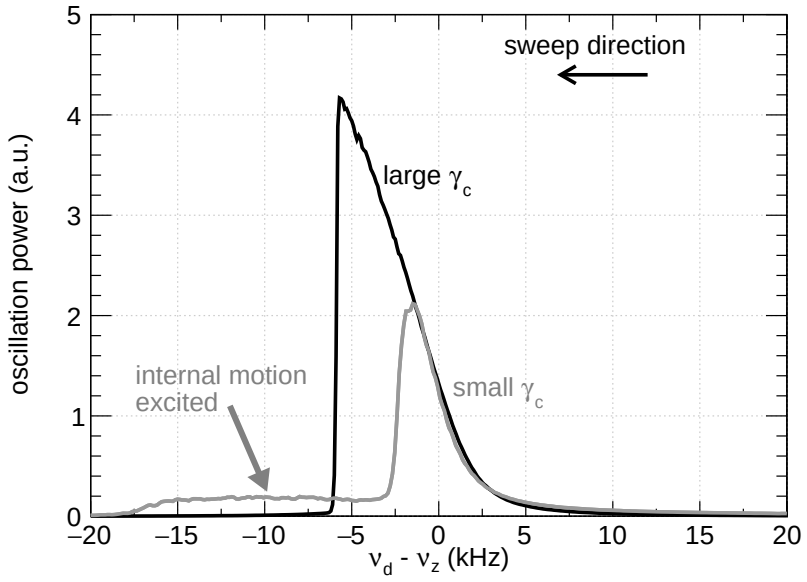


Figure A.7: Center of mass oscillation of a cloud for large and small γ_c's with $C_4 = -0.01$ and $P_{\text{axial}} = -30$ dBm axial drive. γ_c is varied by changing the cyclotron frequency.

familiar in non-neutral plasma physics. However, it has not been investigated very much in such a low temperature and a low number of electrons.

A.2.2 Temperature Effect, Saturation, and Hysteresis

The mapping of the microwave cavity modes by parametric drive shows a clear Lorentzian shape. However the spectrum with axial excitation and magnetron sideband excitation are less attractive due to the saturation in Fig. A.1. Our observations indicate that the saturation is because of completely cooled internal motion, where all electrons move together as a rigid body. We take one very well isolated cavity mode, TM_{127} at 153 GHz, and study the conditions for saturation.

An intuitive way to mitigate saturation is to increase the physical temperature of the Penning trap. Figure A.8 shows a scan of TE_{127} mode with different temperatures. The temperature is measured by a calibrated Ruthenium oxide sensor attached to the vacuum chamber. The interval between each measurement is 12 hours, much longer than the time constant of cooling the electrodes from 1 K to 100 mK (about 3 hours). A gradual transition

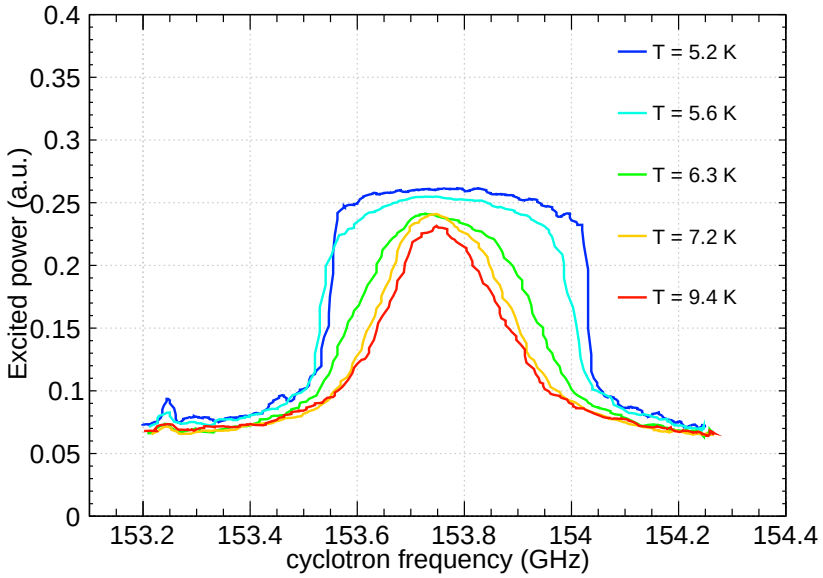


Figure A.8: Scanning the cyclotron frequency around the TM_{127} mode with different temperatures.

from saturated line shape to smooth Lorentzian-like line shape is observed. The trend of weak saturation at high temperatures has been observed for all three drive schemes.

A natural comparable temperature scale is the cyclotron motion's energy $\hbar\omega_c/k_B = 7.3$ K. One hypothesis was that the reduction of saturation is due to occupancy of higher quantum cyclotron states. To check if the temperature effect depends on the magnetic field, the required power to excite internal motion is measured at different magnetic fields (Fig. A.9).

We measure the threshold power to excite the internal motion. A cloud shows a dip when the internal motion is not excited. However, for a drive stronger than the threshold power, the internal motion appears as a bump on the broad noise spectrum (Fig. A.4). The magnetron sideband drive is employed to keep the magnetron radius small during the whole measurement process. The same cloud is used without being damped during the three measurements. It reveals that the temperature scale for internal motion excitation is independent of the magnetic field.

A few concerns need to be addressed. Changing the physical temperature changes many parameters. The dimension of the trap changes due to thermal expansion by only about

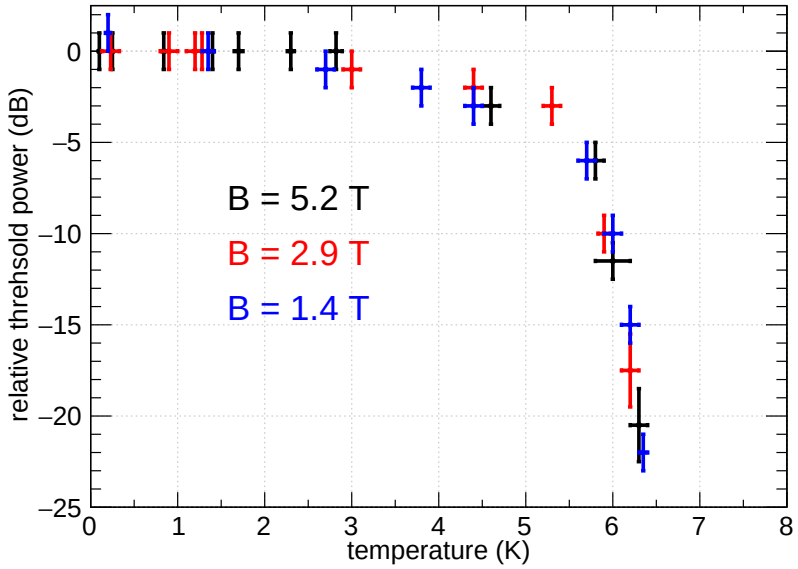


Figure A.9: Dependence of threshold power to excite the internal motion on temperature. Three curves for different magnetic fields are shown.

10^{-5} from 50 mK to 10 K, so this change is small to account for the observed drastic change. At higher temperatures, the difference between internal motion's temperature and the wall's temperature becomes smaller. However, the cloud's oscillation amplitude is estimated to be much higher than 100 K, so this effect should be negligible. We do not exactly know what is causing the weaker saturation at higher temperatures, but the trend itself is reproducible in any of the three drive schemes in many different cooldowns.

The temperature effect needs to be emphasized. Historically, the dependence of parametrically driven oscillation amplitude on the cavity resonances was discovered at 4.2 K [100, 101, 167], where it was found that "the line shapes and widths remain constant as the pump strength and number of electrons is varied over a wide range." However, in the later studies with the same trap dimensions but at 100 mK [7, 50, 51], it was found that they were "not currently always able to robustly produce such spectra." During our measurement campaign, we also find that the mapping with any of the three drives shows less saturation and is more robust at 4 K than at 50 mK. The axial oscillation frequency and damping rate are also tested, but the saturation behavior is the same. These observations suggest that higher

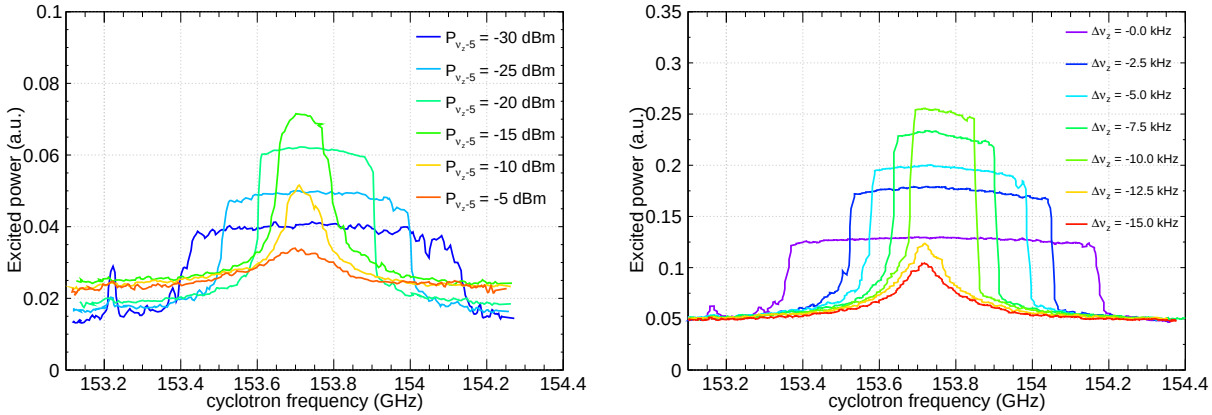


Figure A.10: (a) Mode mapping with different drive power. (b) Mode mapping with different detuning.

temperature helps regardless of axial oscillation conditions. We believe that the physical temperature of the trap is one of the key parameters for reliable mode mapping. Later data are all taken at 4 K to avoid saturation and to reliably observe the ideal line shape.

Another way to avoid saturation even at the same temperature is to put more energy into the internal motion. This can be done by (a) applying a stronger drive or (b) increasing the detuning of the drive (Fig. A.10). Transitions from saturated line shape to smooth Lorentzian-like line shape are observed for both scans.

Hysteresis is also observed when the internal motion is completely cooled and reaches the rigid body limit. Figure A.11 shows the observed hysteresis for (a) axial drive and (b) magnetron sideband drive. In both cases, as the drive power increase, the hysteresis disappears. Notice that no hysteresis is observed when the cloud does not reach the rigid body limit.

A.3 Summary

Excitation and cooling of electrons' internal motion have been observed with three axial drives. All the observed phenomena in this section support the hypothesis based on the internal motion. Theories that can explain these phenomena is required.

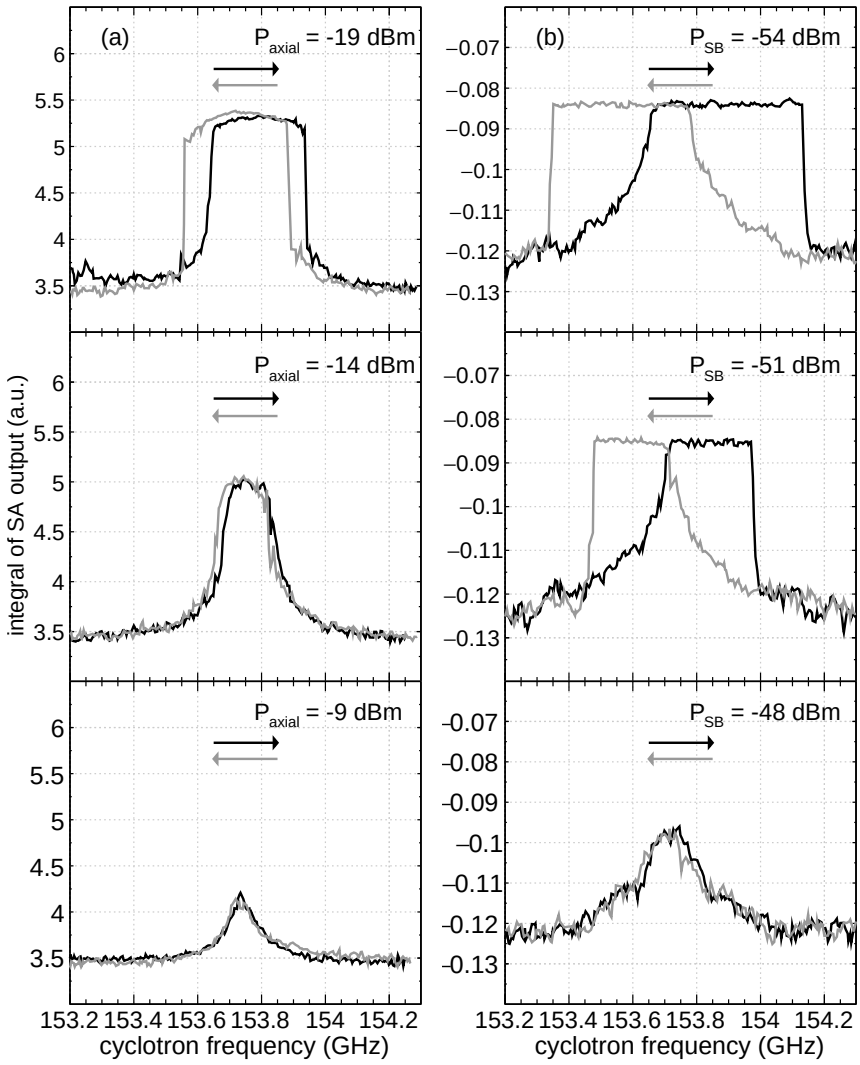


Figure A.11: Observed hysteresis of trapped cloud excited by (a) axial drive and (b) magnetron sideband drive for three different excitation powers.

Even if the exact theory is unknown, the microwave cavity resonances are clearly detected. Characterizing a microwave cavity through the axial oscillations does not require any microwave drive or detection source. The studies here could trigger new studies of the internal motion of trapped charged particles.

Bibliography

[1] P. A. M. Dirac, Proc. R. Soc. Ser. A **117**, 610 (1928).

[2] P. Kusch and H. M. Foley, Phys. Rev. **72**, 1256 (1947).

[3] J. Schwinger, Phys. Rev. **73**, 416 (1948).

[4] S. Tomonaga, Prog. Theor. Phys. **1**, 27 (1946).

[5] R. P. Feynman, Rev. Mod. Phys. **20**, 367 (1948).

[6] J. Schwinger, Phys. Rev. **74**, 1439 (1948).

[7] D. Hanneke, S. Fogwell, and G. Gabrielse, Phys. Rev. Lett. **100**, 120801 (2008).

[8] T. Aoyama, T. Kinoshita, and M. Nio, Atoms **7**, (2019).

[9] C. M. Sommerfield, Annals of Physics **5**, 26 (1958).

[10] A. Petermann, Nuclear Physics **5**, 677 (1958).

[11] S. Laporta and E. Remiddi, Physics Letters B **379**, 283 (1996).

[12] S. Laporta, Physics Letters B **772**, 232 (2017).

[13] T. Aoyama, M. Hayakawa, T. Kinoshita, and M. Nio, Phys. Rev. D **91**, 033006 (2015).

[14] T. Aoyama, T. Kinoshita, and M. Nio, Phys. Rev. D **97**, 036001 (2018).

[15] H. Elend, Physics Letters **20**, 682 (1966).

[16] M. A. Samuel and G. Li, Phys. Rev. D **44**, 3935 (1991).

[17] G. Li, R. Mendel, and M. A. Samuel, Phys. Rev. D **47**, 1723 (1993).

[18] S. Laporta and E. Remiddi, Physics Letters B **301**, 440 (1993).

[19] S. Laporta, Il Nuovo Cimento A (1965-1970) **106**, 675 (1993).

[20] A. Kurz, T. Liu, P. Marquard, and M. Steinhauser, Nuclear Physics B **879**, 1 (2014).

[21] T. Aoyama, M. Hayakawa, T. Kinoshita, and M. Nio, Phys. Rev. Lett. **109**, 111807 (2012).

[22] P. J. Mohr, D. B. Newell, and B. N. Taylor, Rev. Mod. Phys. **88**, 035009 (2016).

[23] M. Tanabashi *et al.*, Phys. Rev. D **98**, 030001 (2018).

[24] Jegerlehner, Fred, EPJ Web Conf. **218**, 01003 (2019).

[25] C. G. Parthey *et al.*, Phys. Rev. Lett. **107**, 203001 (2011).

[26] H. Fleurbaey, S. Galtier, S. Thomas, M. Bonnaud, L. Julien, F. m. c. Biraben, F. m. c. Nez, M. Abgrall, and J. Guéna, Phys. Rev. Lett. **120**, 183001 (2018).

[27] A. Beyer *et al.*, Science **358**, 79 (2017).

[28] M. P. Bradley, J. V. Porto, S. Rainville, J. K. Thompson, and D. E. Pritchard, Phys. Rev. Lett. **83**, 4510 (1999).

[29] S. Sturm, F. Köhler, J. Zatorski, A. Wagner, Z. Harman, G. Werth, W. Quint, C. H. Keitel, and K. Blaum, Nature **506**, 467 (2014).

[30] L. Morel, Z. Yao, P. Cladé, and S. Guellati-Khélifa, Nature **588**, 61 (2020).

[31] R. H. Parker, C. Yu, W. Zhong, B. Estey, and H. Müller, Science **360**, 191 (2018).

[32] A. Beyer *et al.*, Science **358**, 79 (2017).

[33] H. Fleurbaey, S. Galtier, S. Thomas, M. Bonnaud, L. Julien, F. m. c. Biraben, F. m. c. Nez, M. Abgrall, and J. Guéna, Phys. Rev. Lett. **120**, 183001 (2018).

[34] C. G. Parthey *et al.*, Phys. Rev. Lett. **107**, 203001 (2011).

[35] A. Antognini *et al.*, Science **339**, 417 (2013).

[36] E. Tiesinga, P. J. Mohr, D. B. Newell, and B. N. Taylor, Rev. Mod. Phys. **93**, 025010 (2021).

[37] M. Wang, G. Audi, F. G. Kondev, W. Huang, S. Naimi, and X. Xu, Chinese Physics C **41**, 030003 (2017).

[38] F. Khler, S. Sturm, A. Kracke, G. Werth, W. Quint, and K. Blaum, Journal of Physics B: Atomic, Molecular and Optical Physics **48**, 144032 (2015).

[39] B. J. Mount, M. Redshaw, and E. G. Myers, Phys. Rev. A **82**, 042513 (2010).

[40] M. P. Bradley, J. V. Porto, S. Rainville, J. K. Thompson, and D. E. Pritchard, Phys. Rev. Lett. **83**, 4510 (1999).

[41] C. Carlberg, T. Fritioff, and I. Bergström, Phys. Rev. Lett. **83**, 4506 (1999).

[42] D. Banerjee *et al.*, Phys. Rev. Lett. **123**, 121801 (2019).

[43] E. Cortina Gil *et al.*, Journal of High Energy Physics **2019**, 182 (2019).

[44] J. P. Lees *et al.*, Phys. Rev. Lett. **119**, 131804 (2017).

[45] A. V. Artamonov *et al.*, Phys. Rev. D **79**, 092004 (2009).

[46] A. L. Read, Journal of Physics G: Nuclear and Particle Physics **28**, 2693 (2002).

[47] G. W. Bennett and *et al.*, Phys. Rev. D **73**, 072003 (2006).

[48] T. Aoyama *et al.*, Physics Reports **887**, 1 (2020), the anomalous magnetic moment of the muon in the Standard Model.

[49] B. Abi *et al.*, Phys. Rev. Lett. **126**, 141801 (2021).

[50] B. Odom, D. Hanneke, B. D'Urso, and G. Gabrielse, Phys. Rev. Lett. **97**, 030801 (2006).

[51] D. Hanneke, S. Fogwell Hoogerheide, and G. Gabrielse, Phys. Rev. A **83**, 052122 (2011).

[52] L. S. Brown, G. Gabrielse, K. Helmerson, and J. N. Tan, Phys. Rev. A **32**, 3204 (1985).

[53] L. S. Brown, G. Gabrielse, K. Helmerson, and J. Tan, Phys. Rev. Lett. **55**, 44 (1985).

[54] L. S. Brown and G. Gabrielse, Rev. Mod. Phys. **58**, 233 (1986).

[55] L. S. Brown and G. Gabrielse, Phys. Rev. A **25**, 2423 (1982).

[56] G. Gabrielse and H. Dehmelt, Phys. Rev. Lett. **55**, 67 (1985).

[57] R. S. Van Dyck, Jr., P. B. Schwinberg, and H. G. Dehmelt, in *New Frontiers in High Energy Physics*, edited by B. Kursunoglu, A. Perlmutter, and L.Scott (Plenum, New York, 1978), p. 159.

[58] J. Tan and G. Gabrielse, Appl. Phys. Lett. **55**, 2144 (1989).

[59] G. Gabrielse and F. C. MacKintosh, Intl. J. of Mass Spec. and Ion Proc. **57**, 1 (1984).

[60] B. Odom, Ph.D. thesis, Harvard University, 2004, (thesis advisor: G. Gabrielse).

[61] G. Gabrielse, X. Fei, L. A. Orozco, R. L. Tjoelker, J. Haas, H. Kalinowsky, T. A. Trainor, and W. Kells, Phys. Rev. Lett. **65**, 1317 (1990).

[62] S. Sellner *et al.*, New Journal of Physics **19**, 083023 (2017).

[63] G. Gabrielse, Phys. Rev. A **27**, 2277 (1983).

[64] B. D'Urso, Ph.D. thesis, Harvard University, 2003, (thesis advisor: G. Gabrielse).

[65] R. H. Fowler and L. Nordheim, Proceedings of the Royal Society of London. Series A, Containing Papers of a Mathematical and Physical Character **119**, 173 (1928).

[66] D. J. Wineland and H. G. Dehmelt, J. Appl. Phys. **46**, 919 (1975).

[67] B. D'Urso, R. Van Handel, B. Odom, D. Hanneke, and G. Gabrielse, Phys. Rev. Lett. **94**, 113002 (2005).

[68] R. Van Dyck, Jr., P. Ekstrom, and H. Dehmelt, Nature **262**, 776 (1976).

[69] S. Peil and G. Gabrielse, Phys. Rev. Lett. **83**, 1287 (1999).

[70] X. Fan, S. E. Fayer, and G. Gabrielse, Review of Scientific Instruments **90**, 083107 (2019).

[71] J. L. Flowers, B. W. Petley, and M. G. Richards, Metrologia **30**, 75 (1993).

[72] T. R. Gentile, P. J. Nacher, B. Saam, and T. G. Walker, Rev. Mod. Phys. **89**, 045004 (2017).

[73] G. D. Cates, S. R. Schaefer, and W. Happer, Phys. Rev. A **37**, 2877 (1988).

[74] M. Himbert, J. Dupont-Roc, and C. Lhuillier, Phys. Rev. A **39**, 6170 (1989).

[75] E. L. Hahn, Phys. Rev. **80**, 580 (1950).

[76] Quantum Design Inc., `https://www.qdusa.com/products/mpms3.html`.

[77] T. E. Chupp, R. A. Loveman, A. K. Thompson, A. M. Bernstein, and D. R. Tieger, Phys. Rev. C **45**, 915 (1992).

[78] R. Chapman and M. G. Richards, Phys. Rev. Lett. **33**, 18 (1974).

[79] K. Luszczynski, R. E. Norberg, and J. E. Opfer, Phys. Rev. **128**, 186 (1962).

[80] N. R. Newbury, A. S. Barton, G. D. Cates, W. Happer, and H. Middleton, Phys. Rev. A **48**, 4411 (1993).

[81] C. P. Lusher, M. F. Secca, and M. G. Richards, Journal of Low Temperature Physics **72**, 25 (1988).

[82] J. B. Wooten, J. Jacobus, J. E. Gurst, W. Egan, W. G. Rhodes, and K. Wagener, Journal of Chemical Education **56**, 304 (1979).

[83] R. Chapman, Phys. Rev. A **12**, 2333 (1975).

[84] R. Barbé, F. Laloë, and J. Brossel, Phys. Rev. Lett. **34**, 1488 (1975).

[85] F. Kober, P.-. Wolf, J.-L. Leviel, G. Vermeulen, G. Duhamel, A. Delon, J. Derouard, M. Dcorps, and A. Ziegler, Magnetic Resonance in Medicine **41**, 1084 .

[86] W. Zheng, H. Gao, Q. Ye, and Y. Zhang, Phys. Rev. A **83**, 061401 (2011).

[87] P. Bendel, Journal of Magnetic Resonance **86**, 509 (1990).

[88] P. Le Doussal and P. N. Sen, Phys. Rev. B **46**, 3465 (1992).

[89] H. Y. Carr and E. M. Purcell, Phys. Rev. **94**, 630 (1954).

[90] S. Meiboom and D. Gill, Review of Scientific Instruments **29**, 688 (1958).

[91] F. Kober, B. Koenigsberg, V. Belle, M. Viallon, J. Leviel, A. Delon, A. Ziegler, and M. Dcorps, Journal of Magnetic Resonance **138**, 308 (1999).

[92] L. S. Brown, Ann. Phys. (N.Y.) **159**, 62 (1985).

[93] L. S. Brown, Phys. Rev. Lett. **52**, 2013 (1984).

[94] X. Fan and G. Gabrielse, Phys. Rev. A **103**, 022824 (2021).

[95] X. Fan and G. Gabrielse, Phys. Rev. Lett. **126**, 070402 (2021).

[96] in *Charged Particle Traps: Physics and Techniques of Charged Particle Field Confinement* (Springer Berlin Heidelberg, Berlin, Heidelberg, 2005), pp. 139–147.

[97] M. J. Borchert, Challenging the Standard Model by high precision comparisons of the fundamental properties of antiprotons and protons, 2021, presented 28 Jan 2021.

[98] G. Schneider, Ph.D. thesis, Mainz, 2018.

[99] P. R. Bevington and D. K. Robinson, *Data reduction and error analysis for the physical sciences* (PUBLISHER, ADDRESS, 2003).

[100] J. Tan and G. Gabrielse, Phys. Rev. A **48**, 3105 (1993).

[101] J. Tan and G. Gabrielse, Phys. Rev. Lett. **67**, 3090 (1991).

[102] D. Hanneke, Ph.D. thesis, Harvard University, 2007, (thesis advisor: G. Gabriesle).

[103] R. S. Van Dyck, Jr., P. B. Schwinberg, and H. G. Dehmelt, Phys. Rev. Lett. **59**, 26 (1987).

[104] F. L. Palmer, Phys. Rev. A **47**, 2610 (1993).

[105] M. Schmelling, Averaging Measurements with Hidden Correlations and Asymmetric Errors, 2000.

[106] G. Gabrielse, H. Dehmelt, and W. Kells, Phys. Rev. Lett. **54**, 537 (1985).

[107] C. H. Tseng, D. Enzer, G. Gabrielse, and F. L. Walls, Phys. Rev. A **59**, 2094 (1999).

[108] C. Hilbert and J. Clarke, Journal of Low Temperature Physics **61**, 263 (1985).

[109] M. Mück, M.-O. Andr, J. Clarke, J. Gail, and C. Heiden, Applied Physics Letters **72**, 2885 (1998).

[110] ez-SQUID Germany, `http://www.ez-squid.de/`.

[111] M. Mück, J. B. Kycia, and J. Clarke, Applied Physics Letters **78**, 967 (2001).

[112] S. Asztalos *et al.*, Nuclear Instruments and Methods in Physics Research Section A: Accelerators, Spectrometers, Detectors and Associated Equipment **656**, 39 (2011).

[113] S. J. Asztalos *et al.*, Phys. Rev. Lett. **104**, 041301 (2010).

[114] J. Jaycox and M. Ketchen, IEEE Transactions on Magnetics **17**, 400 (1981).

[115] H. Nagahama and *et al.*, Nature Comm. 14084 (2017).

[116] J. DiSciacca *et al.*, Phys. Rev. Lett. **110**, 130801 (2013).

[117] X. Fan, S. E. Fayer, T. G. Myers, B. A. D. Sukra, G. Nahal, and G. Gabrielse, Review of Scientific Instruments **92**, 023201 (2021).

[118] S. Ulmer and *et al.* (BASE Collaboration), Nature **524**, (2015).

[119] G. Schneider *et al.*, Science **358**, 1081 (2017).

[120] C. Smorra *et al.*, Nature **550**, 371 (2017).

[121] X. Fan, G. Gabrielse, P. W. Graham, R. Harnik, T. G. Myers, H. Ramani, B. A. D. Sukra, S. S. Y. Wong, and Y. Xiao, (2022).

[122] F. Zwicky, Helvetica Physica Acta **6**, 110 (1933).

[123] V. C. Rubin, J. Ford, W. K., and N. Thonnard, apj **238**, 471 (1980).

[124] D. Clowe, M. Bradač, A. H. Gonzalez, M. Markevitch, S. W. Randall, C. Jones, and D. Zaritsky, The Astrophysical Journal **648**, L109 (2006).

[125] D. N. Spergel and P. J. Steinhardt, Phys. Rev. Lett. **84**, 3760 (2000).

[126] D. Hooper, D. P. Finkbeiner, and G. Dobler, Phys. Rev. D **76**, 083012 (2007).

[127] Planck Collaboration *et al.*, A&A **641**, A1 (2020).

[128] Planck Collaboration *et al.*, A&A **641**, A1 (2020).

[129] G. Bertone, D. Hooper, and J. Silk, Physics Reports **405**, 279 (2005).

[130] P. Arias, D. Cadamuro, M. Goodsell, J. Jaeckel, J. Redondo, and A. Ringwald, Journal of Cosmology and Astroparticle Physics **2012**, 013 (2012).

[131] W. Hu, R. Barkana, and A. Gruzinov, Phys. Rev. Lett. **85**, 1158 (2000).

[132] K. Gebhardt *et al.*, The Astrophysical Journal **539**, L13 (2000).

[133] G. Arcadi, M. Dutra, P. Ghosh, M. Lindner, Y. Mambrini, M. Pierre, S. Profumo, and F. S. Queiroz, The European Physical Journal C **78**, 203 (2018).

[134] J. Jaeckel and A. Ringwald, Annual Review of Nuclear and Particle Science **60**, 405 (2010).

[135] P. Agnes *et al.*, Phys. Rev. Lett. **121**, 111303 (2018).

[136] P.-A. Amaudruz *et al.*, Phys. Rev. Lett. **121**, 071801 (2018).

[137] D. S. Akerib *et al.*, Phys. Rev. Lett. **118**, 021303 (2017).

[138] E. Aprile *et al.*, Journal of Cosmology and Astroparticle Physics **2016**, 027 (2016).

[139] C. Fu *et al.*, Phys. Rev. Lett. **118**, 071301 (2017).

[140] D. Antypas *et al.*, (2022).

[141] P. W. Graham, J. Mardon, and S. Rajendran, Phys. Rev. D **93**, 103520 (2016).

[142] C. Boutan *et al.*, Phys. Rev. Lett. **121**, 261302 (2018).

[143] R. Khatiwada *et al.*, Review of Scientific Instruments **92**, 124502 (2021).

[144] S. Lee, S. Ahn, J. Choi, B. R. Ko, and Y. K. Semertzidis, Phys. Rev. Lett. **124**, 101802 (2020).

[145] J. Jeong, S. Youn, S. Bae, J. Kim, T. Seong, J. E. Kim, and Y. K. Semertzidis, Phys. Rev. Lett. **125**, 221302 (2020).

[146] O. Kwon *et al.*, Phys. Rev. Lett. **126**, 191802 (2021).

[147] L. Zhong *et al.*, Phys. Rev. D **97**, 092001 (2018).

[148] K. M. Backes *et al.*, Nature **590**, 238 (2021).

[149] M. D. Eisaman, J. Fan, A. Migdall, and S. V. Polyakov, Review of Scientific Instruments **82**, 071101 (2011).

[150] B. Holdom, Physics Letters B **166**, 196 (1986).

[151] N. Vinyoles, A. Serenelli, F. Villante, S. Basu, J. Redondo, and J. Isern, Journal of Cosmology and Astroparticle Physics **2015**, 015 (2015).

[152] S. Chaudhuri, P. W. Graham, K. Irwin, J. Mardon, S. Rajendran, and Y. Zhao, Phys. Rev. D **92**, 075012 (2015).

[153] J. I. Read, Journal of Physics G: Nuclear and Particle Physics **41**, 063101 (2014).

[154] T. A. Savard, K. M. O'Hara, and J. E. Thomas, Phys. Rev. A **56**, R1095 (1997).

[155] R. Loudon, *The Quantum Theory of Light*, 3rd ed. (Oxford University Press, New York, 2000).

[156] J. D. Jackson, *Classical Electrodynamics*, 3rd ed. (John Wiley & Sons, New York, 1999).

[157] W. R. Leo, *Techniques for nuclear and particle physics experiments* (Springer-Verlag, Berlin, 1994).

[158] H. An, M. Pospelov, and J. Pradler, Phys. Rev. Lett. **111**, 041302 (2013).

[159] H. An, M. Pospelov, J. Pradler, and A. Ritz, Phys. Rev. D **102**, 115022 (2020).

[160] E. Aprile *et al.*, Phys. Rev. Lett. **123**, 251801 (2019).

[161] P. Brun *et al.*, The European Physical Journal C **79**, 186 (2019).

[162] S. Peil, Ph.D. thesis, Harvard University, 1999.

[163] L. S. Brown, K. Helmerson, and J. Tan, Phys. Rev. A **34**, 2638 (1986).

[164] S. Kotaka *et al.*, arXiv e-prints arXiv:2205.03679 (2022).

[165] S. Knirck, T. Yamazaki, Y. Okesaku, S. Asai, T. Idehara, and T. Inada, Journal of Cosmology and Astroparticle Physics **2018**, 031 (2018).

[166] E. D. Hunter, N. Evetts, J. Fajans, W. N. Hardy, H. Landsberger, R. Mcpeters, and J. S. Wurtele, Physics of Plasmas **25**, 011602 (2018).

[167] J. N. Tan, Ph.D. thesis, Harvard University, 1992, (thesis advisor: G. Gabrielse).

[168] T. M. ONeil, The Physics of Fluids **23**, 725 (1980).

[169] T. M. O'Neil and D. H. E. Dubin, Phys. Plas. **5**, 2163 (1998).